Lawrence Berkeley National Laboratory
Recent Work

Title

APPLICATION OF CONTROLLED INTERFACIAL PORE STRUCTURES TO PORE PERTURBATION AND PORE DRAG IN ALUMINA

Permalink

https://escholarship.org/uc/item/6r06k187

Author

Rodel, J.H.

Publication Date

1986-11-01

eScholarship.org Powered by the California Digital Library
University of California

LBL-26211

AUG 16 1991

c.2

Lawrence Berkeley Laboratory

UNIVERSITY OF CALIFORNIA

Materials & Chemical Sciences Division

RECEIVED
LAWRENCE
BERKELEY LABORATORY

JAN 25 1989

LIBRARY AND
DOCUMENTS SECTION

Application of Controlled Interfacial Pore Structures to Pore Perturbation and Pore Drag in Alumina

J.W. Rödel
(Ph.D. Thesis)

November 1986

TWO-WEEK LOAN COPY

This is a Library Circulating Copy which may be borrowed for two weeks.



Prepared for the U.S. Department of Energy under Contract Number DE-AC03-76SF00098.

LBL-26211

c.2

DISCLAIMER

This document was prepared as an account of work sponsored by the United States Government. While this document is believed to contain correct information, neither the United States Government nor any agency thereof, nor the Regents of the University of California, nor any of their employees, makes any warranty, express or implied, or assumes any legal responsibility for the accuracy, completeness, or usefulness of any information, apparatus, product, or process disclosed, or represents that its use would not infringe privately owned rights. Reference herein to any specific commercial product, process, or service by its trade name, trademark, manufacturer, or otherwise, does not necessarily constitute or imply its endorsement, recommendation, or favoring by the United States Government or any agency thereof, or the Regents of the University of California. The views and opinions of authors expressed herein do not necessarily state or reflect those of the United States Government or any agency thereof or the Regents of the University of California.

LBL-26211

Application of Controlled Interfacial Pore Structures to Pore Perturbation and Pore Drag in Alumina

Juergen Werner Rödel
(Ph.D. Thesis)

Materials and Chemical Sciences Division
Lawrence Berkeley Laboratory
1 Cyclotron Road
Berkeley, California 94720
USA

November 1986

Supported by the U.S. Department of Energy under Contract Number DE-AC03-76SF00098.

The Application of Controlled Interfacial Pore Structures to Pore Perturbation and Pore Drag in Alumina

by

Juergen Roedel

Abstract

A new technique has been developed which allows generation of intergranular pore structures with pores of almost any size, spacing, shape and number. This method is based on photolithographic techniques, ion beam etching and hot pressing. The material studied is alumina; the purpose of the investigation is a simulation of various aspects of sintering. If an etched sapphire wafer is bonded to an unetched sapphire disk, bicrystals with well-defined pore geometries are produced. These samples are utilized to monitor the evolution of initially instable pore structures such as pore channels and flat cracks. The behavior of these features is found to depend strongly on the crystallographic orientation of the bonding plane, and in the case of pore channels, also depends strongly on the channel direction. As a byproduct, metastable and stable faceted pore geometries as a function of orientation in the bicrystal can be monitored. If an etched sapphire wafer is bonded to a dense polycrystalline matrix (undoped and MgO-doped alumina), grain growth under the influence of pore drag can be studied. Results can be expressed in the form of a surface diffusion coefficient $D_s = 0.55\text{-}1.51 \times 10^{-7}\ cm^2/s$ for undoped

alumina and D_s = 3.47-5.40 x 10^{-7} cm^2/s for MgO-doped alumina (for 1600 °C). In the same experiment, the conditions for pore-boundary separation can be defined. As a byproduct, grain growth in a dense matrix and grain boundary migration of basal plane sapphire into alumina have been measured. Furthermore, the applicability of this method to pore coarsening and pore elimination has been shown.

Acknowledgements

First I would like to thank my supervisor Andy Glaeser who gave me the right amount of both freedom and guidance such that I could succeed where I wanted to. Second I appreciated very much the help given by several researchers in the ceramics group, particularly Rowland Cannon, Craig Carter, Brian Dalgleish and Toni Tomsia. This work would also not have been possible without the very prompt assistance of the staff in the microfabrication laboratory in the EECS department. Without the encouragement and help of Haesla, however, particularly through the first year, I might not have succeeded or might not even have come here. Finally, I would like to thank Prof. Tomandl from the University of Erlangen-Nürnberg for his support during the course of this work.

Schließlich möchte ich meinen Eltern danken, die alles ermöglichten und immer so gut verstanden.

Juergen Roedel

November 1988

Table of Contents

I. Introduction 1

II. A controlled experiment: The method of controlled interfacial pore structures 3

1. Background

1. 1. Model experiments designed to further the understanding of sintering 3

1. 1. 1. The need for model experiments 3

1. 1. 2. Sintering experiments 4

1. 1. 3. Non-sintering experiments 7

1. 2. Computer-controlled pore structures in materials science 9

2. Description of the method 10

2. 1. General procedure 10

2. 1. 1. The general idea 10

2. 1. 2. Mask making 11

2. 1. 3. Photolithography 12

2. 1. 4. Ion beam etching 14

2. 1. 5. Hot pressing 16

2. 2. Opportunities and limitations 17

2. 3. Applications 21

3. Conclusions 22

III. Morphological evolution of pore channels in alumina 24
1. Background 24
2. Experimental approach 29
3. Results 31
3. 1. Description of the evolution 31
3. 2. Kinetics 37
4. Discussion 39
5. Conclusions 45

IV. Pore drag and pore-boundary separation in alumina 46
1. Background 46
1. 1. Experimental methods 46
1. 2. Theoretical models 49
2. Experimental approach 51
2. 1. Sample preparation 51
2. 2. Measurements 54
3. Results 55
4. Discussion 58
5. Conclusions 64

V. Suggestions for future work 66
1. The technique 66
2. Equilibrium structures 67
3. Kinetics of pore instabilites and pore interactions 68
4. Pore and grain boundary mobilities 69
5. Aspects of fracture mechanics 69

VI. Concluding remarks 71

Appendix: 72

A. 1. Surface energy anisotropy in alumina 72

1. 1. The crystallographic structure of alumina 72

1. 2. Descriptions of anisotropic surfaces 72

1. 3. Dihedral angles and interfacial energies in alumina 74

1. 4. Observations on the surface energy anisotropy in alumina 75

A. 2. A study of crack healing in alumina 79

2. 1. Background 79

2. 2. Experimental approach 81

2. 3. Results and discussion 82

2. 4. Conclusions 88

A. 3. A technique to study pore coarsening and pore elimination 90

3. 1. Background 90

3. 2. Experimental approach 92

3. 3. Opportunities 94

3. 4. Conclusions 97

A. 4. Grain growth in dense alumina 98

4. 1. Background 98

4. 2. Experimental approach 99

4. 3. Results and discussion 99

4. 3. 1. Kinetics of grain growth 99

4. 3. 2. Interactions between deformation and grain growth 103

4. 4. Conclusions 103

References 105

Tables 129

Figure captions 133

Figures 142

I. Introduction

The evolution of porous microstructures upon heat treatment is dominated by a competition between two concurrent and interactive processes. Coarsening processes of particles reduce the overall surface grain boundary energy, while coarsening of intergranular pores decreases the surface area but increases the grain boundary area. Densifying mechanisms reduce the overall surface energy to a higher degree than the concurrent increase in grain boundary energy. It is this competition, which, if coupled with the unknown geometry on the particle level, makes sintering an inherently complex process to model.

Our ability to understand these separate mechanisms can be greatly enhanced by developing model experiments, which can describe separate components of the overall evolution. These generally facilitate the comparison between experiments and theoretical predictions greatly.

After it was recognized, that there was a whole series of sintering stages without separable model experiments (see II.I), new techniques were developed to study separate sintering events (see II.2). Controlled interfacial pore structures are central to these new methods.

New model experiments on the morphological evolution of pore channels will be introduced in the following (see III.) as an example of a study of surface diffusion kinetics of immobile pores in a bicrystal. The study on pore drag and pore-boundary separation is representative of observations of mobile pores at a single crystal-polycrystalline interface (see IV.). Preliminary studies on surface

energy anisotropy (see A.I), crack healing (see A.2.) and both pore growth and pore elimination (see A.3.) will complement the more detailed studies in the main part of this work. Finally grain growth in a dense alumina (see A.4.) will be discussed as a byproduct of pore drag studies.

It should be pointed out, that, although all studies discussed here, were performed in alumina, this new technique is not limited to one particular ceramic, but of general applicability.

II. The method of controlled interfacial pore structures

II. 1. Background

II. 1. 1. Model experiments previously available

II. 1. 1. 1. The need for model experiments

Figure 1 illustrates the basic problems that are encountered in sintering of homogeneous single phase materials. Besides the aforementioned interactions between competing processes, and the complicated geometry on the particle level, we also face other problems. The transport coefficients are only (if at all) known with poor accuracy. Moreover, the effect of minor dopant (or impurity) concentrations on these transport coefficients is by and large unknown, and only rudimentarily understood[1,2]. This knowledge ought to be available over a range of temperatures. Thus the activation energies of transport coefficients together with the thermodynamic quantities, such as the solubility limit of dopants as a function of temperature, should be known for a more complete understanding of sintering. Kinetic, thermodynamic and geometric parameters are often only treated as single-valued and only rarely are distributions in the value considered[3]. In particular, solids are often treated as isotropic, and anisotropy effects are neglected. In addition to these problems, rearrangement in the initial stage leads to a change of the local and overall geometry.

It appears, that particularly the call for meaningful measurements of transport coefficients, but also an assessment of effects of anisotropy can only be answered, if the two basic problems with model experiments are solved: the starting geometry ought to be

known, and only one process (in the ideal case) should be active. Only then can we attempt to answer the three basic questions:

1) What is the evolution of the whole process (e.g., what is the influence of the interface reaction on the overall reaction rate, how does one pore affect another)?

2) What are the transport coefficients, and how are they affected by additives?

3) What are the relevant thermodynamic quantities, and how are they influenced by additives?

In the following, existing model experiments which might help us to better understand sintering are discussed briefly. Particular consideration will be given to the problems discussed above. Experimental methods based on simulation of a specific part of the sintering process will be considered first.

II. 1. 1. 2. Sintering experiments

Attention will be directed to the promise and capability existing model experiments offer. Shortcomings of these methods, and needs for further developments of model investigations will be identified. Detailed discussions of particular stages of the sintering process will, however, only be given in the later sections.

Figure 2 contrasts various stages of the sintering process with the actual available model sintering experiments. While there are some stages, where good experimental simulations are available (e.g., grain growth), there are some where the available method is incomplete (e.g., densification) or simply not existent (e.g., pore drag).

Effects of rearrangement have been assessed by observing the reconfiguration of 2-dimensional particle arrays (typically copper) during heat treatment. The dominant change is one of the pore size distribution. These experiments have been conducted, amongst others, by Exner[4,5], and give, from the experimental point of view, a satisfying result.

Neck growth experiments simulate the processes during initial stage sintering, and were performed with spheres on plates[6,7,8], two spheres[9,10] and lines of spheres[11]. They simulate the initial stage of sintering, but usually employ particles of a size orders of magnitudes larger than the particles encountered in a typical ceramic powder. While determination of the appropriate diffusion coefficient might be difficult[12], such experiments nevertheless are able to model the actual behavior in a powder compact.

The intermediate and the final stages of sintering are described by grain growth, pore shrinkage, pore growth (coalescense and Ostwald ripening), pore perturbation and pore drag (Fig. 2). All these processes and the attempts to find model experiments to follow the separate events will be described briefly.

Existing experiments on pore perturbation are solely based on the evolution of flat cracks upon heat treatment[13,14]. During crack healing (see also A.2.), pore channels form, whose morphological evolution then can be followed. Though these experiments have provided some insight into the process, they rely on pore geometries as determined by the outcome of the crack healing experiment and allow neither good experimental control (e.g., the cross section of the channels is not accessible) nor detailed measurement (see also III.1.).

A controlled experiment on pore drag requires monitoring the movement of single pores or an array of pores as a byproduct of grain boundary motion. Ideally, other processes (particularly densification) should not interfere. Before this work started there was no suitable experiment at all for that purpose (see also IV.1).

Observations on densification on the other hand require that grain growth which lead to increased pore spacing and pore size does not interfere. The approach taken so far has been one of accelerating the densification process (by pressure application[15,16]), rather than by reducing the growth rate. Hot pressing is a valuable addition to sintering experiments, but fails to completely eliminate the interfering (to densification) grain growth process (see also A.3.).

Pore growth is caused by two processes: pore coalescense as a byproduct of pore drag and pore coarsening (transport of vacancies from small to large pores). It is this particular duality combined with the fact that the geometry of pore structures was difficult to control, that made interpretation of previous studies difficult[17,18] (see also A.3.).

Grain growth in a 100 % dense matrix appears a particularly worthwhile experiment, as average grain boundary mobilities[19,20] as well as specific mobilities of large seeded grains[21,22,23] can be measured. As no interfering processes occur, this method does not require major improvements (see also A.4.).

The recognition that the sintering process cannot be described in terms of separate processes led to experiments which attempted to assess the competing processes as separable[24,25]. These studies emphasize the relationship between various critical parameters

(grain boundary area vs. surface area[24], grain size vs. density[25]) and thus increased the amount of information extracted from straightforward sintering experiments. Both were inspired by Cannon's modelling effort on the densification - coarsening competition during sintering[26].

Consequently, this review indicates that there is a strong need for further development of new model experiments for sintering. However, before we proceed further towards this goal, we need to briefly assess the contributions made by non-sintering experiments to our understanding of the microstructural evolution of porous compacts.

II. 1. 1. 3. Non-sintering experiments

The purpose of non-sintering experiments is simply to provide materials properties (diffusion coefficients and interfacial energies). The methods used are listed in Figure 3, and their benefits and shortcomings will be contrasted briefly.

Experimental results, wherein a radioactive isotope of one of the constitutive elements of the material is applied to the surface, and the diffusion profile of that isotope measured after various heat treatments were reported for both oxygen[27-29] and aluminum[30] in alumina. Limitations lie in the availability of suitable radioactive isotopes with high specific activity[30], and an accurate measurement of the surface area where the isotope exchange takes place[31]. The calculated grain boundary diffusion coefficients obtained are average values for all possible grain boundaries. Tracer methods are nevertheless considered very beneficial, as results seem very

reproducible if special treatments (e.g. preannealing[28,29]) are accounted for.

Diffusional creep measurements appear to be an excellent means of obtaining information on diffusion processes in polycrystalline ceramics. In fact, most data on the lattice diffusion coefficient D_l and the grain boundary diffusion coefficient D_{gb} (particularly as a function of dopant concentration) in alumina are derived from creep measurements[32]. Interfacial effects related to the annihilation or creation of defects at grain boundary sinks and sources can also be observed, not however, interfacial effects related to defects at surfaces (see also A.3.).

Scratch smoothing measures the surface diffusion coefficient by following the decay of periodic gratings after successive heat treatments[33-35]. Depending on the method used to produce the scratches, this technique might provide very reproducible data, but experimental results can be affected strongly by surface energy anisotropy[33].

The method of grain boundary grooving has the potential to both show and disguise aspects of anisotropy. Bicrystals can be used to study the kinetics of grooving at certain grain boundaries,[36,37] and a polycrystalline material can be used to study the kinetics at random grain boundaries, and thereby to obtain an average value for the surface diffusion coefficient[8,38,39].

Both methods based on the morphological evolution of perturbations on the external surface rely on monitoring very small geometrical changes (see also A.2.), and require very careful

evaluation. Also, they both assess the kinetics only at external surfaces, not at internal surfaces, which are really relevant.

While the overwhelming focus in sintering studies is on the determination of the transport coefficients, the accurate determination of interfacial energies[40-42] is somewhat neglected. These measurements are based on an evaluation of contact angles, and so far have centered their attention on gaining average values only (for relative interfacial energies see also V, A.1.).

These few thoughts might suffice to illustrate the tremendous need for the further development of model experiments to further understand sintering. Again the needs are to tailor controlled microstructures with well-known geometries, which isolate specific processes, and eliminate the normally competitive and interactive processes. In section II.2. these new techniques, which are based on computer-controlled internal pore geometries, will be introduced and developed. Before describing the actual technique developed during the course of this work, however, it might be worthwile to consider other pore geometries, which were also created through computer-controlled means.

II. 1. 2. Computer-controlled pore structures in materials science

Unfortunately the potential of microfabrication techniques for materials research (beyond electronic materials) has yet to be fully realized. While only a few researchers have utilized these techniques to produce controlled surface structures (e.g., Huang et al.[33]), there are even fewer instances in which these technique have been used to

produce controlled interfacial structures. Though these developments are not related to this work, as the kinetic evolution of interfacial features was not followed, it seems appropriate to acknowledge their existence.

Patterned macrovoids (in the range of several hundred microns) were introduced into PZT ceramics using fugitive ink and tape technology[43,44]. This method was developed to enhance the hydrostatic pressure-sensing response of the ceramic.

Burger et al.[45] used photolithographic techniques to introduce flaws into Nb/Al_2O_3 interfaces, which were 5 - 200 μm wide and 2 μm deep. No morphological changes of these cracks could be observed after heat treatment, but the internal surface acted as a preferential site for precipitation of previously dissolved Al_2O_3 during cooling.

II. 2. Description of the method of controlled interfacial pore structures

II. 2. 1. General procedure

II. 2. 1. 1. The general idea

The concept of controlled interfacial pore structures is based on photolithographic techniques, ion beam etching and hot pressing[46]. It was originally conceived in order to create a model experiment to study pore drag, but other possibilities soon became apparent. The photolithographic and etching techniques are utilized to create a controlled-geometry surface structure of etch pits on a single crystal sapphire wafer. Pore width, depth, spacing, shape and number can be varied and controlled. This controlled surface structure is then

transformed into an internal structure via hot pressing. Bonding to an unetched sapphire wafer results in controlled-geometry pore structures in a bicrystal and the creation of immobile pores, while bonding to a dense polycrystalline material leads to possibilities for studying pore drag and pore separation.

While this method is currently exploited only in alumina, it is not limited to this material, but can be used with every material that can be etched and bonded.

As this work might potentially be used as a handbook for future students, a rather detailed outline of the experimental step by step procedure will be given in the following sections.

II. 2. 1. 2. Mask making

Masks are used to transfer the description of the planned features from a computer file onto the sample surface. To create a computer file, a graphics editor (kic[47]) and a color graphics terminal have to be employed. The graphics editor has the ability to create simple geometries (boxes, lines), move, rotate and copy them and combine separate computer files. Two further programs[47] transform the original first "kic cell" into a "mann file" which can be handled by the pattern generator[a]. This exposes a glass disk through an adjustable aperture according to the previously given commands (from the "mann file"). The glass disk is developed and forms the mask which can be used to selectively expose the photoresist-coated sapphire wafer.

The smallest features which can be generated on the mask are 2 μm x 2 μm square elements. The number of features is only

limited by the amount of time available on the pattern generator and on the quality of the mask. So called emulsion masks have lower resolution than chrome oxide and iron oxide masks, but need only 20 % of the time on the pattern generator. High resolution masks can be prepared with up to 200,000 features required pattern generator time about 40 hours).

a: Pattern generator, GCA Corporation, Bedford, Ma.

II. 2. 1. 3. Photolithography

It is a common misconception, that photolithography is a new technique. Let us first clarify this issue by quoting from Thompson and Kerwin[48] (underlining added):

> Lithography, the art of printing from a smooth stone on which the image to be printed is hydrophobic and ink receptive while the clear areas are hydrophilic and ink repellent, was invented in 1798 by Aloys Senefelder of Bavaria. In 1813, after the technique had become popular in Paris, Joseph Nicephore Niepce of Chalon-sur Saone began testing the lithographic properties of natural stones. His son performed all the grease pencil artwork required in these experiments until he was drafted by Napoleon. Niepce then concentrated his efforts for several years on developing a technique to form images on the stone directly, either by light reflected from the object of interest or by contact printing existing etchings made translucent with oil. He succeeded in 1822, using bitumen of Judea as the photoresist and a mixture of oil of lavender and mineral spirits as the developing sovent. His first photograph from nature required an 8-hr exposure. Bitumen of Judea had been in use as a ground or etching resist since the introduction of etching in AD 1500. Its ability to harden on exposure to light had been recognized by the ancient Egyptians who used it to rigidify mummy wrappings.

All processing of surfaces was performed in Class 100 clean rooms in the microfabrication laboratory in the EECS department. Wafer surfaces were first ultrasonically cleaned with a solution of 1 part NH_4OH, 1 part H_2O_2 and 5 parts H_2O (hereafter referred to as SC1) to remove organic residue from the surface, and 1 part HCl, 1 part H_2O_2 and 6 parts H_2O (SC2) to remove trace metals. They were then rinsed in purified water and baked out at 150°C for 20 min. A nitrogen gun was then used to blow off any remaining dust particles, and the wafer placed on a photoresist spinner. A drop of positive photoresist[b] was placed onto the wafer (typically 12 mm x 10 mm x 675 μm), which was then spun at 5000 rpm for 30 seconds to produce a uniform, 1.8 μm thick photoresist layer. Subsequently, wafers were baked out at 90 °C for 20 min on a hot plate. The purpose of the pre-exposure bake-out is to dry the resist film, prevent tackiness and improve adhesion to the substrate. A hot plate is to be preferred to a heating oven to ensure proper drying from the sapphire-photoresist interface.

The thickness of the photoresist can be varied between certain limits. A thin layer is preferred if high resolution and small etch depths are the goal. If a deep etch should be achieved, the photoresist has to be applied in a thicker layer (as the photoresist also erodes under the ion beam). At 2000 rpm, a uniform coating, 2.6 μm thick, is obtained, using the Shipley photoresist[b]. Special photoresists[c] can give thicknesses up to 30 μm, but the resolution of small features deteriorates with increasing thickness due to focusing problems during exposure, and light scattering in the photoresist layer.

In the next step the pattern is transferred from the mask onto the photoresist-coated wafer by exposure with ultraviolet light. This produces photochemical changes in the resist that result in a differential solubility. For this work, all material was exposed in a 4:1 projection printer[d], which reduces the features in the mask by a factor of 4 (which has to be included in the original mask design). Time for exposure and best focus have to be determined in prior experiments to obtain optimum resolution. Figures 4a-c illustrate the effect of repeatedly doubling the exposure time on the structure of monodispersed etch pits in sapphire. Increasing exposure time broadens features considerably, until pores connect as in Fig. 4c.

Finally the photoresist is developed[e] for 1 min, rinsed with water for 1 min, blown dry with a nitrogen gun, and baked out at 95 °C for 10 min.

More details on photoresists, particularly their chemistry, effects of baking, exposure and development are given in review papers by Thompsen et al.[48,49].

b: Shipley 1400:13, Shipley Co., Inc., Santa Clara, CA.

c: AZ 4303 Photoresist, American Hoechst Corporation, Sommerville, NJ.

d: Canon, Santa Clara, CA.

2. 1. 4. Ion beam etching

Sapphire is very inert and can only be etched chemically with boiling phosphoric acid at 203 °C, which gives very poor resolution. For this reason, etching was performed with an argon ion beam in an ion mill[e] under perpendicular incidence. An aluminum substrate was coated with an emulsion of polyphenylether (a low-vapor-pressure

oil) and colloidal silver, and the sapphire was placed on top. The emulsion provides an effective means of removing heat generated during ion bombardment. The aluminum substrate is water-cooled, and a heat shield limits bombardment to a square area of 3 cm edge length. These precautions are necessary to prevent photoresist deterioration during etching. The ion mill chamber is evacuated to $\approx 1.3 \times 10^{-4}$ Pa, and subsequently argon is injected to establish an argon pressure at 1.3×10^{-2} Pa. The substrate is continuously rotated during etching.

Procedures for generation of an argon ion beam are standard, and will not be reported here. Note, however, that the beam is uniform over a diameter of $\approx$ 7 cm (without heat shield), and consequently, a large number of specimens can be etched concurrently under uniform conditions. At an accelerating voltage of 1 kV, the current density was 0.5 mA/cm^2, and the etch rate was $\approx$ 0.6 $\mu m/hr$ on basal plane sapphire[f]. The depth of the larger etch pits (>5μm width) can be measured with a surface profilometer[g]. Depths of surface structures were constant for all structures over the entire 9 cm^2 bombarded area.

A series of review articles[50-53] give information on more detailed issues of ion beam etching, such as sputtering yields[50,51,53], angle of incidence[51,52], problems with redeposition[53], influence of ion gas[50,53] and ion energy[50,53].

After the etching process was completed, the photoresist was removed with acetone, and the sapphire was cleaned with purified water. To remove all organic residue (from the bombarded photoresist and the oil from the emulsion), wafers were cleaned with

solutions SC1, SC2 and heat treated in air for 2 hours at 1200 °C, followed by a second cleaning with SC1 and SC2.

Later sections contain many examples for etched structures. For the present, just one set of bimodal "surface pore" structures is shown in Fig. 5. Note the high resolution of the process, as the smallest pores have a diameter of less than 1 μm. The flexibility and reproduciblity of the method is also illustrated through Fig. 5 (see II. 2. 2 for a more detailed discussion). Spacings between the different sized pores increase from the left to the right and sizes of larger pores increase from top to bottom.

e: Veeco Microetch System, Veeco Instruments Inc., New York, N. J.

f: Adolf Meller Company, Providence, R. I.

g: Alphastep 200, Tencor Instruments, Mountain View, CA.

II. 2. 1. 5. Hot pressing

Before pressure bonding, samples were checked for attached surface particles, and these were removed with either a nitrogen gun or clean room compatible paper[h].

For hot pressing the etched sapphire was placed on top of either another untreated sapphire or dense polycrystalline alumina. Both were loaded into a high purity graphite die[i] in between hot pressed boron nitride spacers[j]. Typical sample dimensions were 12 mm x 10 mm x 0.7 mm. Alignment inside the die was ensured by resting both sapphire disks against a third intermediate pre-cut boron nitride spacer.

Samples were subsequently heated to 1370 °C with a ramp rate of ≈7°C/min and bonded at 15 MPa for 60 min in a vacuum of

2.6×10^{-3} Pa. The bicrystals were continuously bonded and pore structures reflecting the etched surface structures were obtained. Two methods are available to check the quality and continuity of the interfacial bond. The samples can be cut perpendicular to the bonded interface, polished, thermally etched and then examined with an SEM. Figures 6a,b show examples of this technique where the etched sapphire was bonded to a polycrystalline alumina. The structures were originally in the surface of the single crystal (top), and the pores have not yet achieved equilibrium shapes; they are not symmetric about the interface and may undergo further contraction parallel to the boundary and expansion perpendicular to it. The transparency of sapphire also allows (nondestructive) observation of internal features using optical microscopy (Fig. 7 a,b), which affords quick assessment of the interfacial geometry over the whole bonded area. Fig. 7a gives an example of internal pore structures, demonstrating a bimodal pore size distribution, while Fig. 7b illustrates internal features with varying aspect ratio.

h: Techni-Cloth, The Texwipe Company, Upper Saddle River, NJ.

i: Poco Graphite, Inc., Decatur, TX.

j: Union Carbide Corp., Cleveland, OH.

II. 2. 2. Opportunities and limitations

This section addresses both the experimental limitations associated with, and the experimental possibilities afforded by, the described technique for producing well-defined intergranular pore structures. Several possible applications will be introduced in the next section, including a number of novel experimental techniques

that allow the systematic investigation of several aspects of microstructural development in ceramics.

Almost every conceivable pore geometry can be generated on a ceramic surface and transferred to an interface. Pores with both circular and square cross sections and varying aspect ratio can be created. Pore arrays of almost any pore size, spacing and number can be produced.

The number of pores that can be generated at an interface is related to the number of features that can be implemented into a particular mask. This number in turn depends on the capabilities of the particular pattern generator used. However, it is possible to generate about two hundred thousand features on a high resolution mask, and this same mask can be transferred up to 9 times onto different positions on the wafer (accuracy of lateral movements about 0.75 μm) using the stepping capabilities of the Canon mask aligner. This limitation is therefore not expected to be of particular concern. Large pore numbers are only needed for studies of pore elimination (see A. 3.)

Pore size and spacing are limited by the fact that visible light is used to expose the photoresist. Thus, pore sizes and spacings in the sapphire surface will have minimum values of about 1 μm (see small pores in Fig. 5 a-d). This feature size in conjunction with achievable pore depths establishes a minimum equivalent pore volume approximately that of a spherical pore with radius 0.3 μm. However, if electron lithography[48] is used, features with a limit of less than 1000 Å equivalent radius can be produced (see also V.).

The upper and lower limit in the depth of etched features and therefore the etching time should be governed by two considerations. Since it is desirable that etched features, as opposed to unintentional intrinsic surface structures, determine the final intergranular pore structure, the minimum depth of etched pores will depend on the surface finish. This is not a problem for sapphire crystals since they can be obtained with a surface finish of 0.025 μm[f]. However, if theoretically dense polycrystalline samples are to be used, care must be taken to ensure a good surface finish.

A limiting maximum etch pit depth is a consequence of the fact that the ion beam etches both the sapphire and the photoresist. The etch rate of the latter is approximately 3 times that of the sapphire under the conditions used. This establishes a maximum depth of etched features of about 0.8 μm using the Shipley photoresist[b]. Again, if a lower resolution is acceptable, thicker layers of photoresist[c] can be applied and the depth of etched features can be extended to several micrometers. Although one should be aware of these limitations, they should not pose major problems.

A further limitation lies in the fact, that single crystals to be bonded must have compatible thermal expansion coefficients to prevent cracking. This is particularly critical in alumina, where the thermal expansion coefficients along the a-axis and c-axis differ by up to 10 %[53]. Thus all twist boundaries of basal plane sapphire can be produced, but only limited freedom is given if bonding two single crystals along their prismatic planes. All symmetric tilt boundaries are also possible.

Finally, the overall design of surface structures on the sapphire must be considered. If closely spaced etch pits are uniformly distributed on the entire surface, all pores may vanish during hot pressing because of vacancy condensation along the interface. Uniform vacancy condensation requires a vacancy flux that increases linearly with distance from the midpoint between two equisized pores. This process in turn requires a parabolic vacancy concentration profile between the two pores if the concentration gradient is the driving force for the vacancy flux. To reduce the vacancy flux, and hence the pore shrinkage rate, the inter-pore spacing must be increased. Fortunately, this need not be done uniformly and throughout the sample; isolating arrays of specific pore size and spacing with pore-free regions several hundred micrometers wide is sufficient to significantly reduce shrinkage both during hot pressing and subsequent annealing. This particular choice of geometry effects an equilibration of local stresses between points next to the pore surface and the midpoints between pores through a flow of vacancies from the pores to the grain boundaries. This relaxation of local stresses reduces the transport of matter in the regions of pore arrays and has the pore-free ligaments solely carrying the compressive stress applied by the hot press (see also A. 3.).

The exciting opportunities associated with this technique lie of course in the wide variety of geometries and high number of features available. Hundreds of data points can be gathered from the sample and several different experiments can be conducted simultaneously on the same interface. If doped crystals are used, transport

coefficients and relative interfacial energies can be recorded as a function of dopant concentration.

II. 2. 3. Applications

Several experimental studies will be introduced, that exploit the ability to create well-defined intergranular pore structures.

The migration of pore arrays can be studied if pores at either single crystal-polycrystal interfaces or at boundaries originally subtending an acute angle with a free surface[55,56] are produced. The driving force for pore migration (governed by the grain size of the theoretically dense matrix) as well as the pore size and pore spacing of the internal pore structures can conveniently be changed. This method allows study of pore drag effects and pore boundary separation (see IV.).

The morphological evolution of non-equilibrium shapes like pore channels (see III.) and flat plates (see A. 2.) can be conveniently followed. Studies of pore morphology evolution in transparent materials are particularly attractive, because simple optical observations can be performed between successive heat treatments.

If pores are allowed to interact with each other (spaced closely), one is inevitably lead to studies of pore coarsening. Theoretical treatment of these experiments is greatly facilitated if simple, symmetric pore geometries are chosen (see Fig. 5 a-d). As a result, information on the grain-boundary and the lattice diffusion coefficient as well as on effects of interfacial rate control can be obtained. If originally random distributions are chosen, the evolution of steady state distributions can be followed (see A. 3.).

In contrast, vacancy transport from pores to grain boundaries necessitates removal of the pore-free ligament after hot pressing. Vacancies can then diffuse from pore surfaces to grain boundaries and effect pore densification. Again, the relevant transport coefficients as well as the effect of interfacial rate control can be studied (see A. 3.).

Last, but not least, experiments on surface energy anisotropy and the effects of various grain boundaries intersecting a pore should be mentioned. As will be shown, the plane and axial direction of a pore channel have a strong influence on the morphological evolution of these channels. Thus, studies of the equilibrium pore shape in the lattice, or at a grain boundary, are fundamental to an improved understanding of the kinetics associated with changes on pore morphology (see A. 1.).

Only some basic applications have been mentioned here; a discussion of future applications of this method will follow in chapter V. The use of this technique for controlled studies of fracture mechanics in composite materials will also be considered in chapter V.

II. 3. Conclusions.

A new technique for producing intergranular pore structures with controlled pore size, spacing, and number is now available. It combines a photolithographic process, ion beam etching, and hot pressing of an etched single crystal either to a second single crystal or to a polycrystalline material. The range of experimental options accessible by far outweighs the limitations imposed. New experimental opportunities emerge for fundamental studies of grain

growth under the influence of pore drag, pore morphology evolution/crack healing, surface energy anisotropy and interfacial energies, and coarsening and elimination of pores.

III. Morphological evolution of pore channels in alumina

III. 1. Background

Rod-shaped particles or pores are thermodynamically unstable since they can reduce their interfacial energy by either evolving into one sphere or a series of spheres. This phenomenon can occur during intermediate stage sintering and is applicable to the stability of fiber reinforced structures at high temperatures.

The morphological evolution of pore channels (here also termed pore perturbation) during heat treatment can also be used to evaluate surface diffusion kinetics[1-5], as was done predominantly in alumina[1-4]. It is also related to instabilities of a connected structure of pores, which was investigated by Budworth[6] and Beere[7,8] to further elucidate the evolution of a powder compact during the intermediate stage of sintering. Finally the response of thermodynamically unstable elongated structures was considered in various composite materials[9-13]. Before results and shortcomings of these techniques will be discussed, we will turn to an evaluation of the theoretical descriptions available, pertaining to the evolution of elongated structures at high temperatures.

The modelling efforts of the pore perturbation phenomenon can be divided in two groups. In the first group considerations are summarized, which take the surface energy γ and the surface diffusion coefficient D_s as isotropic quantities, assume the cross section of the cylinder to be circular and do not consider any grain boundaries intersecting the pore channel. The efforts described in the second group examine the effects of surface energy anisotropy and the influence of grain boundaries intersecting the pore channels.

Both approaches focus on two aspects. Firstly, the actual morphological evolution of a pore channel, particularly the critical aspect ratio λ_{min} is discussed. This quantity determines if a cylinder breaks up into a series of pores (ovulation: $\lambda > \lambda_{min}$) or evolves into just one pore (spheroidization: $\lambda < \lambda_{min}$). A simple schematic of this distinction is given in Fig. 8. Secondly the kinetics of the perturbation process are investigated. The times to pore pinchoff are calculated for various dominant transport paths.

The first complete analysis of the morphological stability of continuous cylindrical phases has been given by Rayleigh[14]. His analysis predicts that infinitesimal periodic perturbations along the length of the cylinder with a wavelength λ exceeding $2\pi r$ (the cylinder circumference) will reduce the surface energy per unit volume, and thus will increase in amplitude. Growth of perturbations with $\lambda > \lambda_{min}$ ($=2\pi r$) eventually causes the formation of discrete particles (or pores) from an initially continuous phase.

Nichols and Mullins[15-16] considered morphological changes driven by capillarity in considerable detail. Their calculations included the evolution of semi-infinite cylinders[15] and infinite cylinders[16]. The evolution of finite rods was later considered by Nichols[17]. Both their numerical[15,17] and analytical methods[16] were based on a governing equation for the capillarity-induced shape changes of a surface of revolution by surface diffusion (Eq. 1).

$$\frac{\partial n}{\partial t} = \frac{B}{y}\frac{\partial}{\partial s}\left(y\frac{\partial K}{\partial s}\right) \qquad \text{eq.1}$$

with $\partial n/\partial t$ the normal velocity of the surface, y being measured normal to the axis of revolution, s the arc length, K the total surface curvature and B a kinetic parameter determined mainly through the surface diffusion coefficient D_s. Equation 1 was derived by Mullins[18] earlier and has its physical basis in the Gibbs-Thomson relation (Eq. 2):

$$\mu = \Omega\gamma K = \Omega\gamma(K_1 + K_2) \qquad \text{eq. 2}$$

with K_1 and K_2 the two principal curvatures, Ω the atomic volume and γ the surface energy. Equation 2 allows calculation of the chemical potential difference of atoms at different positions on a curved surface and thus gives the driving force for the morphological evolution of curved and initially unstable bodies.

Amongst Nichols and Mullins findings were, that the most rapidly growing wavelength for semi-infinite pore channels was 4.45·D for the case where surface diffusion was the dominant transport mechanism and 6.48·D where lattice diffusion was dominant[15]. For rod-shaped particles of finite length the critical aspect ratio $(L/D)_{crit.}$ is increased (to 7.2) due to the fact that channel ends recede and leave less available length for ovulation to occur[17]. This phenomenon is shown schematically in Fig. 9 for two channels with aspect ratios of 7.00 and 7.64, respectively.

The kinetics of the perturbation process can be described through Eq. 3:

$$\tau = (16/\pi r)^4 Bt \qquad \text{eq. 3}$$

where t is the characteristic time for pinchoff of the first pore at the channel end, the values for τ are dependent on channel length and given by Nichols[17]. The underlying assumption of this evaluation is, that the perturbation process is fastest at the hemispherical end caps of the cylinder and proceeds through consecutive separation of pores from there.

The first discussion of the influence of surface energy anisotropy on morphological changes occurring by surface diffusion can be traced back to Herring[19]. His result for the chemical potential at a point P on a curved surface compared to that on a flat surface forms the generalized Gibbs-Thomson equation (Eq.4):

$$\mu(P) = \Omega[(\gamma+\frac{d^2\gamma}{d\theta_1^2})K_1 +(\gamma+\frac{d^2\gamma}{d\theta_2^2})K_2] \qquad \text{eq.4}$$

where θ_1 (θ_2) is the angle between a general normal lying in the principal plane corresponding to K_1 (K_2) and the normal at P. Equation 4 was used as the basis for a further evaluation of the scratch smoothing problem by Mullins[20]. A more general discussion is given by Brailsford and Gjostein[21] on the influence of surface energy anisotropy. Cahn[22] finally noted, that the critical wavelength depends on $d^2\gamma/d\theta^2$. If $d^2\gamma/d\theta^2$ is positive (if γ is a minimum at θ = 0), the critical wavelength is increased, whereas if $d^2\gamma/d\theta^2$ is negative, the critical wavelength is decreased. Though most crystals do not exhibit transverse isotropy in their surface energy, this general

statement is thought to be true for more complicated situations. The obvious problem in the experimental application of these more advanced theories is that $d^2\gamma/d\theta^2$ is not commonly known. Since the stability of rods is sensitive to this quantity, however, Cahn suggested that this type of experiment might be used to measure this quantity.

Thermodynamic considerations on the morphological stability of elongated phases were presented by Carter and Glaeser[23-25]. The effects of coordination number and dihedral angle on the critical aspect ratio[23,24], as well as the influences of finite amplitude perturbations[25] were discussed.

The primary objective of this work is the investigation of the morphological evolution of pore channels in alumina at high temperature. This experiment can be used to deduce the surface diffusion coefficient in alumina and assess the effects of surface energy anisotropy. Most prior experimental studies investigating this phenomenon had to rely on producing pore channels through the partial healing of a flat crack[1-4]. These cracks were either introduced by inscription of single crystal sapphire with a WC tool[1], by thermal shocking of a polycrystalline alumina[2,3] or incomplete bonding of a bicrystal[4]. As a result, the geometry and crystallographic orientation of pore channels obtained was not very well defined, and it is unclear whether the channels had equilibrated in the cross section. Moreover, the experiments in polycrystalline alumina allow observation of the evolved structures only through fracturing the material, whereas the experiments in sapphire allow at least continuous monitoring of the evolution process with optical microscopy. These

studies tried to establish that pore perturbation indeed occurs through surface diffusion[1-4] by measuring the final pore spacings and sizes, which can then be compared with the theoretical predictions[16]. The measured final pore spacings, however, were about twice those predicted from the kinetic analysis. Nonetheless, a surface diffusion coefficient for alumina as a function of temperature was obtained from the experiments described[1,2]. The results are ambiguous, as the spread for the measured critical aspect ratios was very wide (and depended on the method of measurement as well as on local position[1]). Therefore, all results obtained from the above mentioned experiments on pore perturbation are subject to considerable uncertainty.

Related studies, like the evolution of pore channels in tungsten[5] or the growth of shape instabilities in composite materials[9-13] suffer from similar experimental difficulties. The original geometry of the initially unstable phase is ill-defined and/or it is very difficult to follow the evolution with good resolution and/or the exact crystallographic orientations are not known.

To remedy all these problems the concept of controlled interfacial pore structures was applied to the phenomenon. The detailed experimental approach is described in the next section.

III. 2. Experimental approach

Pore structures were produced using procedures outlined in section II and also described in an earlier publication[26]. Two masks were generated, containing channels of varying width and length. Mask I focused on short channels of varying aspect ratios (Fig. 10);

pore widths were varied from 2.2 to 5.7 μm. Aspect ratios changed from 1 to 73 for the widest channels; adjacent channel edges were spaced 20 μm apart to minimize interactions and transport between channels of differing size. In addition to the short channels, a few 3000 μm long lines were etched with the same widths, but with a spacing of only 4 μm between adjacent edges. Mask II contained channels of intermediate sizes, 3.4 and 5.7 μm wide, with aspect ratios from 20 to 93 μm for the wider channels (Fig. 11). It also featured lines 200 μm long and from 2.2 to 7.7 μm wide (Fig. 12). Shorter channels were used to evaluate critical aspect ratios during the morphological evolution of elongated voids, while larger channels were generated to observe the kinetics of these processes. Spacings between adjacent edges were again 20 μm. The number of identical features per mask varied between 7 and 120. The stepping capabilities of the mask aligner were employed to expose every mask up to 9 times onto one surface.

Features were etched into either basal plane sapphire aligned along directions $[1\bar{1}00]$ and $[11\bar{2}0]$ or into $(11\bar{2}0)$ planes along directions $[1\bar{1}00]$ and [0001]&. Crystallographic orientations of delivered sapphire wafers were verified by Laue backscattering. It is estimated that the etched features could be aligned to the specified directions with an accuracy of 3°. Channel depths (measured by surface profilometry) were 0.18 μm and 0.12μm on the (0001) and $(11\bar{2}0)$ planes, respectively.

Surface structures were transformed to an internal interface by hot pressing (1370 °C, 60 min. 15 MPa, 2.6×10^{-3} Pa) the patterned wafer to an unetched sapphire wafer. Single crystal alumina disks

were cut and half of the pieces etched. Prior to bonding, the unetched wafer was then lifted on top of the etched wafer (wafers were polished on both sides). This procedure (see Fig. 13) avoided possible formation of a bicrystal with a tilt component (as in flipping the second wafer over the first one). Optical micrographs of internal features are shown in Fig. 7 b and 14 a,b.

Subsequently, the bonded samples were annealed under vacuum (1.3×10^{-3} Pa) for varying times at 1800 °C. Structural evolution was monitored in three ways. The change of cross section was assessed by cutting bicrystals edge on and observing polished specimens with an SEM. The transparency of sapphire allows (nondestructive) observation of internal features using optical microscopy; samples were given several heat treatments and characterized intermittently. Alternatively, the bicrystals could be split along the interface, and scanning electron microscopy used to characterize the interfacial pore structure.

&: For details on the crystallographic structure of sapphire see A. 1.

IV. 3. Results

3. 1. Description of the evolution

Results for the (0001) and ($11\bar{2}0$) planes were obtained from several samples of each orientation. For each orientation, >5000 200-μm long channels and >10000 channels of variable aspect ratio were contained in the interfaces.

Equilibration in the cross section is very rapid at 1800 °C, as can be seen in Fig. 15. Pores expand perpendicular and contract parallel to the grain boundary and become symmetric to the

interface after 20 min. in Fig. 15 c),d),g),h) and 10 min. in Fig. 15 e),f). Facetting is evident. The basal plane shows a planar facet, while the other bounding planes in Fig. 15 c)-f) have curved surfaces. If pores are parallel to the c-axis, they become symmetric before they facet (Fig. 15 g),h)). Note that pores in Fig. 15 c)-f) are aligned in the same direction ($[1\bar{1}00]$), but are intersected by mutually orthogonal grain boundaries. The grain boundary in Fig. 15 e),f) distorts the pore shape to the point that the basal plane surface is no longer stable. The actual experiments of pore evolution were performed in bicrystals with twist angles <2 °; this small misorientation preserves the basal plane facet in prismatic bicrystals as will be shown later.

Internal pore structures were monitored by using optical microscopy. Light is reflected back to the observer from channels in the (0001) plane, and away from the observer from channels in the $(11\bar{2}0)$ plane, causing equilibrated pores to appear light and dark, respectively. When using light microscopy, interference between reflections from the front and back faces of the pore channels led to color variations that correlated with axial variations in pore cross-section, thus providing additional information on the three-dimensional evolution of pore shape.

The morphological evolution of pore channels will be described by first using optical microscopy to demonstrate the pore shape changes with time on selected objects. High resolution images from fractured bicrystals are used to give a clearer picture of intermediate and final stages. Finally cross sections of pertubed pores in the final stage will be viewed. We begin with basal plane bicrystals, channels aligned along $[1\bar{1}00]$.

Pore shape changes of a specific six-channel motif (channel length 200 μm), following anneals of 0 to 200 min. at 1800 °C are presented in Figures 16 a)-f). Several features characterized this and other similarly oriented pore arrays. Pore shape equilibration in the plane normal to the channel axis was rapid (Fig. 15). Channels shortened and developed end bulges prior to breakup. The distance over which the end bulge influenced the pore cross section exceeded the wavelength of uniform perturbations that developed along the entire channel by a factor of 2 to 3. Bulges on one side were larger than bulges on the opposite end. When and where pinchoff occurred, considerable readjustment of the end geometry ensued, leading to the development of a "larger wavelength" end bulge.

Repeated pinchoff and readjustment produced an ultimate pore spacing substantially greater than the perturbation wavelength (node spacing) that developed along the channel. Pinchoff at numerous points along the channel, coupled with development of numerous end bulges, led to non-uniform pore sizes and spacings even for the uniform initial geometries studied. The spacing between adjacent cross-sectional minima (nodes) was measured in channels of differing widths using tubular voids of length 200 μm and 3000 μm (Fig. 17). A total of 148 measurements were made; node spacings were between (7.3-13.9) x D, where D is the equivalent circular diameter. The average spacing between 57 adjacent pores varied from (15.1-18.7) x D. Large variations in sizes and spacings in the final pore arrays are evident in Fig. 16 f) and 17 c). Since different pore depths produce different colors in optical microscopy, color images (not included here) demonstrate this irregularity very strikingly.

Results on finite aspect ratio pore channels were obtained from observations of the evolution of about 800 channels of aspect ratios 1 - 93 of diameters 0.6 to 1.0 μm. Only 5 % of the pores with L/D = 47 formed multiple pores, and only 15 % of the highest L/D channels examined (78) evolved into two or more pores. Though short tubular voids necked down in the middle, end bulges continued to recede further and reduced the available length for pinchoff. This case is clearly demonstrated in Fig. 18, which shows the morphological evolution of one pore array presented as in Fig. 10c (left) and two pore arrays presented as in Fig. 10d (right) at 1800 °C. All channels finally evolved into just one pore, even though the intermediate stage suggest channels were on verge of breakup into two pores. A very interesting aspect in Fig. 18 is the competition between the formation of a circular pore and the formation of facetted surfaces. In this particular orientation, an almost circular pore is formed before facetting ensues.

Results obtained by fracturing the bicrystal and examining the interface using SEM are illustrated in Fig. 19 and 20. Figure 19 shows two examples of the now familiar six-channel motif. Again, irregular spacings and sizes of the final pores are evident. Scaling law[27] effects are utilized to produce samples where channels at differing stages of evolution are seen (Fig. 20). Diameters of voids 1 through 5 (top to bottom) are D = 1.1, 1.1, 0.9, 1.3 and 1.7 μm. In Figure 20 a), breakup of channel 3 is almost complete, channels 1 and 2 show the development of uniformly spaced maxima and minima along the channel, while nodes are less well developed in channels 4 and 5.

Figure 20 b) depicts a later stage of pore perturbation, with most channels having evolved into circular pores.

Although fewer (0001) [11$\bar{2}$0]-oriented channels have been studied, the results indicate that the channel direction within the basal plane affects the morphological evolution. Channels oriented either in direction [1$\bar{1}$00] or in direction [11$\bar{2}$0] are contrasted in Figure 21. Wavelength and pore spacings of tubular voids along [11$\bar{2}$0] are considerably larger than their counterparts aligned along [1$\bar{1}$00]. In general, end effects extend over very long distances (several 100 μm), perturbations are much less pronounced (Fig. 22 b) and pore spacings evolved from 3000 μm long channels exceeded 110·D (table 1). End bulges are distinctively non-symmetric to the channel axis and not circular. They appear to bend over before pinchoff, which leaves separated pores off the symmetry axis of the pore channels (Fig. 22 a)*.

Changes in wafer orientation produce again dramatic changes in pore breakup behavior. Fig. 23 a-c) illustrates the evolution of channels etched parallel to the [0001] direction in the (11$\bar{2}$0) plane. As before, channels rapidly become equiaxed in cross section, ends recede and bulge, however, the perturbation form appears quite different from that for basal plane channels. Optical micrographs suggest that the change in cross section appears to be more step function like than sinusoidal; long thin pore channels connect bulged sections, which are not circular but appear to be bound by straight faces. The number of bulged sections and nodes within a channel can change dramatically prior to pinchoff. Consider, for example the lowest tubular void in the left pore array evolving from the shape in Fig.

23 b) to the shape in Fig. 23 c). It seems very surprising, that the thin connecting channel remained stable until both end bulges receded up to the point of coalescense. This pore morphology was also observed by Yen and Coble[1], who compared it to dumbbells being connected by a thin stringer. While the nodes (145 measurements on different channels) have spacings between (19.4 - 27.2) x D, the final pores have spacings of (84.5 - 112.9) x D based on 109 measurements. When pore channels of lower variable aspect ratio (Fig. 24) are studied, only 10 % of the highest aspect ratio channels (L/D = 93) evolved into more than one pore (Table 1).

In contrast to the prior case, channels with orientation $(11\bar{2}0)[1\bar{1}00]$ develop a slight end bulge, but form no other minima or maxima along the channel (Fig. 25). Pore pinchoff occurs almost exclusively at the channel end, and thus, node and pore spacings are equal. Measurements of 263 pore spacings yielded values of (44.4 - 50.5) x D. Only a small fraction of pore channels with L/D < 78 evolved into more than one pore (Fig. 26).

Cross sections of open and closing pore channels after annealing for 48 hours at 1800 °C are depicted in Figures 27 and 28. The twist angle of the bicrystal was 0.7 ° and thermal etching of 2 hours at 1400 °C did not reveal a grain boundary groove. Channels aligned in the direction $[1\bar{1}00]$ appear strongly facetted with a ratio of surface energies of different facets up to 3. Voids oriented in the direction [0001] can be described as 12-sided polygons in the cross section with the surface energies of different facets being very close to equal. Similarly, pores which locally narrow down appear to change their width in a step-wise fashion and show clearly facetted faces

(Fig. 28). It is unclear whether the thin channel in Fig. 28 a) actually connects to another end bulge or not. Voids of that width are too fine to be seen by optical microscopy and could thus have evaded description of Figures 25 and 26. Attempts to fracture at the interface of prismatic plane bicrystals were unfortunately not successful.

Finally, another yet unexplained peculiarity is presented in Figure 29. Traces of unintentionally introduced strings of pores develop after annealing for 1-4 hours at 1800 °C. They intersect the controlled pore arrays and produce local changes confined to a narrow, only few micron wide strip. In this region the location of the larger end bulge is reversed and the evolution is accelerated. While this phenomenon appears very puzzling, a few speculations might be advanced.

These traces of pores might be related to impurities in the bicrystal which adsorb at pore surfaces, alter the relative surface energies and accelerate the surface diffusion kinetics. Controlled experiments with controlled addition of dopants seem to be necessary to elucidate this case.

*: White structure in fig. 22 a,b) originates from crack path deviation from the interface.

3. 2. Kinetics

To determine pinchoff times, samples were given multiple anneals with anneal time increments corresponding to ≈30 % of the standard deviation for the average pinchoff time. The scaling[27] law can, in principle, be used to deduce whether the rate limiting step for pore perturbation is volume- or surface diffusion. Since the channels

observed ranged from 0.6 μm to 1.2 μm width, this was regarded as too narrow a range to meaningfully plot pinchoff times as a function of channel diameter and the scaling law was not applied. Moreover, though different interfaces behaved similarly, break-up times for nearly identical channels of the same orientation at different locations within the same bicrystal interface varied by up to a factor of 30. This variability is currently attributed to effects of local variations in impurity content on D_s or the surface energy anisotropy[22], or possibly both. A typical distribution of pinchoff times for channels of orientation $(11\bar{2}0)$ [0001] is given in Fig. 30. The wavelength for pinchoff was much larger than expected for an isotropic material, and thus only the ≈280 channels of higher aspect ratio (1-3) were used for measurement.

There are obvious difficulties in extracting surface diffusion coefficients from these data. Nichols[17] has proposed the following relationship between D_s and (initial) pinchoff times (t) for channels of equivalent radius r (Eq. 5):

$$D_s = 3.67 \left[\frac{r^4 kT}{t\gamma\Omega^2\varpi}\right] \qquad \text{(eq. 5)}$$

with ϖ being the number of diffusing species per unit surface area. The model assumes isotropic surface energy, a circular cross section, and a hemispherical end cap. The initially flat channels develop equiaxed equilibrium cross-sectional shapes after ≈2 to 5 % of the average time required for pinchoff, however, the shape is not

circular. The model predicts that the kinetically dominant wavelength for surface diffusion controlled perturbation growth is $\sqrt{2}\ \lambda_{min}$, which would lead to center-to-center pore spacings of order 4.4 D. Our measured spacings are ≈4 to 25 times larger. We believe that these differences reflect effects of surface energy anisotropy[22]. If average pinchoff times (at 1800 °C) are force-fit into the expression for D_s, a surface diffusivity of (1.7±1.0) x 10^{-6} cm^2s is calculated for (0001) [$1\bar{1}00$] channels, and (1.05±0.53) x 10^{-6} cm^2s is calculated for ($11\bar{2}0$) [0001] channels.

An even more dramatic departure from isotropic behavior is provided by the ($11\bar{2}0$) [$1\bar{1}00$] channels. Fig. 25 suggests that there is no systematic size dependence to the pinchoff time; times for >850 channels were recorded, and confirm this assertion.

III. 4. Discussion

The approach of using the experimentally determined final pore spacings to determine the dominant transport mechanism[1-4] is obviously a very doubtful one. Not only do pore spacings and node spacings (which are better related to the theoretical derivations) differ significantly, but neither agrees with theoretically predicted values[16] for either surface or lattice transport in our highly controlled experiments. The relative contributions of surface and volume diffusion to mass transport were calculated by Nichols and Mullins[16], and expressed in terms of Φ, as defined in equation 6. This equation combines experimentally determined geometries and known values for the lattice (D_l) and surface diffusion (D_s):

$$\Phi = \frac{B}{A} \frac{\omega K_0(\omega R_0)}{K_1(\omega R_0)} \qquad (eq.6)$$

with R_o the original radius of the cylinder, $\omega = 2\pi/\lambda$, K_0 and K_1 the modified Bessel functions of order 0 and 1, and B and A given by Eq.7 and Eq.8 respectively:

$$B = \frac{D_s \gamma \varpi \Omega^2}{kT} \qquad (eq.7)$$

$$A = \frac{D_1 \gamma \Omega}{f kT} \qquad (eq.8)$$

with f being the correlation factor.

Equation 6 is a product of two terms. The first one, $\Phi_1 = B/A$ is dominated by relative diffusivities and the second one, $\Phi_2 = (\omega K_0(\omega R_0)/K_1(\omega R_0))$ describes the geometry of the cylinder. We proceed by inserting plausible values for Φ_1 and Φ_2 and calculate the relative contributions to pore perturbation by both transport mechanisms in question.

The range of surface diffusion coefficients obtained to date was critically reviewed and compiled by Dynys et al.[28] The lowest value for a surface diffusivity listed was the one by Huang et al.[29] for surface smoothing on the $(11\bar{2}0)$ plane. Choosing this value, together with a maximal value for the lattice diffusivity, should give the minimal ratio for our first term Φ_1. It is widely recognized[30-34] that

the diffusion of oxygen through the lattice is slower than the diffusion of aluminum through the lattice. The highest lattice diffusivity of oxygen is the one given by Reddy and Cooper[33], which can then be inserted into Eq. 8. The correlation factor f for this particular case[35] is $f \approx 0.8$.

The geometrical term Φ_2 was evaluated for a typical wavelength $\lambda=30D$ and $R_0 = 0.5$ μm and the values of the modified Bessel functions obtained from standard tables[36]. Since Φ_2 is not strongly dependent on either λ or R_0, the final result and the conclusion derived therefrom will not be altered by this choice of geometrical parameters. Inserting all parameters, and evaluating Eq. 6 gives $\Phi = 38$. Therefore it is expected that surface diffusion is the dominant transport mechanism for all possible cases. Though this derivation was given for the isotropic model, it is not expected that the situation is different for the anisotropic material. Grain boundary diffusion was neglected in this analysis, since bicrystals are produced such as to diminish the role of the grain boundary, and grain boundary transport alone could not accomplish the shape changes during pore perturbation.

Striking differences exist between observed behavior and that predicted for isotropic materials. Node spacings are in most cases not related to pore spacings. Critical aspect ratios are much higher than expected for isotropic materials, and are orientation dependent, as are the general modes of evolution. The behavior of (0001) $[1\bar{1}00]$ channels most closely approximates isotropic behavior. For the other orientations studied, the perturbation form does not appear to be sinusoidal.

The differences in behavior between (0001) $[1\bar{1}00]$ and $(11\bar{2}0)$ $[1\bar{1}00]$ channels are of particular interest since these channels have the same orientation; the grain boundaries for the two cases are simply orthogonal (Fig. 31). This rather subtle difference apparently causes a significant difference in the morphological evolution; critical aspect ratios differ, as does the size dependence of the pinchoff time. The results then suggest that the grain boundary plane orientation is an important factor to consider in comparing the results from channels that have the same crystallographic orientation.

Though a surface diffusion coefficient can be calculated using the isotropic model, it is clear that this value has to be viewed with great caution. The good agreement between calculated diffusivities and values reported previously[28], is either mere coincidence, or should also shed doubt on previous experimental results, which also used experiments on alumina surfaces to extract diffusion coefficients by comparing with isotropic model calculations. Particularly, experiments with small driving forces (scratch smoothing with flat channels) are prone to really investigate the competition between facetting and morphological evolution. In cases where instability phenomena are driven by large differences in chemical potential, e.g., particle coalescense[25] or pore drag (see IV.), subtle differences in chemical potential associated with different surface planes are simply not recognized. Moreover, if chemical potential differences between different surfaces are very small, facetting occurs as a secondary step. This is evident from Fig. 15 e,h) and Fig. 27 b). The former figure demonstrates, that the pore equilibrates in cross section first by obtaining a symmetrical shape to

the interface before facetting occurs, as the energies of the different bonding planes are almost equal (from Fig. 27 b). If the energies of different bonding planes are clearly different, then facetting occurs before the pore reaches an equiaxed shape (from pore in orientation (0001) $[1\bar{1}00]$ after 10 min. at 1800 °C, not shown here, see also Fig. 15 c,d). The competition between facetting and spherodization is also evident from Fig. 18. Facetting ensues when pores have evolved to an almost circular shape. They then proceed towards a somewhat pear-like appearance, with two straight facets and a third curved edge. This very peculiar shape is not yet fully understood (see also A.1. and A. 3.). One might distinguish the orientation of facets with respect to the atomic flow. Faces perpendicular to the primary orientation of atomic flow (along the pore channel) can facet much more easily (cross sections in Fig. 18, 27 and 28) than all other faces, as the morphological evolution leaves the former very much unperturbed. Channels also can simply narrow down or widen with time by adding additional planes onto these surfaces, whereas the local narrowing or widening (Fig. 28) is achieved by step-wise facetting.

Finally, the dominant observations of the kinetics of $(11\bar{2}0)$ $[1\bar{1}00]$ channels have to be discussed. Fig. 25 suggests that there is no systematic size dependence to the pinchoff time; times for >850 channels were recorded, and confirm this assertion. Since morphological instabilities governed by diffusional transport are subject to the scaling laws, that is, the time to accomplish a certain measure of change is related to the size of the object, another step of the overall process must be rate limiting. Therefore, we consider the creation of mobile species at a facetted surface. Gjostein[37] considered surface

self-diffusion by using the terrace-ledge-kink (TLK) model to describe surfaces in anisotropic materials (Fig. 32). A flow of atoms (or vacancies) along the surface is the combination of the movement of atoms from all possible sites. Adatoms and vacancies in a position of a terrace atom are likely to be the most mobile species. If the extreme case is taken where only these two species dominate the surface transport, then the creation of this adatom-vacancy pair has to be considered. A measure of morphological change involves then creation of a certain number of these pairs on an originally flat surface. An atomic layer on a surface will get increasingly more unstable if more adatom-vacancy pairs are created. If the original creation of these pairs starts at the edge of a particular facet, the width of this facet might not come into play, but only the creation of the first instabilities, that is, the first adatom-vacancy pairs. This is thus a plausible mechanism, which, though very idealized, can describe a size independent morphological evolution of shapes bonded by facetted surfaces. And indeed the faces bonding the $(11\bar{2}0)$ $[1\bar{1}00]$ oriented channels show a very high degree of facetting (Fig. 27 a).

Since interfacial reactions are thought to be rate limiting in the special aforementioned case, their influence (though not as dominant) can also not be excluded in considering morphological changes of voids oriented in the other directions. Channels with more widely different channel widths (see V.) should thus be explored to investigate the validity of the scaling laws. Simultaneously, the relative surface energies in alumina (the γ-plot) and the effects of grain boundaries with varying energies intersecting pore channels (see V., A. 1.) should be investigated to better understand morphological

changes of facetted structures. Influences of dopants on pore perturbation are of particular interest, since their effects on the surface energy anisotropy (through the critical wavelength[22]) and on the surface diffusion coefficient can be assessed.

III. 5. Conclusion

It is demonstrated that the morphological evolution of pore channels is strongly affected by the orientation of the boundary plane and the direction of channels. Experimental results differ strongly from theoretical predictions based on isotropic models. Surface diffusion coefficients derived from these and similar measurements have to be viewed with great caution. Competition between facetting and spheroidization is demonstrated. The understanding of changes unstable pores undergo at high temperatures would greatly benefit from detailed experiments to determine equilibrium pore shapes in the lattice and at different grain boundaries.

Further studies need to focus on the influence of dopants on surface energy anisotropy and on the surface diffusion coefficient D_s, as well as on the detailed mechanism of surface transport, which also seems to include transport controlled by interfacial reaction rates.

IV. Pore drag and pore-boundary separation

IV. 1. Background

IV. 1. 1. Experimental methods

Our understanding of sintering and our ability to interpret sintering data suffer from several difficulties. The geometry of a powder compact (at the particle level) is often poorly defined. Many concurrent, competitive, and interactive processes contribute to what we refer to as "sintering behavior". Cannon focused the attention of the sintering community on the competition between densification and coarsening mechanisms[1]. Depending on what transport path is dominant (grain boundary diffusion or lattice diffusion for densification and lattice diffusion, evaporation/condensation or surface diffusion for coarsening), a family of trajectories in the grain size-density plot can be predicted[1-3]. The final end product, however, will strongly be governed by a parameter Γ, which is derived from the ratio of the dominant coarsening and densification terms. If we take the situation, where mass transport occurs predominantly through surface diffusion and lattice diffusion[4], then this ratio is governed by a term D_s/D_l. The approach of altering the D_s/D_l ratio by the addition of specific dopants, known as ratio control[4,5], thus aims to alter the trajectory on the grain size-density plot. In the case of MgO-doped alumina, however, this path of microstructural evolution appears unaffected by the presence of MgO-dopant[6,7]. In tjis case the effect of MgO additions on the position of the pore separation region[8] must be considered as well.

The prior discussion identifies two experimental needs. Firstly, we need to find model experiments which allow separate

investigation of both the coarsening and the densification process. Secondly, we require model experiments which study pore-boundary separation. Hot pressing already provides the means of conducting a densification experiment with only a small amount of interfering grain growth[9]. This method appears to give a satisfying result, and we can concentrate on coarsening mechanisms. Several attempts were made to study grain growth in a porous matrix, none of which proved to be completely satisfying. Three avenues were explored[6,8,10-21]:

The first approach is simply based on the realization that evaporation/condensation can be excluded as a significant mechanism in alumina at all reasonable pore sizes (<20 μm)[10]. Thus, grain growth, which is governed by pore drag, will be dominated by surface diffusion mechanisms. Consequently, it might be sufficient to use model experiments which give values for a surface diffusion coefficient, e.g., scratch smoothing[11-13], pore perturbation[14-16] and grain boundary grooving[17-20]. Most of these methods[11-18] rely on observations obtained with bicrystals, which gives values which are strongly dependent on crystallographic orientation[16] (see also III.). Furthermore, the driving forces for the morphological evolution are low, and thus the measured changes are very small. Therefore, these approaches do not relate well to ceramic processing conditions.

The second method of studying grain coarsening under the influence of pore drag relies on the generation of controlled pore structures in a polycrystalline matrix. Harmer suggested that such specimens could be prepared either by utilizing a desintering reaction in powders which were hot-pressed to full density[8] or by

producing large model pores using the burnt-out latex sphere method[21]. While particularly the later approach appears valuable as a means of studying the densification-coarsening competition, it appears difficult to extract pore drag data from such an experiment.

The third approach centers on the realization, that, if the competing processes cannot be separated, they might be viewed as separable processes. By plotting the grain growth rate as a function of grain size and density for the case of undoped and MgO-doped alumina, Berry and Harmer[6] found, that the surface diffusion coefficient in Al_2O_3 is increased by a factor of 2.5 by the addition of 250 ppm MgO. Since the pore size and pore size distribution were not well defined, an absolute surface diffusivity could not be extracted. Nevertheless, this result is reassuring as it proves that the sintering behavior can be qualitatively described by straightforward basic models.

To date, pore-boundary separation maps have been obtained only for MgO. Handwerker et al.[2] measured the sizes of grains and attached and separated pores from polished surfaces and found good correlation between their observations and their theoretical predictions. This method is straightforward, but requires great care in obtaining three-dimensional pore and grain sizes from two-dimensional micrographs, and is limited to the naturally occurring pore and grain size regimes. A similar study by Sakarcan et al.[22] included pore distortion measurements to examine the pore/grain boundary separation problem. This additional method again needs great experimental care but is unable to give very precise data.

From the above discussion it becomes evident, that a controlled experiment to study pore drag and pore separation is very desirable. Ideally, this experiment should completely suppress interfering mechanisms like densification and, in the ideal case, should use well controlled geometries, such that the critical parameters like pore size, pore spacing and grain size can be controlled and adjusted at will. This experiment, termed controlled pore drag, will be introduced in section IV. 2.

IV. 1. 2. Theoretical models

The classical discussion of pore drag describes pores as spheres and calculates their maximum velocity as a product of their mobility M_p[23] and the maximum force exerted on them, F_p[24], such that,

$$v_p = M_p F_p \qquad \text{(eq.1.)}$$

with

$$M_p = \frac{D_s \delta \Omega}{\Pi r^4} \qquad \text{(eq.2.)}$$

where δ is the thickness of the high-diffusivity surface layer and r the pore size[23], and

$$F_p = \Pi r \gamma_{gb} \qquad \text{(eq.3.)}$$

with γ_{gb} the grain boundary energy.

This approach was used by Brook[25,26] to compute a pore-boundary separation region by comparing the maximum pore and grain boundary velocities. Carpay[27,28] later modified this approach by introducing the possibility of pores reattaching after separation.

More recently, Hsueh et al.[29] provided a very careful analysis of pore drag, including the dihedral angle Ψ (in radians). A steady-state maximum pore velocity v_p (Eq.4) was obtained:

$$v_p \approx \frac{\Omega D_s \delta_s \gamma_s}{k T r^3} (17.9 - 6.2 \Psi) \qquad \text{(eq.4.)}$$

His analysis of the pore breakaway condition centered on the hypothesis that the maximum pore velocity has to be compared with the maximum grain boundary velocity outside of the influence distance of the pore, which is only valid for rather large pore spacings. This condition was explored for two pore-grain configurations, a pore attached to either a five-sided or a three-sided (disappearing) grain. The most stringent condition for pore separation is given by the latter case, where the critical pore size was found to be independent of grain size.

The method of controlled pore drag, which will be described in the next section, can be used to measure the maximum pore velocity. Therefore, a surface diffusion coefficient can be derived from this type of measurement. Furthermore, the experimental data can be used to predict the dependence of grain size, pore size and pore

spacing on the critical condition for pore separation. Such controlled pore drag experiments, together with hot pressing experiments, allow study of the two idealized or limiting paths of microstructural evolution during sintering, as represented in Figure 33.

IV. 2. Experimental approach

IV. 2. 1. Sample preparation

Controlled pore drag experiments rely on the production of controlled-geometry pore structures[30,31] (see section II.) at the interface between a large grain (single crystal sapphire) and a dense polycrystalline matrix. During subsequent heat treatments, the large "abnormal" grain consumes the adjoining polycrystalline material at a rate determined by the drag force exerted by the interfacial pore arrays*. Since both pore size and spacing can be precisely controlled and varied, a wide range of conditions can be examined.

The theoretically dense polycrystalline alumina samples were fabricated using a two-stage hot pressing and hot isostatic pressing procedure. Prolonged exposure to elevated temperature was avoided in order to limit the amount of grain growth and contamination, thus preserving a fine-grained high purity or intentionally doped matrix.

Undoped alumina[a] was hot pressed at 1410°C for 2 hours under a pressure of 35 MPa, using a boron nitride[b] coated graphite die and boron nitride spacers[b]. This yielded material with a relative density of 99.4 %. Subsequently, hot isostatic pressing at 175 MPa for 1 hour at 1500°C was used to complete densification.

The doped material was produced by mixing alumina powder[a] with sufficient double distilled water-$Mg(NO_3)_2 \cdot 6H_2O$ solution to

introduce 250 atomic ppm MgO. Mixing was performed in a Teflon beaker. The mixed powders were dried at 80°C, and subsequently calcined for 2 hours at 600°C. The powder was lightly crushed with a Teflon rod before loading into the hot pressing die. For this material, hot pressing was performed at 1375°C for 50 min using 35 MPa pressure. This yielded specimen with a density of 98.4%. Hot isostatic pressing for 1 hour at 1500°C at 175 MPa pressure produced a theoretically dense material.

The microstructures of both undoped and doped materials were uniform. After hot pressing the average grain sizes were 3.0 and 2.1 μm for the undoped and doped alumina, respectively (Figure 34). Figure 35 shows the microstructures of both materials after hot isostatic pressing with average grain sizes of 5.6 μm for the undoped and 3.1 μm for the MgO-doped alumina.

Slices were cut from the center of each of the samples and polished to a 0.25 μm finish prior to bonding to etched basal plane sapphire wafers. Simultaneously, slices from each of the materials were crushed with a steel pestle and mortar with subsequent magnetic separation of unintentionally introduced iron flakes. Semi-quantitative spectrographic analysis from each of these specimen revealed a total cationic impurity content (of seven selected elements) of about 100 ppm (Table III.)

A wide range of controlled surface structures was generated on the basal plane of sapphire with the methods described in section II. Examples of resulting structures are illustrated in Fig. 36; the pore width is 3 μm, center-to-center pore spacings are 4, 6, 8, and 10 μm and the pore depth is 0.24 μm[$]. Additional features with wider

pores (5 μm width) are depicted in Fig. 37. Pore structures were combined to form pore arrays 20 pores wide and 1800 to 4000 pores long with interarray spacings of 200 μm (Fig. 38). In addition to the pore arrays, wide channels were etched into the sapphire surface. These allowed convenient measurement of the pore depth using a surface profilometer, and also marked the position of the interface prior to migration into the polycrystalline matrix.

Etched sapphire wafers were subsequently hot pressed against the highly polished dense polycrystals, thus transferring the controlled pore structures from external to internal interfaces. Wide pore-free ligaments surrounding the pore arrays were used to almost completely suppress densification during hot pressing and annealing (see section A. 3.). The final hot pressed samples had dimensions of 2 x 9 x 18 mm.

The as-produced interfaces consisted mainly of pore-free areas (Fig. 39), which allowed observation of the boundary migration rates of sapphire into the polycrystalline matrix. Figures 40 and 41 depict interfacial pore structures, which are related to the surface structures shown in Figures 36 and 37b, respectively. Because of the transparency of sapphire it was possible to resolve the positions of the pore arrays and reference channels by optical microscopy, both after initial sample preparation (Fig. 42) and after subsequent heat treatments.

*: Micrographs from Coble's[32] original experiments, in which single crystal sapphire spheres were used to seed abnormal grain growth, indicate that pores inadvertently generated at the interface were also dragged with the boundary for short distances.

$: This areal density of pores can be transferred to a bulk porosity if certain assumptions are used: The bulk is formed by tetrakaidecahedras of the same volume as the grains in the MgO-doped alumina initially (G=3.1μm), and all grain boundaries have the same areal density of pores as the sapphire-polycrystal interface. The pore volume fractions for the four cases illustrated in Fig. 36 are then: 11.6, 5.1, 2.9, and 1.8%.

a: Sumitomo, A-HPT-F, New York

b: Union Carbide, Cleveland, OH, HCM boron nitride powder and HBC boron nitride rod.

IV. 2. 2. Measurements

Samples with controlled interfacial pore structures were cut into slices, with one edge parallel to one of the primary axes of the square pore pattern. These were then cleaned with organic solvents, embedded in powder of identical composition in a high purity alumina crucible, and heat treated for various times at 1600°C in air. After this step, ≈50 to 100 μm of material was removed, the specimens were polished, thermally etched (1 hour at 1400°C for MgO-doped alumina, 2 hours at 1400°C for undoped alumina), and examined using scanning electron microscopy.

Measurements of the average grain size and the grain boundary displacement rate of the sapphire are reported in section A. 4. Grain boundary migration rates were obtained by measuring boundary positions after various tempering times relative to the initial interface position as marked by the reference channels. The channels essentially served as huge crack-like pores, which - at the tip -

separated from the interface at the onset of motion (Fig. 43). The accuracy of the boundary displacement measurements were limited by: 1) the accuracy in determining the original boundary positions by interpolation between reference channels, and 2) the accuracy with which final boundary positions could be determined when finite width boundary grooves were present. The error in the original boundary position was found to be <0.2 μm; the error in the final boundary position was ±0.3 μm. The total displacement uncertainty of ≈0.5 μm was taken into account in analyzing the data.

It needs to be pointed out that all the data presented here were derived from the behavior of arrays of pores, rather than from the behavior of individual pores. Specimen were polished such that a maximum of pores was exposed to the surface. Therefore data could be taken from several pores at one time. Moreover, the transparency of sapphire facilitates focusing on pore rows below the one exposed. Thus the evolution of several pore arrays can be compared.

IV. 3. Results

There are three issues that require consideration. The first deals with the shape changes of the initially "flat" pores prior to their being dragged along by the migrating boundary. The second is concerned with the actual grain boundary migration rates of interfaces with controlled geometry pore arrays. The third issue finally deals with the conditions for pore-boundary separation.

The first issue is specific to our method of specimen preparation. The pores initially have a width-to-depth ratio >10, and are far from an equilibrium shape. However, this has its advantages, in that

the high effective areal fraction of pores inhibits premature pore-boundary separation, and thus allows pore equilibration to occur. As the pore shapes become more nearly equilibrated, migration of the pore-boundary ensemble initiates*. In the limit where the aspect ratio of pores is large and the grains are smaller than the width of the pores, pores might not equilibrate but will separate into two or more pores. In that case the interfacial pore geometry is poorly described, the kinetics of pore drag cannot be modeled accurately, and separated pore arrays might either reveal one or two pores per pore location (Fig. 44). If the same pore geometry is produced at an interface with larger starting matrix grain size (as with the undoped alumina), this can be avoided (Fig. 45).

We now address grain boundary migration rates under the influence of pore drag. Pore arrays with originally very wide pores are shown in Fig. 45. Equilibration of separate pores was very slow in that case. Concurrent matrix grain growth (which reduced the driving force for pore motion), thus prevented a noticeable pore movement. Once the driving force for pore motion was reduced, pore faceting set in instead (Fig. 45b)$. Therefore, arrays with originally wide (5 μm width) pores were not considered for analysis.

A case of pore drag for MgO-doped alumina is shown in Fig. 46. Two small pores at grain boundary junctions might again have arisen from initial pore instabilities. In general, this phenomenon occurred rarely for the case of pore structures as shown in Fig. 36 ("narrow" pores). Grain boundary migration rates under pore attachment conditions for undoped and doped alumina are presented in Figs. 47a and 47b, respectively. Pores at the undoped alumina-sapphire

interface were initially immobile. Subsequently (after some equilibration), pores with small interpore spacings were dragged along for a short distance without separation. The total extent of motion was limited because concurrent matrix grain growth significantly reduced the driving force for further migration of the pore-laden alumina-sapphire interface. Arrays of pores in the undoped alumina with larger interpore spacing were dragged along for ≈2 μm, versus an ≈8 μm displacement for the pore-free grain boundary in the same time, and then separated from the sapphire-alumina interface. Pore arrays in the MgO-doped alumina remained attached and migrated at a constant rate for 10 hours, and then separated. After 10 hours at 1600°C, the displacement of the pore-laden boundary was ≈6 μm, versus ≈13 μm for the pore-free boundary (see A. 4.).

Pore-boundary separation initiated in all cases at the edges of pore arrays, where the outermost pore was most prone to be separated. This process usually encompassed about 3 or 4 pores, before one of two events happened. Either the pore array as a whole separated or the matrix grain growth had reduced the driving force for grain boundary migration so far, that no further pore-boundary separation occurred. All data presented for the separation condition were gained from the uniform behavior of whole pore arrays Since the center of pore arrays separated as a whole, our results are not believed to be an artefact of the special technique used. A case of partial separation, where pores began to separate at the array edge from the left is shown in Fig. 48. Figure 49 illustrates separated pore

arrays in MgO-doped alumina with two different spacings; samples were annealed for 15 hours at 1600°C.

*: Pores in MgO-doped alumina develop more equiaxed shapes in shorter times than in undoped alumina.

$: This case is related to the competition between faceting and pore shape equilibration of originally flat asymmetric pores as described in section III.

IV. 4. Discussion

It was found that the technique of controlled interfacial pore structures is very valuable for studying pore drag and pore-boundary separation. A few remarks, however, have to be made concerning the experimental parameters employed. Allowance has to be given for an initial time period where pore structures can equilibrate, before they begin to be dragged along. If this time is very long (pores have a high aspect ratio initially) then grain growth in the polycrystalline matrix can reduce the driving force for grain boundary migration to the point where interfacial pores facet. In this limit the theoretical models[29] are not applicable. This case is favored when the aspect ratio is high and the grain boundary mobility of the single crystal is low compared to the average grain boundary mobility of the polycrystalline material. A second limit occurs where the width of pores is larger than the grain width at the interface (Fig. 41). Here pores might not equilibrate, but rather separate into two or more pores (Fig. 44). This process is similar to the crack healing processes described in A. 2., but in this case it is enhanced through grain

boundary grooving in the polycrystalline material adjacent to the pore. Atoms diffuse away from the grain boundary and deposit at the grain surface at the center between grain boundaries, thus extending the grains towards the opposite (sapphire) surface. In the extreme case, these grains can completely bridge the pore space. A similar mechanism was first noted by Bronisz and Douglass[33] in TEM observations of thin films containing small cracks. We, however, prefer, not to associate the term grain growth with this process, as the volume of grains remains unchanged.

Before we come to the pore-boundary separation conditions, let us first turn to an evaluation of pore drag kinetics. While pores equilibrate and change shape from the initial crack-like appearance, the relative contact radius of the leading pore surface at the grain boundary is decreased. This allows attainment of considerably higher pore velocities[29]. The maximum pore velocity is reached prior to pore separation and is a well-defined quantity, given by Eq. 4. Other velocites than this so called peak pore velocity only give some intermediate ill-defined state, which can only be used for quantitative analysis, if either the relative contact radius or the grain boundary inclination are measured very accurately for each case. Since the pore velocities in this study are measured from the onset of motion to the point of separation, a peak pore velocity can clearly be extracted and inserted into Eq. 4. When measurement errors are taken into account, the peak pore velocity, v_p, for undoped alumina is in the range of 0.08 to 0.22 μm/h, whereas the range for MgO-doped alumina is between 0.45 to 0.70 μm/h. For the present purposes we used reported averages for γ_s (0.9 J/m^2) and Ψ ($\approx$115° for undoped

alumina and 117° for MgO-doped alumina). The radius r of a spherical pore of equivalent radius was 0.67 μm in our case. Substituting these values into Eq. 4 yields D_s = 0.55 - 1.51 x 10^{-7} cm^2/s for the undoped alumina and D_s = 3.24 - 5.04 x 10^{-7} cm^2/s for the MgO-doped alumina. This suggests that the addition of 250 ppm MgO increases the surface diffusivity by a factor of 2 to 9 at 1600°C. This is in agreement with the result given by Berry and Harmer[6], who measured an increase of the surface diffusion coefficient in Al_2O_3 by a factor of 2.5 when 250 ppm MgO were added. The absolute values of a surface diffusivity obtained here compare well with the data compiled by Dynys et al.[20]. They agree particularly well with data taken from polycrystalline samples obtained through grain boundary grooving experiments[20]. Experiments performed in a polycrystalline sample, where pores travelled several microns under well controlled conditions, however, appear to be a more reliable way to obtain surface diffusion coefficients which can be applied to sintering. In contrast, data from bicrystals are only specific to a particular orientation and most experiments designed to gain a surface diffusivity (scratch smoothing, grain boundary grooving) rely on the measurement of very small geometrical changes with time.

The calculation of the separation conditions follows the approach taken by Brook[25,26] and Carpay[27,28]. One modification is introduced, namely that the velocity used in the classical model (Eq. 1) is replaced by the peak pore velocity as derived by Hsueh et al.[29] (Eq. 4). For pore separation to occur:

$$v_p < v_b \qquad \text{(eq.5)}$$

with v_b the grain boundary velocity under the influence of pore drag. Using the value for v_b given by Brook[25,26] gives Eq. 6:

$$v_p < M_b (F_b - N F_p) \qquad \text{(eq. 6)}$$

with N the areal density of pores per atom at the grain boundary. Inserting values for the pore and grain boundary velocities (Eq. 4 and Eq. 3 from A. 4.), the maximum force on a pore (Eq. 3) and writing $N=\Omega^{2/3}/f^2$ (f the pore spacing), gives Eq. 7:

$$\delta_s \Omega D_s \gamma_s (17.9\text{-}6.2\Psi) < M_b \left(\frac{2 g_{gb} \Omega^{2/3}}{G} - \frac{\Omega^{2/3}}{f^2} \Pi r \gamma_{gb} \right) \qquad \text{(eq. 7)}$$

After rearrangement the final equation for the condition of pore separation is obtained (Eq. 8):

$$G^{-1} > \frac{\delta_s \Omega^{1/3} D_s \gamma_s (17.9\text{-}6.2\Psi)}{2 k T M_b \gamma_b r^3} + \frac{\Pi r}{f^2} \qquad \text{(eq. 8)}$$

The product $M_b \gamma_b$ is obtained from section A. 4.; all other quantities are known.

This equation allows us to divide grain size-pore size maps into regions in which either pore separation or pore attachment are expected. The ratio of critical coefficients such as D_s and M_b can be measured from the same experiment. The actual and predicted critical conditions for pore-boundary separation can be compared, thus allowing a check of the original results. A condition for separation is clearly defined by the set of parameters (pore size, pore spacing and grain size of the polycrystalline matrix) given at the point where pore-boundary separation occurred. The condition for attachment is less obvious, since it is not clear, when pores have equilibrated from their initial crack-like shape. For example, pores prone to separation at a later stage might be dragged along for several micrometers due to a large contact radius at the grain boundary. This does not imply that they are in the attachment regime during that period. The attachment condition was specified by a certain matrix grain size and pore spacing. The grain size was taken to be the one as used to describe the separation condition of equal-sized pores with larger spacing. It assumes that pores of the same volume equilibrate at the same time irrespective of their spacing. This is not fully correct as an increasing drag force (larger pore spacing) might accelerate the attainment of an equilibrated pore shape.

Two sources of error will affect the closeness of the agreement. The uncertainty in v_p, or equivalently the uncertainty in D_s in Eq. 4 defines a separation area rather than a separation line. In addition, there is some uncertainty in the exact grain size when separation occurred, due to matrix grain growth.

The correspondence between calculated pore-boundary separation conditions and observed behavior is illustrated in Figs. 50a and 50b for undoped and MgO-doped alumina, respectively. The points plotted again represent or characterize the behavior of entire pore arrays, not isolated pores. Given the uncertainties in the values of the interfacial energies, the dihedral angles, and the grain boundary mobility, the agreement between calculated and observed pore-boundary separation conditions is encouraging. For undoped alumina, the correlation is particularly good. The effect of pore spacing is noteworthy. Hsueh et al.[29] compared v_p with the boundary velocity outside the pore's zone of influence, and thus developed a separation criterion independent of pore spacing, i.e. like Eq. 8 with $f=\infty$. Our experiments demonstrate that the influence of the pore-laden boundary must be considered for comparison. For MgO-doped alumina, two data points fall into the region of experimental uncertainty, while two pore arrays show separation as predicted. Further experiments using a coarser grain size matrix are necessary to define the transition condition.

Of particular interest for the future are similar experiments where not the basal plane of sapphire, but a more general plane is bonded against a polycrystalline matrix. Preliminary experiments with a similar specimen, but with the $(\bar{5}052)$ plane growing into a polycrystalline alumina had been performed earlier. These indicated, that the single crystal-polycrystal interface did not stay as planar as noticed in the case discussed above. This might have an effect on the pore-boundary separation condition, but not on the measured surface diffusion coefficient (since the peak pore velocity is not

affected by the particular choice of single crystal-polycrystal interface).

Finally, a few comments pertaining to the MgO concentration at the single crystal-polycrystal interface seem appropriate. Initially, there is a discontinuous change in the MgO concentration at the single crystal-polycrystal interface, from nearly 0 to ≈250 ppm. Interdiffusion will reduce the MgO content of the adjoining polycrystalline matrix. In our case, migration of the interface will at least partially offset this localized depletion of dopant concentration. Furthermore, we anticipate that grain boundary diffusion of the dopant on the polycrystalline side of the interface will tend to reduce concentration gradients in the doped material. As a result, we expect the bulk concentration of MgO in the polycrystalline matrix to lie between 125 and 250 ppm.

IV. Conclusions

It is possible to study the kinetics of pore drag and to assess the conditions for pore-boundary separation using the method of controlled pore drag. Care has to be taken to choose viable pore geometries and pore array dimensions. The applicability of the method has been demonstrated with model experiments in alumina, but the technique can be used for a wide range of materials. Since this method closely simulates pore-boundary interactions during sintering, we anticipate that the information derived will be more directly applicable to modelling microstructural evolution than results obtained from surface diffusion experiments using single crystals. Further work is needed to define more accurately the pore separation

and attachment regions, and the kinetics of pore drag in alumina. Experiments with larger matrix grain size and different orientation of the sapphire are planned (see section V.).

V. Suggestions for future work

V. 1. The technique

The method of controlled interfacial pore structures is well established and has led to several spinoffs. There are predominantly two areas where improvements should be made. Etched features have been produced with dimensions from 1 μm to 200 μm wide and 700 Å to 4000 Å deep. Finer structures can be obtained through the use of electron beam lithography, where pattern delineation is achieved with a focused beam of electrons. The minimum width of features has dropped from about 1000 Å to about 300 Å during the last 10 years[1,2]. An extension of scale to smaller structures would make the application of the scaling law[3] feasible. While it is straightforward to delineate wider patterns, the production of deeper etched features is limited by the competition between erosion of the target and the photoresist material. The use of special ultrathick photoresists[a], however, would allow the generation of structures in sapphire, which could be up to 5 μm deep and might allow creation of interfacial pore structures with cross sections closer to equilibrium than before (see Fig. 15).

Effects of dopants can only be assessed meaningfully, if the impurity level is kept as low as possible. While pressure bonding of bicrystals was so far performed at 2.6×10^{-3} Pa, attempts should be made to improve the vacuum during hot pressing and preferably to use a cleaner system altogether. Concerns about possible boundary contamination arose from bloating at the interface after several hours at 1800°C in vacuum (Fig. 51)*. This is believed to result from oxidation of carbon which was transported as carbon monoxide prior

to bonding in the hot press (pressure bonding is performed in a graphite die).

a: AZ 4903, American Hoechst Corporation, Somerville, NJ 08876

*: Bicrystals which showed extensive bloating were not considered for evaluation.

V. 2. Equilibrium pore structures

A better knowledge of the equilibrium pore shapes in the lattice and at the grain boundary is considered essential for kinetical investigations of pore instabilities. Pores in the lattice could be produced by first generating pore structures at single crystal-polycrystal interfaces, followed by pore-grain boundary separation during subsequent grain growth at high temperatures. If voids at grain boundaries with varying twist angle are generated, general rules of the Ψ-plot[4,5] can be used to predict resulting equilibrium pore shapes (in the cross section). Increasing the twist angle will increase the amount of truncation of pores, starting at the grain boundary intersection. This method allows computation of the relative grain boundary energy as a function of misfit angle.

The possible occurrence of metastable pore shapes and the disappearance of the inversion center are addressed in an experiment suggested by Carter[6]. A series of simple geometric features with varying symmetry (Fig. 52) are etched into a sapphire surface and transferred into an internal surface. More elaborate features (Fig. 53) are designed to predominantly address the question of the occurrence of an inversion center. In addition, all features are

rotated (Fig. 54) to explore possible metastable shapes as a function of orientation with respect to the crystallographic axes in alumina.

V. 3. Kinetics of pore instabilities and pore interactions

Further work on the kinetics of pore instabilities have already been planned and can be found elsewhere[7]. They include more detailed studies of the effects of crystallography, dopants and pore geometry on the morphological evolution of initially unstable internal voids. In particular, features will be introduced into single crystal-single crystal, single crystal-polycrystal and polycrystal-polycrystal sandwiches.

Studies on the transport between pores and between pores and grain boundaries are already in progress unsing LiF as a model material[8]. As mentioned in A. 3., these experiments allow measurements of grain boundary and lattice diffusivities as well as an assessment of the effects of interfacial reactions on the overall process rate. Work to improve the theoretical modelling of these transport rates has to be encouraged in that field.

The use of controlled interfacial pore structures for investigations into cavitational creep has been suggested on various occasions[9-11]. This method investigates the response of internal cavities to external tensile stresses[12]. It is particularly attractive as it allows an assessment of the relative rates of grain boundary to surface diffusion in a material.

V. 4. Pore and grain boundary mobilities

The work on pore drag (section V.) can be extended to include variations in grain size in the grain size - pore spacing plot for pore separation (Fig. 50). For the case of constant pore spacing the effects of pore size on the pore-boundary interactions can be studied by using pore structures such as given in Fig. 55. Finally, obtained values for a surface diffusivity can be checked by repeating the same experiment but for a different surface orientation of the sapphire (e.g. from a basal to a prismatic plane).

Simultaneously, grain boundary mobilities for various sapphire orientations can be obtained. Of particular interest here is the influence of MgO-dopant on the spread of grain boundary mobilities with orientation. The grain structure in MgO-doped Al_2O_3 is more equiaxed than in undoped Al_2O_3, thus the spread of grain boundary mobilities ought to be reduced through additions of MgO.

The interactions of deformation and grain growth, however, appear to be most promising as they offer a completely new experimental method (see A.4.). These types of experiments introduce long range effects and the influence of direction into our understanding of grain growth.

V. 5. Aspects in fracture mechanics

The introduction of controlled interfacial pore structures into thin metal layers has already shown considerable success[13-15], as the fracture toughness of metal/ceramic interfaces could be increased by a factor of 4 - 80. This technique was summarized by Oh[16].

The use of photolithographic methods combined with ion beam etching to create reference lines across metal/ceramic interfaces has been demonstrated by Dalgleish et al.[17]. Metal deformation and interfacial debonding can be monitored using this technique.

While both these applications are expected to be employed in further studies, the creation of 2-dimensional controlled-geometry composites appears to be the next logical step. These model systems can be produced by creating two-dimensional open pore structures, which subsequently have to be infiltrated with a second phase. If these composite materials are machined into compact tensile specimen, two possible geometries can be utilized (Fig. 56). Rod-shaped second phases can be either aligned perpendicular to the crack plane (Fig. 56a) or can lie in the crack plane (Fig. 56b). If the original porous structure is infiltrated with metals, both geometries can investigate the R-curve behavior in controlled-geometry metal/ceramic composites; particularly metal deformation and interface debonding. If glass is taken as the second phase, the geometry in Fig. 56b) can be used to examine crack bridging, if the crack is forced to follow the interface between the glass and the primary phase.

Finally, samples containing controlled interfacial pore structures, can be utilized as standards for non-destructive testing. These could help assess the capability of a variety of testing techniques available now[18] and would certainly be an improvement to voids seeded by randomly distributed plastic spheres[19].

VI. Concluding remarks

The new method of controlled interfacial pore structures allows generation of pore geometries with an unprecedented degree of precision and reproducibility. At the same time, nonequilibrium pore geometries that would not occur naturally (straight flat channels) can be produced and their evolution can be studied. This is clearly advantageous. All geometries are very well defined and theoretical models can be used to a certain degree. Pore geometries can be produced which span extremes of behavior (e.g. pore attachment to pore separation), thus allowing a complete range of microstructural processes to be studied. The competition between the evolution of pore shapes due to driving forces which aim to reduce the interfacial area (grain growth, equilibration with respect to an intersecting grain boundary, pore ovulation) and driving forces which tend to produce faceted pores is highlighted in various cases. The main conclusion to be drawn simply is, that if the first driving force is high enough compared to the second, faceting does not occur and the material appears to behave like an isotropic material. Experiments with small driving forces for morphological changes (e.g. scratch smoothing), however, are prone to investigate the kinetics of faceted structures, which certainly are not applicable to powder compacts undergoing rapid microstructural changes. Finally, while several questions could be answered, it is expected that the method of controlled pore structures will find many more applications in the future. (see V., Fig. 51).

A. Appendix

A. 1. Surface energy anisotropy in alumina

A. 1. 1. The crystallographic structure of alumina

The crystallographic phase of interest here is the α-phase (α-Al_2O_3) or, in its single-crystalline form, sapphire. It was excellently described by Kronberg[1] and is given in standard books on crystal structures[2]. Sapphire has a rhombohedral unit cell, a space group $R\bar{3}C$ and point group $\bar{3}m$. It thus has an inversion center. Figure 58 shows the packing of atoms on the basal plane of α-Al_2O_3, while Fig. 59 shows the aluminum sublattice. The structure can be viewed as an hcp sublattice of oxygen ions, with 2/3 of the octahedral interstices being filled with aluminum ions in an ordered array. The planes (0001), $\{1\bar{1}00\}$ and $\{11\bar{2}0\}$ are frequently referred to in various chapters. They are distinguished, as the basal plane as well as $\{1\bar{1}00\}$ show alternate densest packing of either oxygen or aluminum ions, wheras the $\{11\bar{2}0\}$ planes consist of alternate rows of both aluminum and oxygen ions.

A. 1. 2. Description of anisotropic surfaces

One of the more important questions in surface thermodynamics is that of the equilibrium shape of a constant volume particle or cavity. The mathematical formulation is simple. The surface free energy F, the integral over all surfaces S, multiplied by their respective energies γ, must be a minimum (Eq. 1):

$$F = \int \gamma \, dS = \min. \qquad \text{(eq. 1)}$$

The solution of this equation gives the equilibrium pore shape. For the case of an isotropic material, the equilibrium shape is a sphere. For the case of an anisotropic solid, the solution is given by the Wulff construction[3]. This result and the characteristics of the underlying γ-plot are thoroughly discussed by Herring[4,5]. A typical polar plot of surface free energy and the Wulff construction associated with it are given in Figure 60. First, γ is plotted radially as a function of the direction of $\vec{n}$, which might result in an outer curve as given in Fig. 60 and might include cusped& minima corresponding to surfaces of low Miller indices. Planes perpendicular to the radius are constructed at each point of this polar plot. The inside envelope of these planes is then, according to Wulff, geometrically similar to the equilibrium shape for the crystal. This construction is shown by the dashed lines in Figure 60. It can result in a variety of shapes, with straight and curved sides, depending on the depth of cusps of the polar plot, as discussed by Herring[4,5]. This equilibrium shape is a function of temperature, as thermal fluctuations tend to blunt the cusps in the γ-plot. The Wulff construction is not only of relevance for small particles, but also for large shapes where complete equilibrium cannot be reached as it would involve transport over large distances driven by small driving forces. In that case, however, neigboring surface configurations can be compared. By doing this, Herring[4] obtained the result, that, if a given surface does occur in the equilibrium shape, it will be stable; if it does not occur in the equilibrium shape, it will dissociate into a hill and valley structure.

While anisotropic surfaces are commonly described by the scalar function $\gamma(\vec{n})$ as advocated by Herring, a more recent treatment by Cahn and Hoffman[6,7] employs a vector function $\psi(\vec{n})$ to consider problems related to this field. Applications of this vector formalism include the equilibrium pore (or particle) shapes at grain boundaries and surfaces, which, of course, are of particular interest here. In particular, the chemical potential at faceted or curved surfaces is proportional to the surface divergence of the vector function Ψ.[7]

&: A cusp is a point with $\partial\gamma/\partial\theta$ finite, but discontinuous (θ the angle in the polar plot).

A. 1. 3. Dihedral angles and interfacial energies in alumina

Interfacial energies were experimentally obtained by means of equilibrium interfacial angle measurements[8-10], where a series of equilibria (solid-solid-vapor, solid-liquid-vapor, solid-solid-liquid) had to be established to determine absolute values. This data was thought to be obtainable with an accuracy of about 20 % by one of the investigators[8]. Handwerker[11,12] used a metal reference line technique to measure dihedral angles Φ in pure and MgO doped Al_2O_3. Results of both types of measurements are summarized in Table 3, where measured or suggested temperature cofficients[8-10] were used to obtain comparable values at 1800°C. Uncertainty of all values is indeed about 20 %. The dihedral angle mesurements by Handwerker appear to give the most reliable data, since they are based on the most sophisticated technique. Additional measurements of dihedral angles are reviewed by Handwerker et al.[12] It is suggested that $\Phi = 115,117^*$ for pure and MgO-doped alumina,

respectively and γ_s=0.9 J/m^2 at 1800°C. Experimentally obtained surface energies can be compared with theoretically derived values given by Tasker[13] for 5 low-index surfaces (at 0 K). His values range from 2.57 J/m^2 (for $10\bar{1}2$) to 3.27 J/m^2 (for $10\bar{1}1$). They compare well to the data extrapolated by Nikolopoulos to 0 K, γ_s=2.56 J/m^2 for the surface energy of a polycrystalline alumina.

*: The errors associated with measurements of dihedral angles can be substantial and are discussed by Handwerker et al.[12]

A. 1. 4. Some observations on the surface energy anisotropy in alumina

Many features discussed in sections III., A. 2., A. 3. and to a lesser degree in IV. are strongly related to the surface energy anisotropy in alumina. While some correlations between morphological evolution and surface thermodynamics are straightforward (e.g. the stability of the basal plane surface in crack healing, see A. 2.), some are not and difficult to explain, while again others appear to be common to several experiments. It is this last group which shall be discussed in the first part of this section. The second part will be devoted to controlled experiments designed to assess the relative surface energies in alumina.

There is a series of observations, which appears in conflict with the described crystallographic structure of α-Al_2O_3. These are the evolution of different-sized end bulges during perturbation and crack healing, the appearance of pear-shaped pores (pore perturbaton and pore coarsening, see Fig. 61) and more generally, the disappearance of an inversion center (primarily during crack

healing). All these phenomena were found in bicrystals with very small misalignment (<1°) and can be clearly characterized (e.g. by optical observation of pore structures through either side of the bicrystal and through scanning electron microscopy of both fracture surfaces). Since adsorption phenomena alter identical surfaces in the same manner, effects of impurities cannot account for the loss of the inversion center. They, however, might be responsible for the reversal of pore shapes as described in Fig. 29. Channels are originally etched only into one sapphire disk before bonding. The starting pore structure thus is devoid of an inversion center, but develops a symmetrical configuration in the cross section very early on in the morphological evolution (e.g. Fig. 15). Kinetical effects can also be excluded, since the same pear-like shape is approached from various original configurations. Explanations solely based on the influence of external fields (e.g. temperature gradients) are not satisfying. Therefore the most plausible explanation at this point, is, that the misalignment of both sapphire wafers, though very minor, exerts sufficient bias, so that all pore structures cannot exhibit an inversion center. Finally, a last point should be made with respect to the pear-shaped pores. In these features, straight edges always lie perpendicular to the $[11\bar{2}0]$ direction (Fig. 22a)*.

Clearly, determination of equilibrium pore structures as a function of misorientation angle (see also V.) will further elucidate this question.

Equilibrium pore shapes can be used to deduce relative surface energies from the Wulff construction, as done recently for LiF[14]. Particular care has to be taken that indeed stable and not just

metastable pore shapes are considered. It was Herring[5], who pointed out, that early observations[15] of cavities in rock salt clearly demonstrated the occurrence of both stable cubic and metastable rectangular pores. This concern was recently also voiced by Searcy[16]. Since by utilizing controlled pore structures pores of all kinds of shapes and in all directions can be produced, this problem can be eliminated. While possibilities for future studies were given already in section V., the available material (equilibrium cross sections) will be examined a bit more closely with respect to the measurement of relative surface energies. Figure 27 a,b) gives pore shapes at an interface with a misfit angle of 0.7°. Though the specimen was thermally etched for 2 hours at 1400°C (a strong etching treatment), no grain boundary could be resolved. Pore faces, particularly in Fig. 27a) are straight, which points to the existence of cusps in the γ-plot even at 1800°C in alumina. Both pore cross sections are viewed along primary, low-index directions (27a along $[1\bar{1}00]$, 27b along [0001]). If the sample is tilted, internal pore faces can be observed as being smooth, in contrast to the pore faces of closing pores (Fig. 28) which exhibit a hill and valley structure. It is therefore assumed that the observed edges represent planes which contain the direction of observation. In the case of Fig. 27b), the pore faces can be very easily described. The 12 bounding planes are obviously simply all prismatic planes $\{1\bar{1}00\}$ and $\{11\bar{2}0\}$, with an angle of 150° between neighboring planes. The pore shape appears somewhat flattened, which is consistent with the general rule of truncation for ψ-plots for pore shapes at interfaces, proposed by Cahn[7]. The very small degree of flattening corresponds to the very low energy of the grain boundary, which is present.

The very elongated pore shape in Fig. 27a) indicates, that surface energies of faceted planes can vary by as much as a factor of 2.3, which is very much greater than the differences Tasker[13] found between 5 low-index planes.

The data available on the surface energy anisotropy in alumina are very scarce so far. It is expected that the method of controlled interfacial pore structures will prove very useful for this field (for further descriptions see section V.).

*: Figures 18 and 61 are from bicrystals manufactured early on, where it cannot be assured whether the assembly was performed as described in Fig. 13.

A. 2. Crack healing

A. 2. 1. Background

> Crack healing in ceramics is a phenomenon wherein the deleterious effects of surface microcracks on strength are progressively reduced by heat treatment.[1]

If a process is described by its final effect rather than its step by step morphological evolution, two possible reasons come to mind. Firstly, the effect might be of overwhelming relevance, such that the actual evolution is secondary. Secondly, the actual step by step evolution cannot be described clearly. For crack healing, both reasons appear to apply.

Let us first look at the different experimental approaches taken in the studies of crack healing.

Cracks were introduced by inscription with a WC tool[2], thermal shocking[3-7], cleavage[8], incomplete bonding of bicrystals[9], indenting[10] or stressing of precracks[11]. The objectives were manifold. Cracks were produced in order to

1) study pore perturbation[2,4] (see III.),

2) examine strength recovery[3,5-7,11],

3) evaluate the actual evolution of the crack healing process[8-10]

Here, however, consideration will be given solely to the actual step by step evolution of the process.

As Nichols and Mullins[12] point out, planar cracks are stable against the development of undulations on the faces. Surface tension, however, causes the edge to recede and form a wide annulus spanned by the remainder of the crack. This rim is unstable against

perturbations along its length. As illustrated in Fig. 62, Nichols and Mullins then expect the rim to break up into a concentric ring of spheres. Lange and Clarke[13] demonstrated the morphological changes a thin intergranular film undergoes during heat treatment. This process is related to crack healing as it is also driven by capillary processes. The film was described as slowly reducing its area by forming thin fingers at the crack edge. They were also able to calculate the fastest growing wavelength of an edge perturbation. In his review of crack healing, Gupta[1] proposes two modes of crack healing. It either proceeds through continuous regression of the crack tip or through discontinuous pinching of the crack. From a comparison of the available literature on the behavior in alumina and other materials he suggests that the mode of crack healing depends on the method of introducing the crack. If the material remains stress free (after scratching, indenting or stressing), crack regression is dominant; if the material retains stored energy or residual stress (after thermal shocking), crack pinching prevails. Al_2O_3 seemed to follow this rule, however, NaCl did not. This distinction appears very arbitrary and lacks any physical basis. While the mode of crack regression might occur similar to Lange's[13] film regression, the mode of crack pinching is quite unclear. It might be speculated, however, that surface roughness and grain boundary grooving[14] (see also section IV.) help to connect asperities from both crack surfaces and thus promote crack pinching.

Kinetics of either crack pinching or crack regression could never be followed accurately in an experiment, as "cylinderization" is extremely rapid and cannot be documented for analysis[1]. No

complete theoretical analysis of the kinetics of either crack healing mode is known. Raj et al.[8] give qualitative equations for crack regression in order to distinguish between various transport paths. Charles and Evans[11] assume the dissociation of protruding cylinders into short pores to be the rate limiting step for strength recovery and thus avoid a discussion of the crack regression step. Finally, Dutton[15] proposes that crack healing occurs through grain boundary diffusion, which requires condensation of vacancies from the crack along the grain boundary of the material. This is only viable, if the crack extends through most of the specimen or the sample is very porous, otherwise the part of the sample which cannot densify will impose a constraint on the crack, preventing any shrinkage to occur.

After this brief analysis, we note that three issues are of prime interest:

a) What is the decisive factor controlling the mode of crack evolution?

b) What kinetics are followed?

c) What are the effects of surface energy anisotropy?

A. 2. 2. Experimental approach

Cracks of rectangular shape, 200 μm long and 100 μm wide, with a spacing between adjacent edges of 20 μm, were produced using previously described techniques. They were introduced into both basal plane bicrystals and prismatic plane $(11\bar{2}0)$ bicrystals with the misorientations of both bicrystals being less than 2 °. The crack depths were measured with a surface profilometer, and verified after bonding by SEM observations of interfacial cracks viewed edge

on. In basal plane bicrystals the cracks were 1800 Å deep and their edges aligned along $[1\bar{1}00]$ and $[11\bar{2}0]$. Prismatic plane bicrystals had cracks 1200 Å deep, aligned along [0001] and $[1\bar{1}00]$. About 200 cracks were produced and annealed under vacuum (1.3×10^{-3} Pa) at 1800°C.

Again, the morphological evolution of flat cracks was characterized in three ways. Samples were given several heat treatments and characterized intermittently by (nondestructive) observation of internal features using optical microscopy. This characterization allows quick assessment of the overall process and gives hints to special features worthy of further detailed investigation. Polished cross sections taken perpendicular to the crack plane can be examined using SEM. Similarly, higher resolution images can be obtained after fracturing the bicrystal at the interface and again employing scanning electron microscopy.

A. 2. 3. Results and discussion

While at least 10 successive heat treatments were performed per sample (and pictures taken), the evolution of internal features will be shown through composites of 4 or less micrographs. This is sufficient, as crack healing can be divided into a sequence of definite stages. Moreover, the evolution need only be followed to the point where channels are formed, since the final break-up into separate pores is discussed in section III.

Fig. 63 details the evolution of two flat cracks (the brighter areas) in a basal plane bicrystal at 1800 °C after 0, 60, 90 and 135 min, respectively. While the crack interior remains unperturbed, the

edges recede and form a thick rim around the crack. The rim is unstable to perturbations along its length and forms bulges and nodes. This variation of thickness leads to a differential regression of the edge (positions with thin annulus retract faster), which leaves the crack center connected to protruding cylinders more or less perpendicular to the original crack edge. From here the evolution shows the already known stages; regression of channel ends, ovulation and/or spheroidization. Lange and Clarke[13] made similar observations on the morphological changes of an intergranular thin film. Our method, however, is more conducive to detailed experimental investigation.

The regression of the crack edge occurs very rapidly, which explains, why it had been so difficult , to follow the overall evolution of the whole process[1]. The average velocity of the crack edge (as demonstrated through Figure 63 a-d) is 70 Å/s or about 25 μm/hr. The corners of rectangular cracks represent special sites. Here vacancies arrive from the regression of two edges, pile up and form an even thicker annulus (compared to the flat edges). These sites therefore lag behind in the general process of crack regression and lead to the formation of particularly long and thick protruding cylinders. Similar features can be expected during crack healing in a polycrystalline material, where some crack segments might be bound by faceted grains.

A final observation from Fig. 63 is particularly puzzling. The bottom edges of the crack appear considerably more unstable to perturbation than the top edges. Accordingly, protruding cylinders are only formed in the bottom half of the crack. As alumina has an inversion center (see A. 1.), both (top and bottom edges) ought to be

undistinguishable. This phenomenon was observed to a varying degree in about 60 cracks, no exceptions were found.

While the very similar behavior of the two cracks in Fig. 63 suggests, that the overall evolution of the healing step is very reproducible, detailed observations of many cracks reveal two possible variations, one kinetic, the other geometric. A wide spread in rates of morphological evolution, ranging from much lower to somewhat higher than illustrated, is found. Secondly, the perturbation of the thick annulus around the crack can set in at a much earlier stage, as shown in Fig. 64. In that case, protruding cylinders in the final stage will have much smaller diameter and will feature finer scale breakup compared to the process with a large initial contribution of crack regression. This distinction between the evolution of cracks in Figs. 63 and 64 emphasizes that the healing process occurs as a competition between crack regression and rim perturbation. Accordingly, cracks will evolve into a multitude of thin channels (if perturbation dominates) or a few much thicker tubular voids (if regression prevails). Both types of healing have been observed at the same interface; differences in local impurity content, which affect both the surface diffusion coefficients and the facetting behavior appear to provide the best acceptable explanation at this point. Note also, that the bottom edge of the cracks in Fig. 64 is considerably more unstable to perturbation than the top edge; the inversion center appears again lost in this mode of crack healing.

The cross section of a crack in a basal plane bicrystal, which predominantly showed crack regression, is shown in Fig. 65 after 10 min. at 1800 °C. The overall view of Fig. 65 a) allows assessment of

the uniformity of crack depth. Figures 65 b,c) focus on the thick end bulge. In this example (as in pore perturbation examples) they are not symmetric*. They show both faceting behavior, with the larger end bulge faceting also on the basal plane, which accounts for the constant thickness of this end bulge over a length of 1.5 μm. Crack regression only appears to influence a very localized region around the crack front, whereas the crack faces of the interior appear unperturbed.

Crack regression (with a late onset of rim perturbation) appears to be a 2-dimensional problem (there is only negligible variation looking into the crack as in Fig. 65 b). Therefore, this process appears to be very attractive for an investigation of the kinetics of faceted pore structures†.

Scanning electron micrographs of intermediate stages of crack healing are provided in Fig. 66 and 67#. Again the very different behavior of bottom vs. top (and left vs. right) crack edges is very apparent. The left and bottom edges adjust to an angle of about 80 °. The crack interior (in Figs. 66 a), 67 a,b)) appears unperturbed, crack regression results in a localized deep rim around the crack. While Fig. 67 a) can be visualized as a later stage of Fig. 66 a), Figure 66 b) proves, that kinetics of crack healing vary strongly. The crack represented appears to be in a final stage, where the resulting structure consists of channels (or pores) with increased girth; the unperturbed interior has been consumed. A definition to distinguish crack healing and pore perturbation might center on the disappearance of an unperturbed crack interior. Before this event, the

morphological evolution of the original crack might be termed crack healing, whereas later, pore perturbation might be more appropriate.

The evolution of flat cracks in prismatic plane bicrystals appears to be quite different (Figs. 68,69). While crack regression can again be found, the perturbation of a thick rim bounding the crack interior has not been observed. On the contrary, crack pinching was found to be a dominant process competing with crack regression. The outcome of this competition would dominate the evolution of the healing process. Moreover, two forms of crack pinching could be distinguished. Figure 68 demonstrates the appearance of small, apparently square pillars connecting the top and bottom crack faces. These would develop in the crack interior at a very early stage of the healing process, then would stay constant in number but would expand with time through a process similar to crack regression (neck growth, if viewed from the solid). After some time they would impinge on each other leaving "islands" separated by pore channels[$]. As cracks in an isotropic medium are stable against perturbations of their flat faces, this phenomenon must be related to the anisotropy of the material.

Another mode of crack pinching is illustrated in Fig. 69. Here crack pinching occurs directly behind the thick annulus created through a regression of the crack edge. This phenomenon creates pore channels parallel to the original crack front and occurs continuously until the crack has evolved into a series of parallel tubular voids. A loss of the inversion center as in crack healing in basal plane bicrystals is not observed here.

It is unclear at this point, what the governing parameters are which define the modes of crack pinching (interior vs. near-crack front). The fact that interior crack pinching occurs only in a very early stage of crack healing leads to the suspicion that the surface roughness of crack faces (which might smooth out during the initial stage) facilitates the creation of these internal crack pillars. Experiments with varying degrees of crack surface roughness and crack depth might give some further insight. Attempts to split prismatic plane bicrystals were unfortunately unsuccessful.

Cross sections of crack edges of this particular orientation are shown in Fig. 70 after 10 min. at 1800 °C. The evolution of the particular crack presented was dominated by crack regression and pinch-off at the edges. Facetting of the end bulges is again apparent. As shown previously in Fig. 15 e,f), there appears to be no low energy plane parallel to the grain boundary, which in this case forces the crack faces to dissociate into a hill and valley structure of low energy planes, which in turn leads to crack pinching. Differences in relative surface energy (the "crack tip Wulff plot")[&] are thus shown to be a reason for the different modes of crack healing behavior (crack regression vs. crack pinching).

Cross sections of a very late stage of crack healing (actually the pore perturbation stage according to the previous definition) are given in Fig. 71. Both micrographs show the outermost (and first evolved) pore channels created through crack pinching (the remainder of the healed crack is to the left in both cases). While Fig. 71 a) allows still visualization of the crack pinching process, Fig. 71 b) represents a cross section of a pore channel, which appears close to

local equilibrium. These micrographs demonstrate again the effect of surface energy anisotropy, and in the case where impurities might affect the g-plot in a certain manner, can be used as finger prints to show that (particular) impurites are present.

Finally an example of the very strong effect of impurities on the kinetics of evolution is shown in Fig. 72. It is estimated that the evolution of the crack to the right (B) occurred about 300 times faster than that of the crack to the left (A) will occur. This effect was solely confined to crack B. Though this remarkable difference in kinetics is not yet proven to be impurity related, an inclusion of some foreign species into crack B during bonding remains the most plausible explanation. This example also again demonstrates how critical maintenance of high purity processing is as well as illustrates what modifications can be achieved with small voluntary changes of composition.

*: Number of cracks observed in this way appears not sufficient for a generalizing statement.

†: The equations proposed by Raj et al.[8] are clearly only approximations.

#: Interfaces were fractured by manually applying a torque with a razor blade.

$: Pore channels appear dark in this orientation, as light gets scattered off the direction perpendicular to the original crack.

&: Combined with a difference in crack width.Both contributions could not be separated yet.

A. 2. 4. Conclusions

The morphological evolution of cracks at interfaces is strongly dependent on crystallographic plane and direction. Cracks at interfaces between two basal plane sapphire wafers demonstrate a

competition between crack regression and rim perturbation, which leads to the evolution of pore channels perpendicular to the original crack front. During this process the inversion center appears to be lost. Facetting of crack faces is apparent. Crack regression appears to be a very appealing experiment to model surface diffusion kinetics of facetted structures.

Cracks at interfaces between two prismatic plane sapphire disks show a competition between crack regression and crack pinching, which leads to the evolution of pore channels parallel to the original crack front. Crack pinching can also occur at a very early stage in the crack interior.

Influences of crystallography can thus be clearly demonstrated. Effects of crack depth and particularly influences of impurities remain the major fields for future investigations.

A. 3. A technique to study pore coarsening and pore elimination

A. 3. 1. Background

Pore coarsening and pore elimination are treated together in this chapter as experiments on either process can complement understanding of the other. While pore coarsening features pore-pore transport, pore elimination is based on pore-grain boundary transport. Pore coarsening can be divided into a sequence of three steps: vacancies detach from the surface of the smaller pore, diffuse to the surface of the larger pore, and attach at this new surface. A similar sequence is followed during pore elimination: vacancies detach from pore surfaces, diffuse to the grain boundary, and condense there. Diffusion can be accomplished through either grain boundary or lattice diffusion. Thus a brief review should discuss the transport between pores, and between pores and grain boundaries based on either diffusion mechanism, as well as mechanisms involving interfacial reactions (detachment and attachment of vacancies).

The coarsening of particles (or pores) in a saturated solid[1] or liquid[2] solution is a classical problem and reaches back to the work by Ostwald[3], hence the name Ostwald ripening. Lifshitz and Slyozow treated the problem assuming that lattice diffusion is rate controlling during the coarsening of a volume distribution of precipitates. Ardell[4] later considered the effect of volume fraction of precipitates, but arrived at the same basic conclusion as Lifshitz and Slyozow, namely that the average particle radius $\bar{r}$ changes with time t as:

$$\bar{r}^{-3} - \bar{r}_0^{-3} = k_1 t \qquad \text{(eq.1)}$$

with the distinction, however, that Ardell's k_1 differed from the one given by Lifshitz and Slyozow (r_0 is the average particle radius at t = 0).

Later models considered the coarsening of grain boundary precipitates under the assumption that diffusion occurs predominantly through the grain boundary[5-7]. In distinction to the prior case, this process has a different time dependence as given in Eq. (2):

$$\bar{r}^{-4} - \bar{r}_0^{-4} = k_2 t \qquad \text{(eq.2)}$$

with k_2 a parameter containing geometric and materials parameters.

For pore elimination the diffusion flux equation has not been solved for the case of pores situated at a grain boundary[8]. Coble[8], however, showed a solution for the case of cylindrical pores and outlines the problem for the spherical case.

Interfacial reactions occur at both the pore surface and the grain boundary. Reactions at pore surfaces were only recently discussed in more detail[9] . Condensation of vacancies at the grain boundary has been treated by considering the detailed nature and number of sinks and sources in the grain boundaries. Ashby et al.[10,11] modelled the condensation of vacancies at the grain boundary through a movement of dislocations, which can become the rate controlling step. This limit is favored if impurity levels are high, grains are small and temperatures are low. Experimental evidence for this model was provided by McCoy and Wills[12] who studied hot isostatic pressing of alumina powders at low temperatures.

Experimental description of both pore coarsening and pore elimination seems scarce. Gupta and Coble[13] observed pore coarsening in the final stage sintering of ZnO, but had to separate interfering effects of grain growth and thus pore coalescense. Kolar et al.[14] prepared model samples by swaging copper wire inserted into a copper tube of slightly larger diameter. This method allowed creation of pore structures which were confined to the interface between the copper wire and copper tube and thus eliminated pore growth through pore coalescense to a large degree. The coarsening of pores through Ostwald ripening was followed qualitatively but quantitative description was impossible due to the ill-defined initial pore structure.

Pore elimination experiments without the interference of other competing processes were not available earlier. Experiments using hot pressing dilatometry[15] came closest to reproducing an ideal situation of densification without grain growth.

A. 3. 2. Experimental approach

Using the approach of controlled interfacial pore structures, the actual pore geometry at the interface can be chosen to facilitate later theoretical evaluation. For that reason, simple monomodal pore size distributions (Fig. 36) and bimodal pore size distributions (Fig. 73 a-d, see also Fig. 5 a-d) can be utilized to study either pore eliminaton or pore coarsening. Figure 74 a-d provides micrographs of bonded sapphire bicrystals containing the bimodal pore structures as given in Fig. 73 a-d. Again, after bonding, bicrystals can be heated whereby flat pores will contract parallel to the grain boundary and expand

perpendicular to it. Examples of this initial stage of local equilibration are given in Fig. 75 a,b and Fig. 76 a,b. SEM micrographs show in both cases monomodal (a) and bimodal (b) pore size distributions viewed edge on (samples were cut, annealed for 20 min. at 1800 °C and thermally etched). Fig. 75 gives interfacial structures in a bicrystal with two basal plane sapphires bonded with a remaining twist angle of 0.4±0.5 °, whereas Fig. 76 gives features in a bicrystal with two prismatic plane sapphires $(11\bar{2}0)$ bonded with a remaining twist angle of 5.0±0.5 °. Both figures again demonstrate the flexibility of the method, and the very different facetting behavior as a function of bonding plane and twist angle.

A relaxation of local stress will accompany the local change of pore geometry (Fig. 77. a,b) in the early stage of the process. Immediately after bonding (and partly already during bonding), tensile stresses near pore surfaces and compressive stresses at the midpoints will equilibrate[16] by vacancy transport from pore surfaces to the grain boundaries. Stress levels will change during that process from those indicated by the full lines to those of the dashed lines. At that point an increased amount of the compressive stress in the system will be carried by the wide ligaments surrounding the pore structures. Pore coarsening can ensue as the change of chemical potential between different-sized pores is expected to be simply linear. For pore elimination to occur, the wide pore-free ligaments, however, have to be removed (cut off), which will enable the pore assemble to shrink and revert the stress levels to the original full lines.

A. 3. 3. Opportunities

The ability to control the volume fraction, size, size distribution and spatial distribution of interfacial pores, and to systematically vary each of these parameters over wide ranges allows essentially complete control over the topological characteristics that can affect coarsening and densification. In addition, a wide variety of bicrystals with varying bonding plane and twist angle can be produced[17] (see Fig. 75,76).

Let us first assume, that interfacial reaction rates are sufficiently high that kinetics are controlled by diffusion. Though the exact diffusion equations pertinent to simple bimodal and monomodal pore size distributions have yet to be developed, a summary of experimental opportunities can be given here.

If bicrystals with zero misorientation are produced, pore coarsening must occur by lattice transport, and the activation energy for lattice diffusion can thus be deduced from the temperature dependence of the coarsening rate. Increases in boundary misorientation can be used to change the relative contributions of grain boundary and lattice diffusion to the overall coarsening rate. Both bicrystal geometries can also be used to assess pore elimination with the additional complication, that (close to) zero misorientation bicrystals will have a very low density of vacancy sinks and thus, will tend to have kinetics controlled by interfacial reactions.

Transport due to grain boundary diffusion and lattice diffusion might possibly also be separated through their different time and size geometrical dependencies. As pointed out before, the pore coarsening rate by lattice transport has a weaker time dependence

(Eq. 1) than pore coarsening by grain boundary transport (Eq. 2). Similarly, both transport mechanisms scale differently with the critical geometric parameters (pore spacing)[8,18] and can thus be identified through pore coarsening experiments conducted in the same bicrystal with varying pore spacing.

Concurrent observations of different geometries in the same specimen are, of course, essential to a consistent (same impurity level) experimentation technique. While this is easy with pore coarsening studies, where only a few hundred pores are required per geometrical arrangement, studies on pore elimination require huge numbers of pores per sample. A uniform monomodal pore size distribution of pores with spacing 8 μm in a 4 mm x 4 mm bicrystal will require 250 000 pores. As this is a huge number for one mask, the stepping capabilities of the mask aligners might have to be employed to expose the same mask several times in adjacent positions (which reduces the overall accuracy slightly). It is, however, easy, to generate bicrystals with both monomodal and bimodal pore size distributions (in order to have the identical boundary misorientation) and then cut them up before experimentation.

As before, two options are given for monitoring the actual sizes of internal pore structures. Optical observation provides continuous, but low resolution measurements, while observations using scanning electron microscopy require fracturing the interface, and thus are discontinuous. Again, attention has to be paid to effects of anisotropy (see Fig. 61). It might be advisable to create original pore structures

according to crystal symmetry, in order to avoid a movement of pore centers as seen in Fig. 61.

Questions, whether interfacial reactions control the kinetics of either the coarsening or densification process, can be addressed by comparing results from both methods. Diffusivities extracted from coarsening studies can be used to predict pore shrinkage rates; if significantly lower shrinkage rates are observed, the elimination of vacancies at grain boundaries may be rate limiting.

Pore elimination experiments under varying levels of hydrostatic stress lead to additional opportunities. While diffusional transport is enhanced proportionally to the applied stress[19], interfacial reactions (if limited by dislocation mobility at the grain boundary) are increased proportionally to the square of the applied stress[11]. Therefore, the dependence of the densification rate on the external stress applied can be used to find the rate controlling step for pore elimination.

Similarly, if interfacial reactions at free surfaces are of interest, pore elimination of facetted and unfacetted pores can be compared. Facetted structures can be produced by incorporating an additional tempering step, following hot pressing and preceding removal of the pore-free boundary (which suppresses pore elimination).

Finally, the experimental techniques can be applied equally well to doped and undoped materials. Comparisons between the behavior of doped and undoped materials, coupled with the ability to control and reproduce pore geometries and boundary misorientation offers the potential to clearly identify the effects of dopants on

diffusion coefficients and/or the conditions leading to interfacial reaction control.

A. 3. 4. Conclusions

A number of experimental techniques that lend themselves to determination of transport coefficients and effects of interfacial reactions were suggested. The ability to simultaneously control and vary pore size and location may provide unique opportunities to obtain reliable experimental data. Finally, the reproducibility of the pore geometry and boundary misorientation allows the effects of other variables such as temperature, pressure, and dopant content to be isolated and studied.

A. 4. Grain growth in dense alumina

A. 4. 1. Background

Grain growth in alumina has been studied by either measuring the average grain growth rate in a polycrystalline sample or by observing the grain boundary displacement of seeded, large grains embedded in a polycrystalline matrix. Bennison and Harmer[1,2] used the former method for grain growth studies at 1600°C for undoped and MgO-doped Al_2O_3 (200 or 250 ppm MgO) and fitted their data to a kinetic law of the form (Eq. 1):

$$G^3 - G^3_0 = Kt \qquad (eq.\ 1)$$

where K is a temperature-dependent growth-rate constant, G the grain size at time t and G_o the original grain size. Their value K was decreased by a factor of 50 through the addition of 250 ppm MgO-dopant[2], but also depended strongly on the presence of a liquid phase[1].

Coble and Burke were the first to introduce large grains in the form of single crystal sapphire into a polycrystalline matrix[3]. This method was later followed up by Monahan and Halloran[4] and Kinoshita[5]. Glaeser and Chen[5] seeded large grains by employing localized laser heating. All of these studies neglected a possible influence of orientation of the single crystal on the grain boundary migration rate. Since typical microstructures of undoped alumina reveal very elongated grain shapes (where it is not clear here, if this is solely due to a glassy phase at the grain boundary), different grain growth rates

for different directions are expected. This issue was only recently investigated by Finkelstein et al.[7].

In this chapter, average grain growth data for a polycrystalline matrix as well as grain boundary migration rates for basal plane sapphire are presented, both as a function of MgO-content. The grain boundary displacement rate for the sapphire will be obtained and can be used for the pore-boundary separation analysis in section IV.

A. 4. 2. Experimental

Samples were used as described in section IV, with the chemical analysis of the polycrystalline specimen given in Table II. All experiments were performed at 1600°C in air with annealing times from 2.5 to 100 hours. The grain size of the polycrystalline matrix was determined with the linear intercept method. At least 100 grains were measured per annealing time.

A. 4. 3. Results and discussion

4. 3. 1. Kinetics of grain growth

The microstructural evolution of dense undoped and dense MgO-doped alumina as a function of time at 1600°C is depicted in Figures 80 and 81. In the undoped matrix grains are often of elongated shape, but with only few straight facets. During grain growth, grains facet* and develop small pores at grain boundary junctions. In the MgO-doped alumina the grain morphology appears equiaxed. Only few pores develop even after 100 hours at 1600°C, grain boundary faceting is less dominant. Both bloating and faceting might cause the creation of pores at grain boundary junctions. Bloating can

occur due to the conversion of residual carbon at grain boundaries into carbon monoxide, if oxygen diffuses into the sample. This process is not restricted to triple grain junctions, but can also occur at grain boundary faces. Desintering is due to the preferred occupation of low energy grain boundaries, which in turn imposes additional geometrical constraints on the matrix and can lead to a reduction in density. This process is accompanied by faceted grain boundaries and develops pores only at grain boundary junctions. Desintering thus appears to give the better explanation for the creation of pores next to grain boundary facets in triple grain junctions, as observed here. Their existence limits meaningful grain growth measurements in the undoped alumina to times less or equal to 40 hours at 1600°C, while the measurements in the MgO-doped alumina were performed for up to 100 hours at 1600°C.

The results of these observations are given in Figure 80 a,b. The undoped matrix had a larger starting average grain size and showed a higher degree of growth than the MgO-doped alumina. Data could be fitted very well by Equation 1 with a correlation coefficient higher than 0.97 for both materials. The growth rate constant K was found to be 1.03×10^{-20} m^3 s^{-1} for the MgO-doped alumina and 5.68×10^{-20} m^3 s^{-1} for the undoped alumina. This compares very well to the data obtained by Bennison and Harmer[1,2] (Table IV.).

The boundary migration rates for the basal plane sapphire into undoped and MgO-doped alumina are presented in Figure 81 a,b. The data agreed well (correlation factor >0.97) with an equation of the form:

$$\Delta G^2 = ft \qquad \text{(eq.2)}$$

with ΔG being the sapphire/polycrystal interfacial displacement and f a growth constant.

The parabolic law is based on the classical discussion of grain growth[8] (Eq.3):

$$v_b = (2\gamma_b M_b \Omega^{2/3})/G \qquad \text{(eq.3)}$$

with v_b the velocity of the grain boundary, γ_b the grain boundary energy and Ω the atomic volume.

Equations 1-3 can be used to extract the product $\gamma_b M_b$ as a description of the mobility of the sapphire/polycrystal interface, which is needed in section IV for a calculation of the pore-boundary separation condition. The velocity (Eq. 3) of the growing single crystal is obtained by differentiating Eq. 2 with respect to time at the point of separation (10 hours). The grain size of the polycrystalline matrix at the point of separation is given by Eq. 1. Inserting all values yields a product $\gamma_b M_b$ of 2.79 x 10^4/s for the undoped alumina and 3.54 x 10^4/s for the MgO-doped alumina. If a grain boundary energy of γ_b = 0.95 J/m^2 is assumed (which can be derived from the values for a surface energy and the dihedral angle), then grain boundary mobilities M_b for the undoped alumina of 3.72 x 10^{10} µm/Ns and 2.94 x 10^{10} µm/Ns for the MgO-doped alumina are obtained.

Both the cubic grain growth law for the growth kinetics in a polycrystalline matrix[1,2] as well as the parabolic law for the

migration rate of a single crystal into a polycrystalline matrix[4] are routinely used. The cubic law often simply gives the best fit and can best be justified by invoking segregation drag[9,10], which, however, is limited to a lower grain size regime. Moreover, if Eq. 1 is inserted into Eq. 3, the predicted migration rates have a grain size exponent of 1.5 rather than 2. While the classical grain growth model appears to be insufficient in this case, refuge might be taken to the recent theoretical efforts on the stochastic theory of grain growth[11] and the computer modeling of grain growth[12]. Both predict grain growth exponents of 2.4 for certain grain growth regimes. This value has the potential to give better data fits without obvious discrepancies, with the disadvantage that the clear physical concepts of a driving force for grain growth and the concept of a grain boundary mobility are lost. The classical concept can then only be uphold by invoking a driving force proportional to G^n with n not an integer or a grain size dependent mobility of atoms at the grain boundary (with the dependence being governed by the anisotropy of the material).

For our primary purpose, namely the computation of the pore-boundary separation regime, a grain boundary velocity of the basal plane of sapphire can be deduced from Fig. 81.

*: The duality between local faceting and the evolution towards global equilibrium (grain growth) is related to the duality between surface faceting and pore movement with respect to the grain boundary (see A.1.).

4. 3. 2. Interactions between deformation and grain growth

The difference in thermal expansion[13] between the basal plane in sapphire and the polycrystalline matrix creates a stress field, which, if enhanced through crack-like pores, can generate a complex deformation field as seen in Figures 82 and 83. These deformed zones, which are believed to be twins, enhance the grain growth rate at the single crystal-polycrystal interface by about a factor of 2 and lead to regions tens of microns wide, where the sapphire intrudes into the polycrystalline material. This phenomenon was only seen in some MgO-doped aluminas with small grain sizes. It is believed that creep has to occur in the polycrystalline matrix to accomodate the shear deformation of the sapphire, which is why materials with a large grain size (which are more creep resistent) do not have similar deformation zones.

While this particular behavior is not well understood, great opportunities appear to lie in the study of these special mechanisms, as they point out the very anisotropic nature of grain growth and thus reach further than models based on isotropic behavior[12].

4. 4. Conclusions

Grain growth kinetics which compare favorably with prior studies in this field have been obtained for both the polycrystalline matrix as well as the interface between basal plane sapphire and polycrystalline alumina. Data have been gained which can be inserted into theoretical predictions for the pore-boundary separation region.

Inconsistencies and difficulties in our current understanding and treatment of these problems have been pointed out. Novel experiments based on the interactions between deformation and grain growth, however, might improve our understanding of grain growth, particularly in an anisotropic matrix.

References:

II. A controlled experiment: The method of controlled interfacial pore structures

1. H. K. Bowen, "Was the Sintering Paradigm too Simplistic", to be published in Advances in Ceramics, ed. by C. A. Handwerker.
2. R. J. Brook, "Frontiers of Sinterability", to be published in Advances in Ceramics, ed. by C. A. Handwerker.
3. M. F. Yan, R. M. Cannon, H. K. Bowen and U. Chowdhry, "Effect of Grain Size Distribution on Sintered Density", Mat. Sci. and Eng., 60, 275 (1983).
4. H. E. Exner, "Grundlagen von Sintervorgängen", Gebrüder Bornträger, Berlin Stuttgart 1978.

   H. E. Exner, "Principles of Single Phase Sintering", Freud Publ. House Ltd., Tel-Aviv (1979).
5. G. Petzow and H. E. Exner, "Particle Rearrangement in Solid State Sintering", Z. Metallkunde 67, 611 (1976).
6. G. C. Kuczynski, "Self-Diffusion in Sintering of Metallic Particles", Trans. AIME185, 169 (1949).
7. R. L. Coble, "Initial Sintering of Alumina and Hematite", J. Am. Cer. Soc., 41[1] 60, 1950.
8. J. M. Dynys, R. L. Coble, W. S. Coblenz and R. M. Cannon, "Mechanisms of Atom Transport During Initial Stage Sintering of Al_2O_3", in Sintering Processes, Mat. Res. Vol. 13, ed. by G. C. Kuczynski, 391 (1980).

9. W. D. Kingery and M. Berg, J. Appl. Phys., 20, 1205 (1955).

10. P. Sajgalik, Z. Panek, M. Uhrik, "The Surface Diffusion Coefficients of MgO and Al_2O_3", J. Mat. Sci., 22 [12] 4460 (1987).

11. R. L. Eadie, D. S. Wilkinson and G. C. Weatherley, "The Rate of Shrinkage during the Initial Stage of Sintering", Acta Metall. 22, 1185 (1974).

12. W. S. Coblenz, J. M. Dynys, R. M. Cannon and R. L. Coble, "Initial Stage Solid State Sintering Models. A Critical Analysis and Assessment", in Sintering Processes, Mat. Res. 13, ed. by G. C. Kuczynski, (1980).

13. C. F. Yen and R. L. Coble, "Spheroidization of Tubular Voids in Al_2O_3 Crystals at High Temperatures", J. Am. Cer. Soc., 55 [10], 507 (1972).

14. T. K. Gupta, "Instability of Cylindrical Voids in Alumina", J. Am. Cer. Soc. 61 [5-6] 191 (1978).

15. M. P. Harmer and R. J. Brook, "The effect of MgO additions on the kinetics of hot pressing in Al_2O_3", J. Mat. Sci., 15, 3017 (1980).

16. J. K. McCoy and R. R. Willis, "Densification by Interface-Reaction Controlled Grain-Boundary Diffusion", Acta Metall., 135 [3] 577 (1987).

17. T. K. Gupta and R. L. Coble, "Sintering Of ZnO : II, Density Decrease and Pore Growth During the Final Stage of the Process", J. Am. Cer. Soc., (51) [9] 525 (1968).

18. D. Kolar, G. C. Kuczynski and S. K. Chiang, "On the Mechanism of Pore Coarsening", Mat. Sci. Res., 16, 81 (1984).

19. S. J. Bennison and M. P. Harmer, "Effect Of MgO Solute on the Kinetics of Grain Growth in Al_2O_3", J. Am. Cer. Soc., C-90 (66) [5] (1983).

20. S. J. Bennison and M. P. Harmer, "Grain Growth Kinetics for Alumina in the Absence of a Liquid Phase", J. Am. Cer. Soc., (68) [1] C-22 (1985).

21. M. Kinoshita, "Boundary Migration of Single Crystal in Polycrystalline Alumina", Yogyo-Kyokai-Shi 295 (1974).

22. R. D. Monahan and J. W. Halloran, "Single Crystal Boundary Migration in Hot-Pressed Aluminum Oxide", J. Am. Cer. Soc., (62) [11-12] 564 (1979).

23. A. M. Glaeser and J. C. Chen, "Technique for Measuring Grain-Boundary Mobility : Application to MgO-Doped Al_2O_3", J. Am. Cer. Soc., (65) [7] C-98 (1982).

24. N. J. Shaw and R. J. Brook, "Structure and Grain Coarsening During the Sintering of Alumina", J. Am. Cer. Soc., (69) [2] 107 (1986).

25. K. A. Berry and M. P. Harmer, "Effect of MgO Solute on Microstructure Development in Al_2O_3", J. Am. Cer. Soc., (69) [2] 143 (1986).

26. R. M. Cannon, "Sintering : A Densification-Coarsening Competition", unpublished research.

27. Y. Oishi and W. D. Kingery, "Self-Diffusion of Oxygen in Single Crystal and Polycrystalline Aluminum Oxide", J. Chem. Phys., (33) [2] 480 (1960).

28. D. J. Reed and B. J. Wuensch, "Ion-Probe Measurements of Oxygen Self-Diffusion in Single-Crystal Al_2O_3", J. Am. Cer. Soc., 63 [1-2] 88 (1980).

29. K. P. R. Reddy and A. R. Cooper, "Oxygen Diffusion in Sapphire", J. Am. Cer. Soc., 65 [12] 634 (1982).

30. A. E. Paladino and W. D. Kingery, "Aluminum Ion Diffusion in Aluminum Oxide", J. Chem. Phys., 37 [5] 957 (1962).

31. Y. Oishi, K. Ando, N. Suga and W. D. kingery, "Effect of Surface Condition on Oxygen Self-Diffusion Coefficients for Single Crystal Al_2O_3", J. Am. Cer. Soc., 66 [8] C-130 (1983).

32. R. S. Gordon, "Understanding Defect Structure and Mass Transport in Polycrystalline Al_2O_3 and MgO via the Study of Diffusional Creep", Advances in Ceramics, Vol. 10, W. D. Kingery, Ed., 418 (1984).

33. F. H. Huang, R. A. Henricksen and Che-Yu Li, "A Study of Capillarity and Mass Transport on the Al_2O_3 Surface", Mat. Sci. Res. Vol. 10,173 (1975).

34. T. Maruyama and W. Komatsu, "Surface Diffusion of Single Crystal Al_2O_3 by Scratch-Smoothing Method", J. Am. Cer. Soc., 58 (7-8) 338 (1975).

35. C. Monty, J. le Duigou, "The Influence of the Addition of MgO on the Surface Mass Transport of Alumina", High Temperatures - High Pressures, 14, 709 (1982).

36. J. F. Shackelford and W. D. Scott, "Relative Energies of [$\bar{1}100$] Tilt Boundaries in Aluminum Oxide", J. Am. Cer. Soc., 51 [12] 688 (1968).

37. A. R. Gaddipati, W. D. Scott, "Surface Mass Transport of Alumina", J. Mat. Sci., 21, 419 (1986).

38. W. M. Robertson and F. E. Ekstrom, "Impurity Effects in Surface Diffusion on Aluminum Oxide", Mat. Sci. Res. Vol., 4, 271 (1969).

39. P. V. McAllister and I. B. Cutler, "Thermal Grooving of MgO and Al_2O_3", J. Am. Cer. Soc., 59, [7] 351 (1972).

40. W. D. Kingery, "Metal-Ceramic Interactions : IV, Absolute Measurement of Metal-Ceramic Interfacial Energy and the Interfacial Adsorption of Silicon from Iron-Silicon Alloys", J. Am. Cer. Soc., 37 [2] 42 (1954).

41. S. K. Rhee, "Critical Surface Energies of Al_2O_3 and Graphite", J. Am. Cer. Soc., 55 [6] 300 (1972).

42. P. Nikolopoulos, "Surface, Grain-Boundary and Interfacial Energies in Al_2O_3 and Al_2O_3-Sn, Al_2O_3-Co Systems", J. Mat. Sci., 20, 3993 (1985).

43. M. Kahn and B. Kriese, "Patterned Macrovoids for Dielectric Constant Control of High Frequency Circuit Substrates", in Electronic Packaging Materials Science II, K. A. Jackson, R. C. Pohanker, D. R. Uhlmann, D. R. Ulrich, Ed., Mat. Res. Soc. Vol., 72, 35 (1986).

44. M. Kahn, A. Dalzell and B. Kovel, "PZT-Air Composites for Hydrostatic Sensing", Adv. Cer. Mat., 2 [4] 836 (1987).

45. K. Burger, W. Mader and M. Rühle, "Structure, Chemistry and Diffusion Bonding of Metal/Ceramic Interfaces", Ultramicroscopy 22 [1] 1 (1987).

46. J. Rödel and A. M. Glaeser, "Production of Controlled-Morphology Pore Arrays : Implications and Opportunities", J. Am. Cer. Soc., 70 [8] C-172 (1987).

47. G. Billingsley and K. Keller, "KIC : A Graphics Editor for Integrated Circuits".

48. L. F. Thompson and R. E. Kerwin, "Polymer Resist Systems for Photo- and Electron Lithography", Ann. Rev. of Mater. Sci., 6, 267 (1976).

49. E. Reichmanis and L. F. Thompson, "Polymer Materials for Microlithography", Ann. Rev. Mater. Sci., 17 , 235 (1987).

50. N. Laegreid and G. K. Wehner, "Sputtering Yields of Metals for Ar^+ and Ne^+ Ions with Energies from 50 to 600 eV", J. Appl. Phys., 32 [3] 365 (1961).

51. P. G. Glöersen, "Ion-Beam Etching", J. Vac. Sci. Technol., 12 [1] 28 (1975).

52. S. Somekh, "Introduction to Ion and Plasma Etching", J. Vac. Sci. Technol., 13 [5] 1003 (1976).

53. C. M. Melliar-Smith, "Ion Etching for Pattern Delineation", J. Vac. Sci. Technol., 13 [5] 1008 (1976).

54. E. Dörre and H. Hübner, "Alumina", Springer Verlag Berlin 1984.

55. R. C. Sun and C. L. Bauer, "Measurement of Grain Boundary Mobilities Through Magnification of Capillary Forces", Acta Metall.,18 [6] 635 (1970).

56. R. C. Sun and C. L. Bauer, "Tilt Boundary Migration in Nacl Bicrystals", Acta Metall., 18 [0] 639 (1970).

III. Morphological evolution of pore channels in alumina

1. C. F. Yen and R. L. Coble, "Spheroidization of Tubular Voids in Al_2O_3 Crystals at High Temperatures", J. Am. Cer. Soc., 55 [10] 507 (1972).
2. T.K. Gupta, "Instability of Cylindrical Voids in Alumina", J. Am. Cer. Soc., 61 [5-6] 191 (1978).
3. T.K. Gupta, "Crack Healing in Al_2O_3, MgO, and Related Materials", in "Structure and Properties of MgO and Al_2O_3 Ceramics", ed. by W.D.Kingery, The American Ceramic Society, Columbus, 1984.
4. O. Maruyama and W. Komatsu, "Observations on the Grain-Boundary of Al_2O_3 Bicrystals", Ceramurgia International 5 [2] 51 (1979).
5. D.M. Moon and R.C. Koo, "Mechanism and Kinetics of Bubble Formation in Doped Tungsten", Met. Trans. 2, 2115 (1971).
6. D.W. Budworth, "Theory of Pore Closure during Sintering", Trans. Brit. Cer. Soc., 69 [1] 29 (1970).
7. W. Beere, "The Sintering and Morphology of Interconnected Porosity in UO_2 Powder Compacts", J. Mat. Sci., 8, 1717 (1973).
8. W. Beere, "A Unifying Theory of the Stability of Penetrating Liquid Phases and Sintering Pores", Acta Metall., 23 [1] 131 (1975).
9. H. E. Cline, "Shape Instabilities of Eutectic Composites at Elevated Temperatures", Acta Metall., 19 [6] 481 (1971).
10. Y.G. Nakagawa and G.C. Weatherly, "The Thermal Stability of the Rod Al_3Ni-Al Eutectic", Acta Metall., 20 [3] 345 (1972).

11. A.J. Stapley and C.J. Beevers, "The Stability of Sapphire Whiskers in Nickel at Elevated Temperatures", J. Mat. Sci., 8, 1287 (1973).

12. M. McLean, "The Kinetics of Spheroidization of Lead Inclusions in Aluminum", Phil Mag., 27, 1253 (1973).

13. M. McLean, "In-Situ Observations of the Annealing of Liquid Lead Inclusions Entrained in an Aluminum Matrix", J. Mat. Sci., 9, 1104 (1974).

14. Lord Rayleigh, "On the Instability of Jets", Proc. London Math. Soc., 10, 4 (1879).

15. F.A. Nichols and W.W. Mullins, "Morphological Changes of a Surface of Revolution due to Capillarity-Induced Surface Diffusion", J. Appl. Phys., 36 [6] 1826 (1965).

16. F.A. Nichols and W.W. Mullins, "Surface- (Interface-) and Volume-Diffusion Contributions to Morphological Changes Driven by Capillarity", Trans. AIME 233, 1840 (1965).

17. F.A. Nichols , "On the Speroidization of Rod-shaped Particles of finite Length", J. Mat. Sci., 11, 1077 (1976).

18. W.W. Mullins, "Theory of Thermal Grooving", J. Appl. Phys., 28 [3] 333 (1957).

19. C. Herring, "The Use of Classical Miacroscopic Concepts in Surface-Energy Problems", in Structure and Properties of Solid Surfaces, ed. R.Gomer and C.S. Smith, The University of Chicago Press 1953, p.5.

20. W.W. Mullins, "Solid Surface Morphologies Governed by Capillarity", in "Metal Surfaces: Structure, Energetics and Kinetics", Am. Soc. for Metals, Metals Park, Ohio, 1963.

21. A.D. Brailsford and N.A. Gjostein, "Influence of Surface Energy Anisotropy on Morphological Changes by Surface Diffusion", J. Appl. Phys., 46 [6] 2390 (1975).

22. J.W. Cahn, "Stability of Rods with Anisotropic Surface Free Energy", Scr. Met., 13 [11] 1069 (1979).

23. W.C. Carter and A.M. Glaeser, "The Morphological Stability of Continuous Intergranular Phases: Thermodynamic Considerations", Acta Metall., 35 [1] 237 (1987).

24. W.C. Carter and A.M. Glaeser, "The Effect of Finite Amplitude Perturbations on the Stability of Continuous Phases", Mat. Sci. and Eng., 89, L41 (1987).

25. A.M. Glaeser, "On the Morphological Stability of Finite Length Intergranular Phases", Mat. Letters, 5 [7-8] 239 (1987).

26. J. Rödel and A.M. Glaeser, "Morphological Evolution of Pore Channels in Alumina", Advances in Ceramics, ed. C.A. Handwerker, The Am. Cer. Soc., Inc., Ohio, in press.

27. C. Herring, "Effect of Change of Scale on Sintering Phenomena", J. Appl. Phys., 21 [4] 301 (1950).

28. J.M. Dynys, R.L. Coble, W.S. Coblenz and R.M. Cannon, "Mechanisms of Atom Transport during Initial Stage Sintering of Al_2O_3", in Sintering Processes, ed. G.C. Kuczynski, Plenum Publishing Corporation 1980, p.391.

29. F.H. Huang, R.A. Henrichsen and Che-Yu Li, "A Study of Capillarity and Mass Transport on the Al_2O_3 Surface", Mat. Sci. Res. Vol., 10, 173 (1975).

30. Y. Oishy and W.D. Kingery, "Self-Diffusion of Oxygen in Single Crystal and Polycrystalline Aluminum Oxide", J. Chem. Phys., 33 [2] 480 (1960).

31. A.E. Paladino and W.D. Kingery, "Aluminum Ion Diffusion in Aluminum Oxide", J. Chem. Phys., 37 [5] 957 (1962).

32. D.J. Reed and B.J. Wuensch, "Ion-Probe Measurement of Oxygen Self-Diffusion in Single Crystal Al_2O_3" J. Am. Cer. Soc., 63 [1-2] 88 (1980).

33. K.P.R. Reddy and A.R. Cooper, "Oxygen Diffusion in Sapphire", J. Am. Cer. Soc. 65 [12] 634 (1982).

34. Y. Oishi, K. Ando, N. Suga and W.D. Kingery, "Effect of Surface Condition on Oxygen Self-Diffusion Coefficients for Single-Crystal Al_2O_3", J. Am. Cer. Soc., 66 [8] C-130 (1983).

35. P.G. Shewmon, "Diffusion in Solids", McGraw Hill (1971).

36. M. Abramowitz and I.A. Stegun, "Handbook of Mathematical Functions", National Bureau of Standards (1966).

37. N.A. Gjostein, "Surface Self-Diffusion", in "Metal Surfaces: Structure, Energetics and Kinetics", Am. Soc. for Metals, Metals Park, Ohio (1963), p. 99.

IV. Pore drag and pore-boundary separation

1. R.M. Cannon, "Sintering: A Densification-Coarsening Competition", unpublished research.
2. C.A. Handwerker, R.M. Cannon and R.L. Coble, "Final-Stage Sintering of MgO", Adv. in Ceramics, Vol. 10, ed. by W.D. Kingery, 619 (1984).
3. M.F. Yan, "Microstructural Control in the Processing of Electronic Ceramics", Mat. Sci. and Eng., 48, 53 (1981).
4. R.J. Brook, "Fabrication Principles for the Production of Ceramics with Superior Mechanical Properties", Proc. Br. Cer. Soc., 7 (1982).
5. S. Wu, E. Gilbart and R.J. Brook, "Solid State Sintering: The Attainment of High Density", Adv. in Ceramics, Vol. 10, ed. by W.D. Kingery, 575 (1984).
6. K.A. Berry and M.P. Harmer, "Effect of MgO Solute on Microstructure Development in Al_2O_3", J. Am. Cer. Soc., 69 [2] 143 (1986).
7. N.J. Shaw and R.J. Brook, "Structure and Grain Coarsening During the Sintering of Alumina", J. Am. Cer. Soc., 69 [2] 107 (1986).
8. M.P. Harmer, "Use of Solid-Solution Additives in Ceramic Processing", Adv. in Ceramics, Vol. 10, ed. by W.D. Kingery, 679 (1984).
9. M.P. Harmer and R. J. Brook, "The Effect of MgO Additions on the Kinetics of Hot Pressing in Al_2O_3", J. Mat. Sci., 15, 3017 (1980).

10. C.H. Hsueh and A.G. Evans, "Microstructure Evolution during Sintering: The Role of Evaporation/Condensation", Acta Metall., 31, 189 (1983).

11. F.H. Huang, R.A. Henrichsen and Che-Yu Li, "A Study of Capillarity and Mass Transport on the Al_2O_3 Surface", Mat. Sci. Res., Vol. 10, 173 (1975).

12. T. Maruyama and W. Komatsu, "Surface Diffusion of Single Crystal Al_2O_3 by Scratch-Smoothing Method", J. Am. Cer. Soc., 58 [7-8] 338 (1975).

13. C. Monty and J. Le Duigou, "The Influence of the Addition of MgO on the Surface Mass Transport of Alumina", High Temperatures-High Pressures, 14, 709 (1982).

14. C. F. Yen and R. L. Coble, "Spheroidization of Tubular Voids in Al_2O_3 Crystals at High Temperatures", J. Am. Cer. Soc., 55 [10], 507 (1972).

15. T.K. Gupta, "Instability of Cylindrical Voids in Alumina". J. Am. Cer. Soc., 61 [5-6] 191 (1978).

16. J. Rödel and A.M. Glaeser, "Morphological Evolution of Pore Channels in Alumina", Adv. in Ceramics, ed. by C.A. Handwerker, in press.

17. J.F. Shackelford and W.D. Scott, "Relative Energies of [$\bar{1}$100] Tilt Boundaries in Aluminum Oxide", Mat. Sci. Res., 4, 271 (1969).

18. A.R. Gaddipati and W.D. Scott, "Surface Mass Transport of Alumina", J. Mat. Sci., 21, 419 (1986).

19. W.M. Robertson and F.E. Ekstrom, "Impurity Effects in Surface Diffusion on Aluminum Oxide", Mat. Sci. Res., 4, 271 (1969).

20. J.M. Dynys, R.L. Coble, W.S. Coblenz and R.M. Cannon, "Mechanisms of Atom Transport during Initial Stage Sintering of Al_2O_3", in Sintering Processes, ed. G.C. Kuczynski, Plenum Publishing Corporation 1980, p.391.

21. J. Zhao and M.P. Harmer, "Effect of Pore Distribution on Microstructural Development: II, First- and Second-Generation Pores", J. Am. Cer. Soc., 71 [7] 530 (1988).

22. M. Sakarcan, C.H. Hsueh and A.G. Evans, "Experimental Assessment of Pore Breakaway During Sintering", J. Am. Cer. Soc., 66 [6] 456 (1983).

23. P.G. Shewmon, "The Movement of Small Inclusions in Solids by a Temperature Gradient", Trans. AIME 230, 1134 (1964).

24. F.A. Nichols, "Kinetics of Diffusional Motion of Pores in Solids", J. Nucl. Mat., 30, 143 (1969).

25. R.J. Brook, "Pore-Grain Boundary Interactions and Grain Growth", J. Am. Cer. Soc., 52 [1] 56 (1969).

26. R.J. Brook, "Controlled Grain Growth", in Treatise on Mat. Sci. and Techn., Vol. 9, 331,ed. by F.F.Y. Wang, Academic Press, New York, 1976.

27. F.M.A. Carpay, "Discontinuous Grain Growth and Pore Drag", J. Am. Cer. Soc., 60 [1-2] 82 (1977).

28. F.M.A. Carpay, "The Effect of Pore Drag on Ceramic Microstructures", in Ceramic Microstructures, p. 261, ed. by J. Pask 1976.

29. C.H. Hsueh, A.G. Evans and R.L. Coble, "Microstructural Development during Final/Intermediate Stage Sintering -I.

Pore/Grain Boundary Separation", Acta Metall., 30, 1269 (1982).

30. J. Rödel and A.M. Glaeser, "Production of Controlled-Morphology Pore Arrays: Implications and Opportunites", J. Am. Cer. Soc., 70 [8] C-172 (1987).
31. J. Rödel and A.M. Glaeser, "Pore Drag in Alumina", Adv. in Ceramics, ed. C.A. Handwerker, The Am. Cer. Soc., OH, in press.
32. R.L. Coble and J.E. Burke, "Sintering in Ceramics", Progr. in Cer. Science, Vol. 3, 197 (1963).
33. S.E. Bronisz and D.L. Douglass, "Grain Growth in Thin Films of ThO_2, NpO_2 and PuO_2", phys. stat. sol., 29, K95 (1968).

V. Suggestions for future work

1) L.F. Thompson and R.E. Kerwin, "Polymer Resist Systems for Photo- and Electron Lithography", Ann. Rev. Mat., Sci. 6, 267 (1976).

2) G. Calvin, "Up Close: National Nanofabrication Facility at Cornell University", MRS Bulletin, 13 [7] 31 (1988).

3) C. Herring, "Effect of Change of Scale on Sintering Phenomena", J. Appl. Phys., 21,301 (1950).

4) J.W. Cahn and D.W. Hoffman, "A Vector Thermodynamics for Anisotropic Surfaces - II. Curved and Faceted Surfaces", Acta Metall., 22 [10] 1205 (1974).

5) J.W. Cahn, private communication.

6) J. Rödel, W.C. Carter and A.M. Glaeser, unpublished research.

7) A.M. Glaeser and R. Gronsky, unpublished research.

8) J. Bierach and A.W. Searcy, unpublished research.

9) M. Drory, private communication.

10) J. Schneibel, private communication.

11) G. Pharr, private comunication.

12) J.R. Rice and T-J. Chuang, "Energy Variations in Diffusive Cavity Growth", J. Am. Cer. Soc., 64 [1] 46 (1981).

13) T.S.Oh, R.M. Cannon, J. Rödel, A.M. Glaeser and R.O. Ritchie, "Effects of near Interfacial Microstructure on Toughness and Subcritical Crack Growth in Ceramic/Metal Systems", in Interfaces in Polymer, Ceramic and Metal Matrix Composites, H. Ishida, Ed., Elsevier Science, New York 567-581 (1988).

14) T.S. Oh, J. Rödel, R.M. Cannon and R.O. Ritchie, "Ceramic/Metal Interfacial Crack Growth: Toughening by Controlled Microcracks and Interfacial Geometries", Acta Metall., (1988).

15) R.M. Cannon, T.S. Oh. J. Rödel, A.M. Glaeser and R.O. Ritchie "Toughening Ceramic-Metal Interfaces using Patterned Arrays of Near-Interfacial Pores", submitted to J. Am. Cer. Soc., (1988).

16) T.S. Oh, "Critical and Subcritical Crack Growth Behavior along Toughened Ceramic/Metal Interfaces, Ph.D. Thesis, Berkeley, September (1988).

17) B. Dalgleish, J. Rödel and A.G. Evans, "Fracture Characteristics of Metal/Ceramic Interfaces, to be published.

18) M.C. Bhardwaj, "Principles and Methods of Ultrasonic Characterization of Materials", Adv. Cer. Mat., 1 [4], 311 (1986).

19) D.J. Roth and G.Y. Bauklini, "Reliability of Scanning Laser Acoustic Microscopy for Detecting Internal Voids in Ceramics", Adv. Cer. Mat., 1 [3], 252 (1986).

A. 1. Surface energy anisotropy in alumina

1) M L. Kronberg, "Plastic Deformation of Single Crystals of Sapphire: Basal Slip and Twinning", Acta Metall., 5 [9] 507 (1957).

2) R.W.G. Wyckoff, "Crystal Structures", Vol. 2, Interscience Publishers, New York 1964.

3) G. Wulff, "Zur Frage der Geschwindigkeit des Wachsthums und der Auflösung der Kristallflächen", Zeitschrift der Krystallogr., 34, 449 (1901).

4) C. Herring, "Some Theorems on the Free Energies of Crystal Surfaces", Phys. Rev., 82 [1] 87 (1951).

5) C. Herring, "The Use of Classical Macroscopic Concepts in Surface-Energy Problems", in "Structure and Properties of Solid Surfaces", ed. R. Gomer and C.S. Smith, The University of Chicago Press, Chicago 1953.

6) D.W. Hoffman and J.W. Cahn, "A Vector Thermodynamics for Anisotropic Surfaces - I. Fundamentals and Application to Plane Surface Junctions", Surface Science 31, 368 (1972).

7) J.W. Cahn and D.W. Hoffman, "A Vector Thermodynamics for Anisotropic Surfaces - II. Curved and Faceted Surfaces", Acta Metall., 22 [10] 1205 (1974).

8) W.D. Kingery, "Metal-Ceramic Interactions: IV. Absolute Measurement of Metal-Ceramic Interfacial Energy and the Interfacial Adsorption from Iron-Silicon Alloys", J. Am. Cer. Soc., 37 [2] 42 (1954).

9) S.K. Rhee, "Critical Surface Energies of Al_2O_3 and Graphite", J. Am. Cer. Soc., 55 [6] 300 (1972).

10) P. Nikolopoulos, "Surface, Grain-boundary and Interfacial Energies in Al_2O_3 and Al_2O_3-Sn, Al_2O_3-Co Systems", J. Mat. Sci., 20, 3993 (1985).

11) J.E. Blendell and C.A. Handwerker, "Effect of Chemical Composition on Sintering of Ceramics", J. Crystal. Growth 75, 138 (1986).

12) C.A. Handwerker, J.M. Dynys, R.M. Cannon R.L. Coble, "Dihedral Angles in MgO and Al_2O_3. I. Distributions from Surface Thermal Grooves", submitted to J. Am. Cer. Soc., 1988.

13) P.W. Tasker, "Surfaces of Magnesia and Alumina", in "Structure and Properties of MgO and Al_2O_3 Ceramics", Adv. in Ceramics, Vol. 10, ed. W.D. Kingery, The American Ceramic Society, 1984, 176.

14) Z.Y. Wang, M.P. Harmer and Y.T. Chou, "Pore-Grain Boundary Configurations in Lithium Fluoride", J. Am. Cer. Soc., 69 [10] 735 (1986).

15) H.G. Müller, "Zur Natur der Rekristallisationsvorgänge. II. Untersuchungen an Rekristallisations-Einkristallen", Zeitschr. f. Physik 96, 307 (1935).

16) A.W. Searcy, D.J. Meschi and D. Beruto, "Kinetics of Neck Growth and Pore Closure in Faceted Solids", to be published in Adv. in Ceramics, ed. C.A. Handwerker, The American Ceramic Society, 1988.

A. 2. Crack Healing

1. T.K. Gupta, "Crack Healing in Al_2O_3, MgO, and Related Materials", in "Structure and Properties of MgO and Al_2O_3 Ceramics", ed. by W.D.Kingery, The American Ceramic Society, Columbus, 1984.
2. C. F. Yen and R. L. Coble, "Spheroidization of Tubular Voids in Al_2O_3 Crystals at High Temperatures", J. Am. Cer. Soc., 55 [10], 507 (1972).
3. T.K. Gupta, "Crack Healing and Strengthening of Thermally Shocked Alumina", J. Am. Cer. Soc., 59 [5-6] 259 (1976).
4. T.K. Gupta, "Instability of Cylindrical Voids in Alumina". J. Am. Cer. Soc., 61 [5-6] 191 (1978).
5. J.T.A. Roberts and B.J. Wrona, "Crack Healing in UO_2", J. Am. Cer. Soc., 56 [6] 297 (1973).
6. G. Bandyopadhyay and J.T.A. Roberts, "Crack Healing and Strength Recovery and UO_2", J. Am. Cer. Soc., 59 [9-10] 415 (1976).
7. G. Bandyopadhyay and C.R. Kennedy, "Isothermal Crack Healing and Strength Recovery in UO_2 Subjected to Varying Degrees of Thermal Shock", J. Am. Cer. Soc., 60 [1-2] 48 (1977).
8. R. Raj, W. Pavinich and C.N. Ahlquist, "On the Sintering Rate of Cleavage Cracks", Acta Metall., 25 [8] 919 (1977).
9. O. Maruyama and W. Komatsu, "Observations on the Grain-Boundary of Al_2O_3 Bicrystals", Ceramurgia International 5 [2] 51 (1979).

10. B. J. Hockey and B.R. Lawn, "Electron Microscopy of Microcracking about Indentations in Aluminum Oxide and Silicon Carbide", J. Mat. Sci.,10, 1275 (1975).

11. A.G. Evans and E.A. Charles, "Strength Recovery by Diffusive Crack Healing", Acta Metall., 25, 919 (1977).

12. F. A. Nichols and W.W. Mullins, "Surface- (Interface-) and Volume-Diffusion Contributions to Morphological Changes Driven by Capillarity", Trans AIME 233, 1840 (1965).

13. F.F. Lange and D.R. Clarke, "Morphological Changes of an Intergranular Film in a Polycrystalline Spinel", J. Am. Cer. Soc., 65 [10] 502 (1982).

14. J.E. Bronisz and D.L. Douglass, "Grain Growth in Thin Films of ThO_2, NpO_2, and PuO_2", phys. stat. sol., 29, K95 (1968).

15. R. Dutton, "Comments on 'Crack Healing in UO_2' ", J. Am. Cer. Soc., 56 [12] 660 (1973); "Correction: Comments on 'Crack Healing in UO_2' ", ibid., 59 [1-2] 88 (1976).

A. 3. A technique to study pore coarsening and pore elimination.

1. M. Lifshitz and V. V. Slyozow, "The Kinetics of Precipitation from Supersaturated Solid Solutions", J. Phys. Chem. Solids, 19 [1,2] 35 (1961).
2. C. Wagner, "Theorie der Alterung von Niederschlägen durch Umlösen", Zeitschrift für Elektrochemie 65 [7,8] 581 (1961).
3. W. Ostwald, "Über die vermeintliche Isomerie des roten und gelben Quecksilberoxids und die Oberflächenspannung fester Körper", Zeitschrift für phys. Chemie 34, 495 (1900).
4. A. J. Ardell, "The Effect of Volume Fraction on Particle Coarsening : Theoretical Considerations", Acta Metall., 20 [1] 61 (1972).
5. A. J. Ardell, "On the Coarsening of Grain Boundary Precipitates", Acta Metall., 20 [4] 601 (1972).
6. M. V. Speight, "Growth Kinetics of Grain -Boundary Precipitates", Acta Metall., 16 [1] 133 (1968).
7. H. O. K. Kirchner, "Coarsening of Grain-Boundary Precipitates", Met. Trans. 2 (10) 2861 (1971).
8. R. L. Coble, "Sintering Crystalline Solids. I. Intermediate and Final State Diffusion", J. Appl. Phys., 32 [5] 787 (1961).
9. A. W. Searcy, D. J. Meschi and D. Berato, "Kinetics of Neck Growth and Pore Closure", to be published in Adv. in Ceramics, C. Handwerker, ed., The American Ceramic Society.
10. M. F. Ashby, "On Interface-Reaction Control of Nabarro-Herring Creep and Sintering", Scripta Met., 3, 837 (1969).

11. E. Arzt, M. F. Ashby and R. A. Verrall, "Interface Controlled Diffusional Creep", Acta Metall., 31 [12] 1977 (1983).

12. J. K. McCoy and R. R. Wills, "Densification by Interface-Reaction Controlled Grain Boundary Diffusion", Acta Metall., 35 [3] 577 (1987).

13. T. K. Gupta and R. L. Coble, "Sintering of ZnO : II, Density Decrease and Pore Growth During the Final Stage of the Process", J. Am. Cer. Soc., 51 [9] 525 (1968).

14. D. Kolar, G. C. Kuczynski and S. K. Chiang, "On the Mechanisms of Pore Coarsening", Mat. Sci. Res., 16, 81 (1984).

15. M. P. Harmer and R. J. Brook, "The Effect of MgO Additions on the Kinetics of Hot Pressing in Al_2O_3", J. Mat. Sci., 15, 3017 (1980).

16. D. L. Johnson, "New Method of Obtaining Volume, Grain-Boundary, and Surface Diffusion Coefficients from Sintering Data", J. Appl. Phys., 40 [1] 192 (1969).

17. J. Rödel and A.M. Glaeser, A Technique for Investigating the Elimination and Coarsening of Model Pore Arrays", accepted at Materials Letters (March 1988)

18. C. Herring, "Effect of Change of Scale on Sintering Phenomena", J. Appl. Phys., 21 [4] 301 (1950).

19. R. L. Coble, "Diffusion Models for Hot Pressing with Surface Energy and Pressure Effects as Driving Forces" J. Appl. Phys. 41 [11] 4798 (1970).

A. 4. Grain growth in dense alumina

1. S.J. Bennison and M.P. Harmer, "Effect of MgO Solute on the Kinetics of Grain Growth in Al_2O_3", J. Am. Cer. Soc., 66 [5] C-90 (1983).
2. S.J. Bennison and M.P. Harmer, "Grain Growth Kinetics for Alumina in the Absence of a Liquid Phase", J. Am. Cer. Soc., 68 [1] C-22 (1985).
3. R.L. Coble and J.E. Burke, "Sintering in Ceramics", Progress in Ceramic Science 3, 197 (1963).
4. R.D. Monahan and J.W. Halloran, "Single-Crystal Boundary Migration in Hot-Pressed Aluminum Oxide", J. Am. Cer. Soc., 62 [12] 564 (1979).
5. M. Kinoshita, "Boundary Migration of Single Crystal in Polycrystalline Alumina", Yogyo-Kyokai-Shi 82 [5] 295 (1974).
6. A.M. Glaeser and J.C. Chen, "Technique for Measuring Grain-Boundary Mobility: Application to MgO-Doped Al_2O_3", J. Am. Cer. Soc., 65 [7] C-98 (1982).
7. Y. Finkelstein, B.J. Hockey, S.W. Wiederhorn, J.E. Blendell and C.A. Handwerker, "Migration of Sapphire into Alumina", to be published in Adv. in Ceramics, ed. C.A. Handwerker, The American Ceramic Society, OH (1988).
8. D. Turnbull, "Theory of Grain Boundary Migration Rates", Trans AIME 19 [8] 661 (1951).
9. J.W. Cahn, "The Impurity Drag Effect in Grain Boundary Motion", Acta Metall., 10 [9] 789 (1962).

10. R.J. Brook, "The Impurity-Drag Effect and Grain Growth Kinetics", Scripta Met., 2 [7] 375 (1968).

11. I-Wei Chen, "A Stochastic Theory of Grain Growth", Acta Metall., 35 [7] 1723 (1987).

12. M.P. Anderson, "Computer Simulation of Grain Growth - I. Kinetics", Acta Metall., 32 [5] 783 (1984).

13. E. Dörre and H. Hübner, "Alumina", Springer Verlag, Berlin 1984.

Table 1: Normalized perturbation characteristics as a function of orientation.

	(0001)[$1\bar{1}00$]	(0001)[$11\bar{2}0$]	($11\bar{2}0$)[0001]	($11\bar{2}0$)[$1\bar{1}00$]
(Node spacing)/D	7.3-13.9	--	19.4-27.2	44.4-50.5
(Pore spacing)/D	15.1-18.7	>100	84.5-112.9	44.4-50.5
CriticalL/D	>78	--	>93	>93

Table 2: Impurity content of cations (in ppm) in polycrystalline alumina matrix

	undoped alumina	MgO-doped alumina
Mg	< 10	200
Si	< 30	< 30
Ca	10	< 10
Fe	< 30	< 30
Ni	10	--
Mn	< 10	< 10
Cu	< 5	< 5

Table 3: Interfacial energies and dihedral angles for alumina at 1800°C.

	γ_{gb} (J/m^2)	γ_s (J/m^2)	Φ (°)
Kingery	0.44	0.91	152
Rhee	--	0.67	--
Nikolopoulos	0.65	0.93	139
Handwerker	--	--	115,117*

*: MgO-doped alumina.

Table 4: Comparison of experimental rate constants K

Source	K in undoped Al_2O_3 ($m^3\ s^{-1}$)	K in MgO-doped Al_2O_3 ($m^3\ s^{-1}$)
single phase[1]	5.17×10^{-19}	1.04×10^{-20}
with liquid phase[2]	1.74×10^{-19}	3.90×10^{-20}
current work	5.68×10^{-20}	1.03×10^{-20}

Figure captions

Fig. 1: Schematic illustrating the problems encountered in discussing sintering of homogenuous single phase materials.

Fig. 2: Separation of sintering into separate processes.

Fig. 3: Available non-sintering experiments for a better understanding of sintering.

Fig. 4: Effect of exposure time on final feature geometry; exposure times: a) 0.75 sec, b) 1.5 sec, c) 3 sec.

Fig. 5: SEM of bimodal pore size distributions; pore spacing (between centers of different-sized pores): a) 3.5 μm, b) 4.5 μm, c) 4.2 μm, d) 5.6 μm; width of larger pore: a,b) 3 μm, c,d) 4 μm; width of smaller pore: 0.8 μm.

Fig. 6: Pores in single crystal-polycrystal interface; a) pore array, b) high magnification of single pore.

Fig. 7: Optical micrographs of internal pore structures: a) bimodal pore size distribution, b) pores with varying aspect ratio.

Fig. 8: Schematic of pore ovulation and pore spheroidization.

Fig. 9: Predicted shape changes for rod of initial aspect ratio of a) 7.00 and b) 7.64.

Fig.10: Variety of pore structures for pore perturbation; a) width w=2.2μm, k=1, b) w=3.4μm, k=2, c) w=4.7μm, k=3, d) w=5.7μm, k=4; length l=ks, where s=1,....20.

Fig.11: Intermediate length pore structures; a) width w=2.2μm, k=2, b) w=5.7μm, k=4; length l=ks, where s=16,...35 for a), s=6,...25 for b).

Fig.12: Array of long channels, widths varying from 2.2 to 7.7μm, length=200μm.

Fig.13: Relative orientation of the wafer disks is shown by demonstrating assembly of the bicrystal from a single crystal wafer. Original wafer is cut and one part lifted on top of the other, A goes into A'.

Fig.14: Pore channels of a) intermediate and b) 200μm-length in as-bonded bicrystal.

Fig.15: Cross sections of pore channels in sapphire bicrystals; a),b) as bonded; c),d) after 20 min. at 1800°C in basal plane bicrystal; e),f) after 10 min. in prismatic plane bicrystal, g),h) after 20 min. in prismatic plane bicrystal; e=[$11\bar{2}0$], f=[0001], g=[$1\bar{1}00$]; twist angles im prismatic plane bicrystals: c),d) 0.4°, e)-h): 5.0°.

Fig.16: The morphological evolution of a specific (0001)[$1\bar{1}00$] oriented six-channel motif, following anneals of a) 0, b) 40, c) 60, d) 90, e) 135 and f) 200 min. at 1800°C; e=[$11\bar{2}0$], g=[$1\bar{1}00$].

Fig.17: The morphological evolution of a 5-channel array. Channels 1 through 5 (top to bottom) have diameters of 1.1, 1.1, 0.9, 1.3 and 1.7μm; e=[$11\bar{2}0$], g=[$1\bar{1}00$].

Fig.18: The morphological evolution of short channels with varying aspect ratios, following anneals of a) 0, b) 8, c) 17 hrs. at 1800°C; e=[$11\bar{2}0$], g=[$1\bar{1}00$].

Fig.19: SEM micrographs at bicrystal fracture surface with 6-channel motif, both after 5 1/2 hrs. at 1800°C; e=[$11\bar{2}0$], g=[$1\bar{1}00$].

Fig.20: Examples (a,b) of SEM micrographs of bicrystal fracture surface with 5-channel array (geometries as fig.17 after 25 hrs. at 1800°C.).

Fig.21: Optical micrographs comparing 6-channel motifs, channels oriented either in direction e=[11$\bar{2}$0] or g=[1$\bar{1}$00].

Fig.22: SEM micrographs of bicrystal fracture surface with 6-channel motif, channels oriented in direction e=[11$\bar{2}$0], g=[1$\bar{1}$00].

Fig.23: (11$\bar{2}$0)[0001]-oriented pore channels after: a) 0, b) 7 1/2 and c) 48 hrs. at 1800°C.

Fig.24: (11$\bar{2}$0)[0001]-oriented short pore channels after: a) 0, b) 3 1/2, c) 7 1/2 and d) 48 hrs. at 1800°C.

Fig.25: (11$\bar{2}$0)[1$\bar{1}$00]-oriented pore channels after: a) 5 min., b) 1 1/2 hrs., c) 5 hrs. and d) 48 hrs. at 1800°C.

Fig.26: (11$\bar{2}$0)[1$\bar{1}$00]-oriented short pore channels after: a) 5 min., b) 1 1/2 hrs., c) 5 hrs. and d) 48 hrs. at 1800°C.

Fig.27: Cross sections of open pore channels after 48 hrs. at 1800°C, aligned in direction a) g=[1$\bar{1}$00], b) f=[0001]; e=[11$\bar{2}$0].

Fig.28: Cross sections of closing pore channels after 48 hrs. at 1800°C, aligned in direction a) g=[1$\bar{1}$00], b) f=[0001]; e=[11$\bar{2}$0].

Fig.29: Effect of perturbations (presumably impurities) on morphological evolution of pore channels after 2 hrs. at 1800°C; e=[11$\bar{2}$0], g=[1$\bar{1}$00].

Fig.30: Distribution of pinchoff times for (0001)[1$\bar{1}$00]-oriented channels with width 0.72μm.

Fig.31: Sketch of geometrical relationship between (0001)[1$\bar{1}$00]-oriented and (11$\bar{2}$0)[1$\bar{1}$00]-oriented channels.

Fig.32: Schematic representation of terrace-ledge-kink model of surface structure. Atoms residing in different sites are designated by their coordination number; N=3 (adatom), and N=9 (terrace atom). These particular coordination numbers refer to a (111) plane (from Gjostein)[38].

Fig.33: Sketch of sintering trajectory including idealized paths corresponding to hot pressing (zero coarsening) and controlled pore drag (zero densification) experiments.

Fig.34: Scanning electron micrographs of hot pressed a) undoped alumina, and b) MgO-doped alumina.

Fig.35: Scanning electron micrographs of first hot pressed, then hot isostatically pressed a) undoped alumina, and b) MgO-doped alumina.

Fig.36: Examples of surface structures used for controlled pore drag experiments. The pore width is 3 μm, center-to-center pore spacings are a) 4 μm, b) 6 μm, c) 8 μm, and d) 10 μm, and the pore depth is 0.24 μm.

Fig.37: Examples of surface structures used for controlled pore drag experiments. The pore width is 5 μm, center-to-center pore spacings are a) 6 μm, and b) 8 μm, and the pore depth is 0.24 μm.

Fig.38: Segment of whole pore array on sapphire. Structure as in Fig. 36a.

Fig.39: Micrograph of interface between single crystal and polycrystalline MgO-doped alumina.

Fig.40: Pore structures at the interface between sapphire and MgO-doped alumina. Pore spacings and structures are identical to those in Fig. 36.

Fig.41: Pore structures at the interface between sapphire and MgO-doped alumina. Pore spacings and structures are identical to those in Fig. 37b; a) low magnification, and b) high magnification.

Fig.42: Optical micrograph of as-bonded interface containing pore structures as shown in Fig. 37.

Fig.43: Large crack-like pore marking original position of interface after 30 hours at 1600°C.

Fig.44: Pore separation of originally instable pore arrays in MgO-doped alumina after 7.5 hours at 1600°C; pore structure as given in Fig. 37b.

Fig.45: Morphological evolution of initially flat pores in alumina after a) 10 hours, and b) 20 hours at 1600°C; pore structures as given in Fig. 37b.

Fig.46: Illustration of pore drag in MgO-doped alumina after 5 hours at 1600°C.

Fig.47: Grain boundary migration versus time at 1600°C for various pore spacings; a) undoped alumina, and b) MgO-doped alumina.

Fig.48: Partial separation of MgO-doped alumina after 15 hours at 1600°C, pore structures as in Fig. 37a.

Fig.49: Pore-boundary separation in MgO-doped alumina at two different pore spacings f; a) f = 6 μm, and b) f = 10 μm.

Sample was annealed for 15 hours at 1600°C. Separation occured after ≈ 10 hours.

Fig.50: Calculated and observed separation conditions for a) undoped, and b) MgO-doped alumina.

Fig.51: SEM micrographs showing bloating after 16 hrs. at 1800°C in basal plane bicrystal in area a) containing pore channels, b) without controlled pore structure; e=[11$\bar{2}$0], f=[1$\bar{1}$00].

Fig.52: Simple geometric features with varying symmetry for investigation of metastable pore structures; a) circle, b) triangle, c) square, d) hexagon.

Fig.53: Features produced to investigate metastable and stable pore structures; a) chevron, b) hexagon in hexagon, c) triangle up in triangle, d) triangle down in triangle.

Fig.54: Examples for rotations of original geometries; a) square successively rotated by 15°, b) chevron successively rotated by 45°.

Fig.55: Pore structures with constant pore spacing and varying pore size; pore spacing 8 μm, pore width: a) 2.0 μm, b) 3.0 μm, c) 3.7 μm, d) 4.7 μm.

Fig.56: Compact tensile specimen outlining possible geometries for 2-dimensional controlled-geometry composites; a) rod-shaped second phase aligned perpendicular to the crack plane, b) in the crack plane.

Fig.57: Explanation marks and question marks are produced from crack healing and stand symbolic for questions answered and new questions posed during the course of this work.

Fig.58: Packing of aluminum and oxygen ions in the basal plane. The upper layer of oxygen ions is not shown. Basal hexagonal cell vectors and directions are indicated (from Kronberg[1]).

Fig.59: Distribution of aluminum ions and holes on the simple hexagonal lattice. The smallest rhombohedral cell which correctly describes the positions of the cations is shown along with the corresponding hexagonal cell vectors (from Kronberg[1]).

Fig.60: Typical polar plot of surface free energy for a crystal and the Wulff construction associated with it.

Fig.61: Scanning electron micrograph from bimodal pore size distribution in basal plane bicrystal after 25 hrs. at 1800°C, original structure will be given in Fig. 41 c,d); a=[11$\bar{2}$0], b=[1$\bar{1}$00].

Fig.62: Schematic representation of speroidization of a precipitate plate (after Nichols and Mullins[8]).

Fig. 63: Examples for morphological evoluton of cracks during annealing at 1800 °C after a) 0 min., b) 60 min., c) 90 min., d) 135 min.; e=[11$\bar{2}$0], g=[1$\bar{1}$00] (crack regression is dominant).

Fig. 64: Examples for morphological evoluton of cracks during annealing at 1800 °C after a) 0 min., b) 60 min., c) 90 min., d) 135 min.; e=[11$\bar{2}$0], g=[1$\bar{1}$00] (rim perturbation is dominant).

Fig. 65: Cross section of crack in basal plane bicrystal after 10 min. at 1800 °C; a) low magnification view of whole crack, b,c) high magnification micrographs of left and right end bulges, respectively; e=[11$\bar{2}$0], f=[0001].

Fig.66: Scanning electron micrographs from healed cracks after 5 1/2 hrs. at1800 °C; e=[11$\bar{2}$0], g=[1$\bar{1}$00].

Fig.67: Scanning electron micrographs from healed cracks after 16 hrs. at 1800 °C; e=[11$\bar{2}$0], g=[1$\bar{1}$00].

Fig. 68: Examples for morphological evoluton of cracks during annealing at 1800 °C after a) 5 min., b) 210 min.; f=[0001], g=[1$\bar{1}$00].

Fig. 69: Examples for morphological evolution of cracks during annealing at 1800 °C after a) 3 1/2 hrs., b) 6 1/2 hrs.; c) 16 hrs.; f=[0001], g=[1$\bar{1}$00].

Fig.70: Cross section of crack edges in prismatic plane bicrystal after 10 min. at 1800 °C, a,b) left and right end bulges, respectively; e=[11$\bar{2}$0], f=[0001].

Fig.71: Cross sections of pinched-off channels in late stage crack healing in prismatic plane bicrystal after 48 hours at 1800 °C; e=[11$\bar{2}$0], f=[0001],g=[1$\bar{1}$00].

Fig.72: Examples of crack healing at 1800 °C in basal plane bicrystals illustrating extreme differences in kinetics of overall process; after a) 0 min., b) 5 min., c) 200 min.; e=[11$\bar{2}$0], f=[0001].

Fig.73: Bimodal pore size distributions as used for studies of pore coarsening. Width of larger pores: a,b) 4 μm, c,d) 6 μm; width of small pores: a-d) 2 μm; spacings: a) 6 μm, b,c) 8.5 μm, d) 10 μm.

Fig.74: Optical micrographs of interfacial bimodal pore size distributions. Size and spacings as in Fig. 73.

Fig.75: Monomodal (a) and bimodal (b) pore size distributions viewed edge on. Pores on basal plane in bicrystal with 0.4±0.5 ° misorientation; e=[11$\bar{2}$0], f=[0001].

Fig.76: Monomodal (a) and bimodal (b) pore size distributions viewed edge on. Pores on prismatic plane (11$\bar{2}$0) in bicrystal with 5.0±0.5 ° misorientation; e=[11$\bar{2}$0], f=[0001].

Fig.77: Schematic illustration of local stress levels in bicrystal with monomodal (a) and bimodal (b) pore size distributions.

Fig.78: Grain structure of dense, undoped alumina after a) 5, b) 15, c) 20 and d) 60 hours at 1600°C.

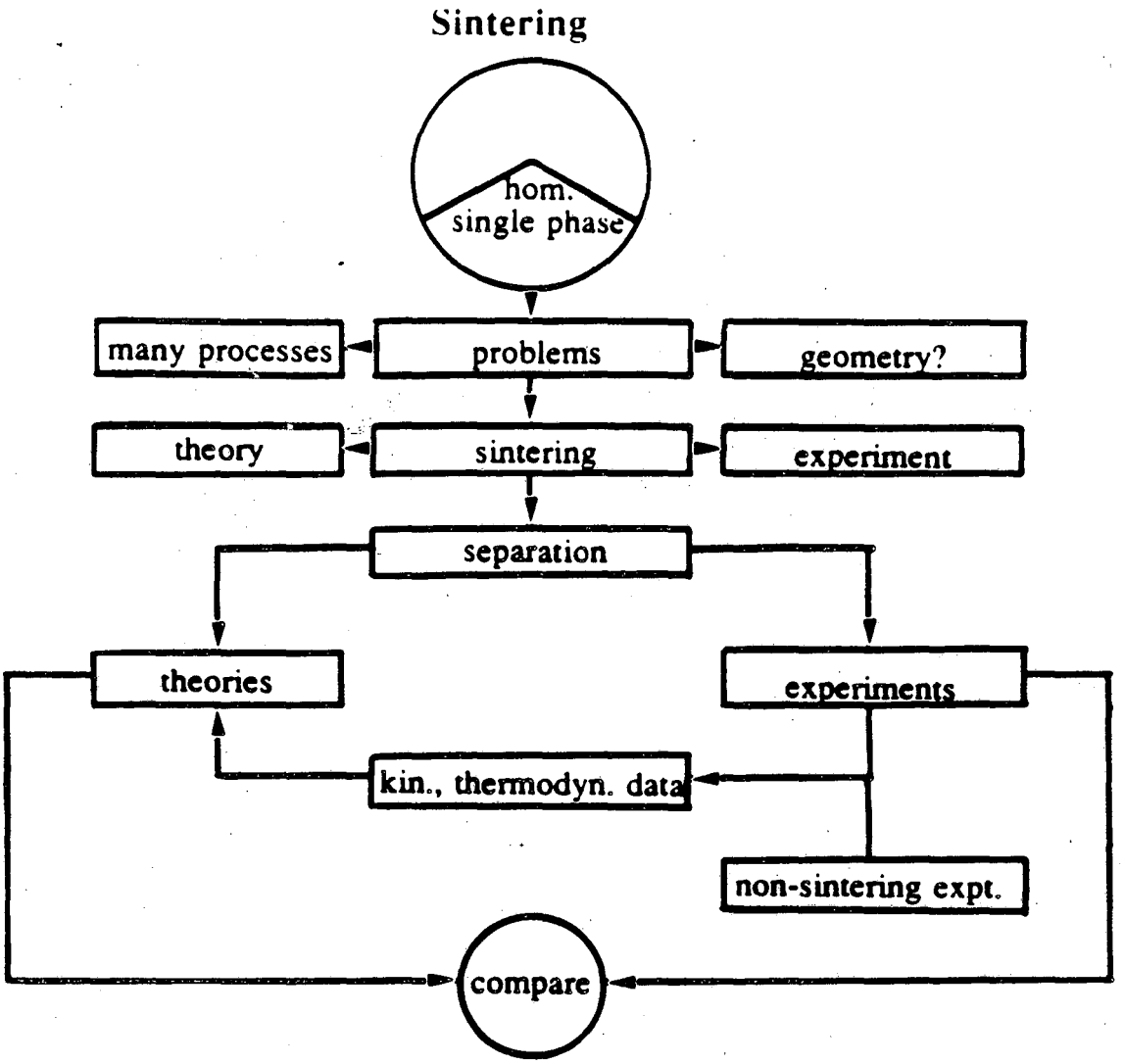
Fig.79: Grain structure of dense, MgO-doped alumina after a) 0, b) 7.5, c) 15 and d) 100 hours at 1600°C.

Fig.80: Grain growth kinetics of undoped and MgO-doped alumina at 1600°C.

Fig.81: Dependence of boundary migration of basal plane sapphire on annealing time at 1600°C.

Fig.82: Optical micrographs depicting deformation zone in the sapphire a) at the single crystal-polycrystal interface, b) at the surface. Sample was annealed for 100 hours at 1600°C.

Fig.83: Enhanced grain growth as related to deformation zone in the sapphire; a) low, b) high magnification. Sample was annealed for 30 hours at 1600°C.



Next steps: influence of T, dopant conc.

XBL 8810-3541 A

Figure 1

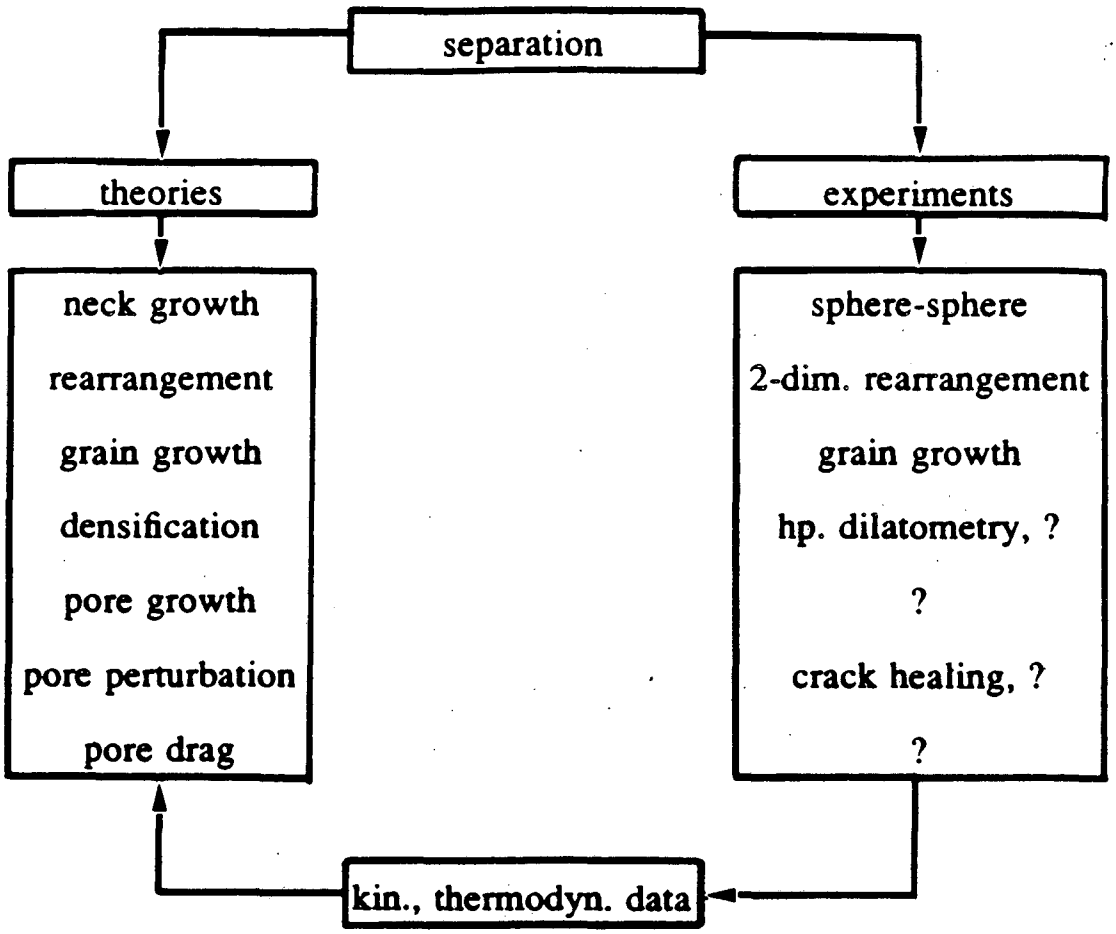

separation
theories
experiments
neck growth
rearrangement
grain growth
densification
pore growth
pore perturbation
pore drag
sphere-sphere
2-dim. rearrangement
grain growth
hp. dilatometry, ?
?
crack healing, ?
?
kin., thermodyn. data
XBL 8810-3540 A

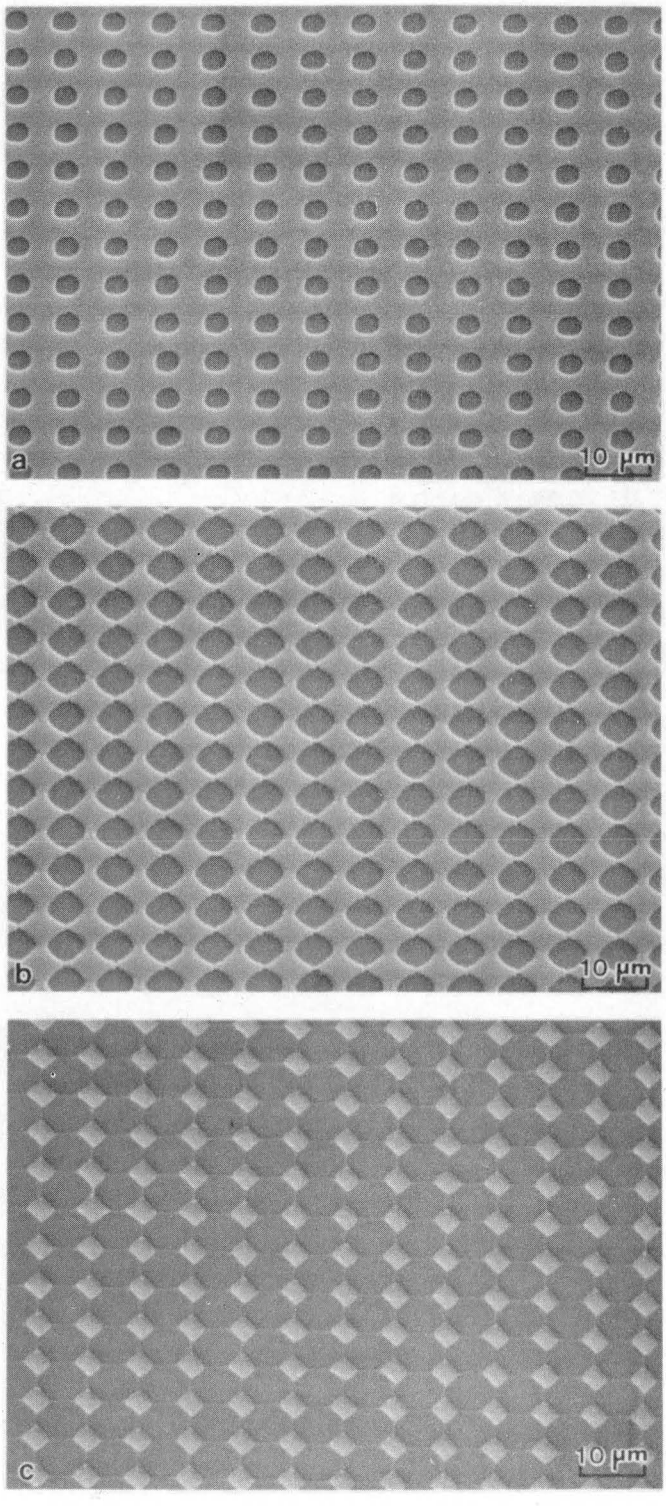
Figure 2

Non-sintering Experiments

Experiments	Quantity obtained
tracer techniques, diffusional creep	lattice diff. coefficient, grain b. diff. coefficient
scratch smoothing, grain boundary grooving	surf. diff. coefficient

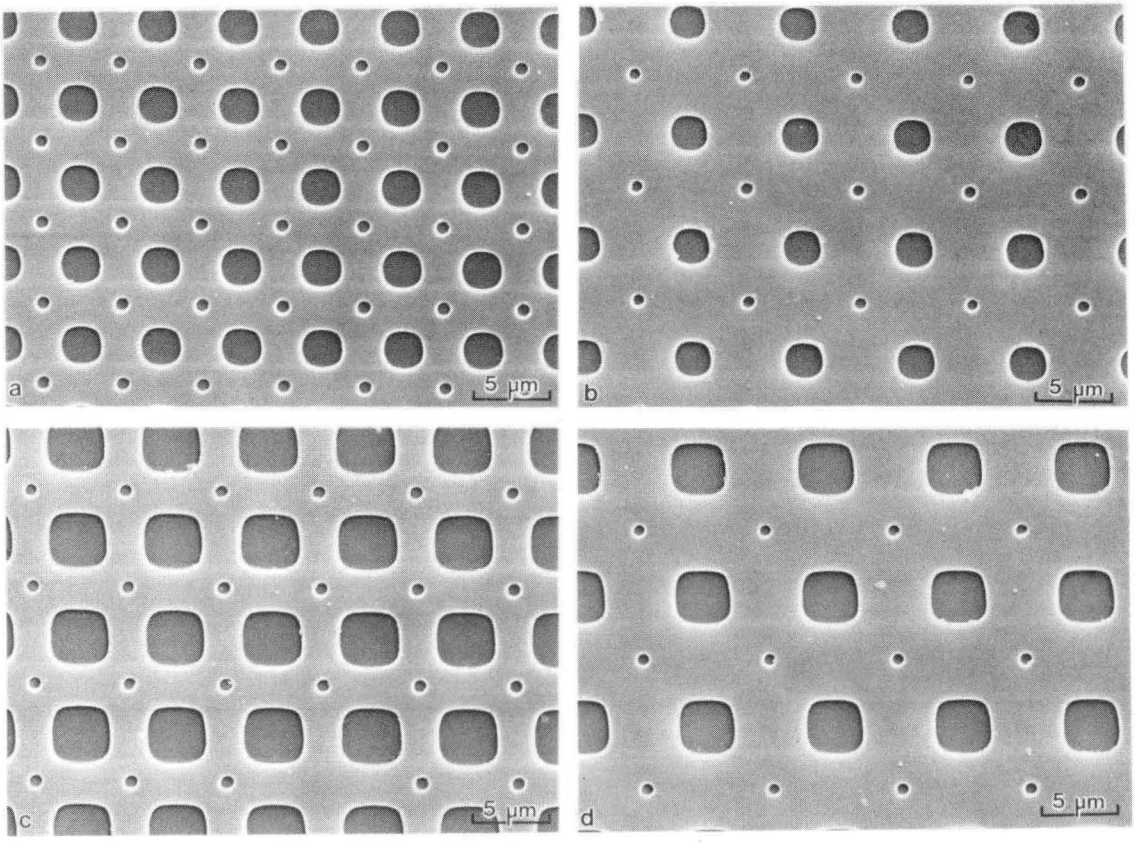
XBL 8810-3545 A

Figure 3



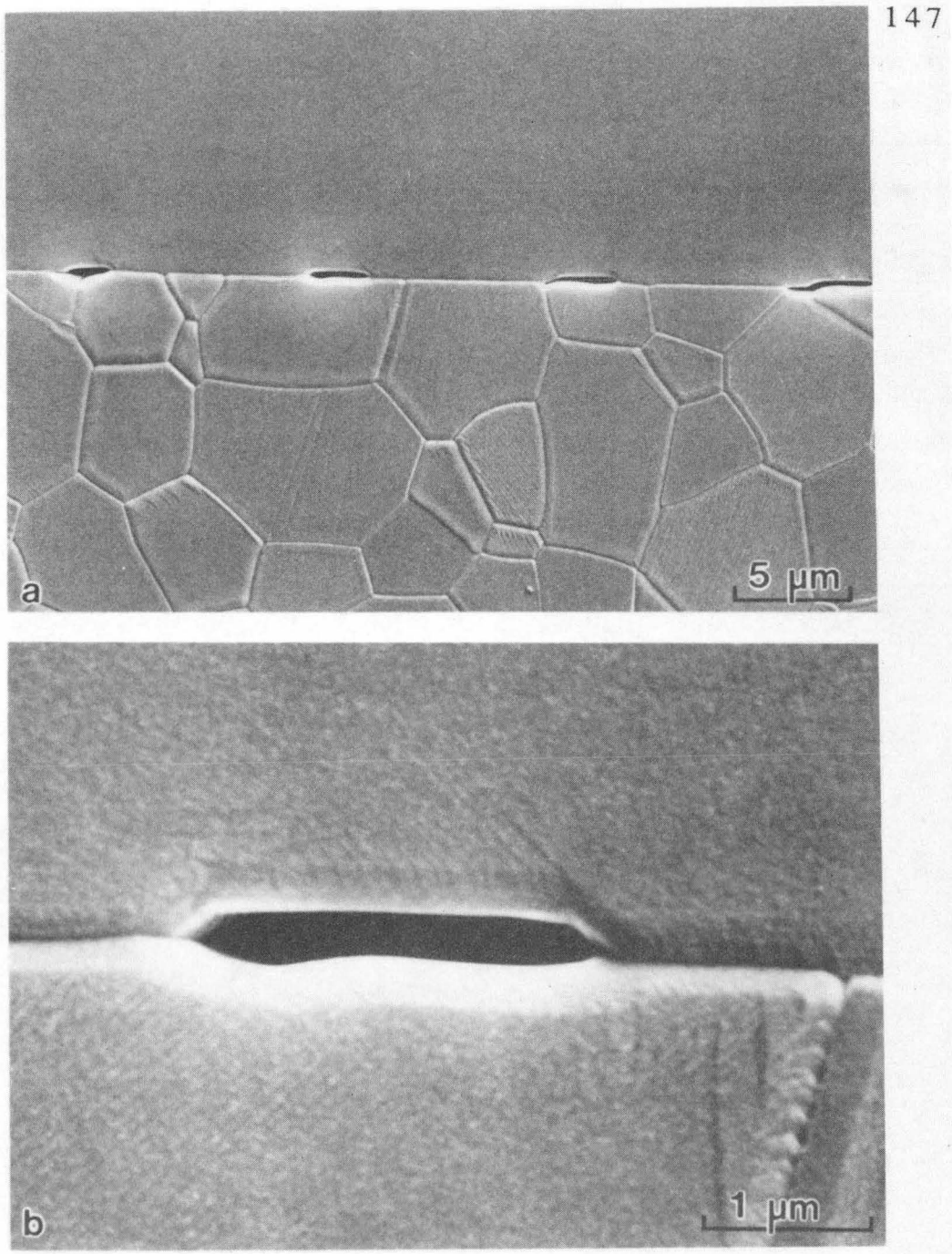
XBB 889-9064-B

Figure 4



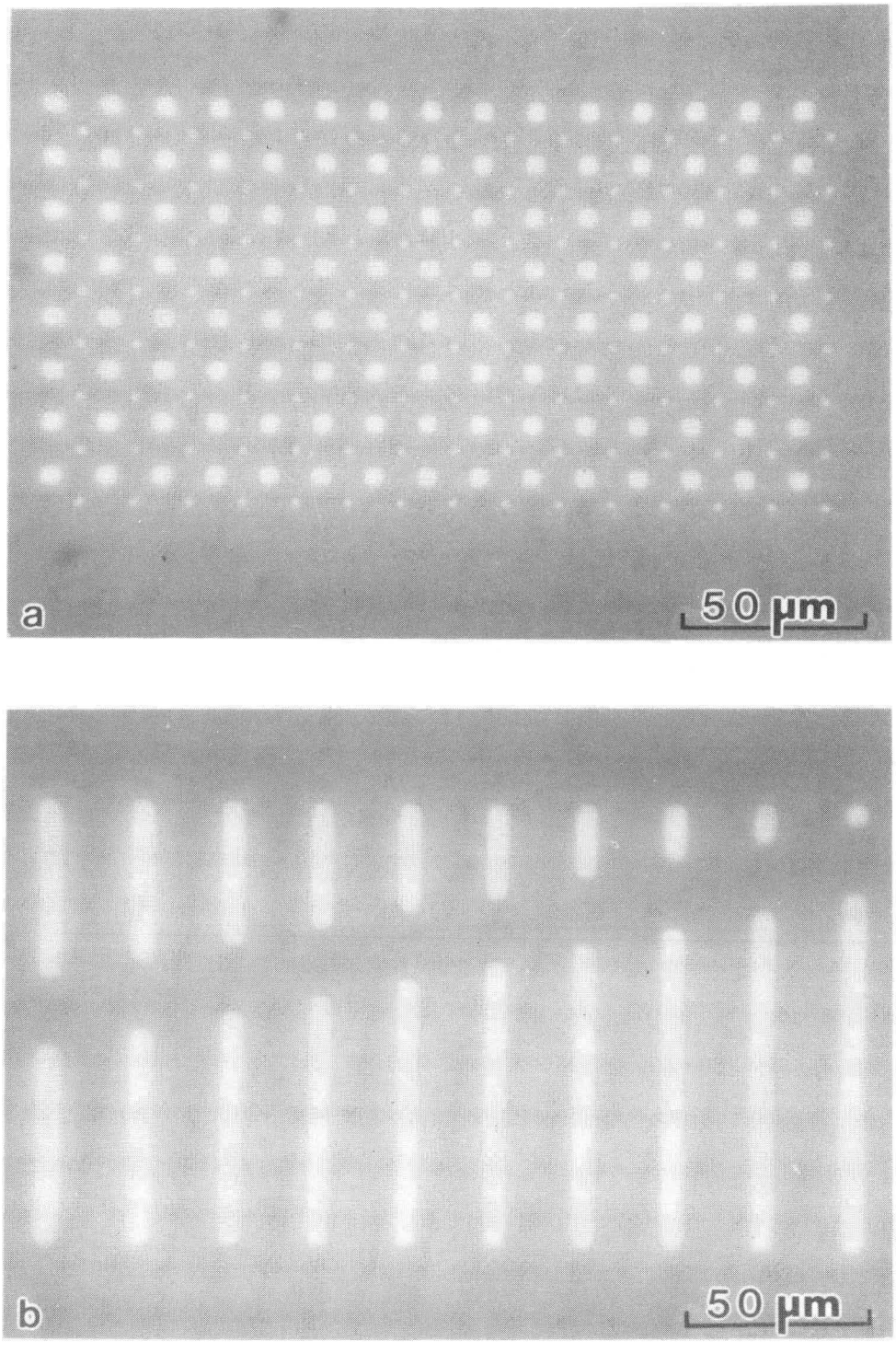
XBB 887-6673

Figure 5



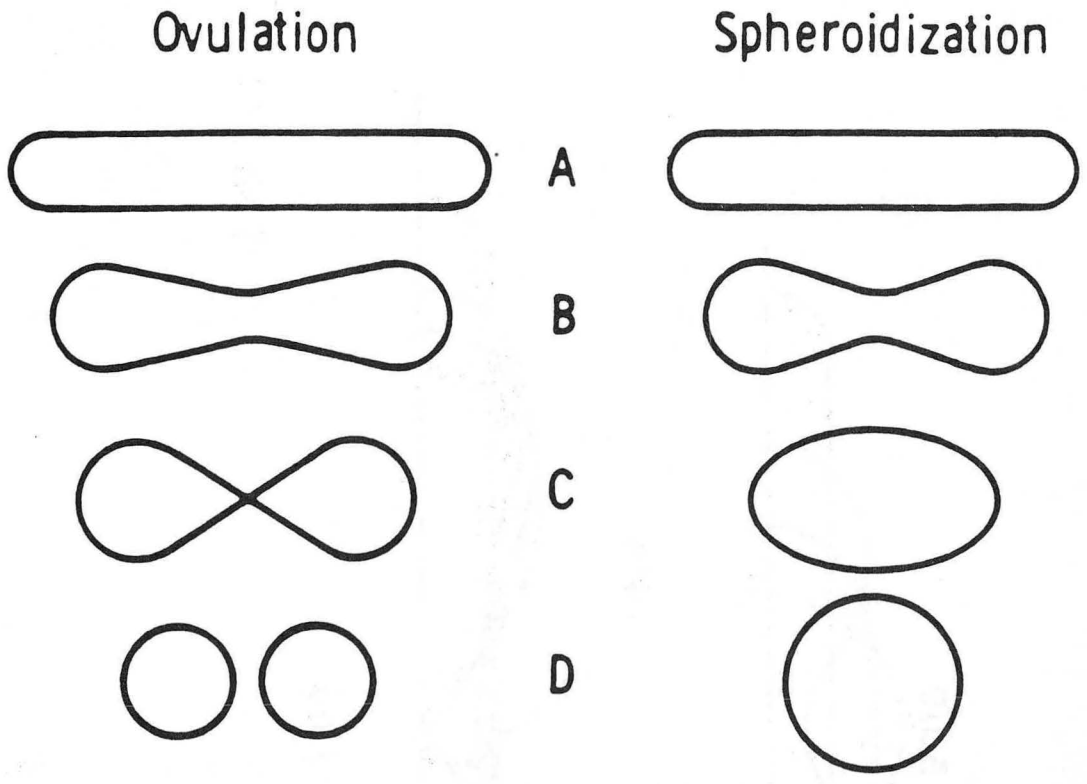
XBB 837-6674-A

Figure 6



XBB 887-6672-A

Figure 7

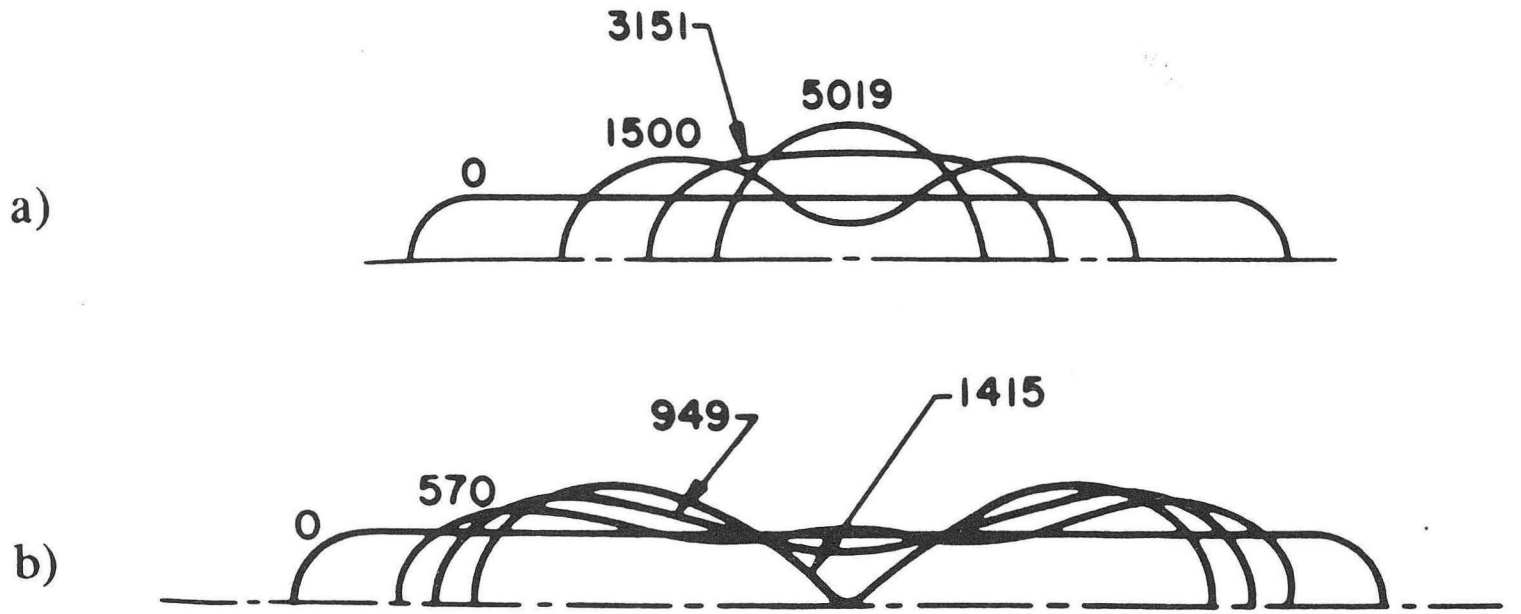


$$\lambda_{min} = 2 \pi R_o$$

λ_{min} = wavelength of perturbation

XBL 8810-3537 A

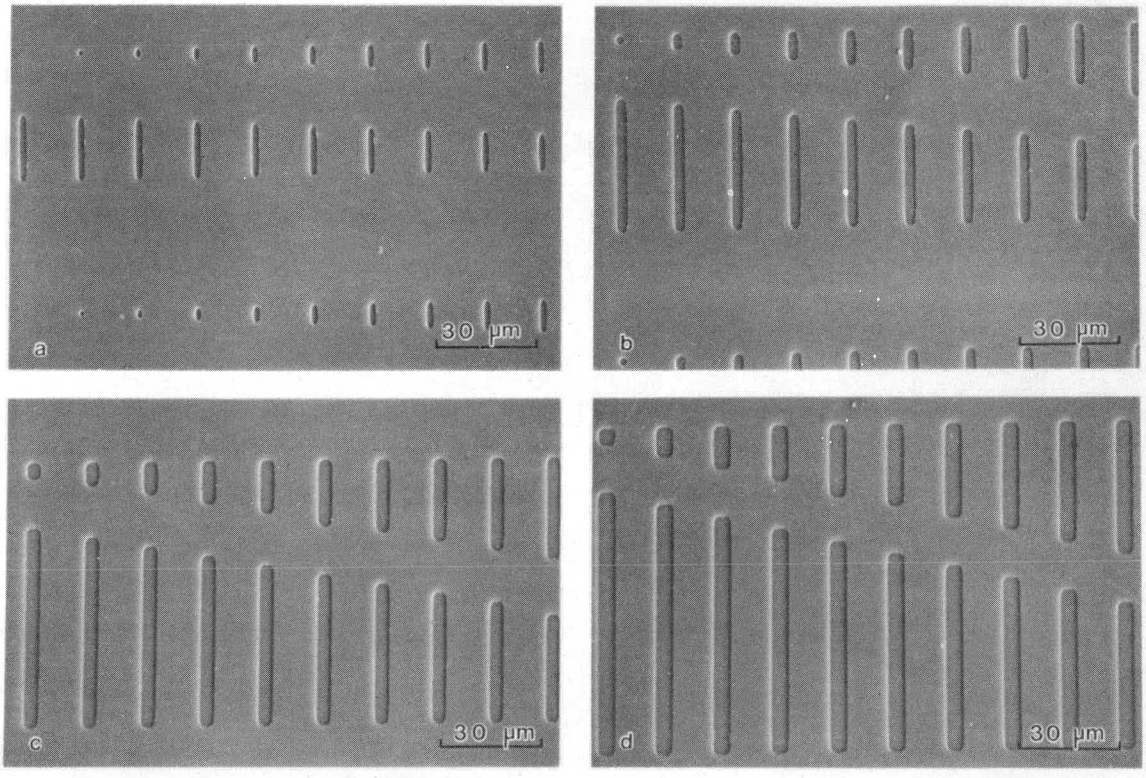
Figure 8



a) aspect ratio = 7, b) aspect ratio = 7.64

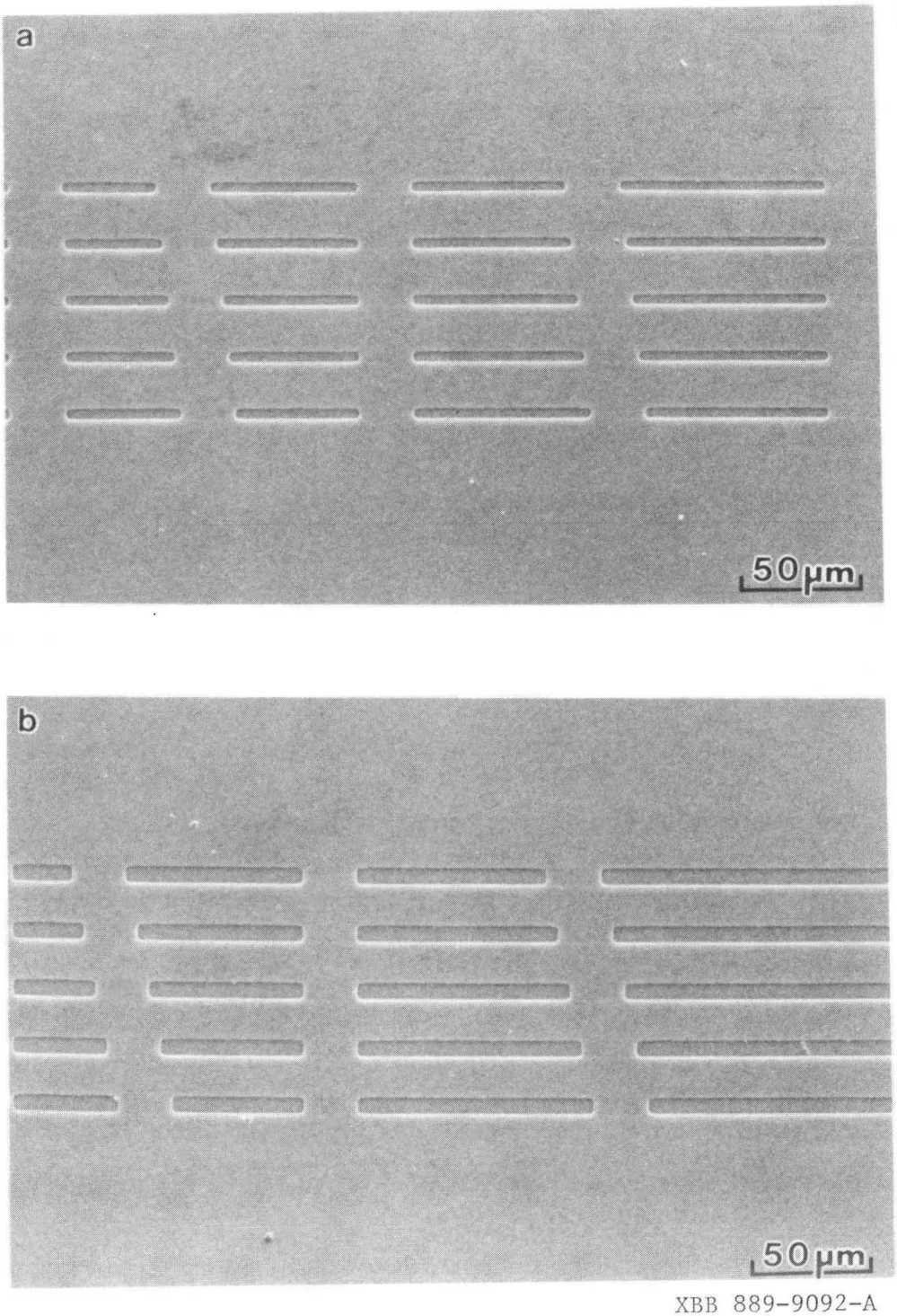
XBL 8810-3536 A

Figure 9



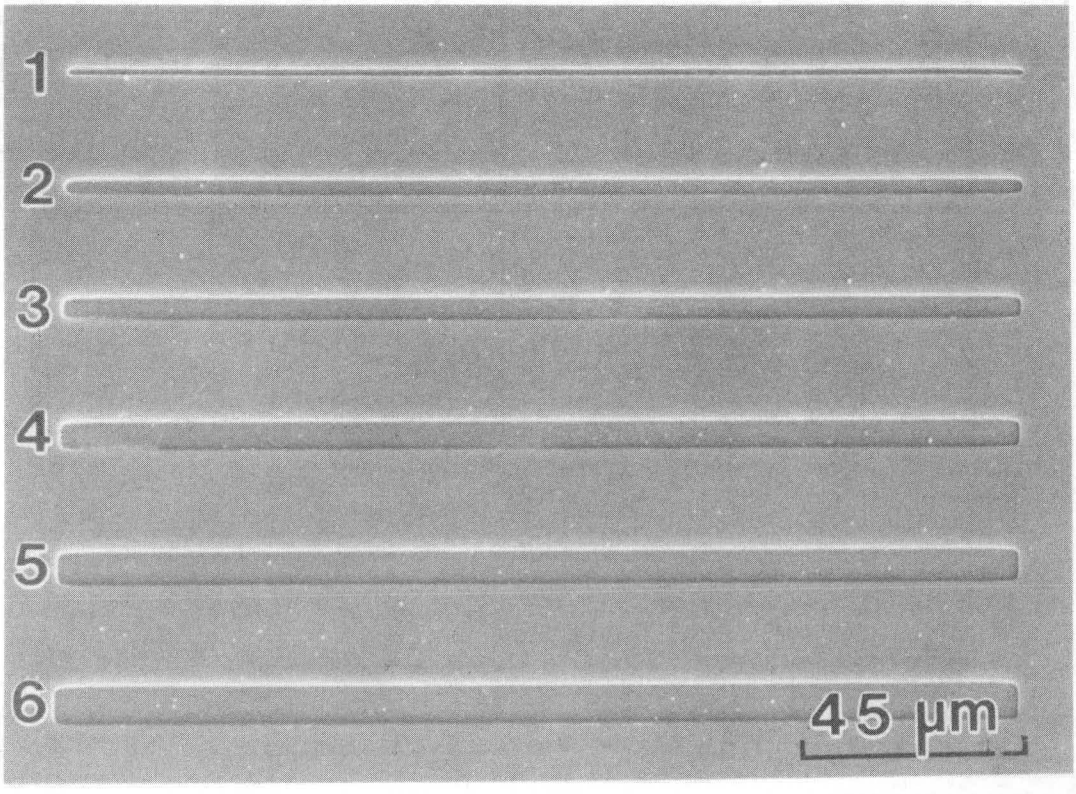
XBB 878-6525-A

Figure 10



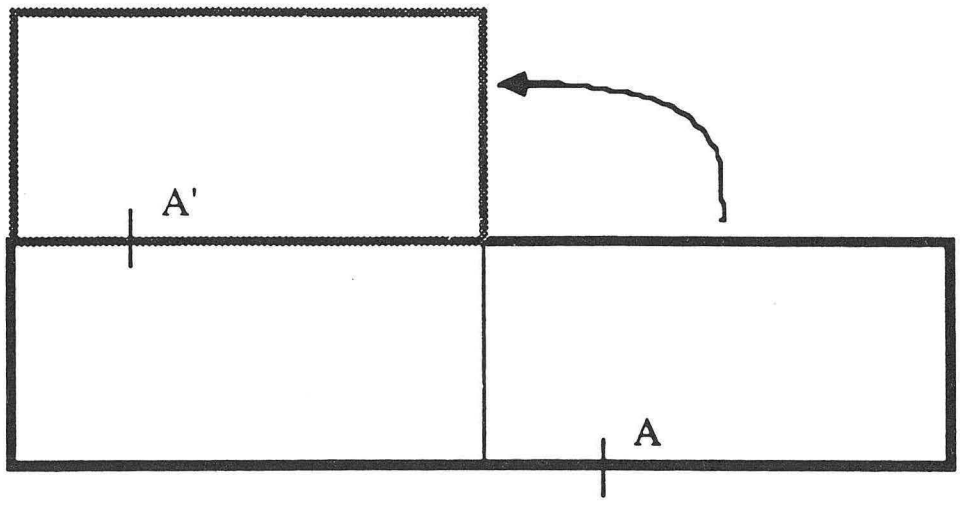
XBB 889-9092-A

Figure 11



XBB 883-2569-A

Figure 12



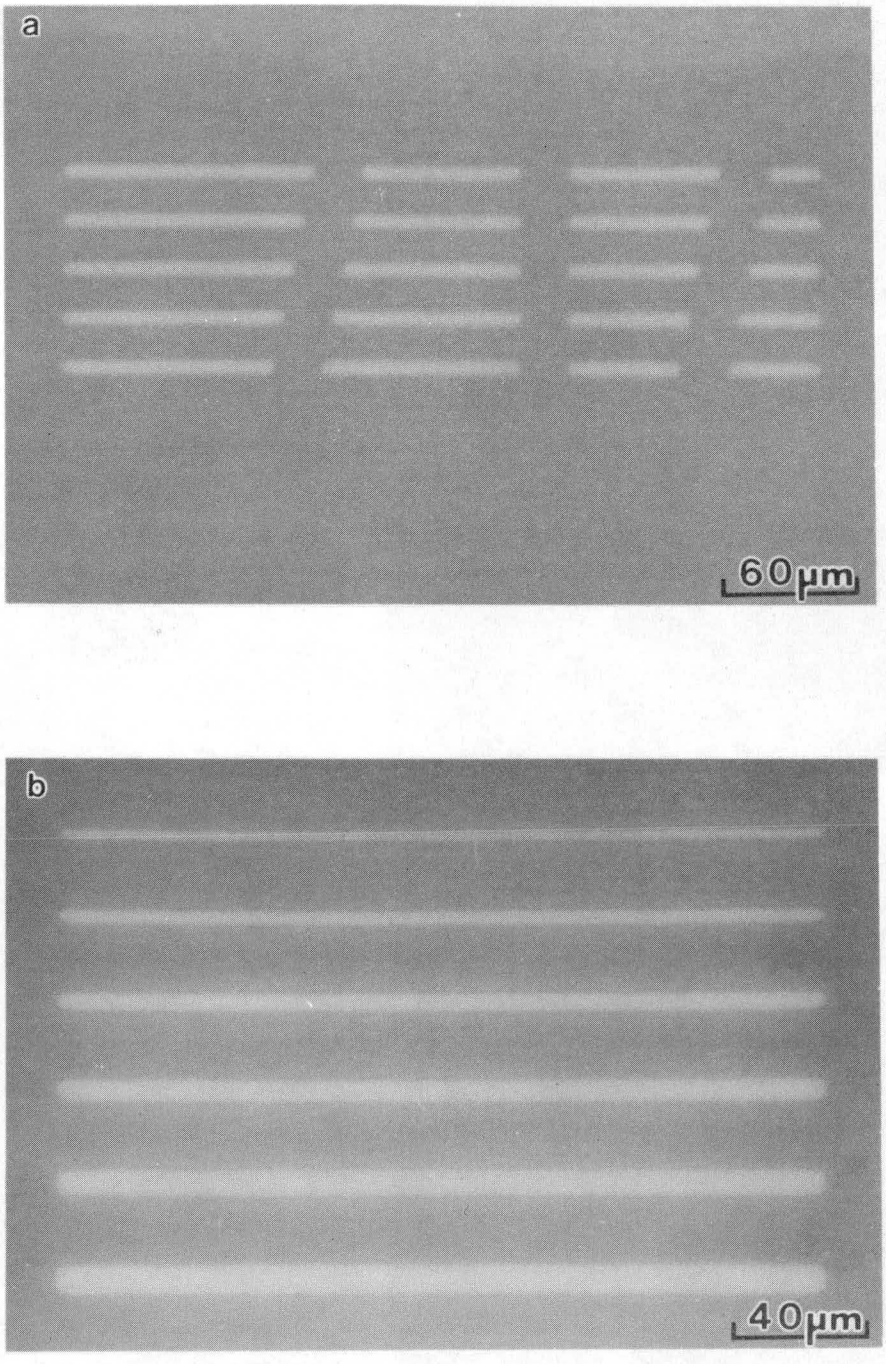
original wafer:

separation line:

upper part of bicrystal:

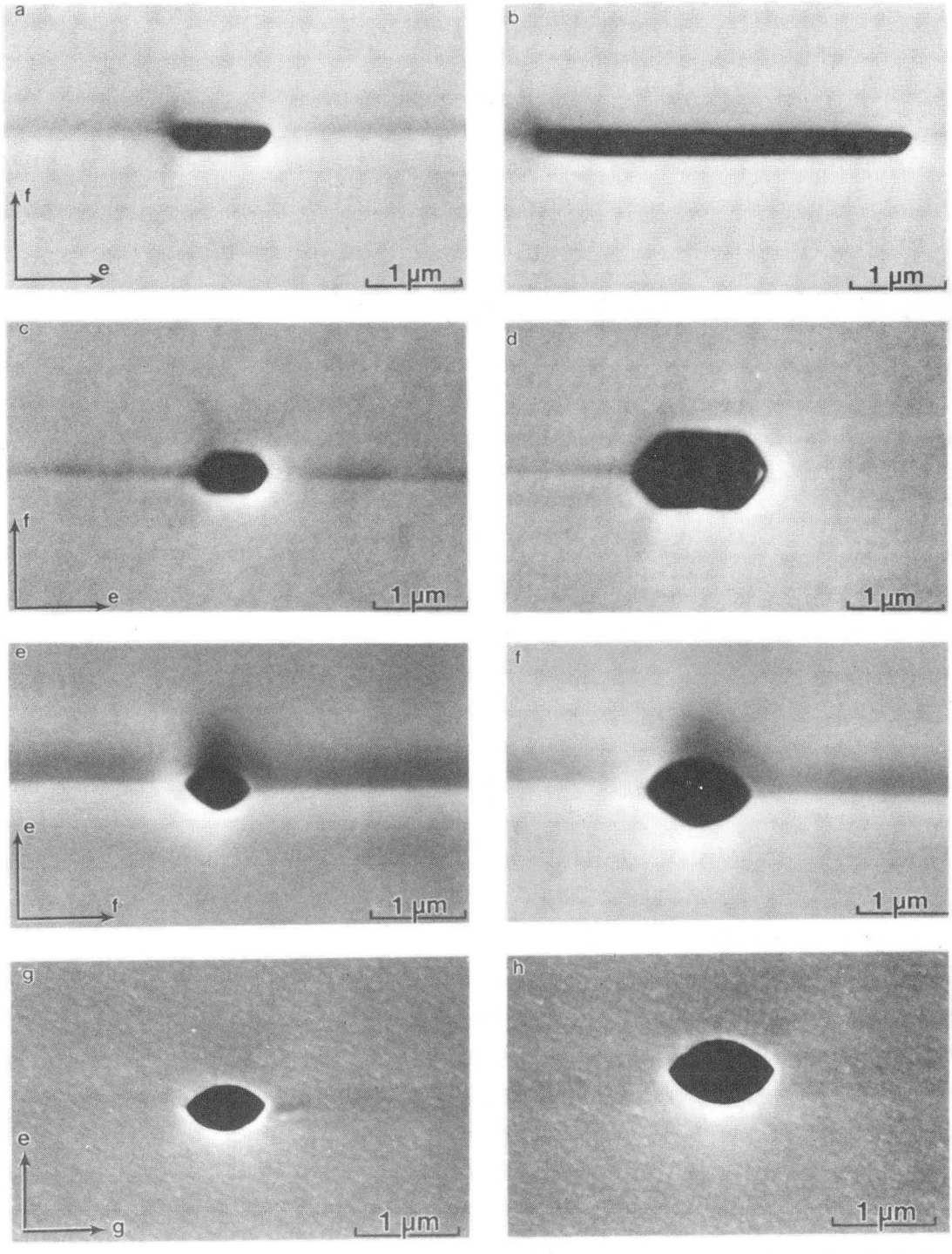
XBL 8810-3544 A

Figure 13



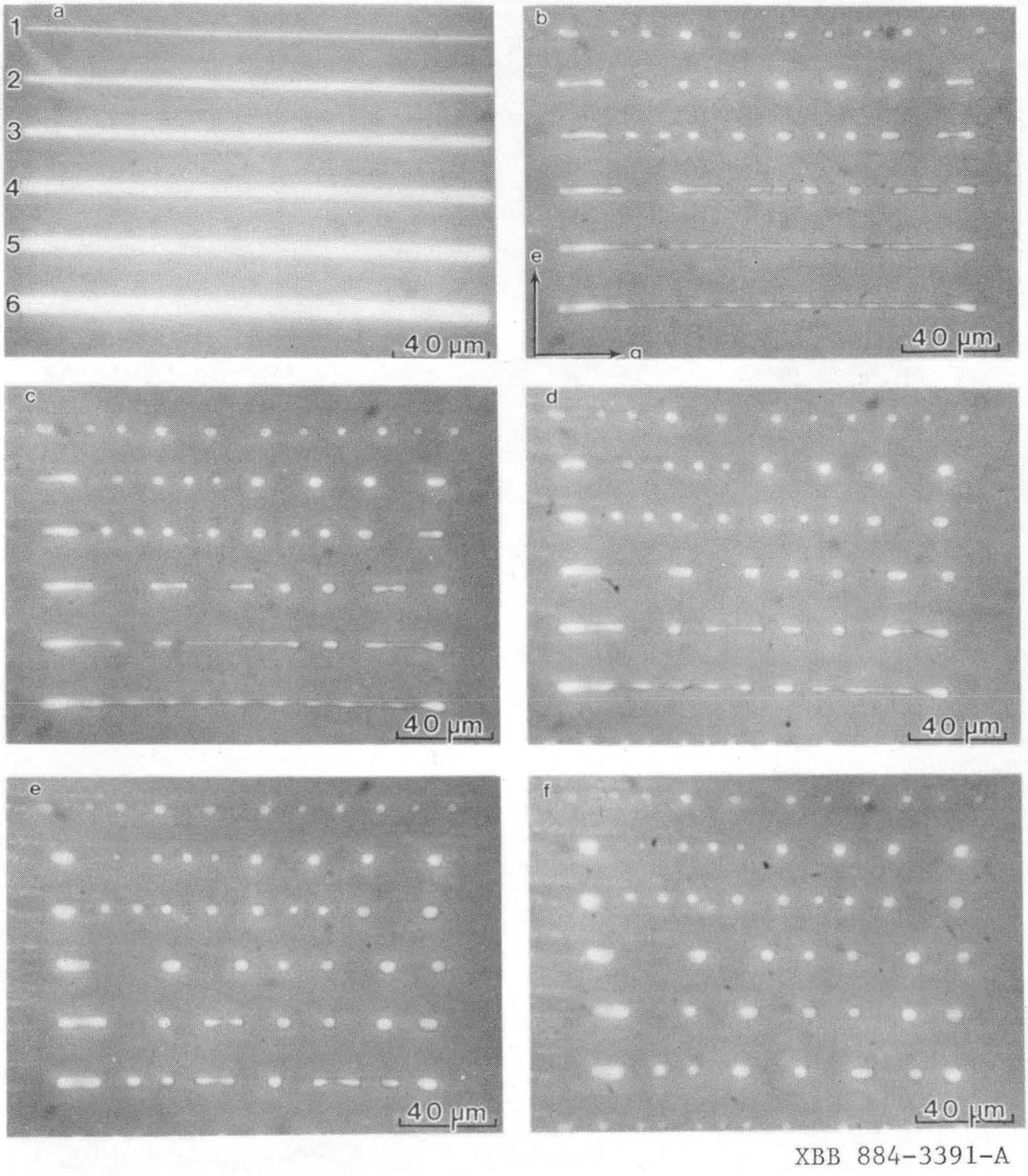
XBB 889-9093-A

Figure 14



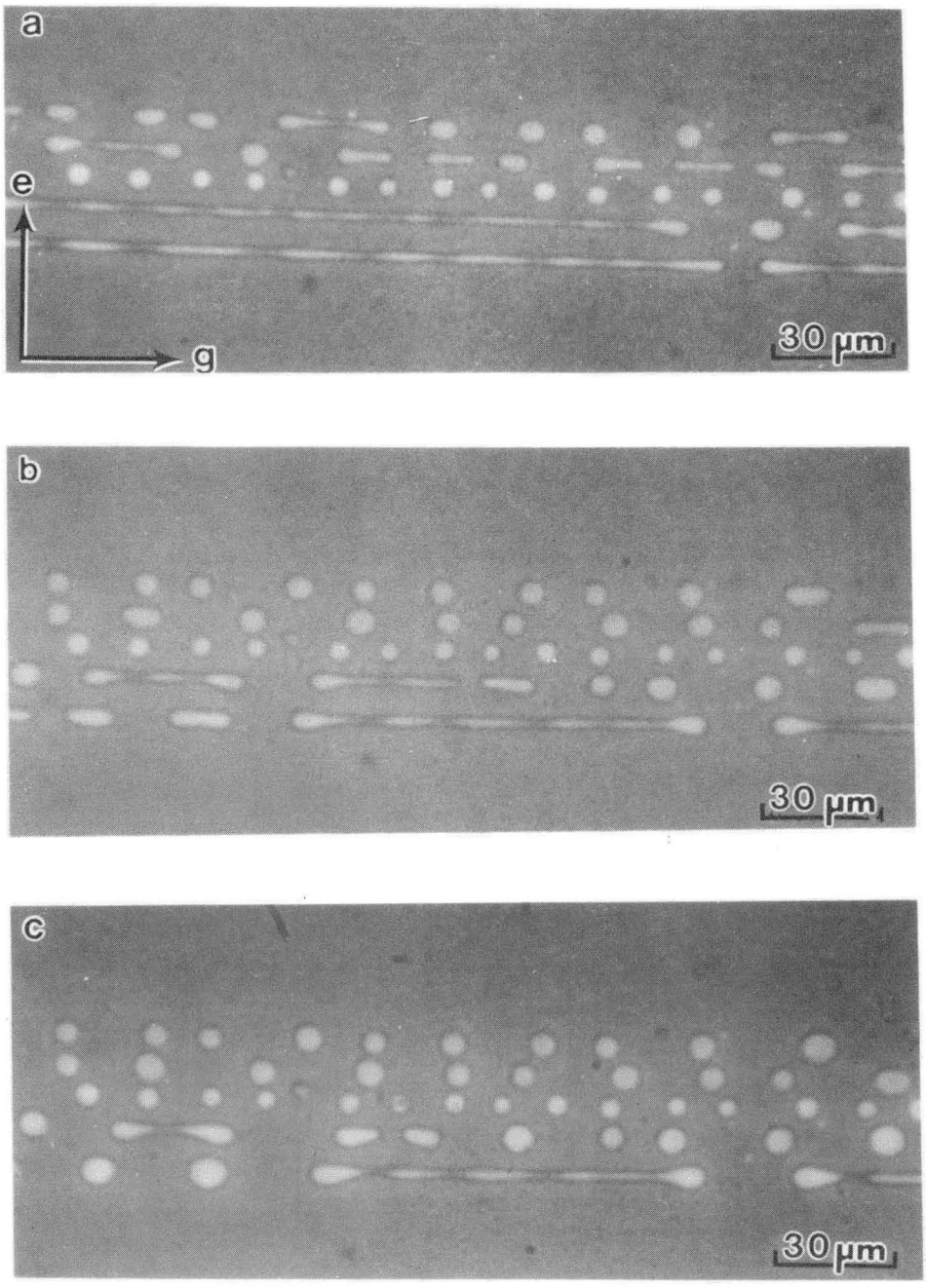
XBB 855-8194-A

Figure 15



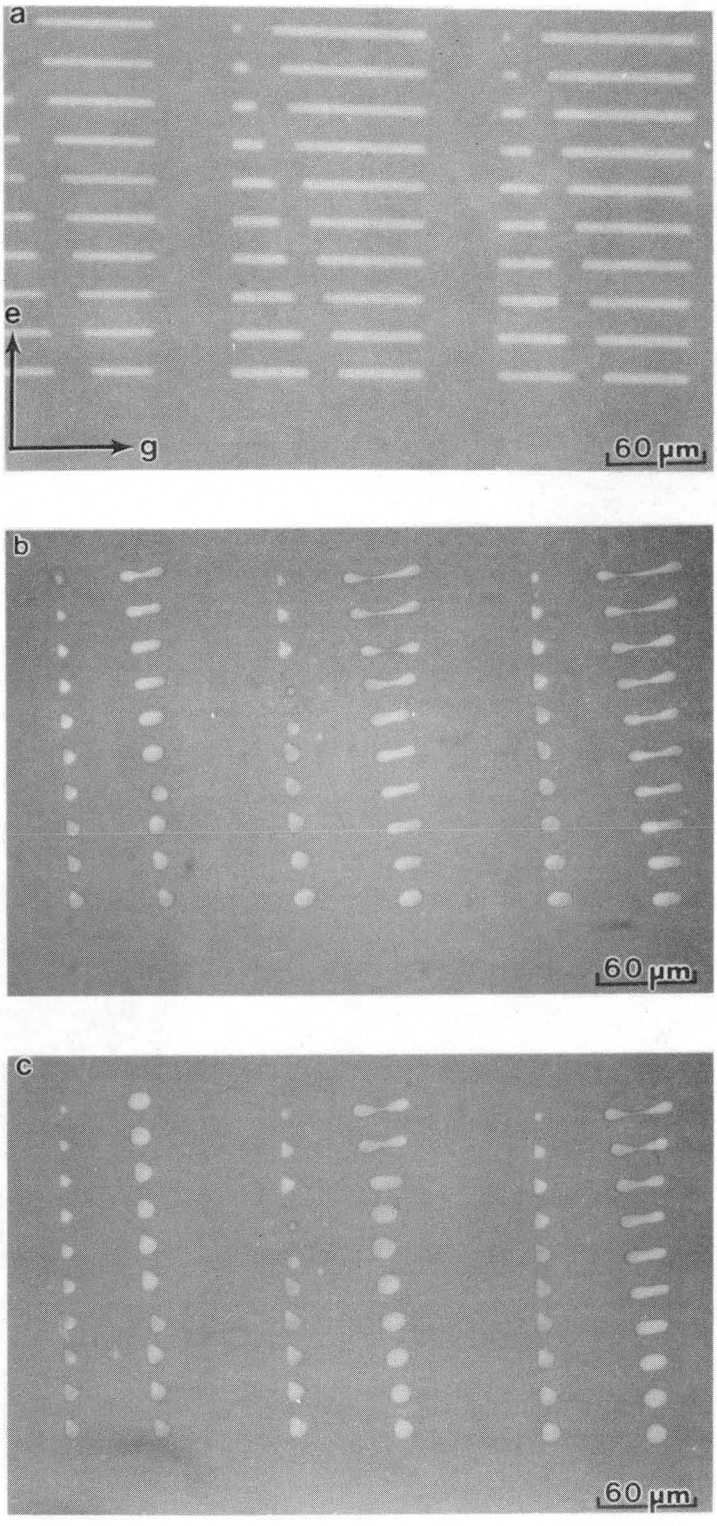
XBB 884-3391-A

Figure 16



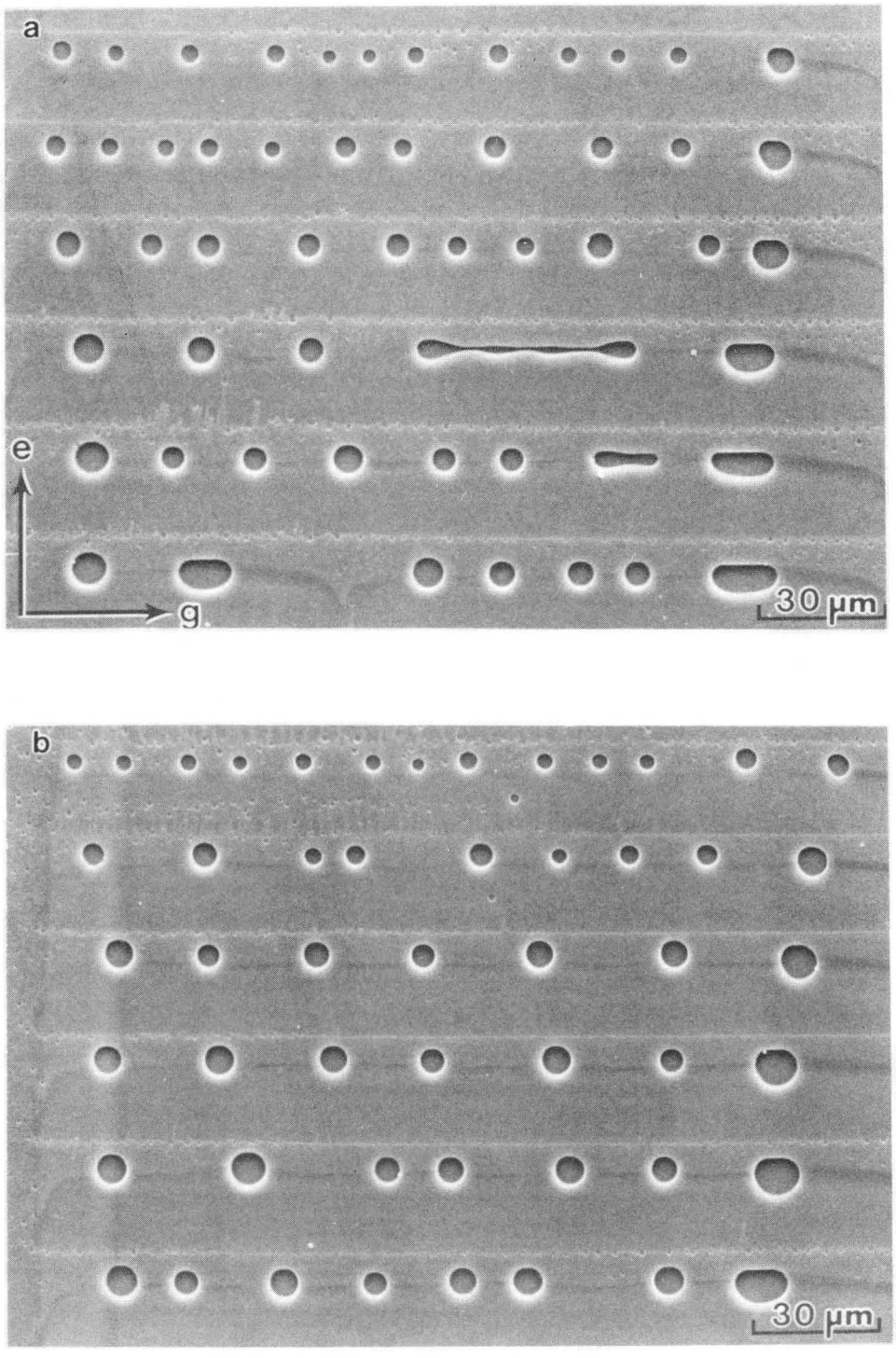
XBB 889-9059-A

Figure 17



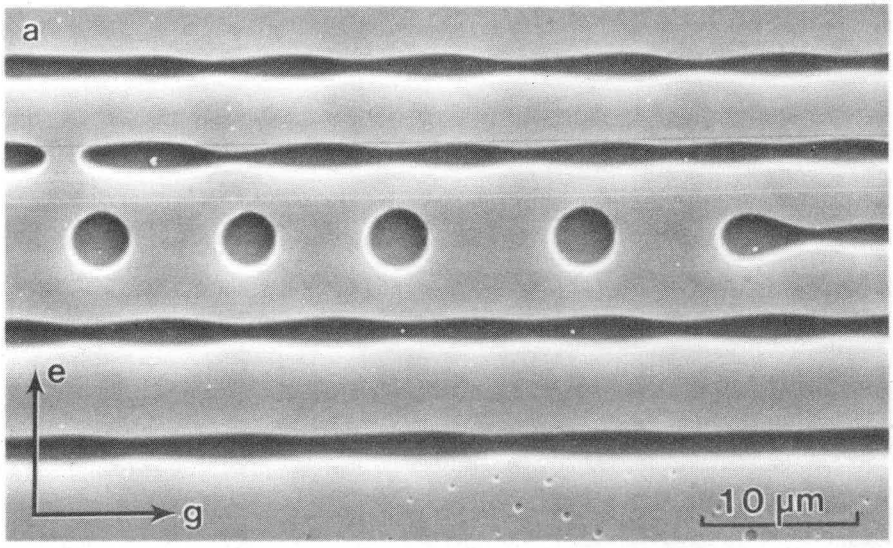
XBB 889-9064-A

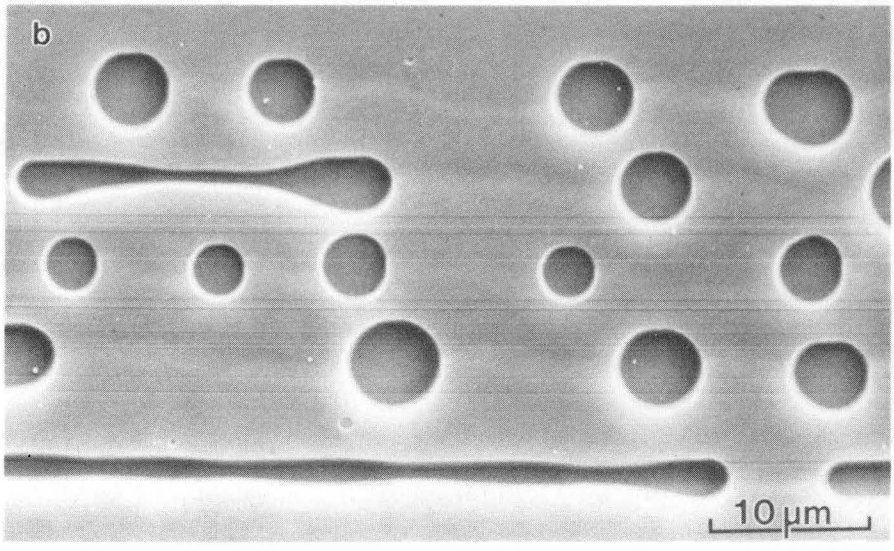
Figure 18



XBB 889-9063-A

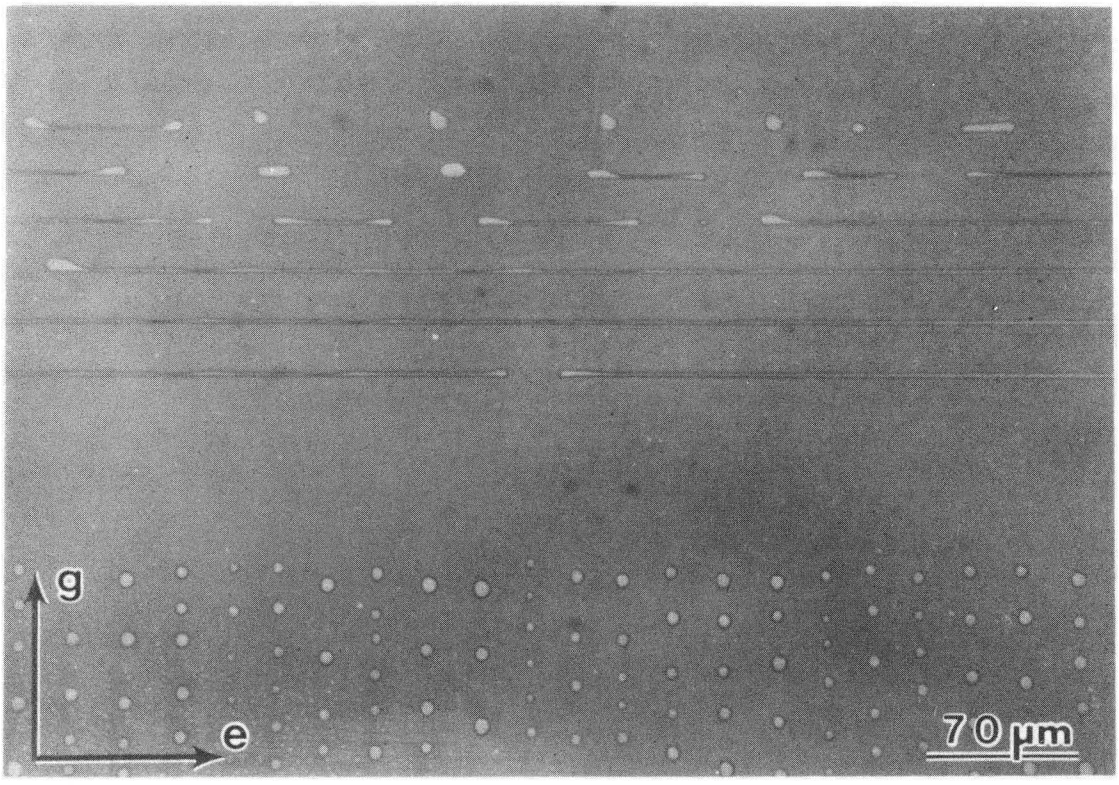
Figure 19





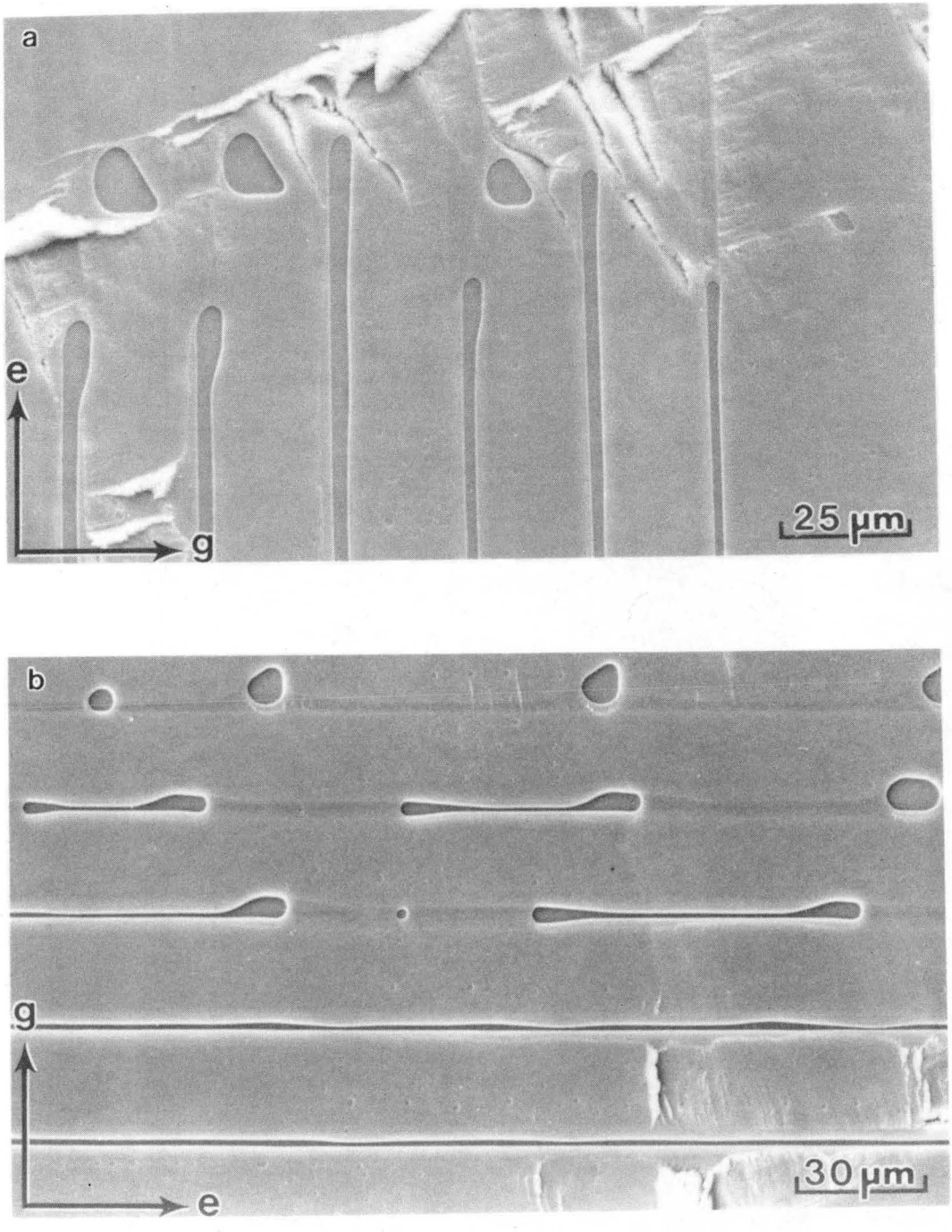
XBB 889-9058-A

Figure 20



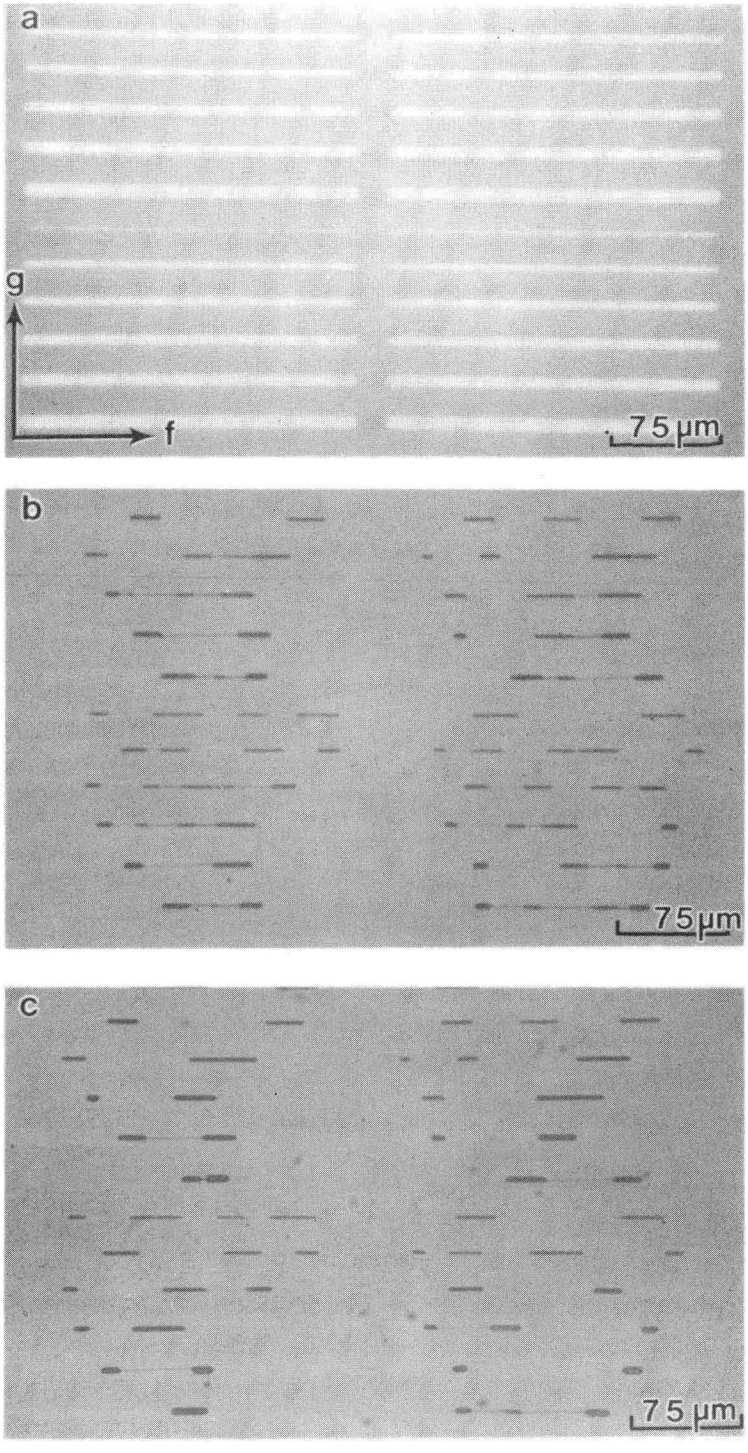
XBB 884-3399-A

Figure 21



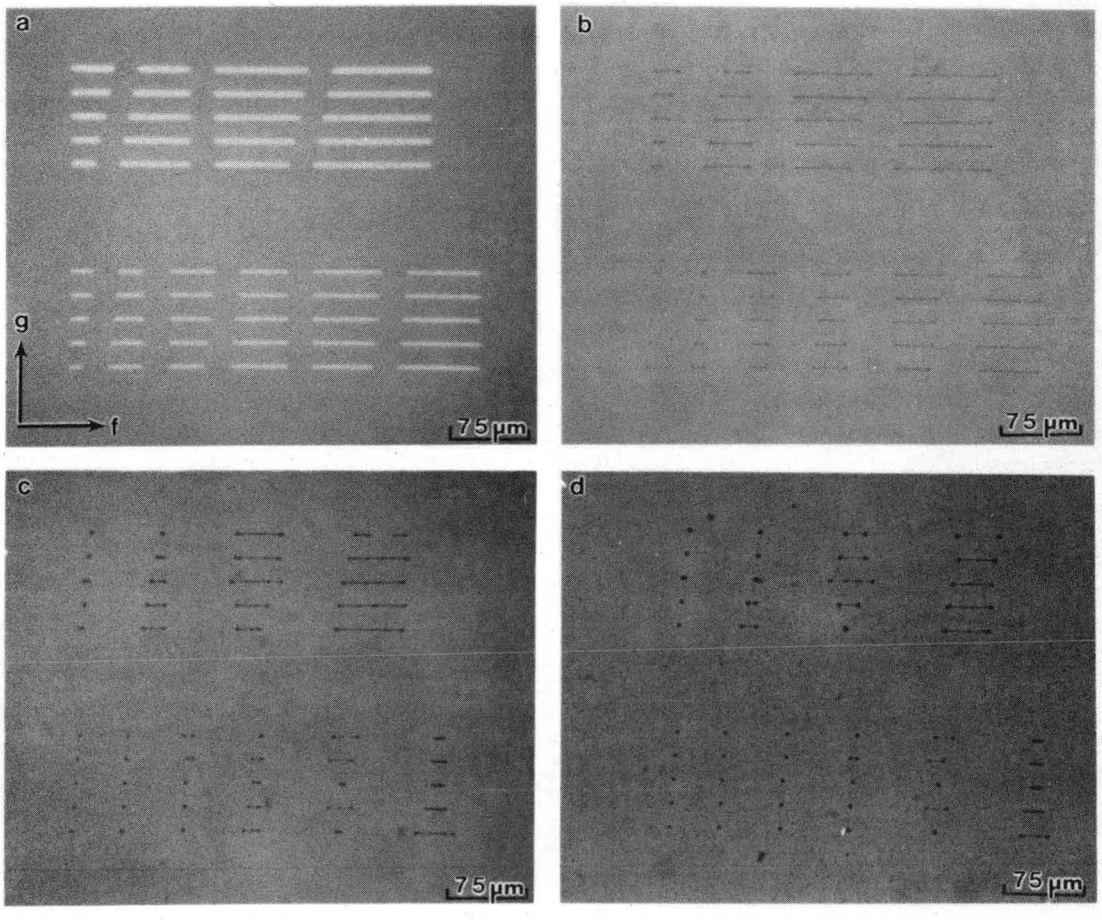
XBB 889-9094-A

Figure 22



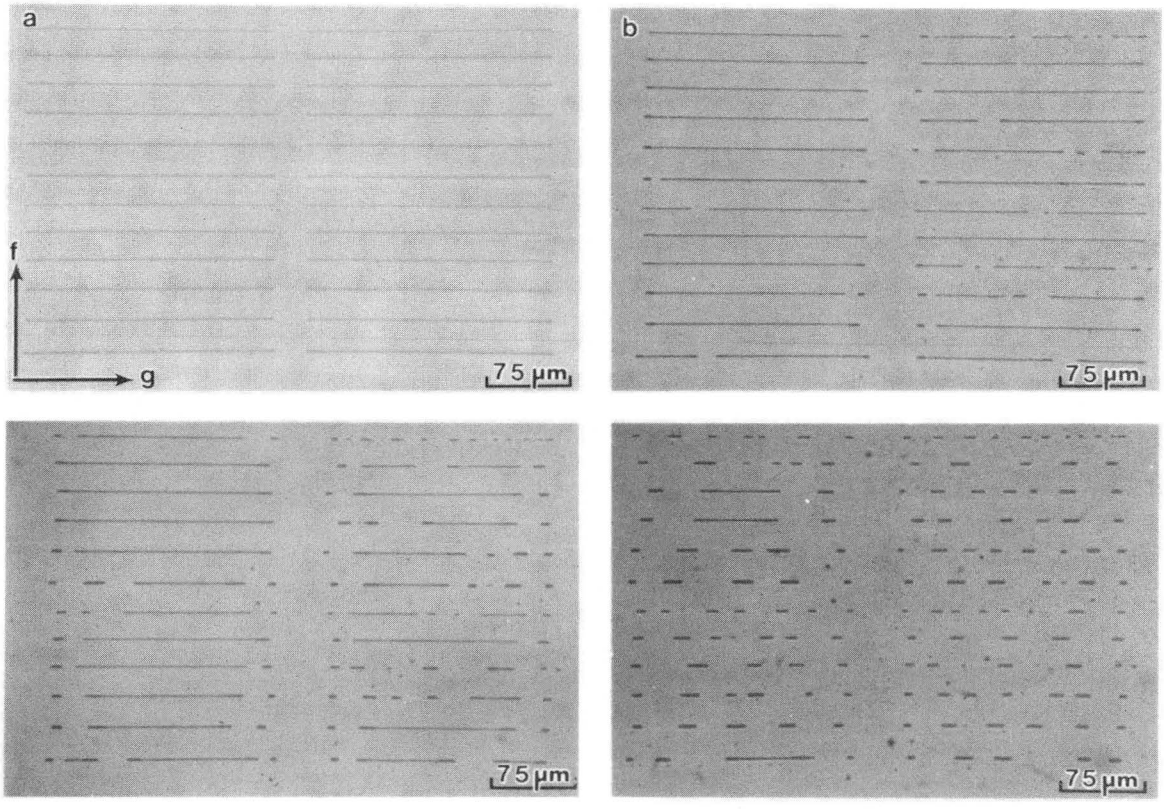
XBB 884-3394-A

Figure 23



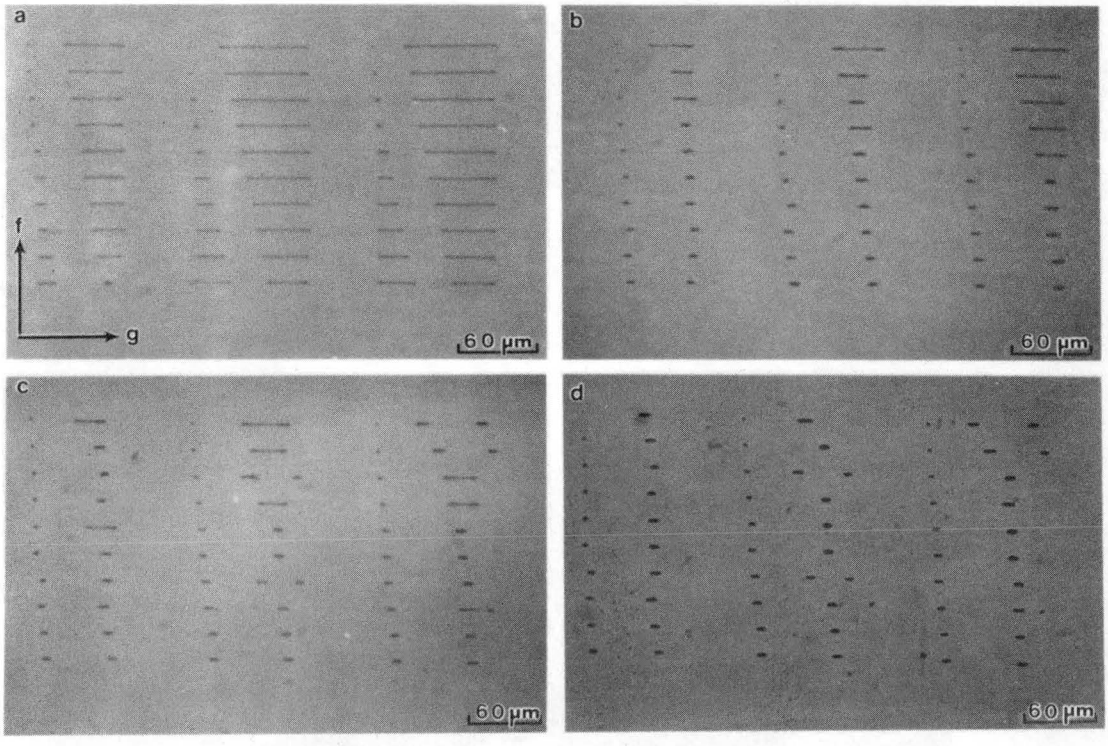
XBB 884-3389-A

Figure 24



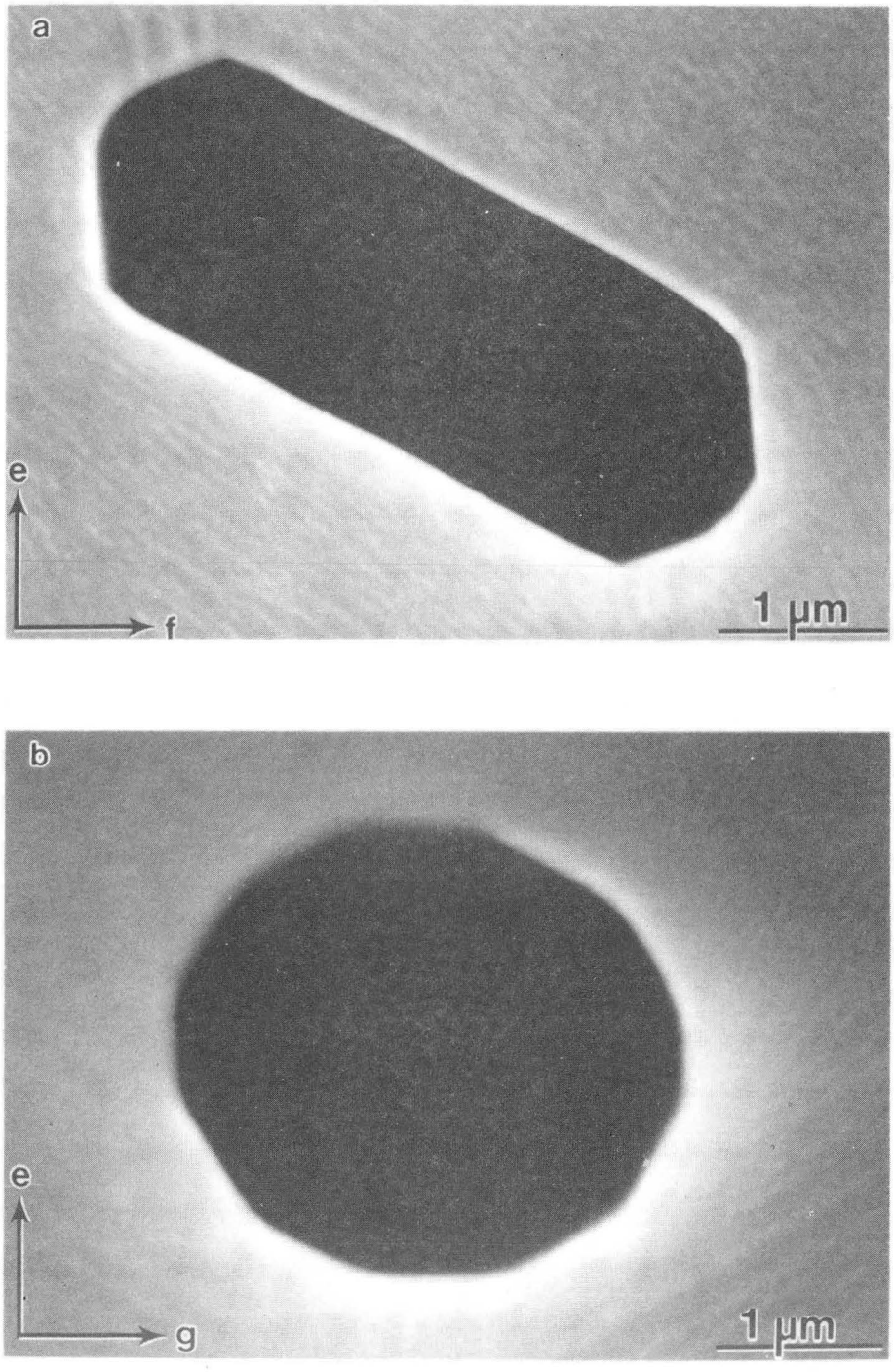
XBB 884-3390-A

Figure 25



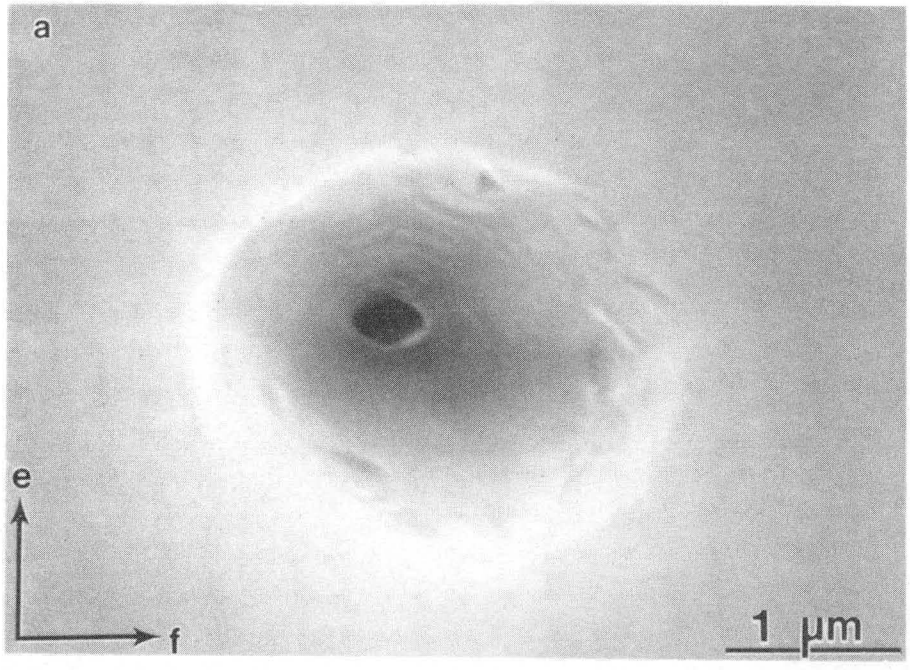
XBB 884-3397-A

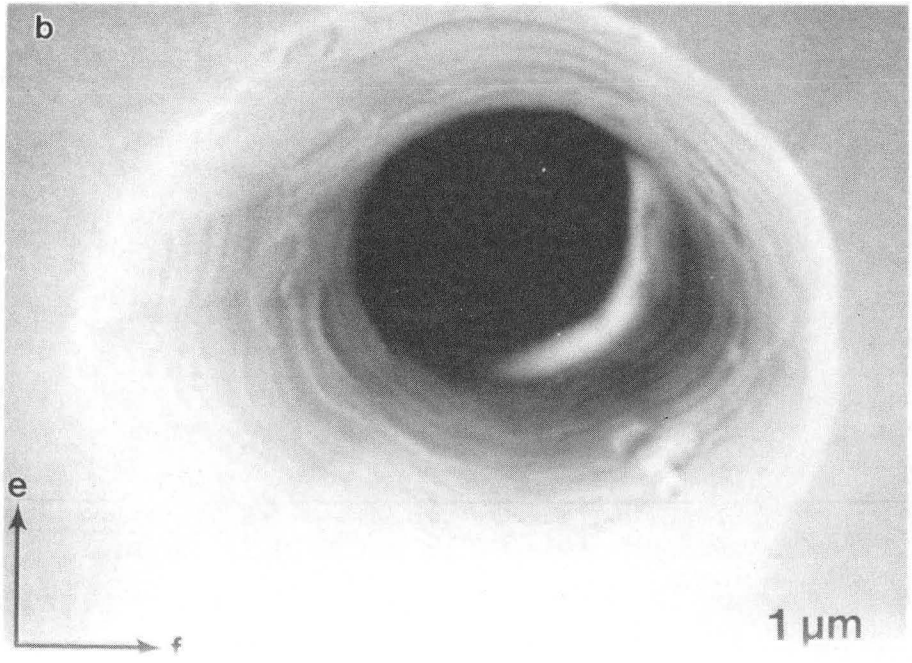
Figure 26



XBB 889-9091-A

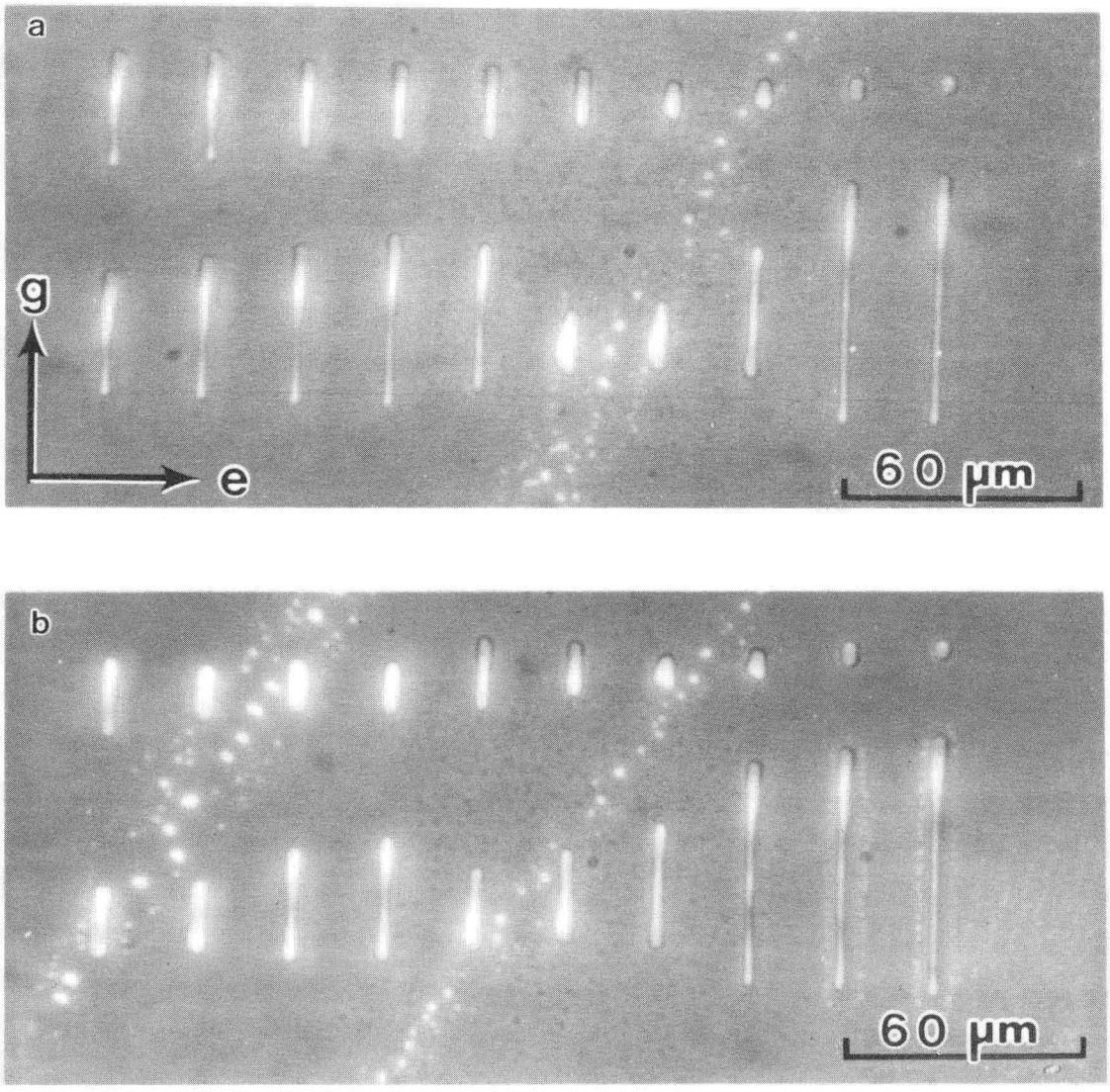
Figure 27





XBB 889-9095-A

Figure 28



XBB 884-3398-A

Figure 29

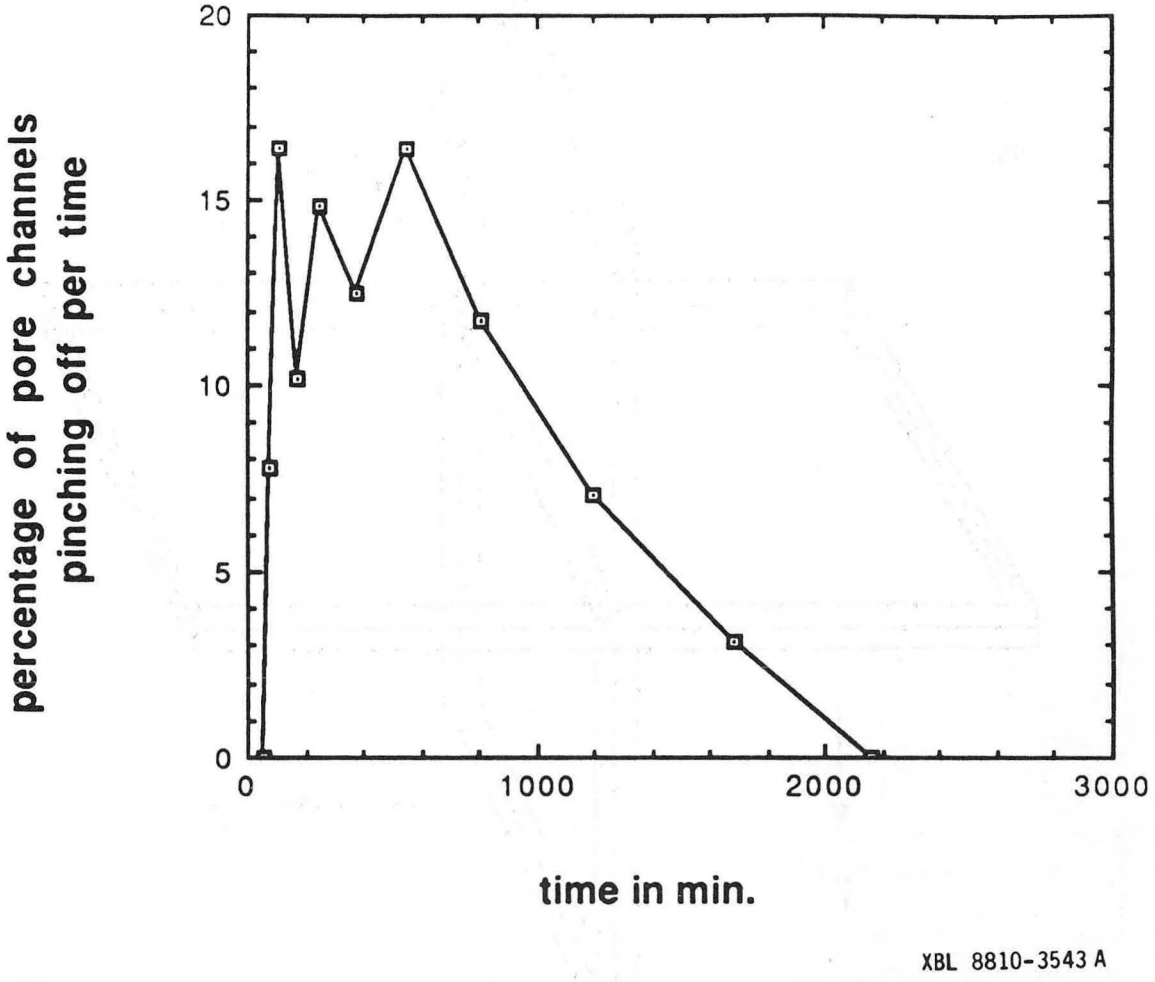
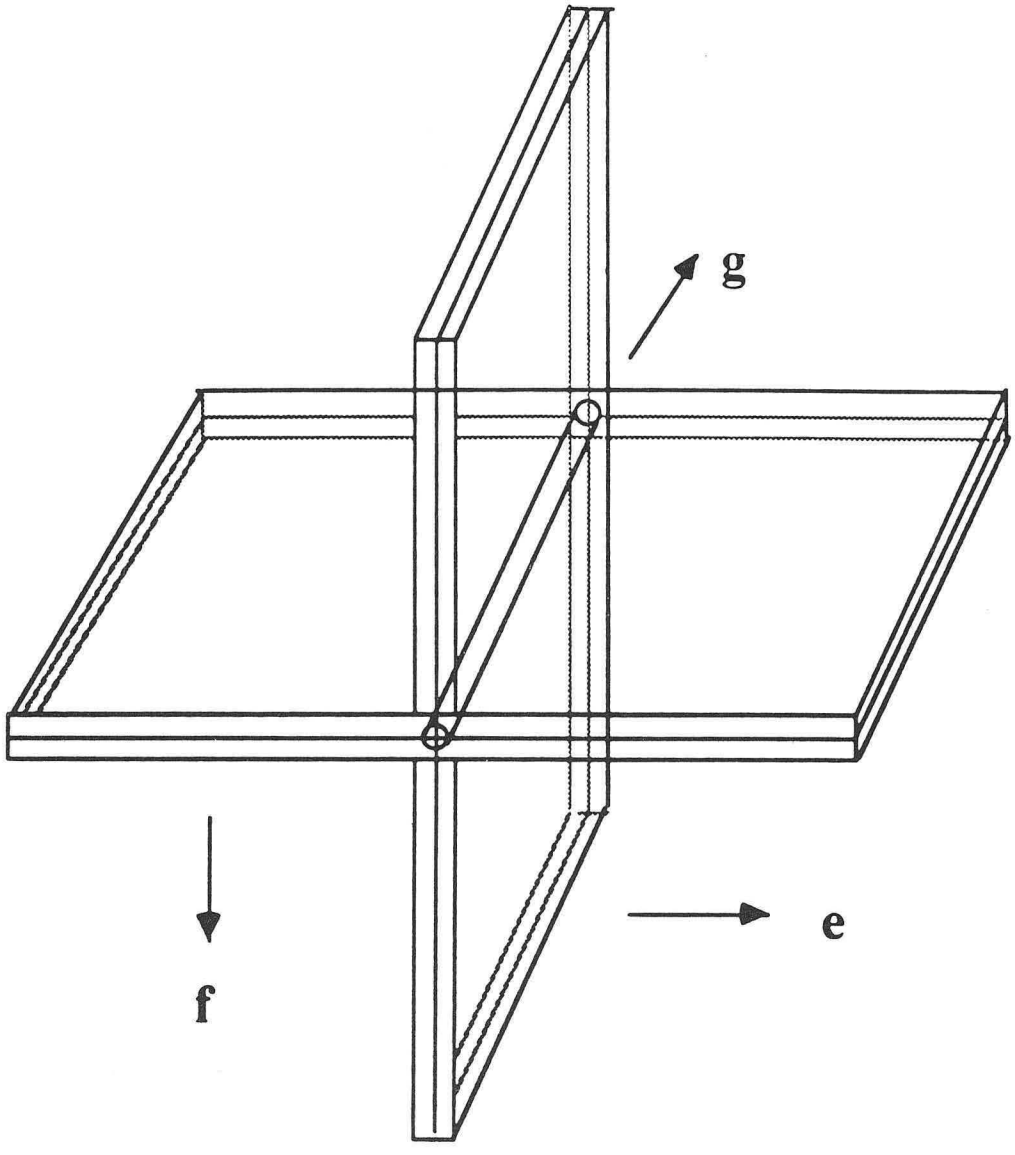

percentage of pore channels pinching off per time
20
15
10
5
0
0
1000
2000
3000
time in min.
XBL 8810-3543 A

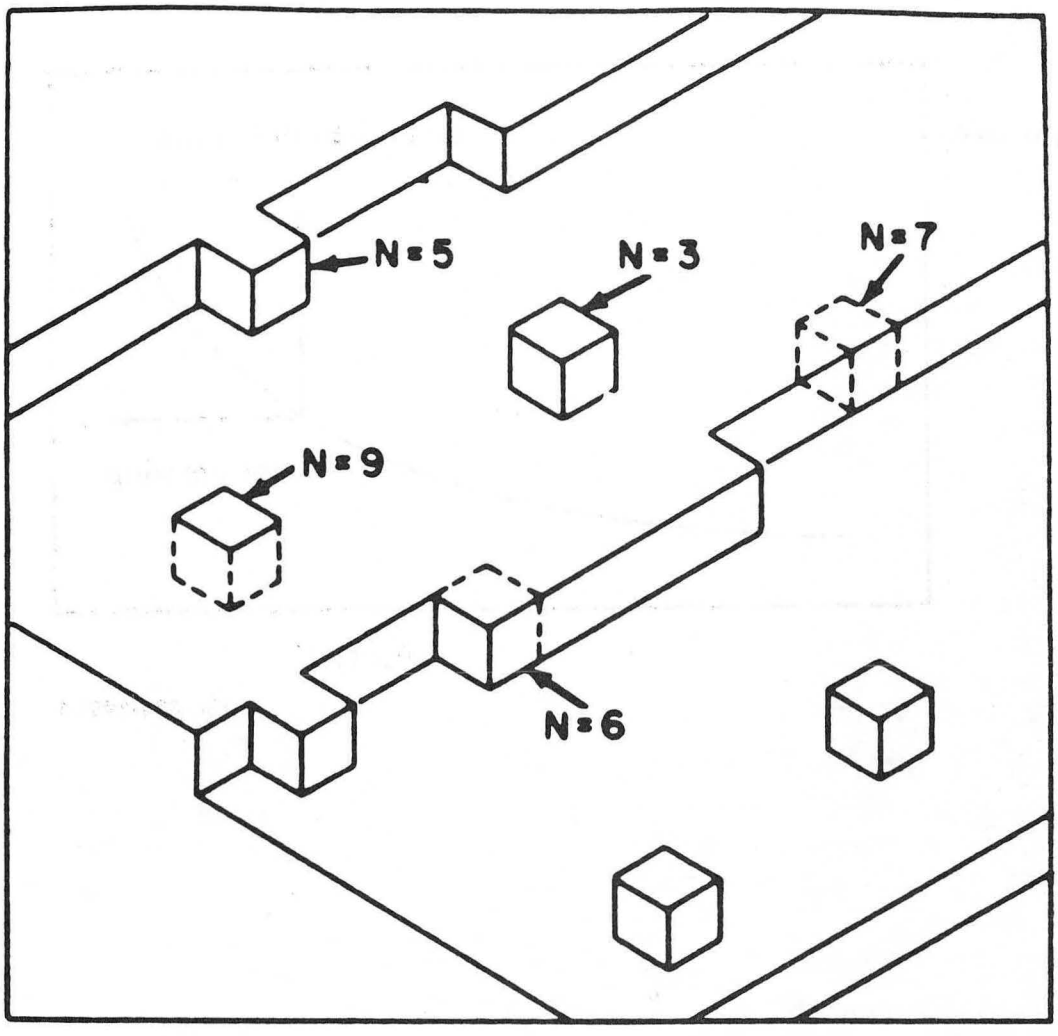
Figure 30



e: $[11\bar{2}0]$
f: $[0001]$
g: $[1\bar{1}00]$

XBL 8810-3539 A

Figure 31



XBL 8810-3534 A

Figure 32

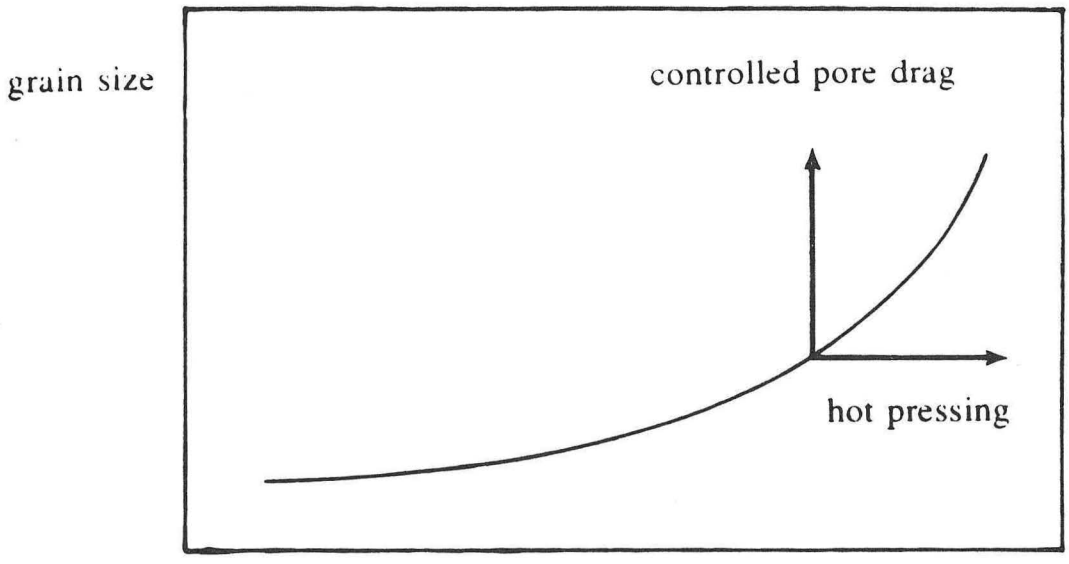
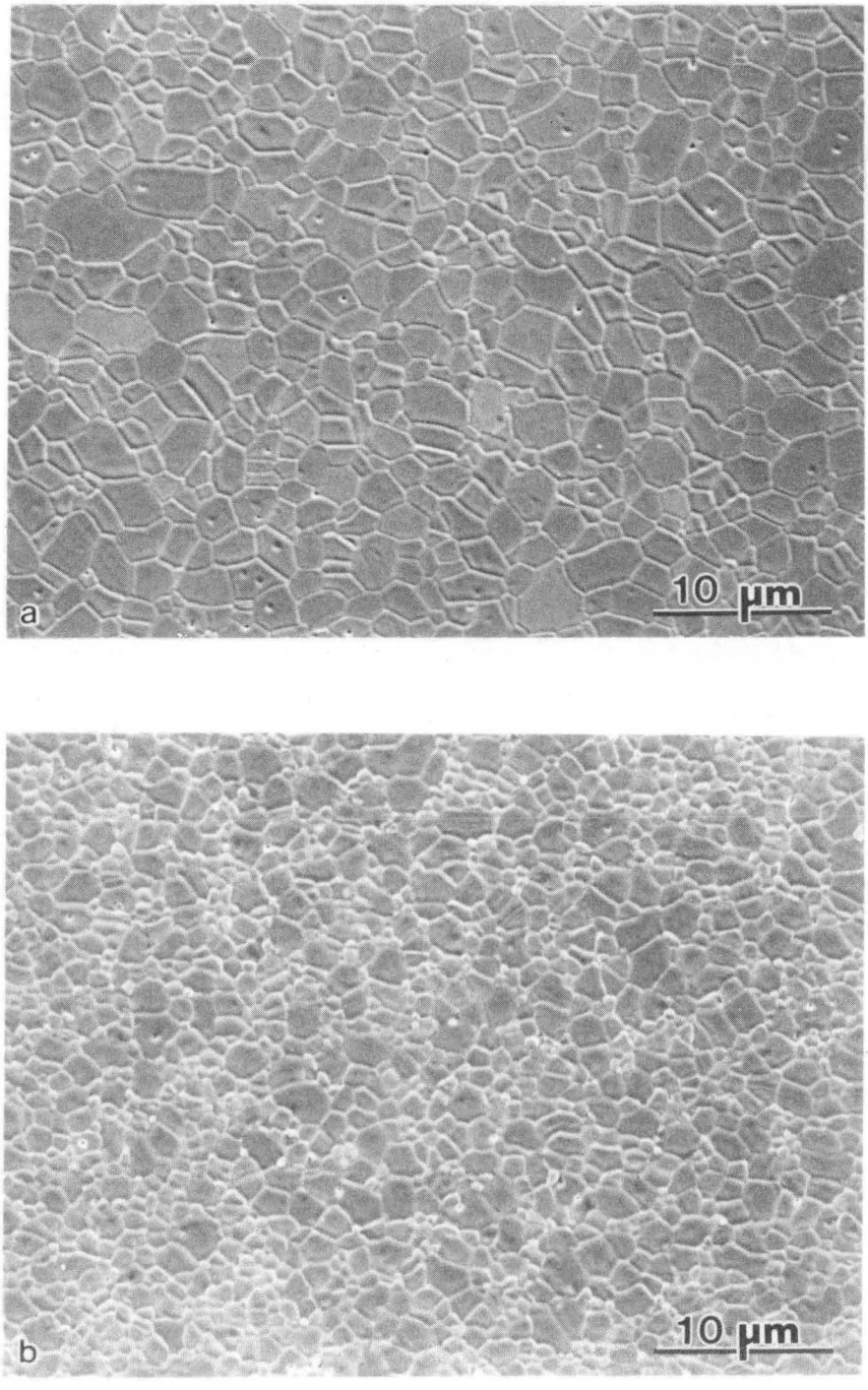
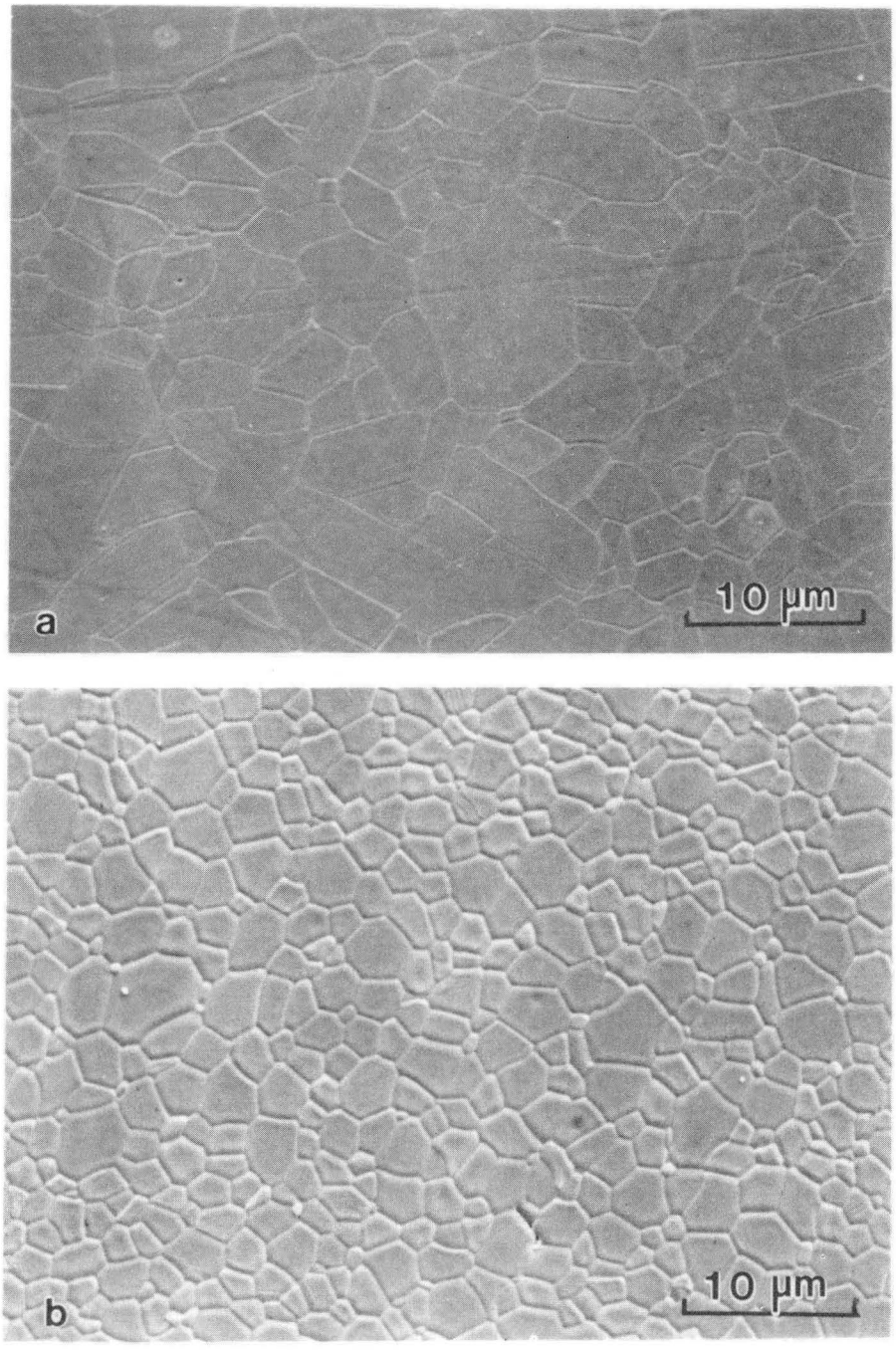

grain size
controlled pore drag
hot pressing
density
XBL 884-1455 A

Figure 33



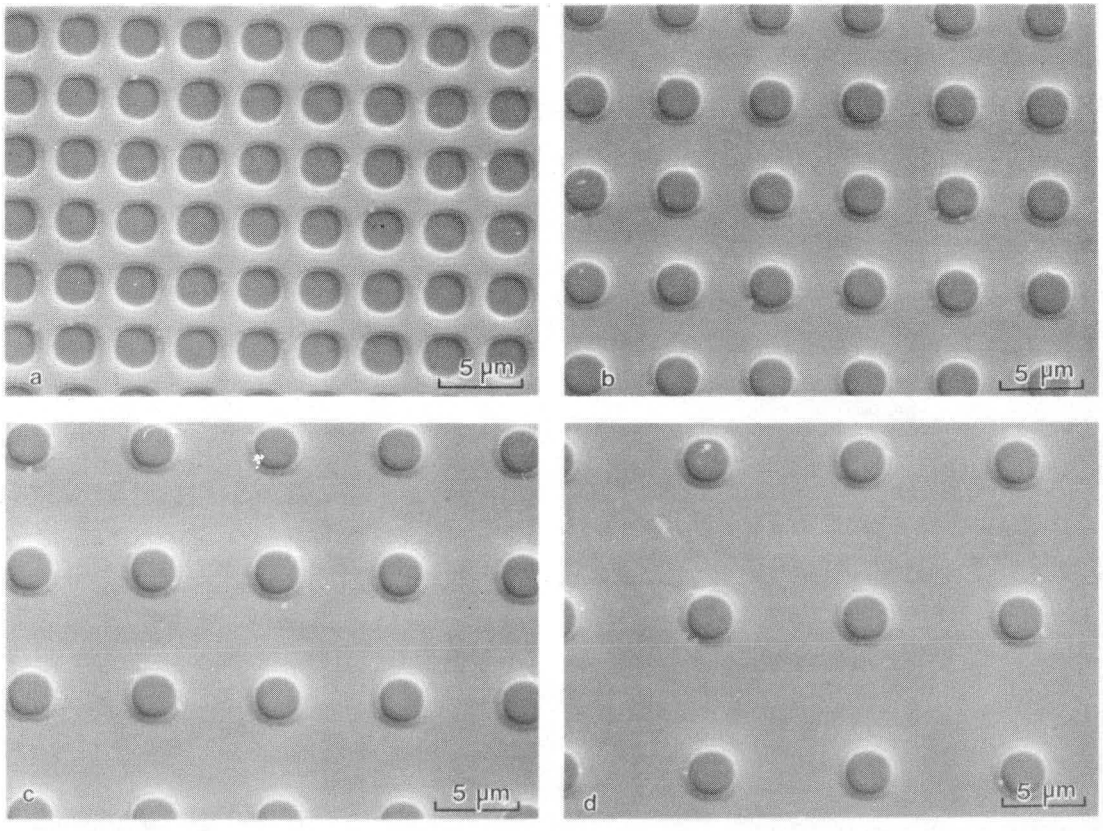
XBB 889-9060-A

Figure 34



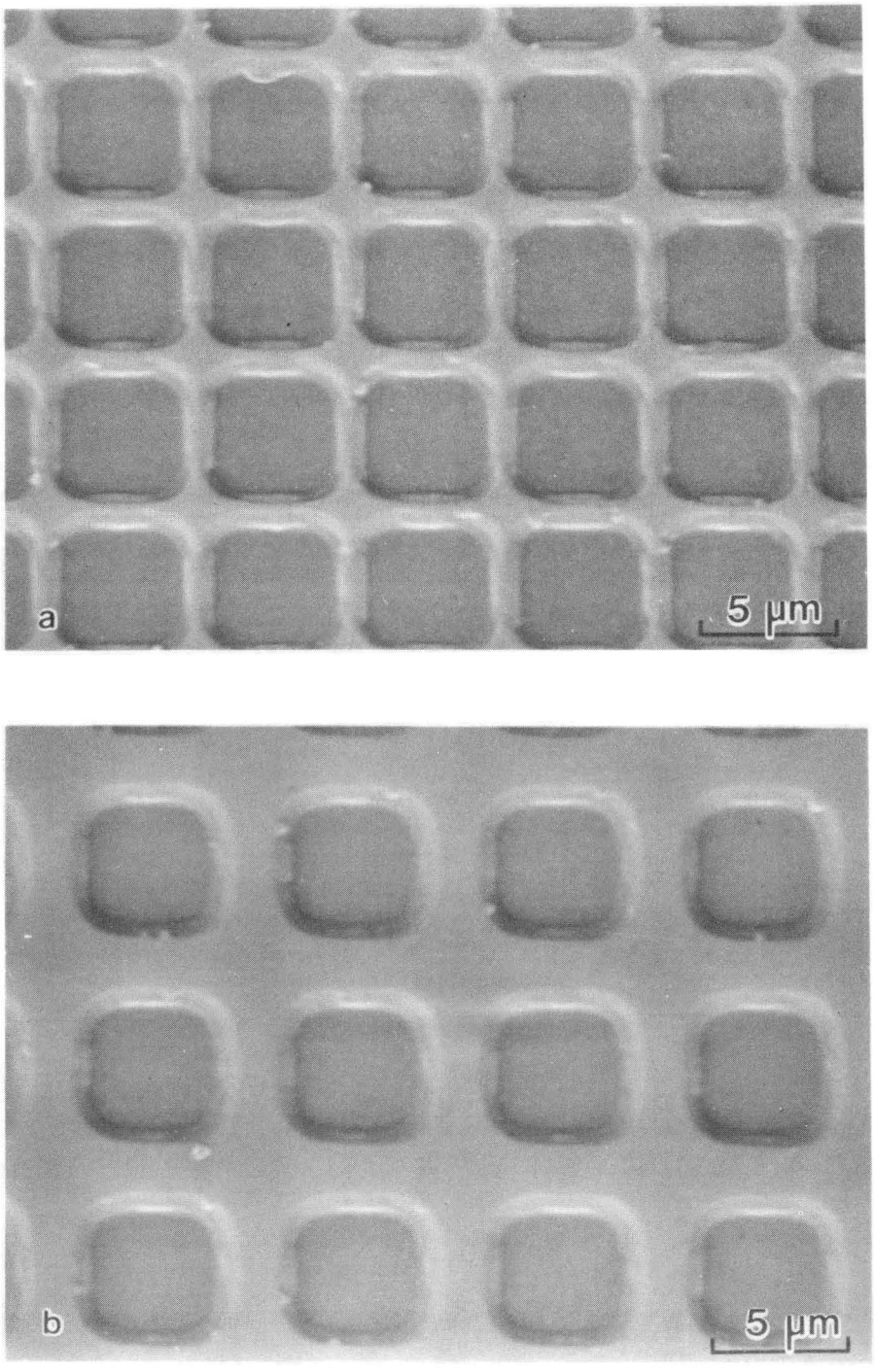
XBB 884-4065-A

Figure 35



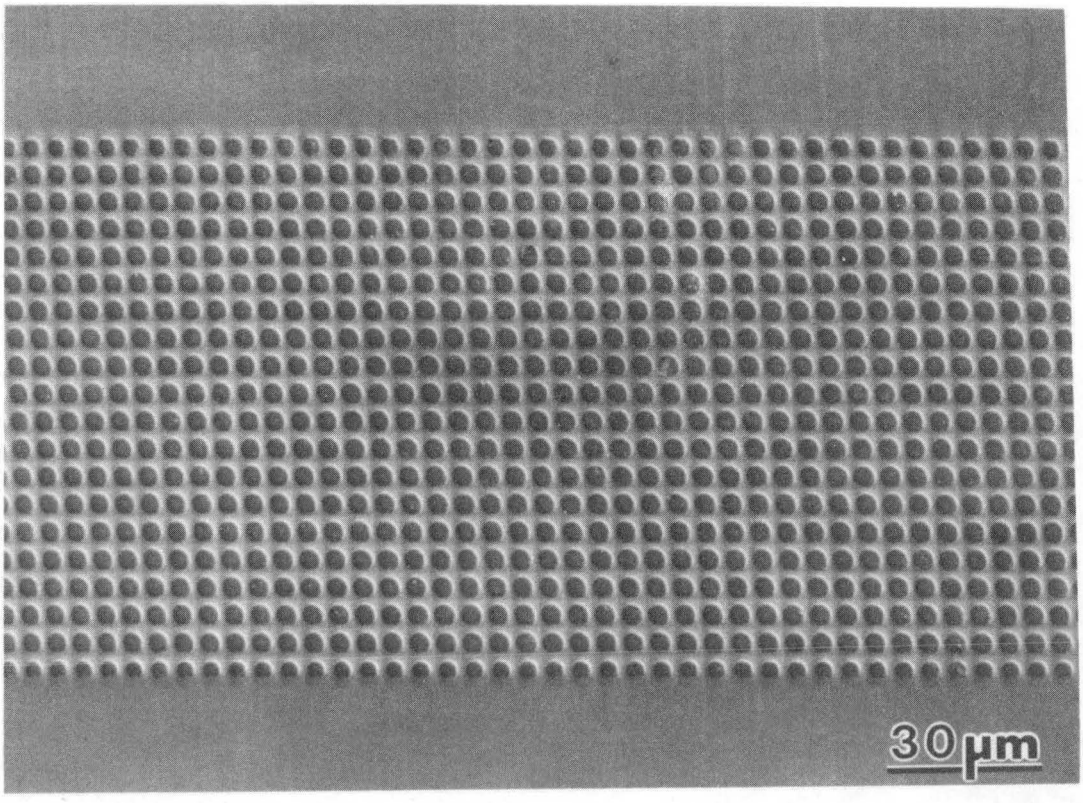
XBB 889-9107-A

Figure 36



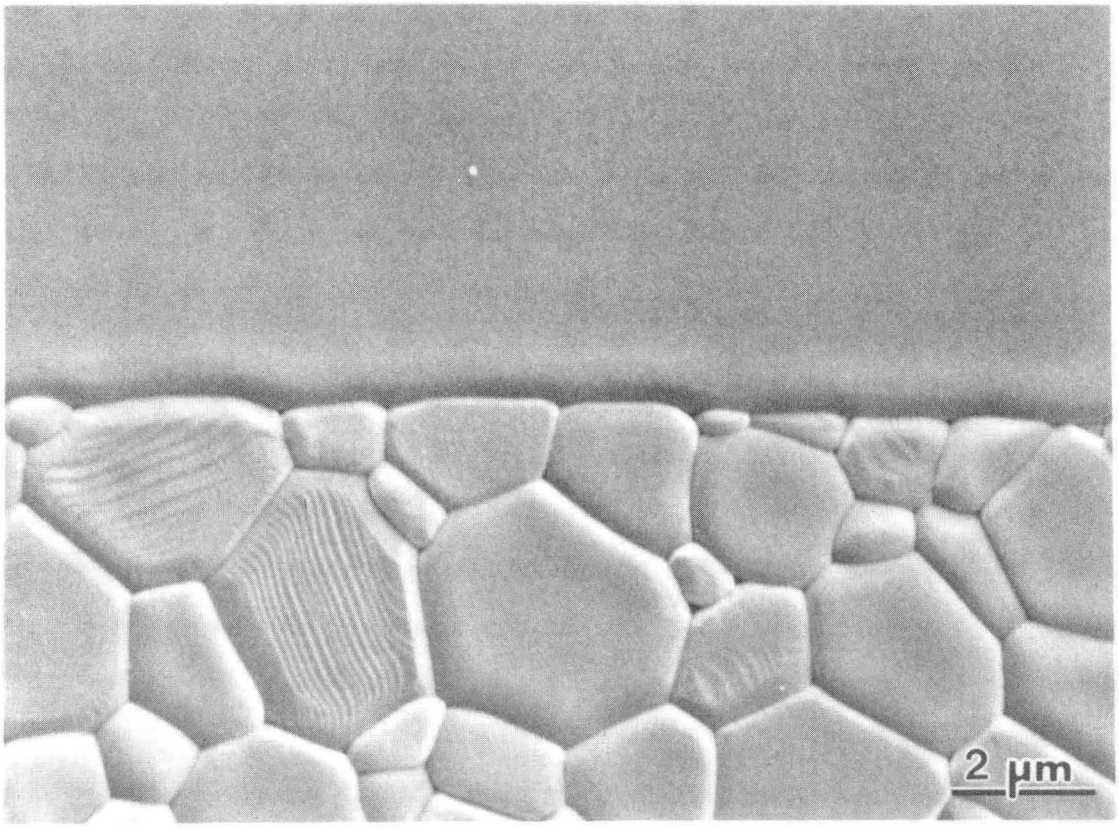
XBB 889-9096-A

Figure 37



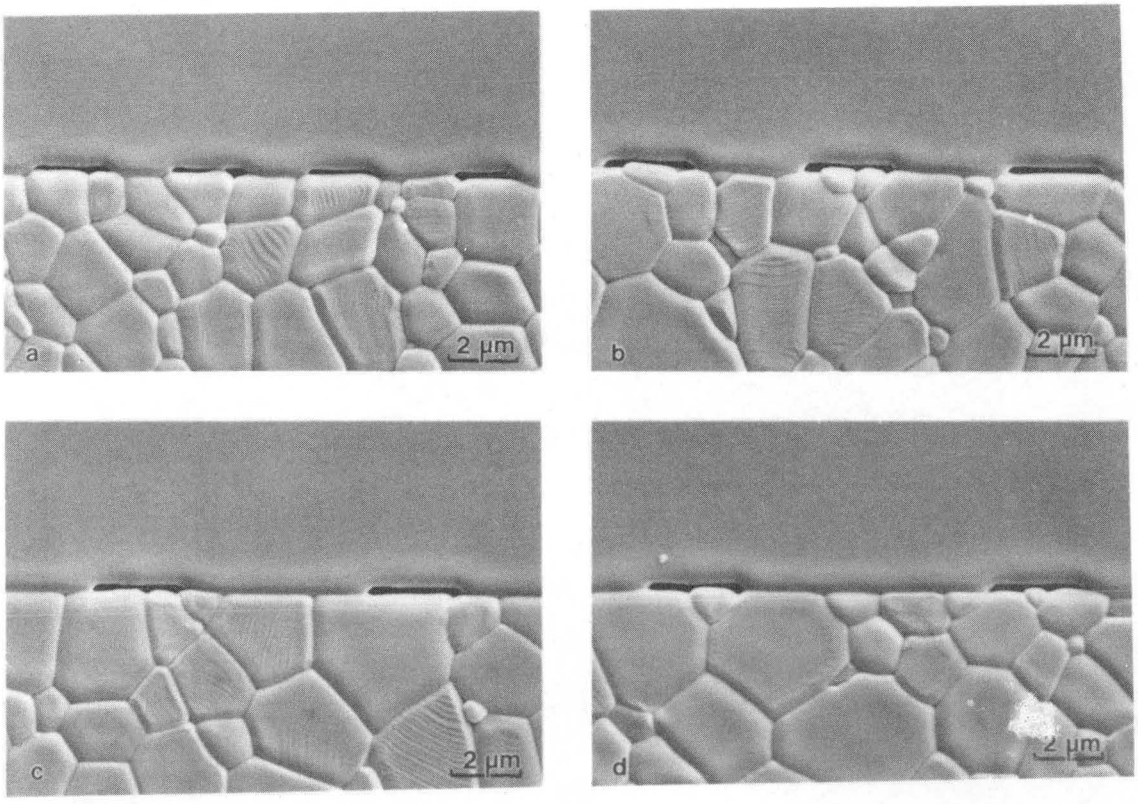
XBB 889-9109-A

Figure 38



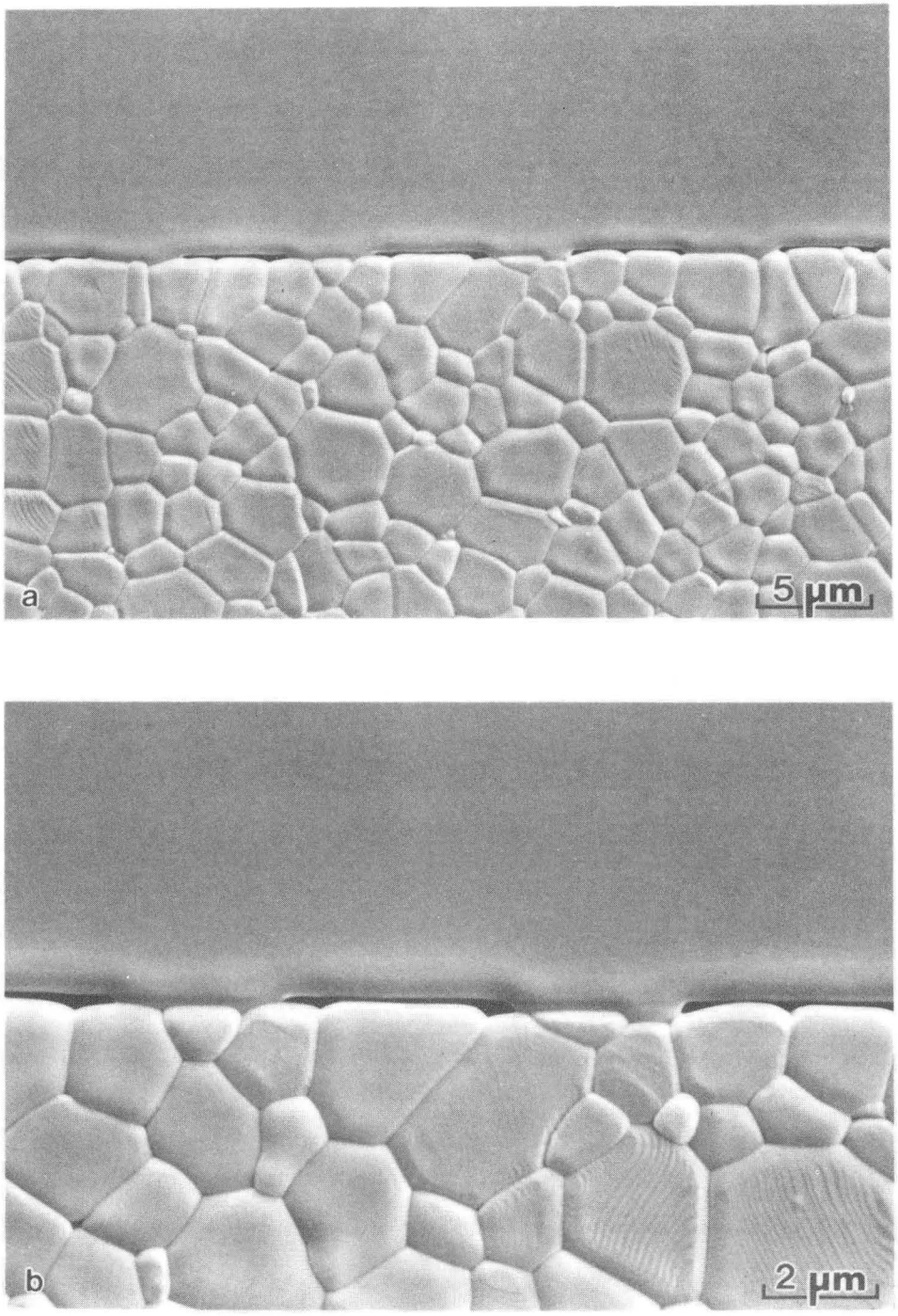
XBB 889-9057-A

Figure 39



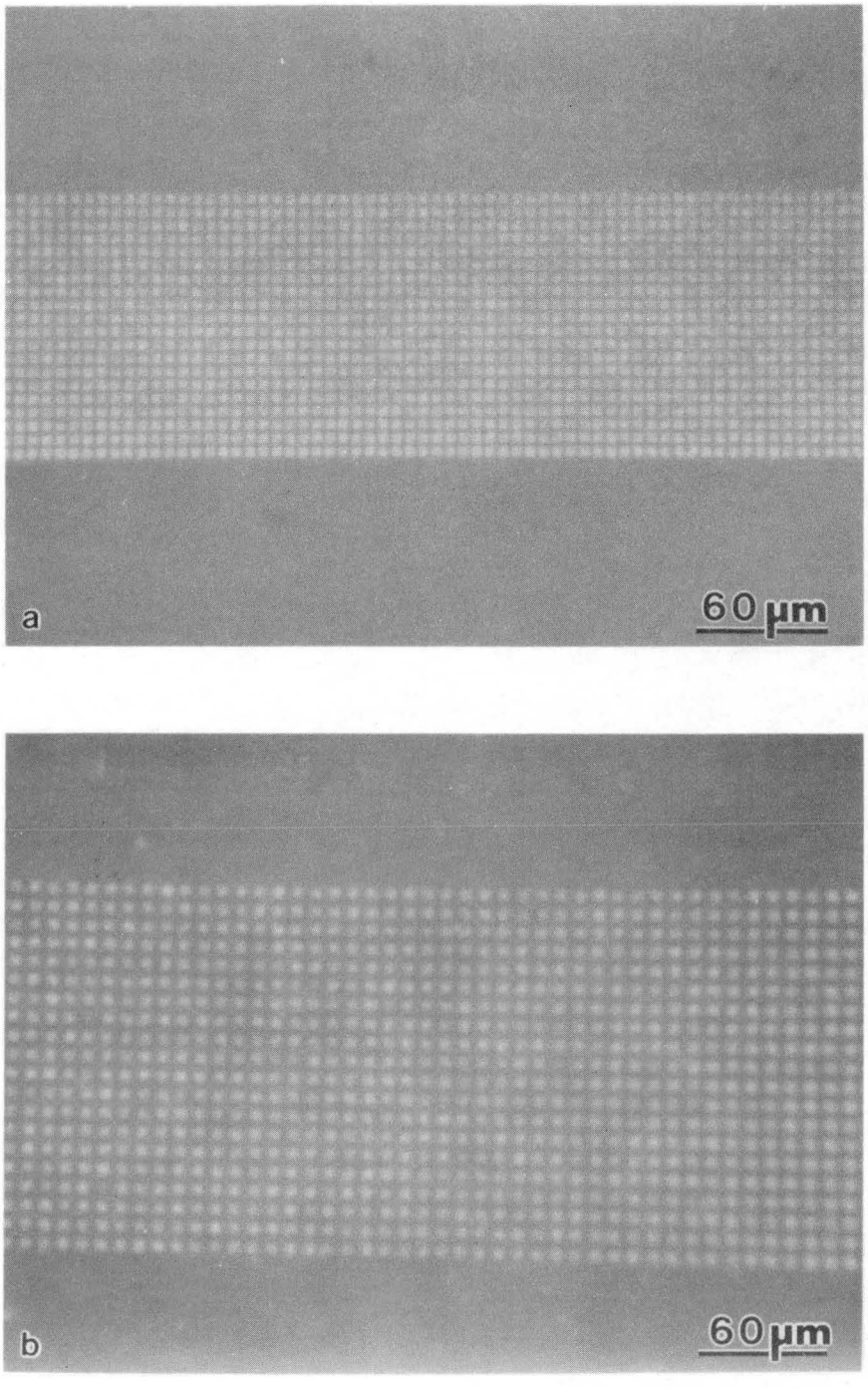
XBB 882-742-A

Figure 40



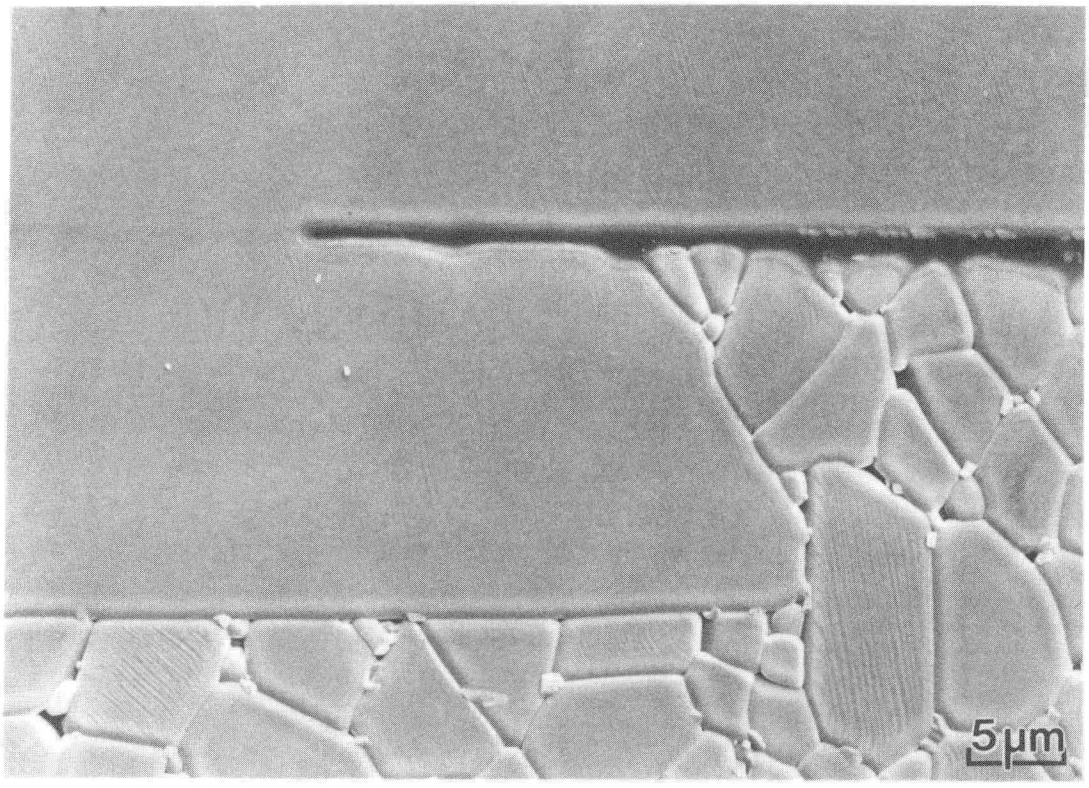
XBB 889-9097-A

Figure 41



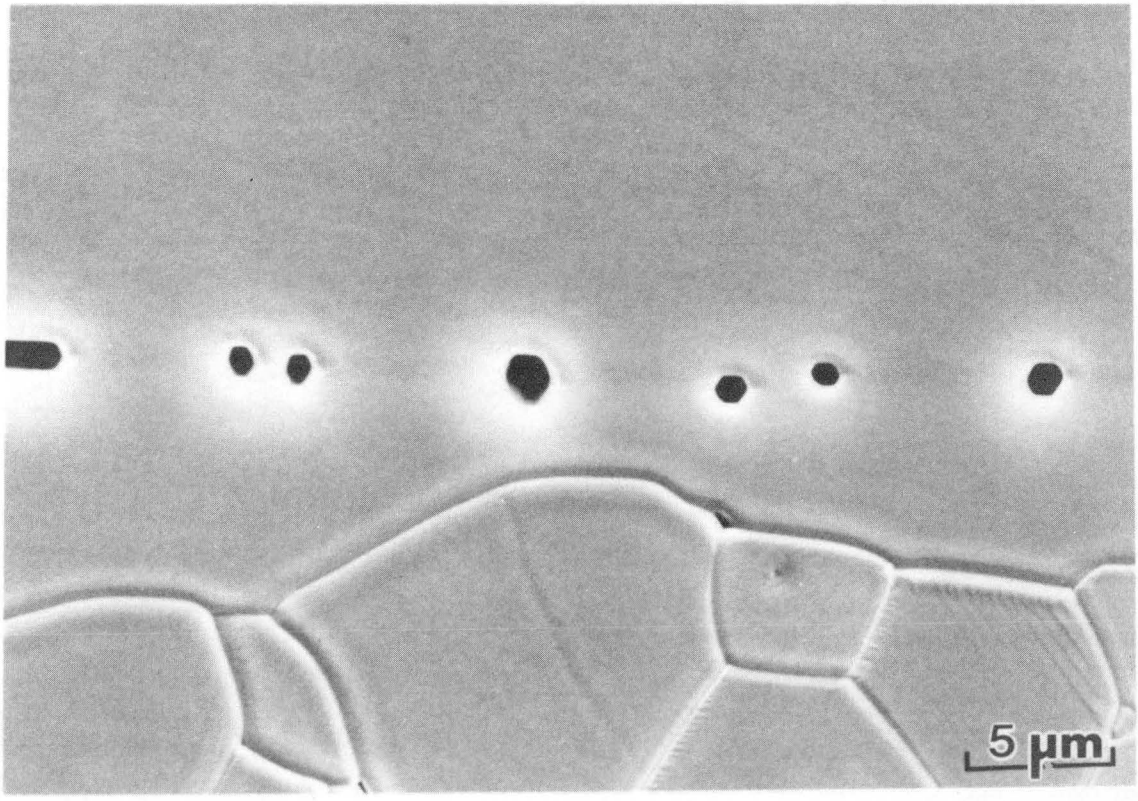
XBB 889-9098-A

Figure 42



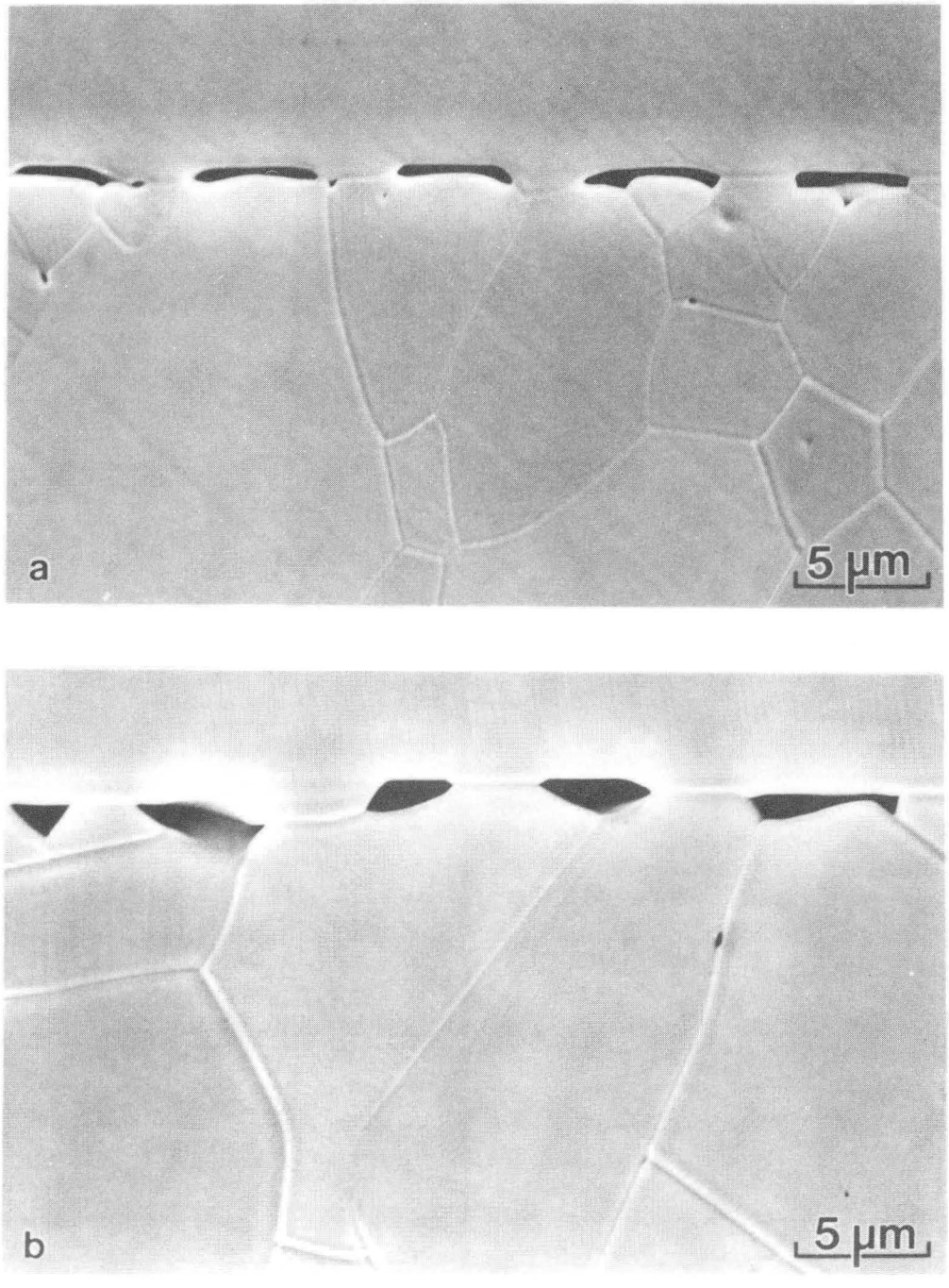
XBB 884-3499-A

Figure 43



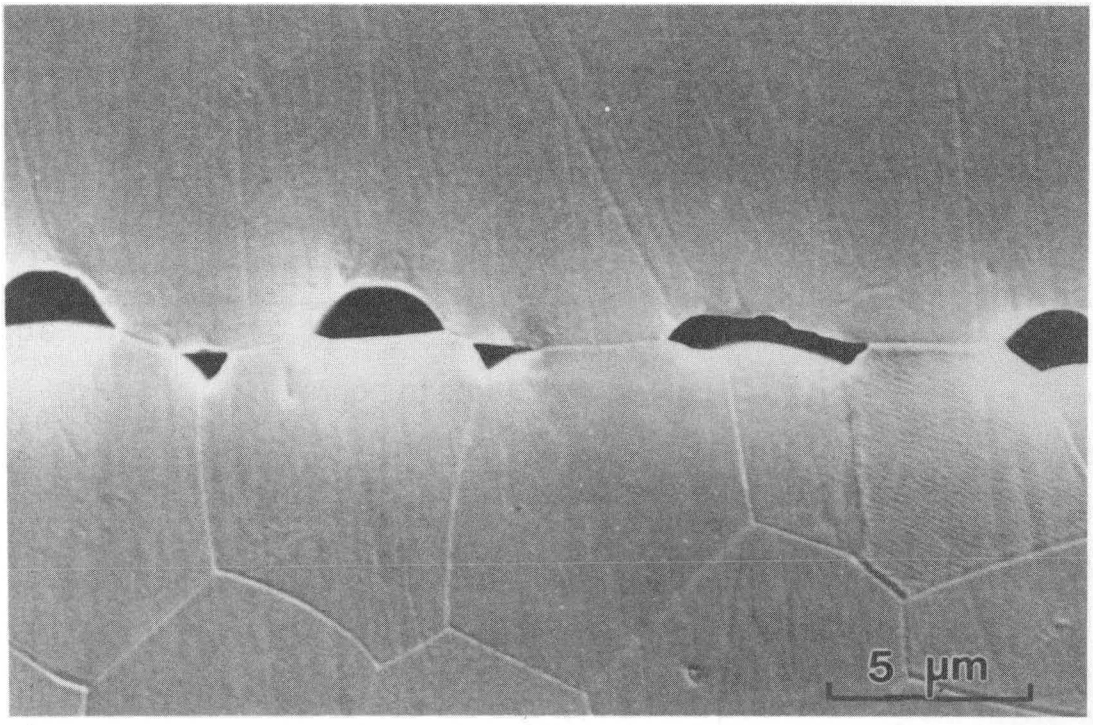
XBB 889-9108-A

Figure 44



XBB 889-9099-A

Figure 45



XBB 882-743-A

Figure 46

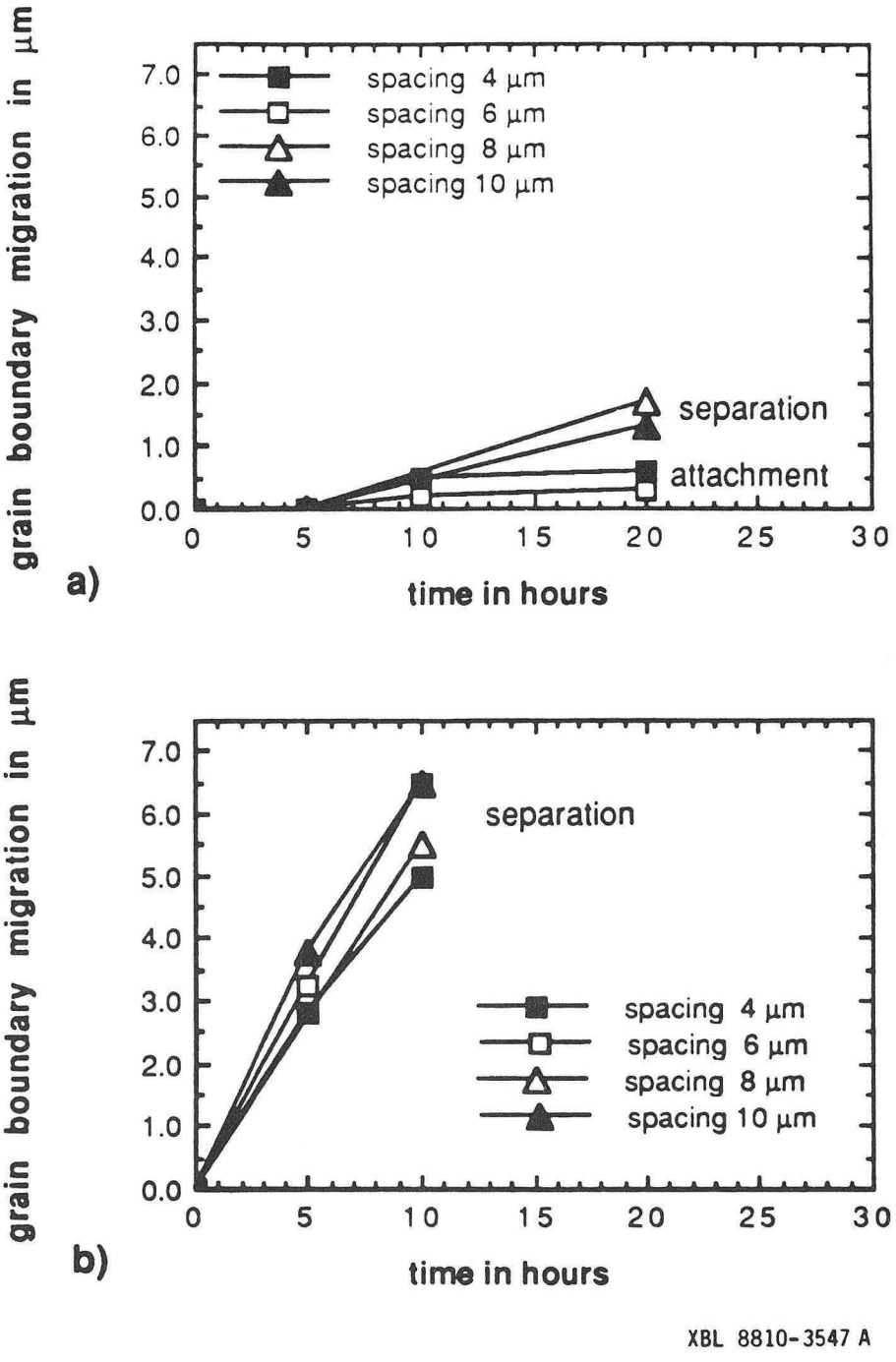
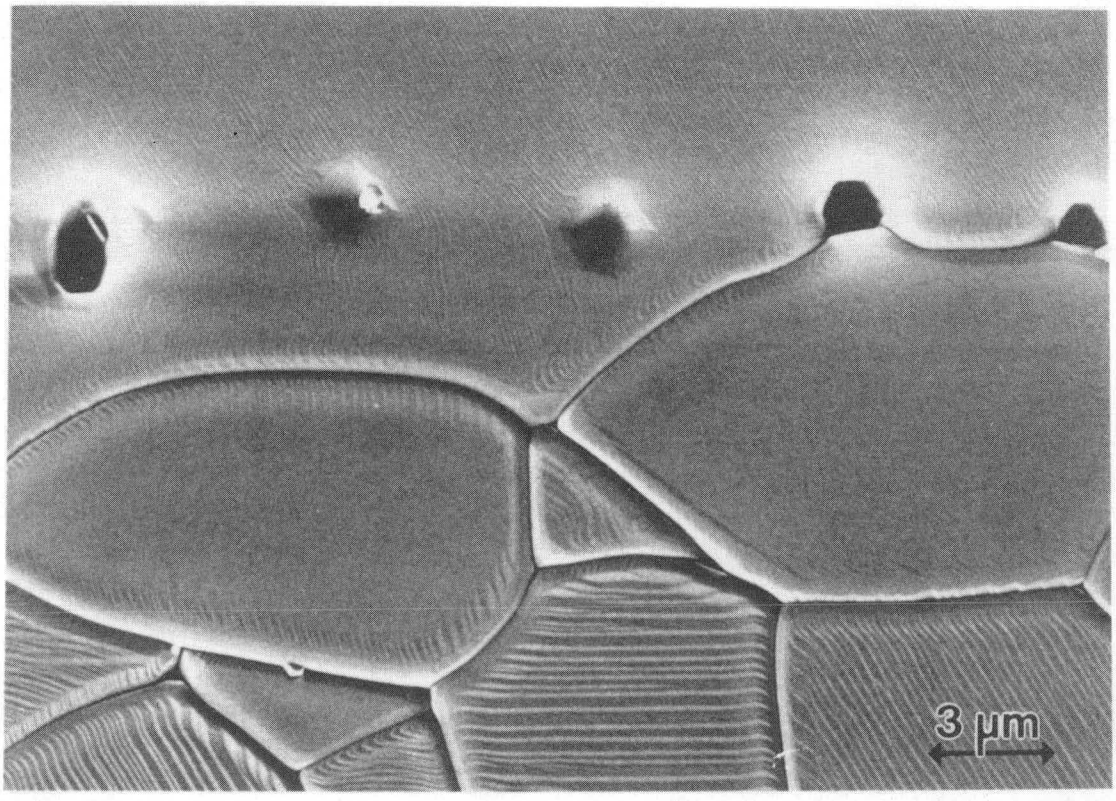
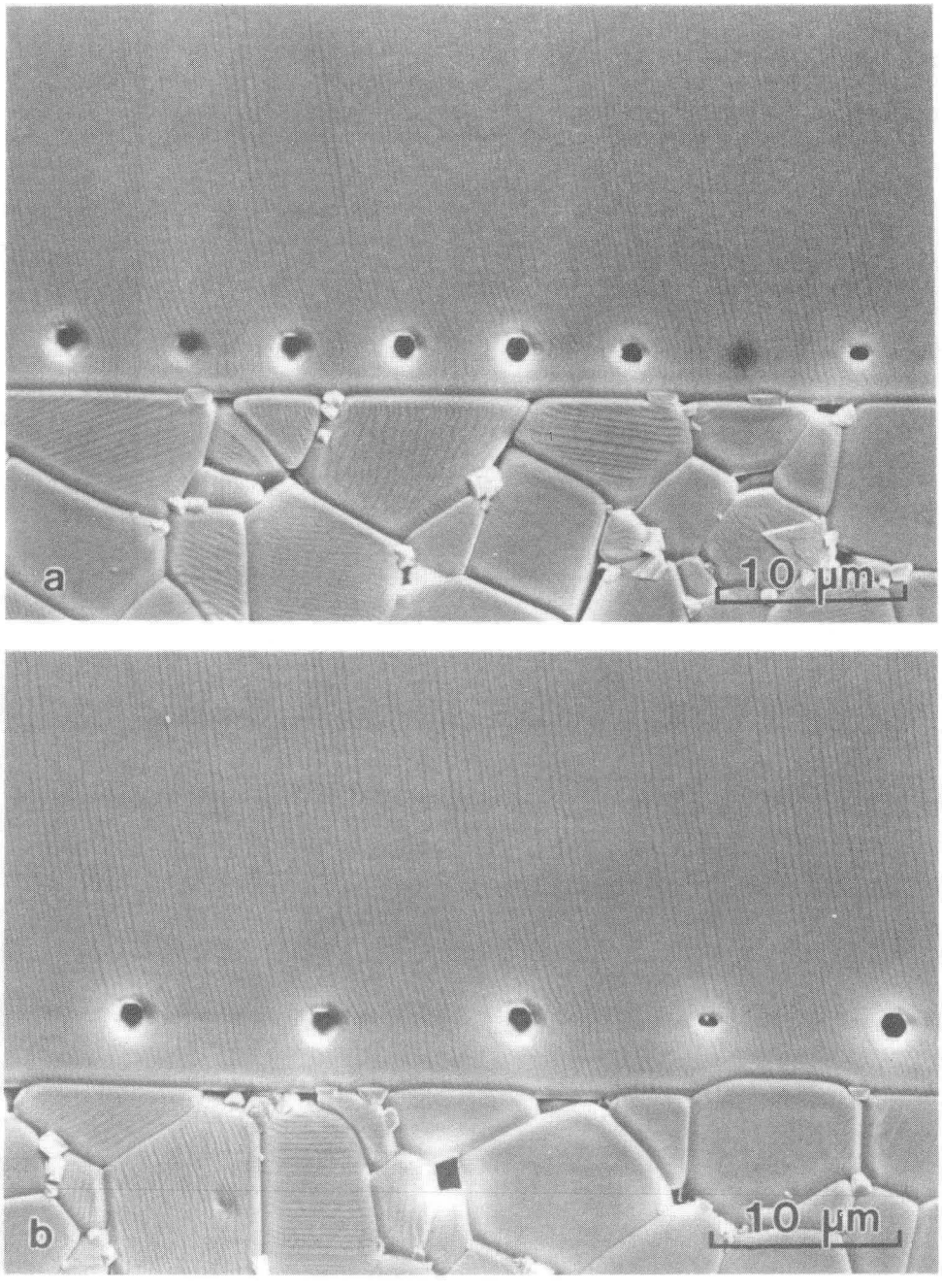

grain boundary migration in μm
7.0
6.0
5.0
4.0
3.0
2.0
1.0
0.0
spacing 4 μm
spacing 6 μm
spacing 8 μm
spacing 10 μm
separation
attachment
0
5
10
15
20
25
30
time in hours
a)
grain boundary migration in μm
7.0
6.0
5.0
4.0
3.0
2.0
1.0
0.0
separation
spacing 4 μm
spacing 6 μm
spacing 8 μm
spacing 10 μm
0
5
10
15
20
25
30
time in hours
b)
XBL 8810-3547 A

Figure 47



XBB 883-2405-A

Figure 48



XBB 882-746-A

Figure 49

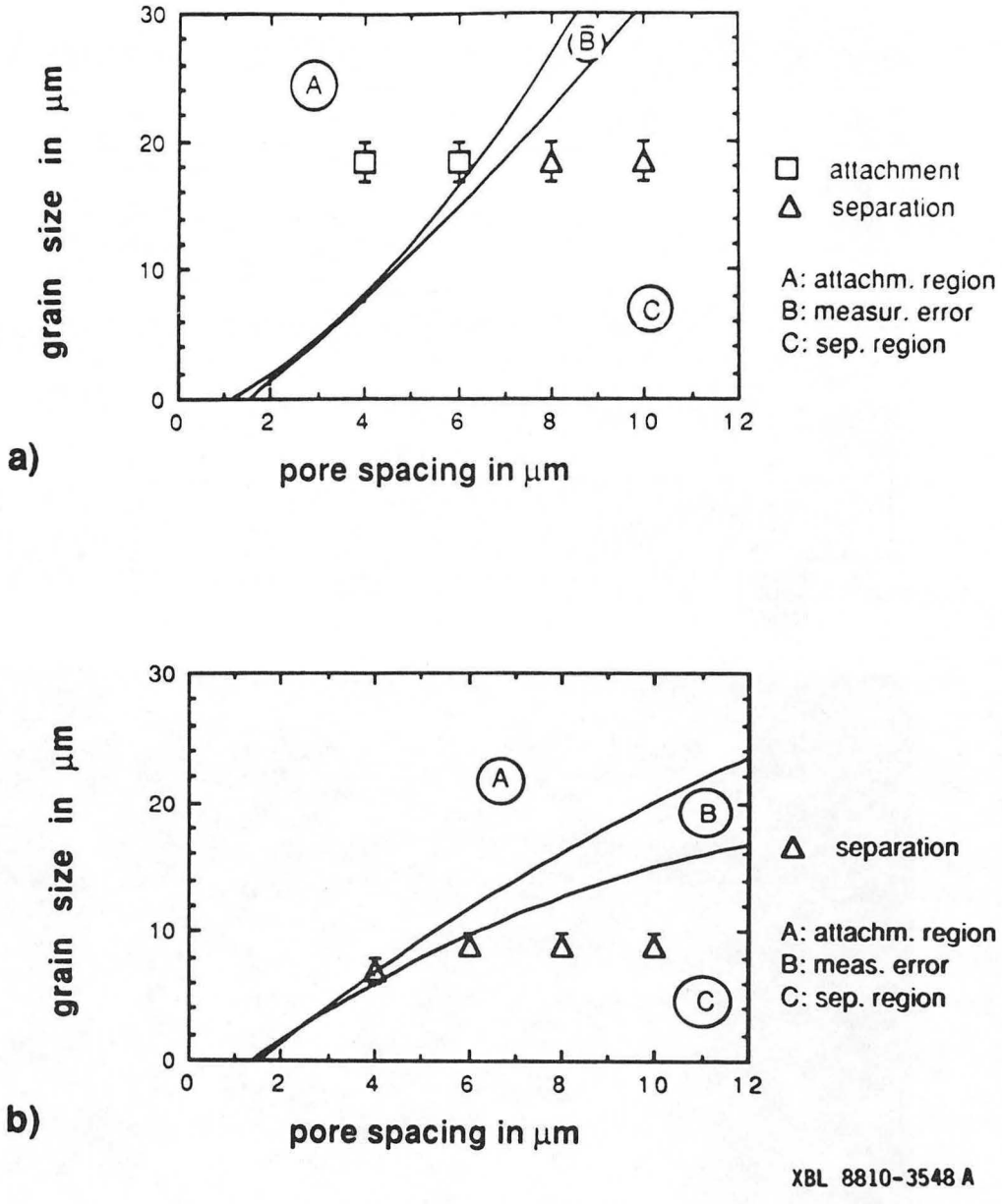
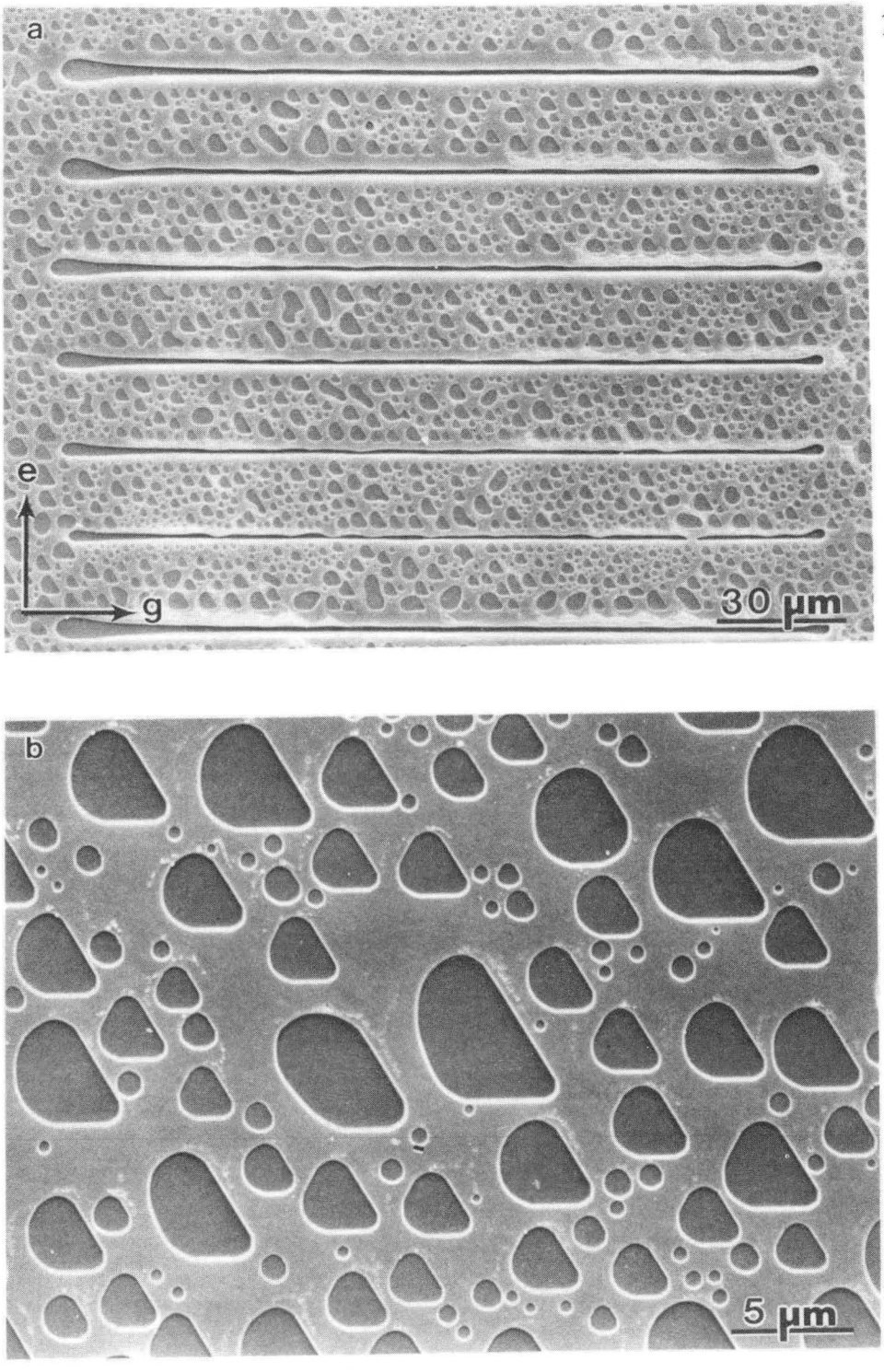
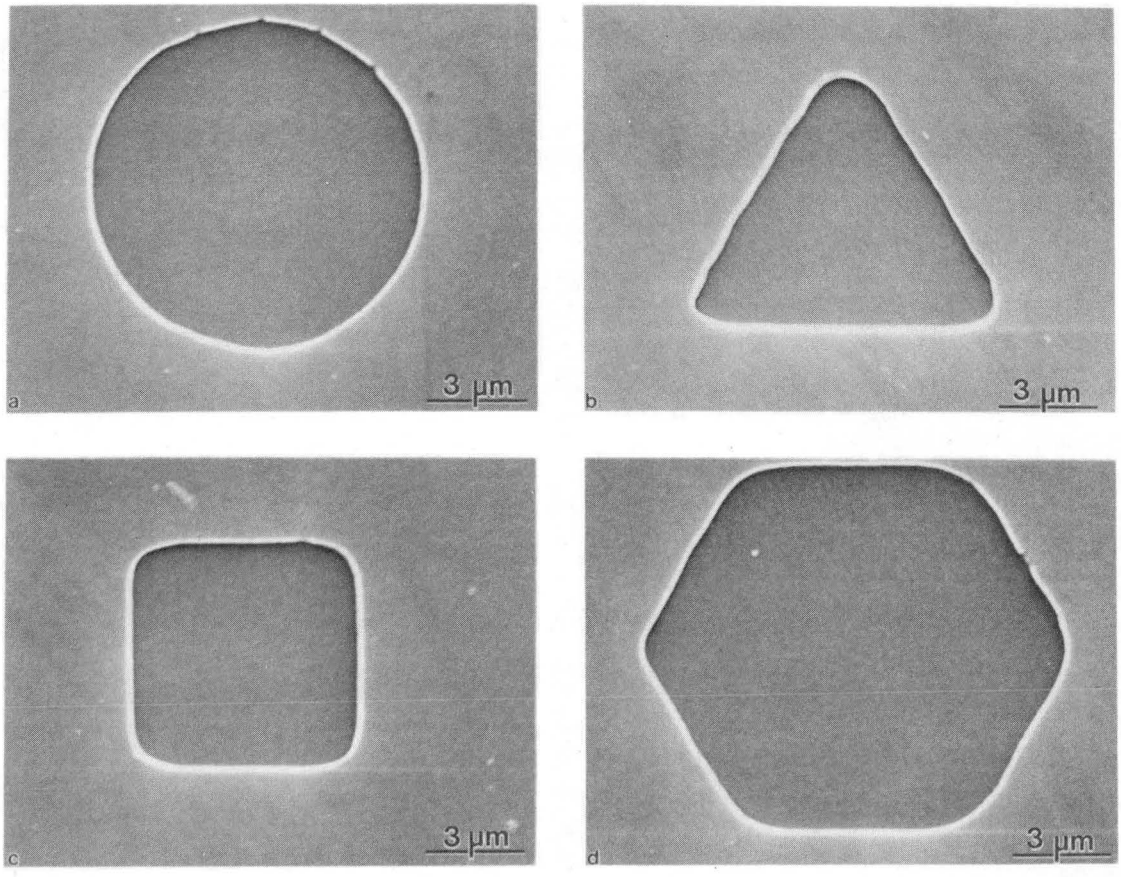

a)
grain size in μm
pore spacing in μm
A
B
C
attachment
separation
A: attachm. region
B: measur. error
C: sep. region
b)
grain size in μm
pore spacing in μm
A
B
C
separation
A: attachm. region
B: meas. error
C: sep. region
XBL 8810-3548 A

Figure 50



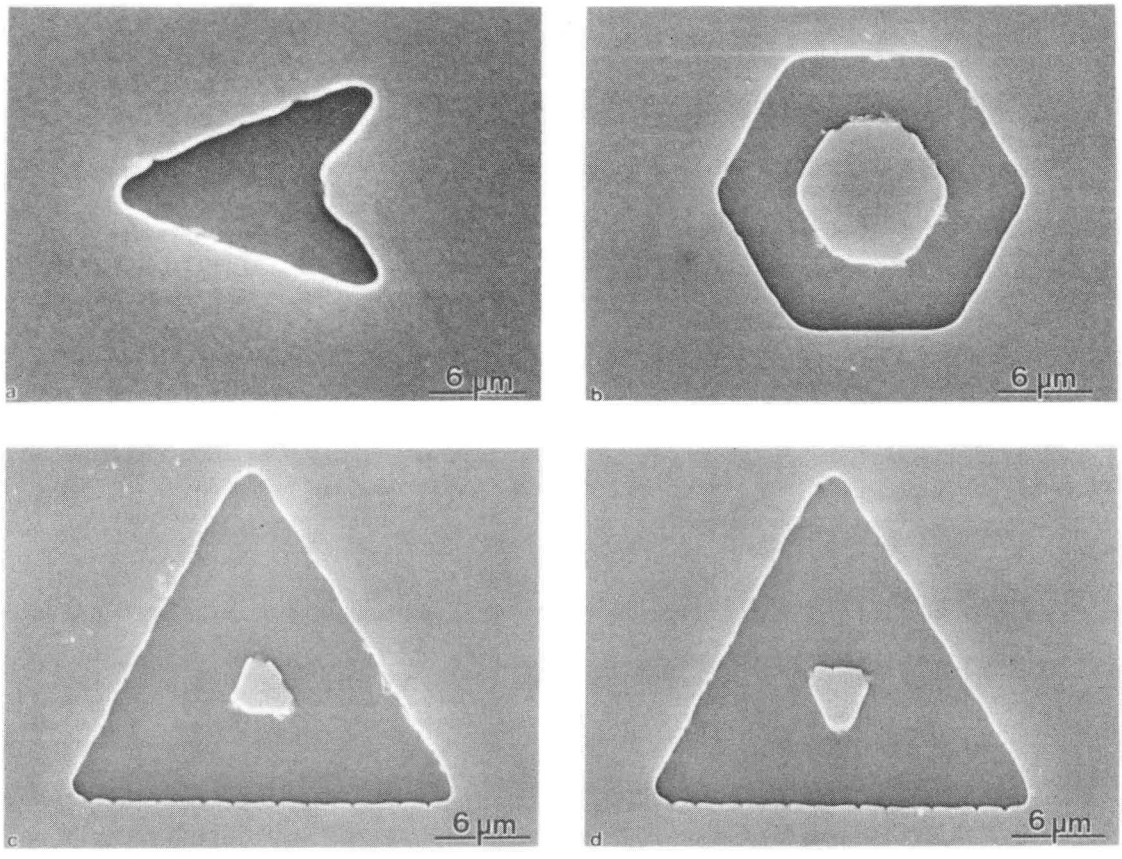
XBB 889-9062-A

Figure 51



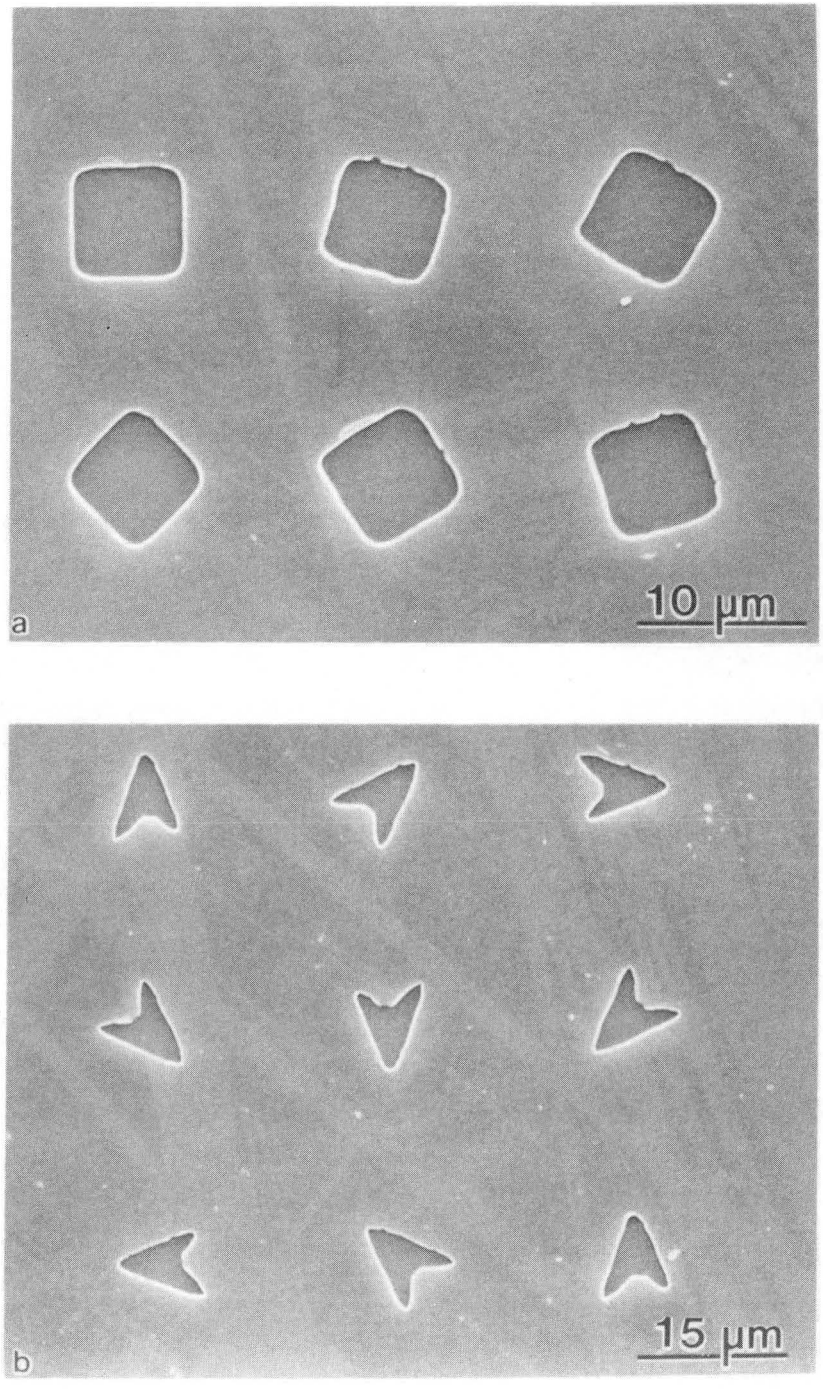
XBB 889-9111-A

Figure 52



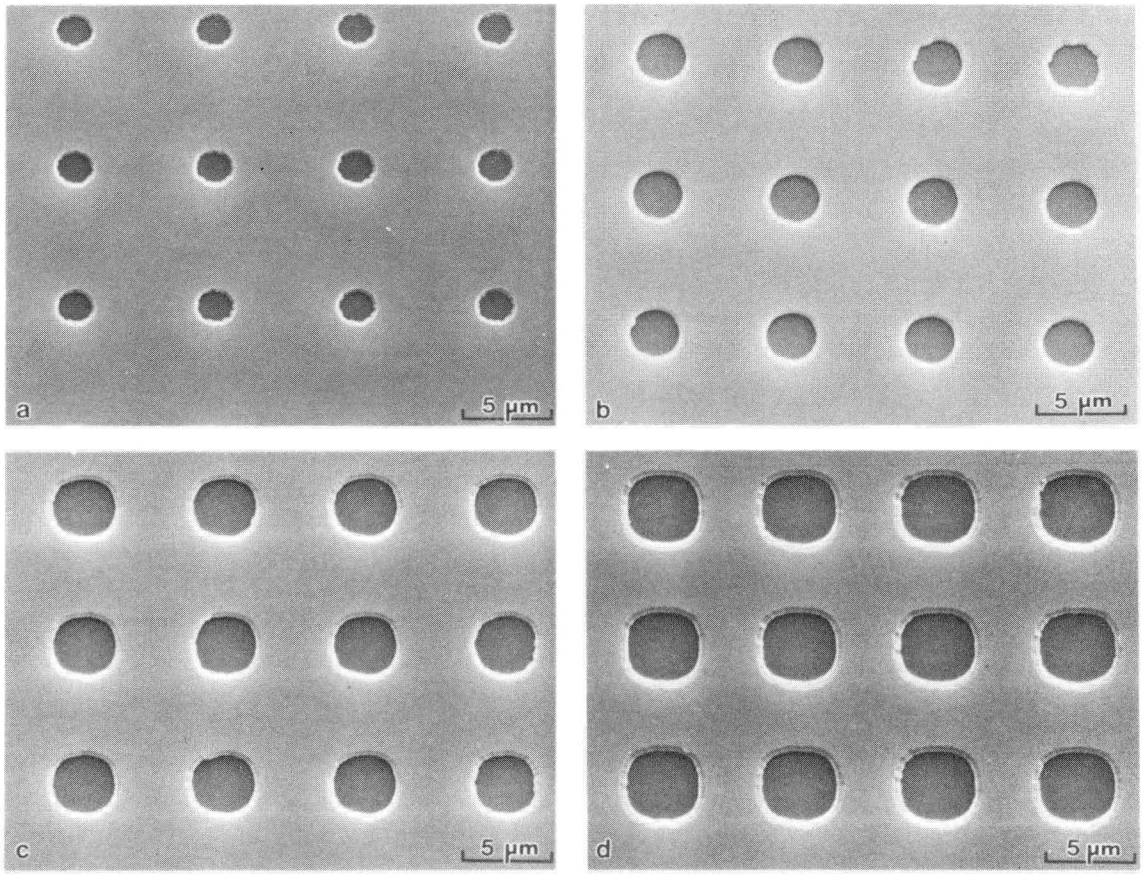
XBB 889-9119-A

Figure 53



XBB 889-9100-A

Figure 54



XBB 887-6748-A

Figure 55

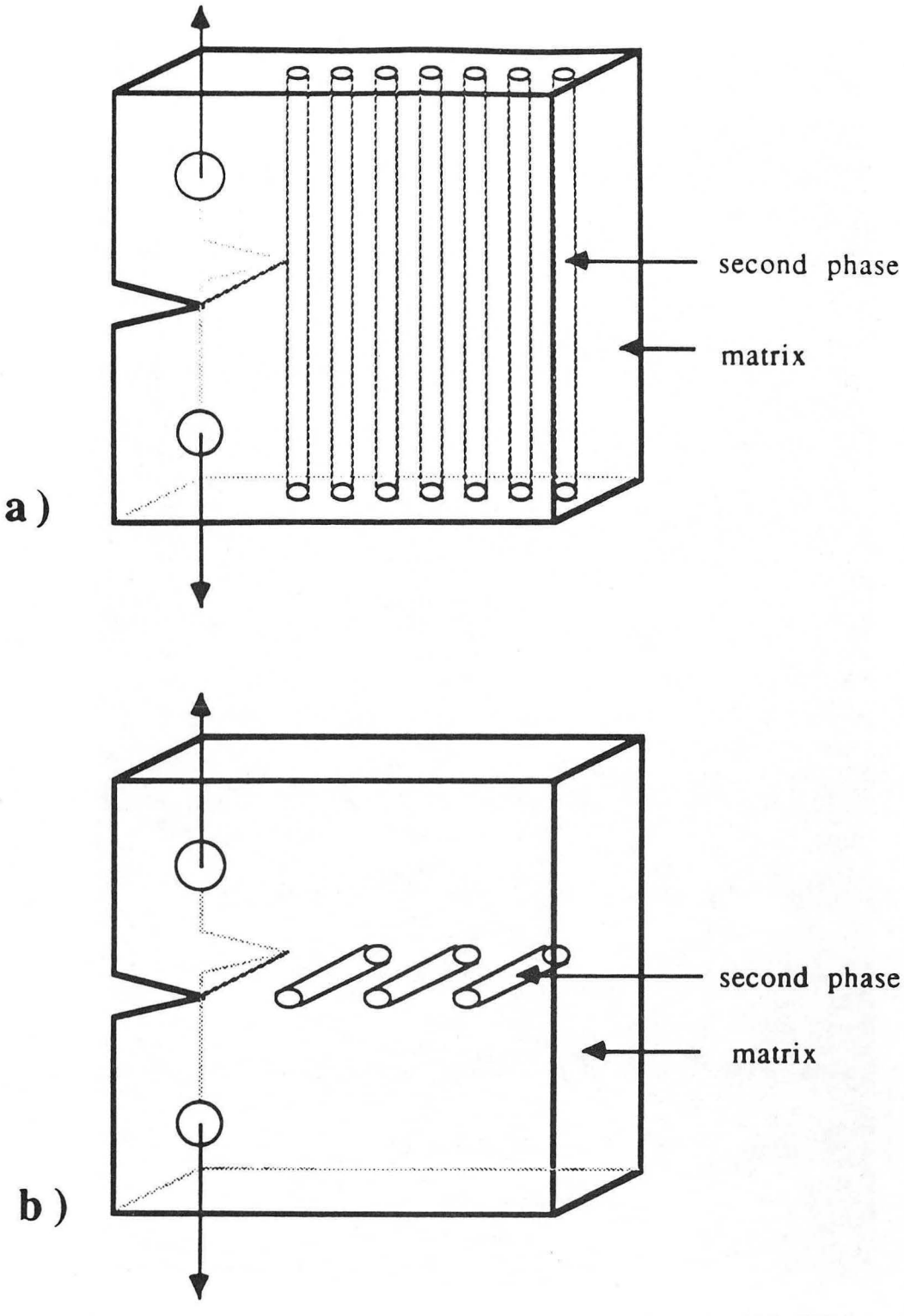
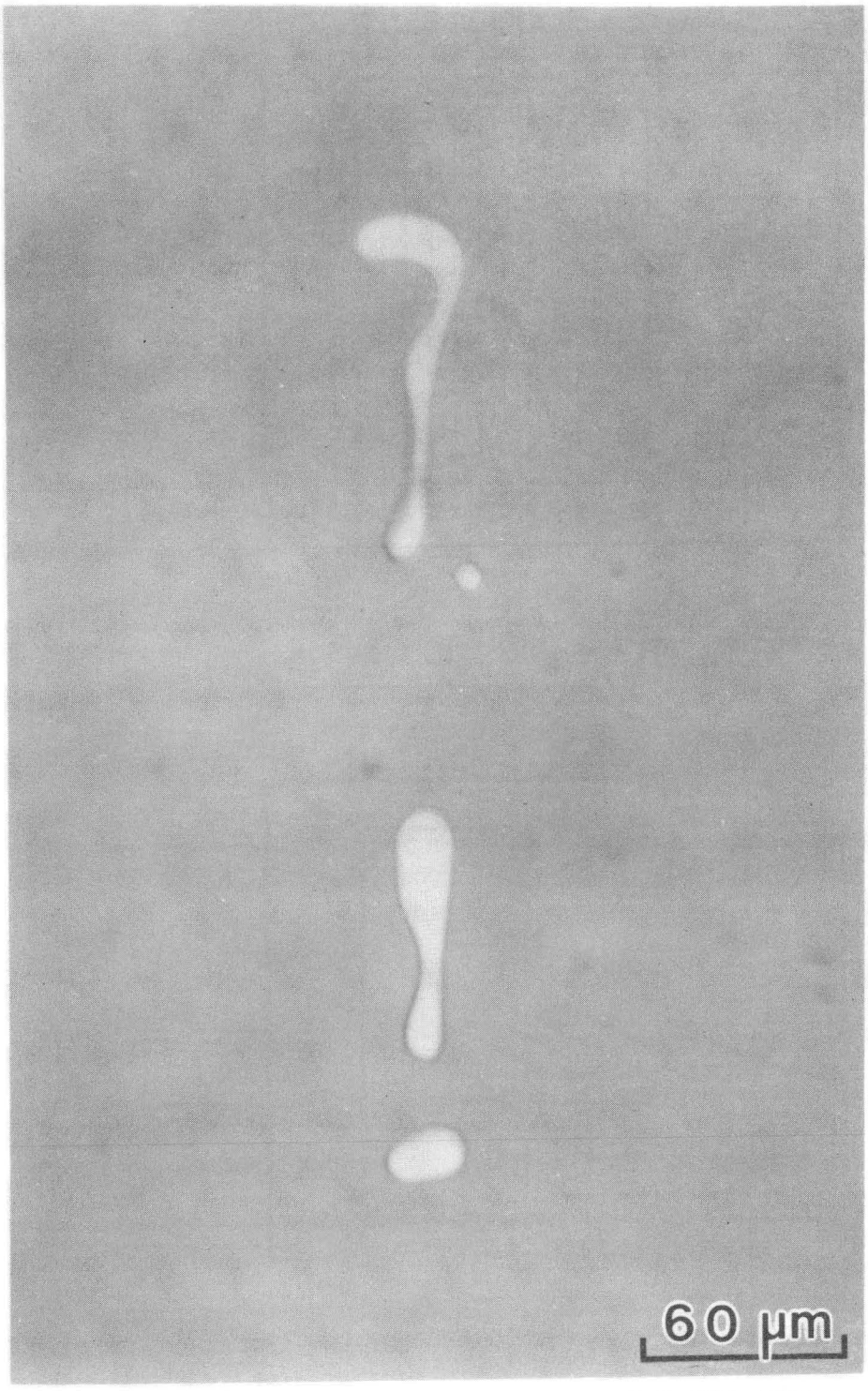
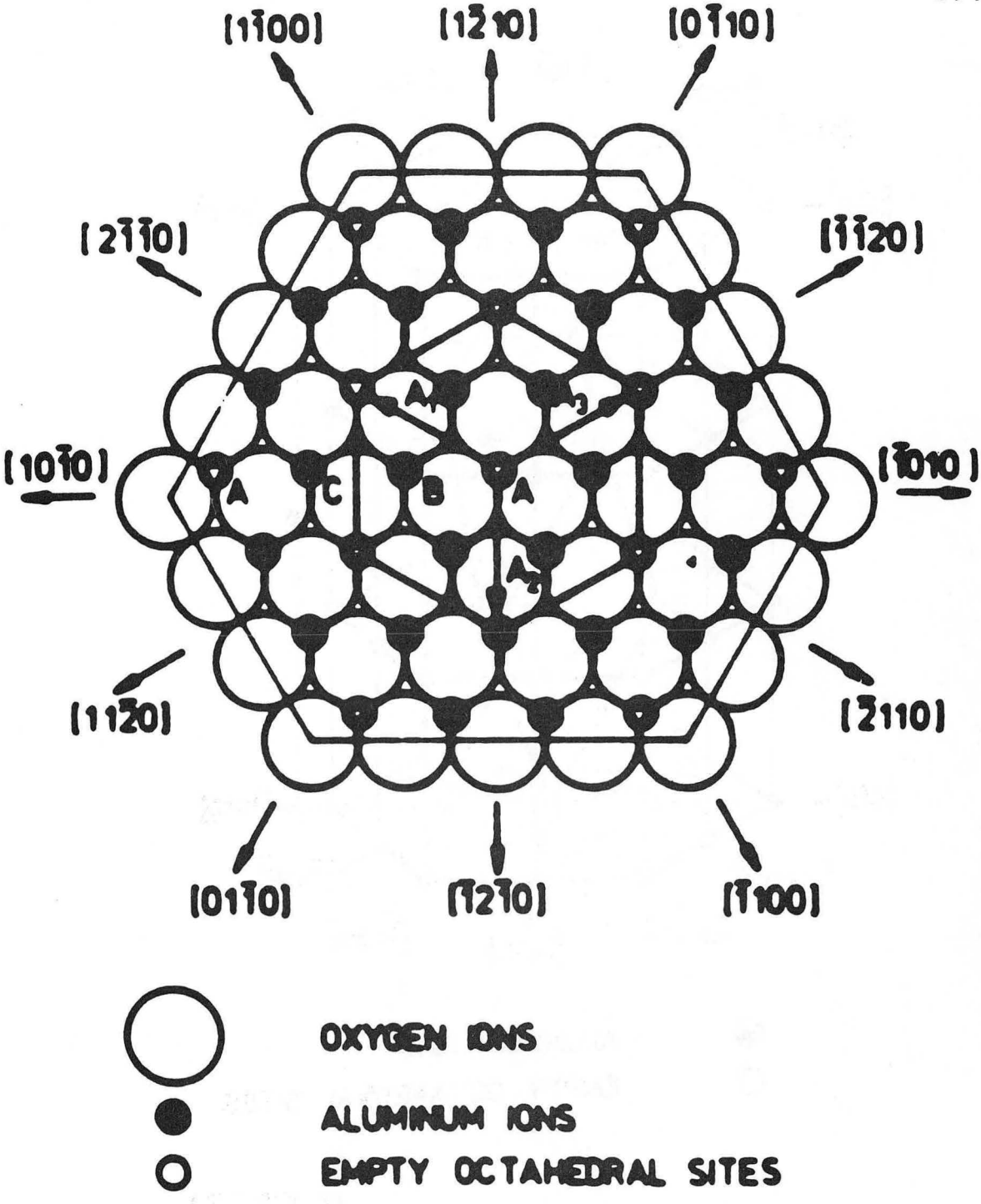


Figure 56



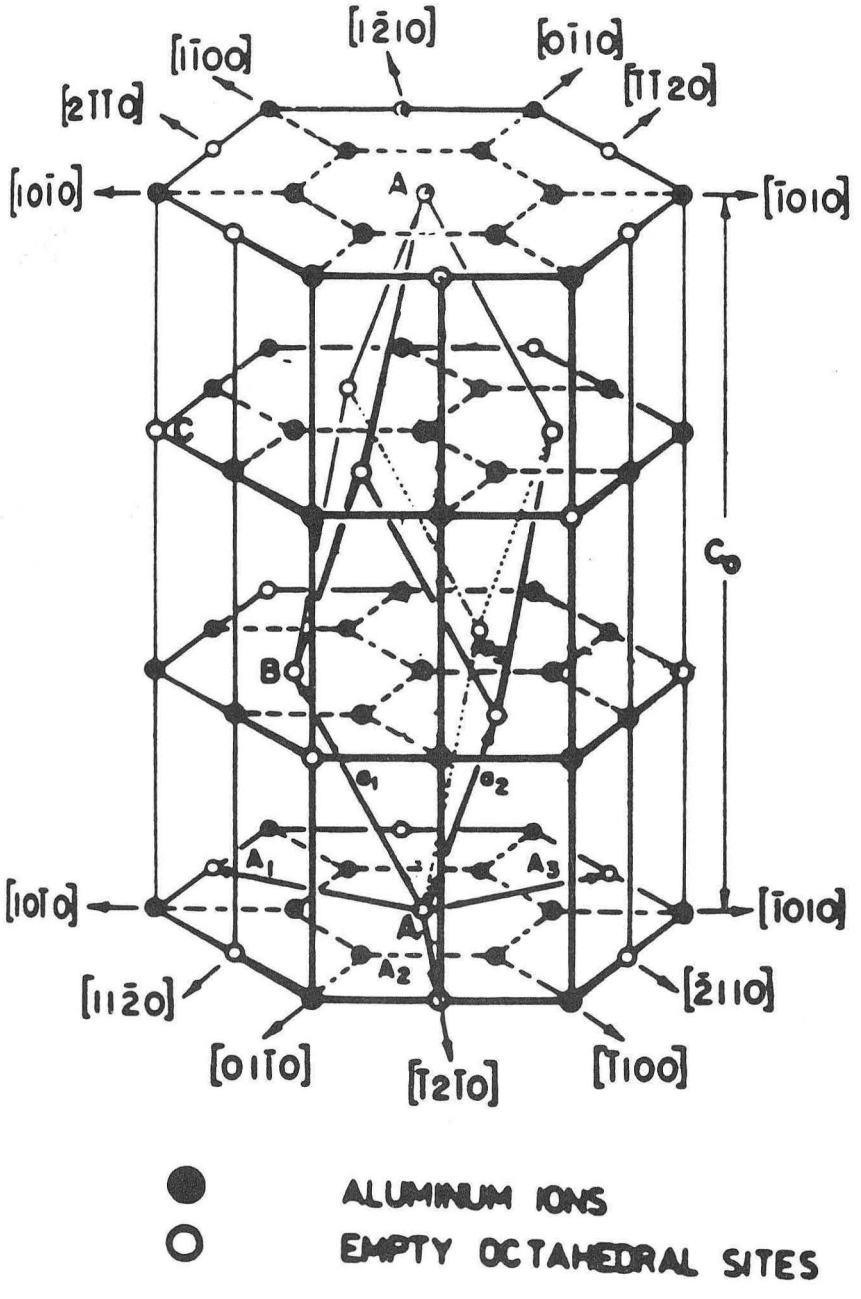
XBB 883-2634-A

Figure 57



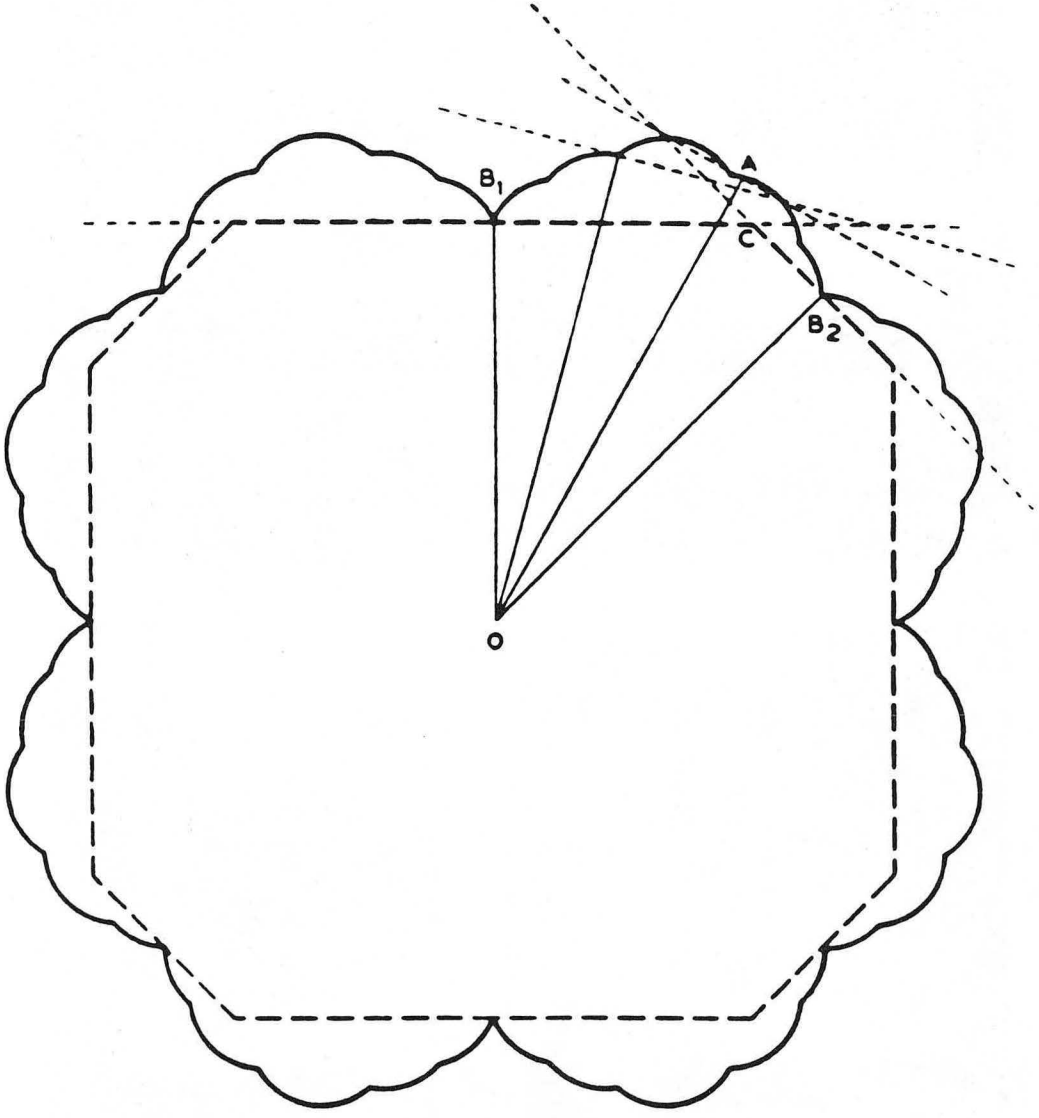
XBL 8810-3533 A

Figure 58



XBL 8810-3532 A

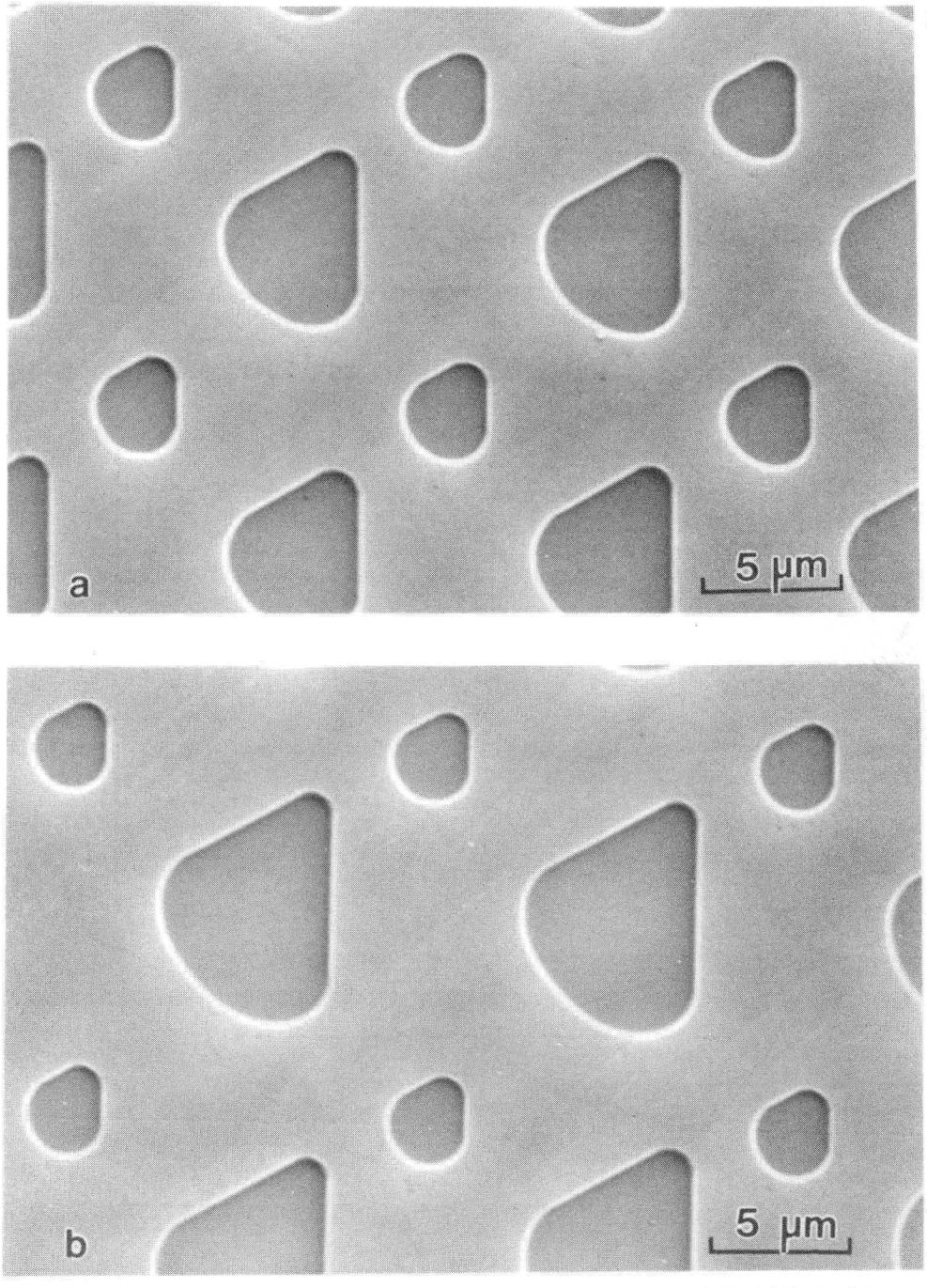
Figure 59



—— POLAR PLOT OF SURFACE FREE ENERGY
----- SAMPLES OF PLANES NORMAL TO RADIUS VECTORS OF THIS PLOT
— — EQUILIBRIUM POLYHEDRON

XBL 8810-3535 A

Figure 60



XBB 882-2566-A

Figure 61

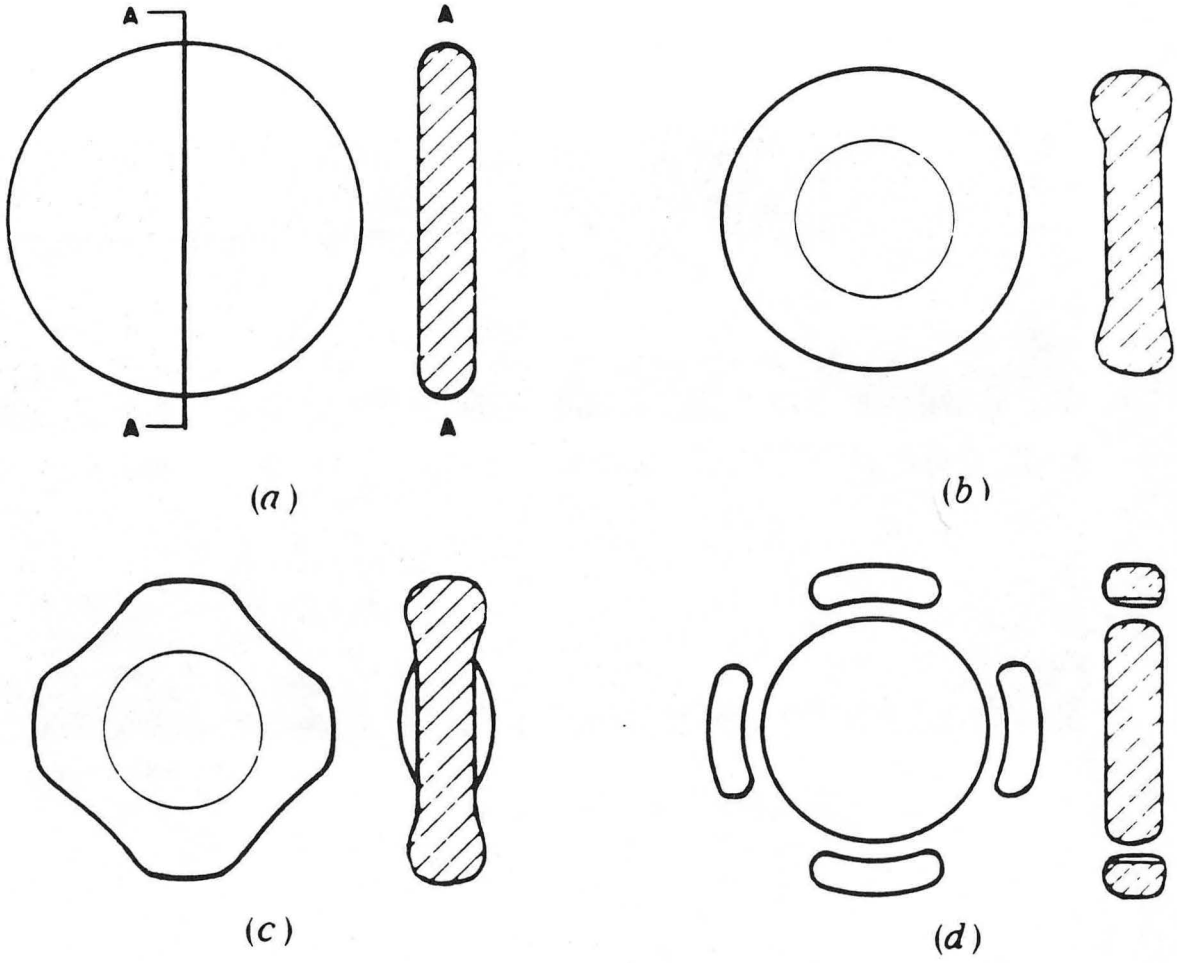
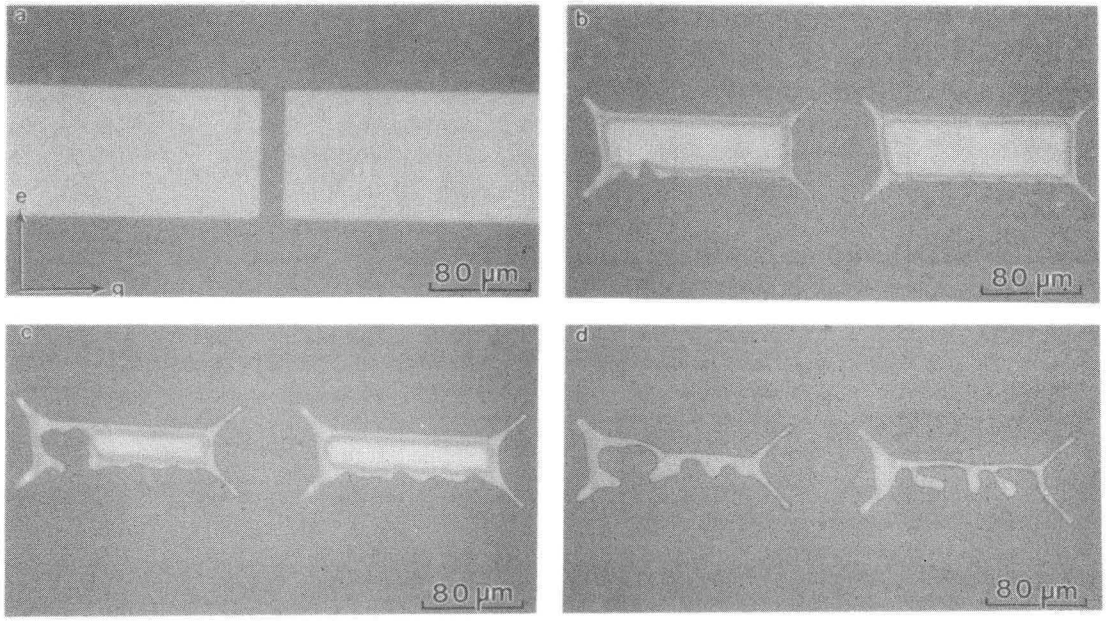
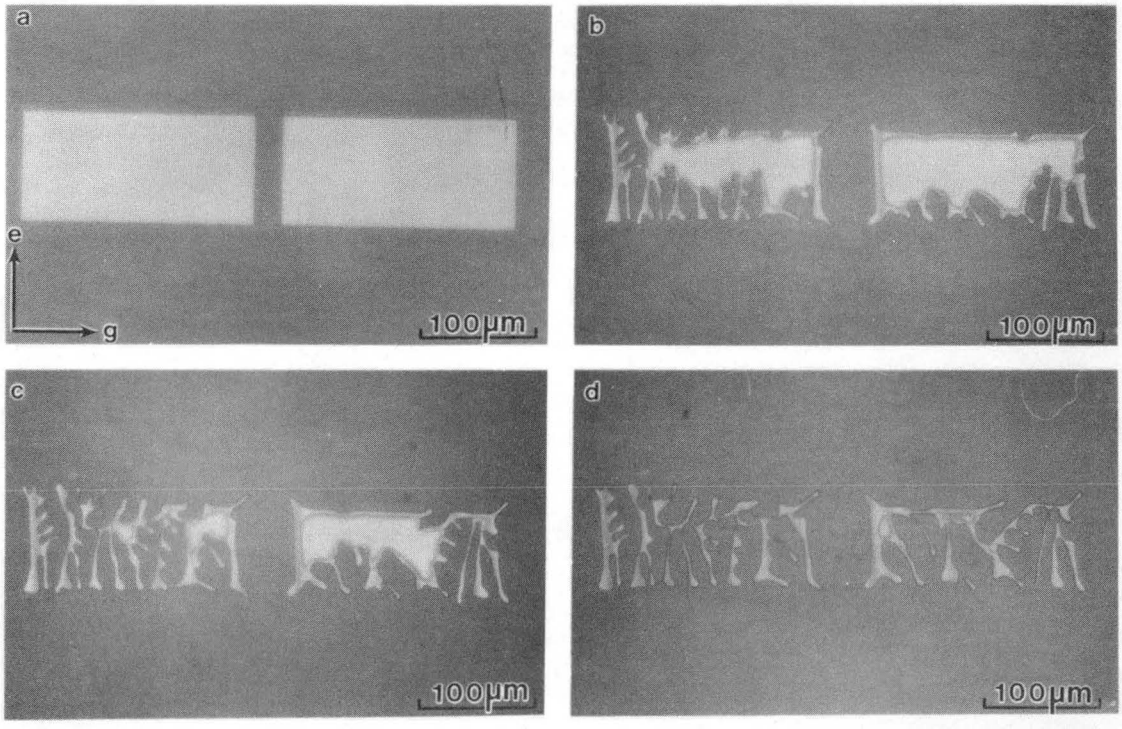


Figure 62



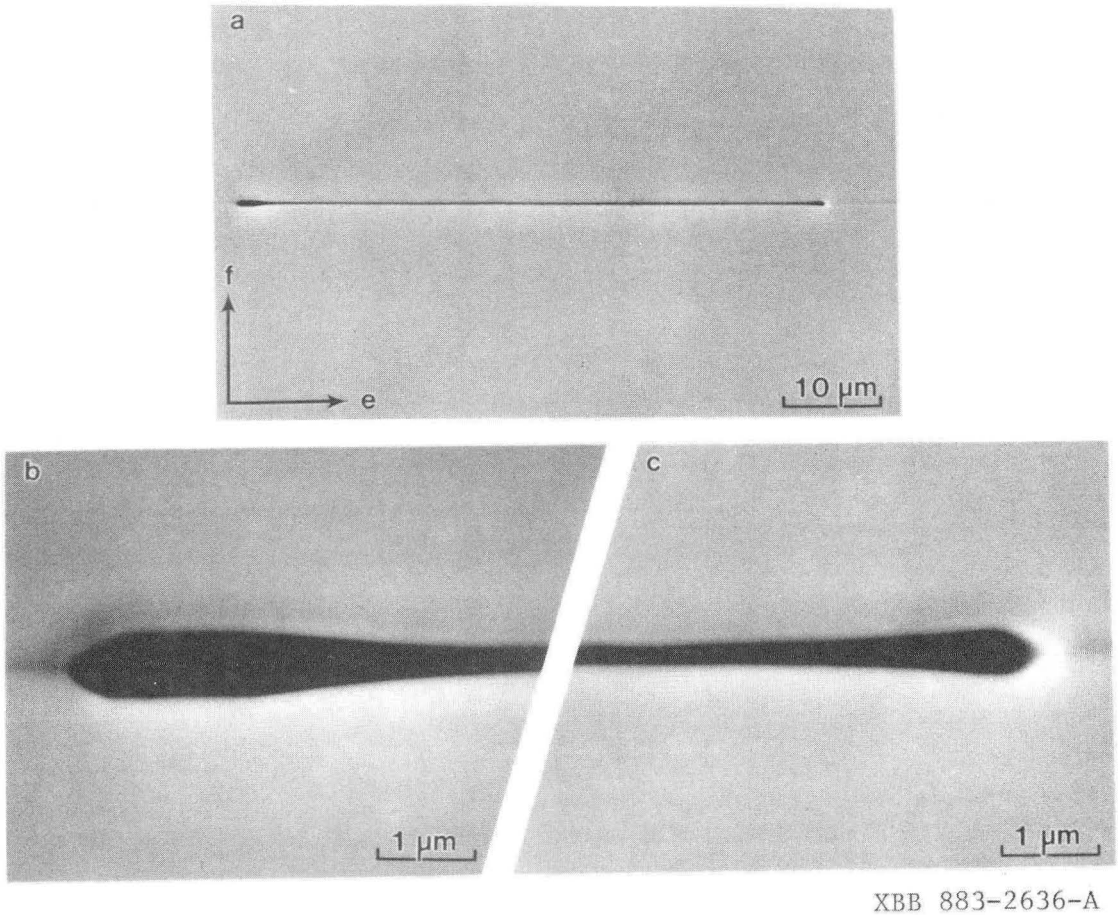
XBB 883-2566-A

Figure 63



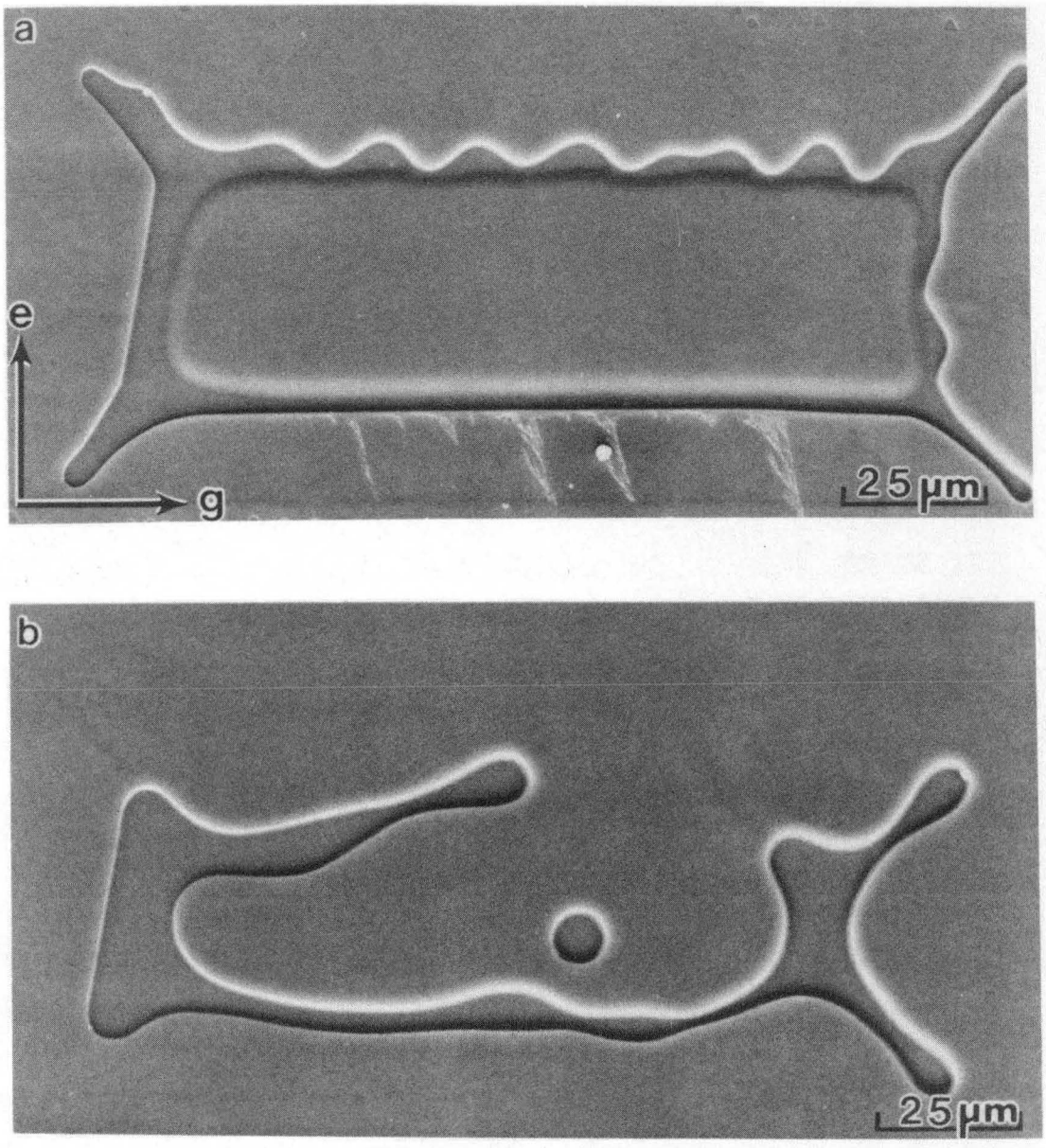
XBB 885-4242-A

Figure 64



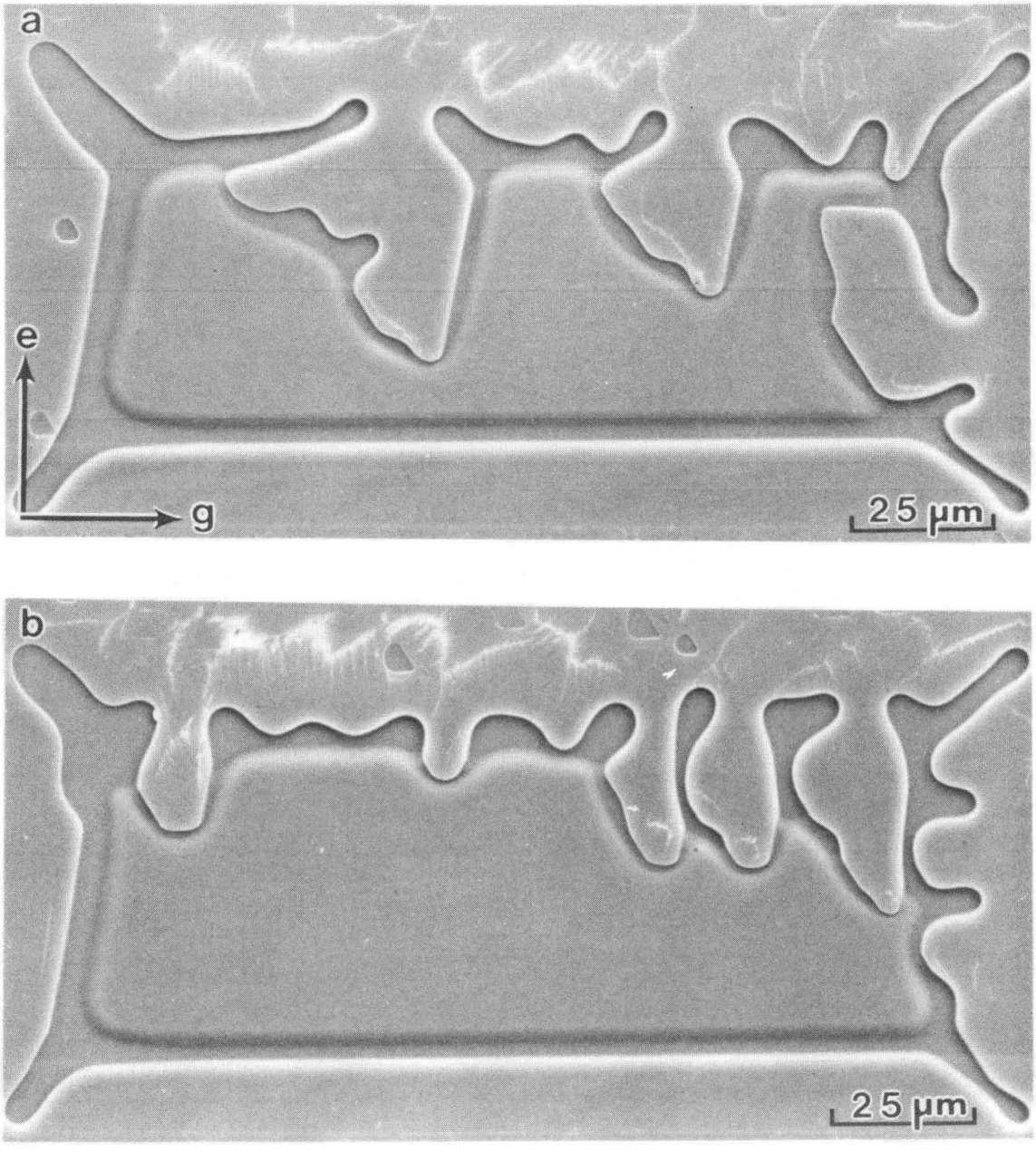
XBB 883-2636-A

Figure 65



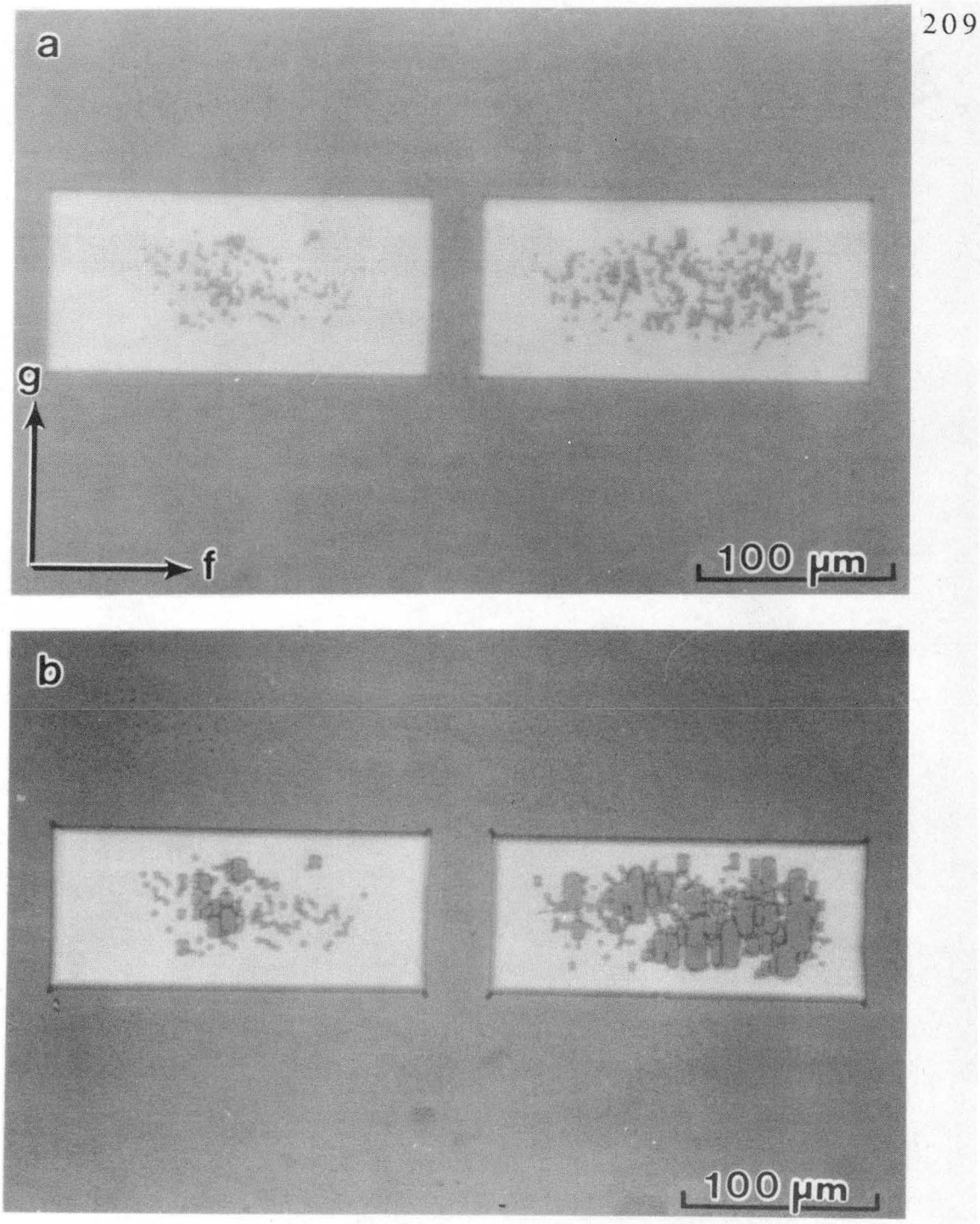
XBB 889-9103-A

Figure 66



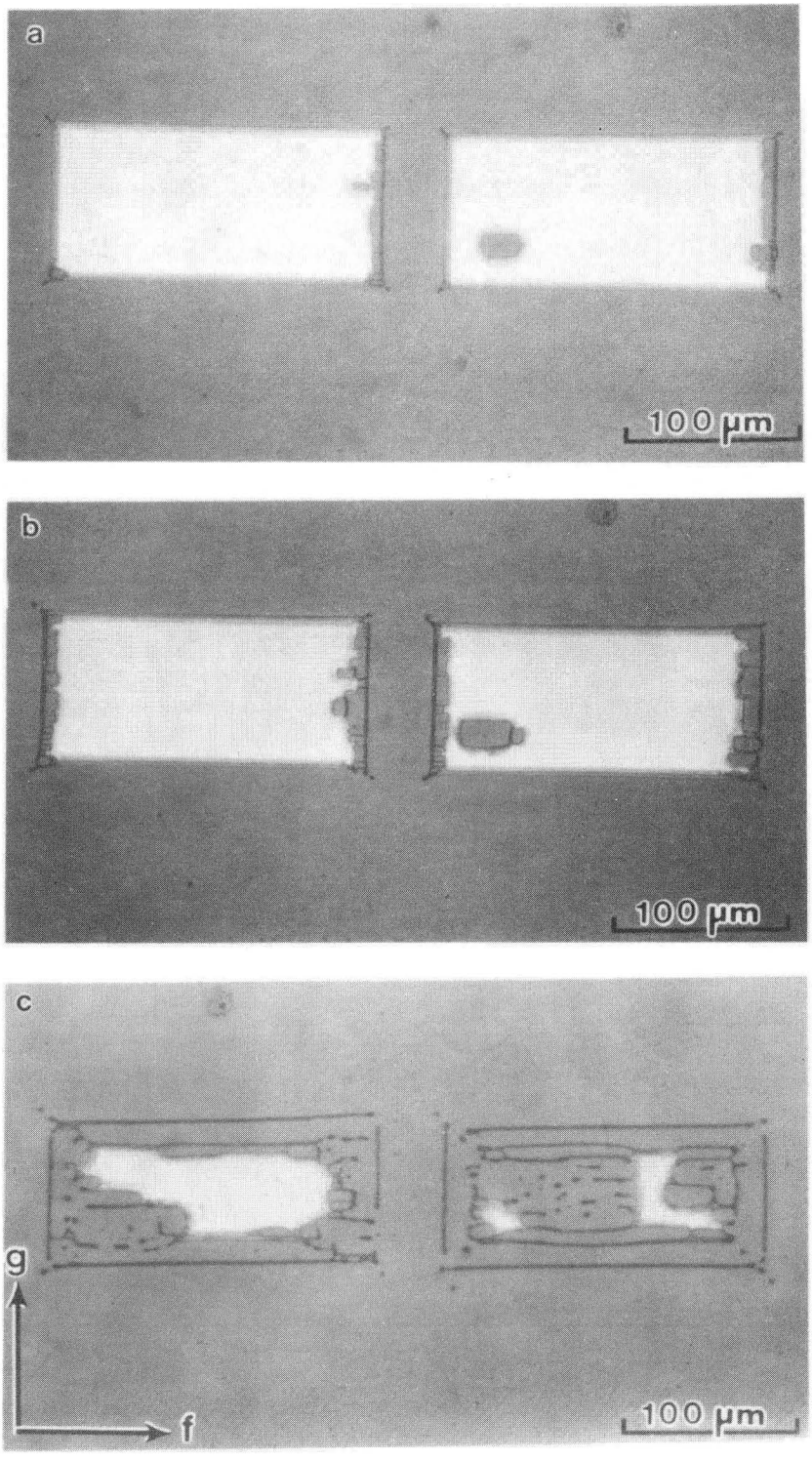
XBB 887-6748-A

Figure 67



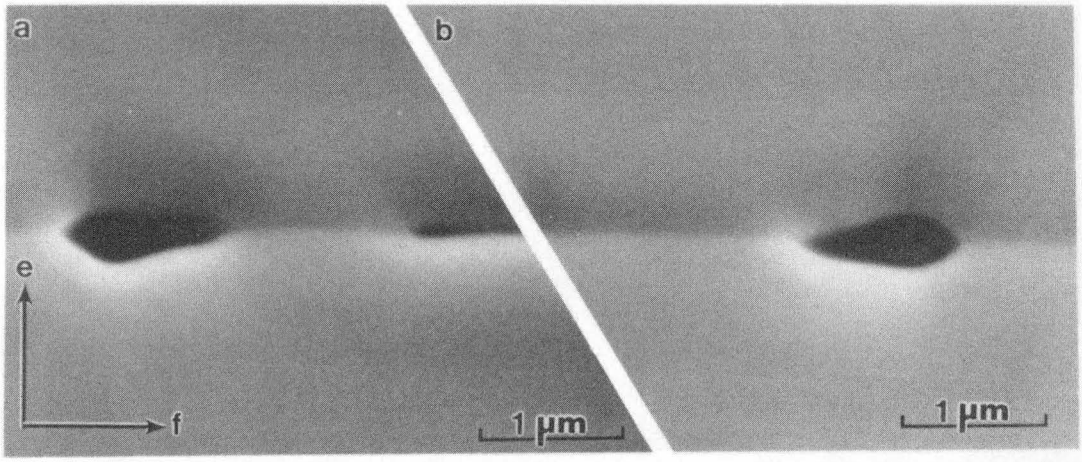
XBB 885-4843-A

Figure 68



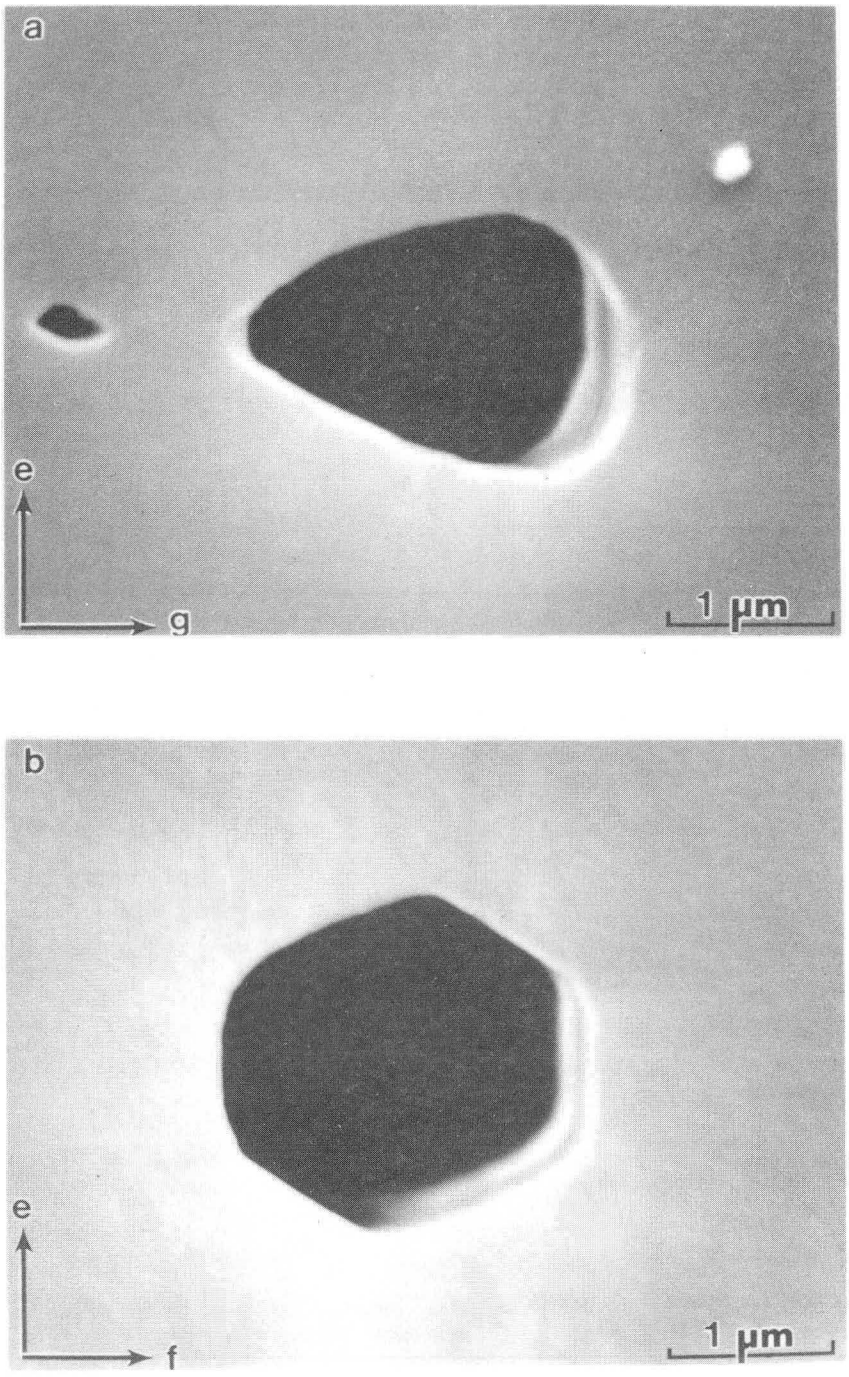
XBB 885-4845-A

Figure 69



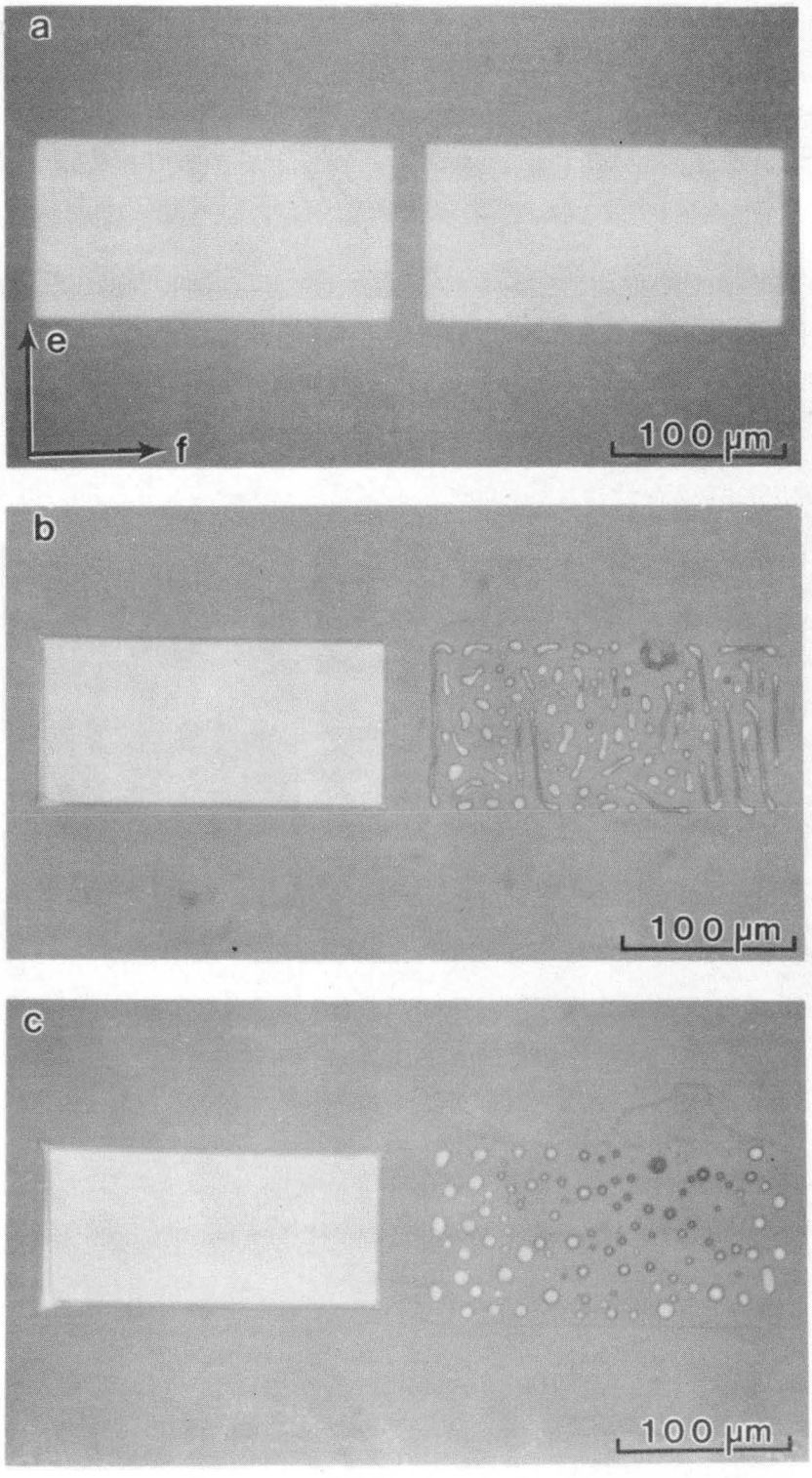
XBB 885-4844-A

Figure 70



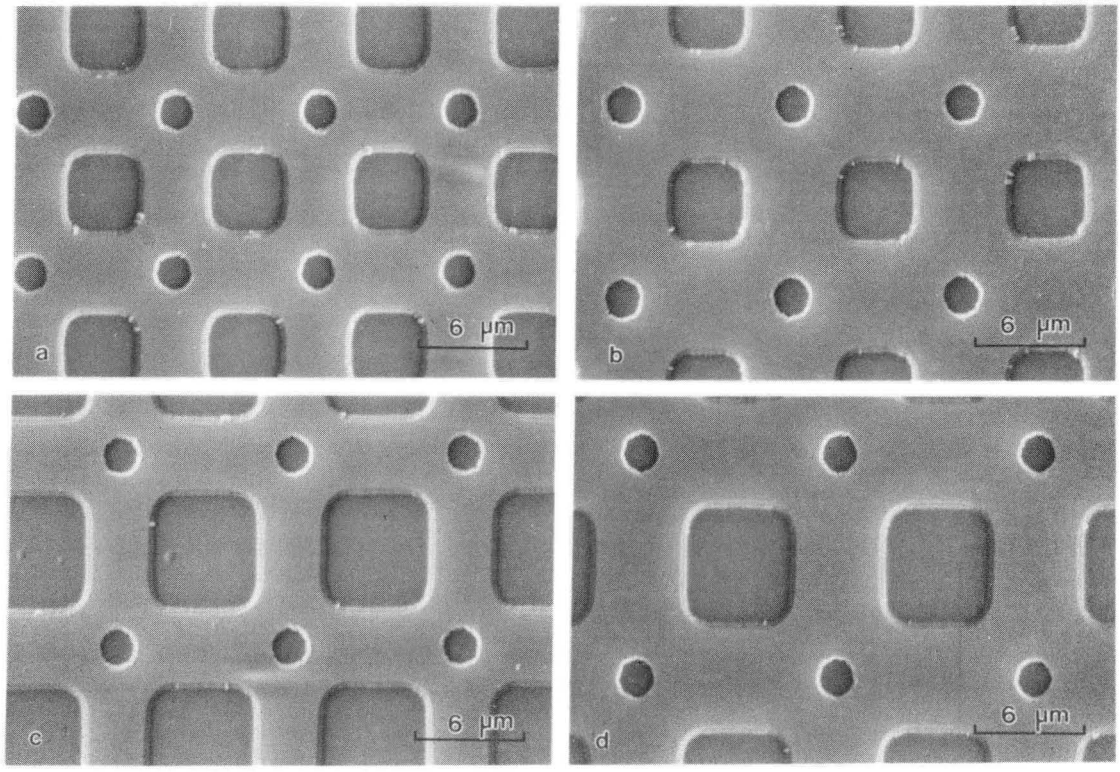
XBB 889-9102-A

Figure 71



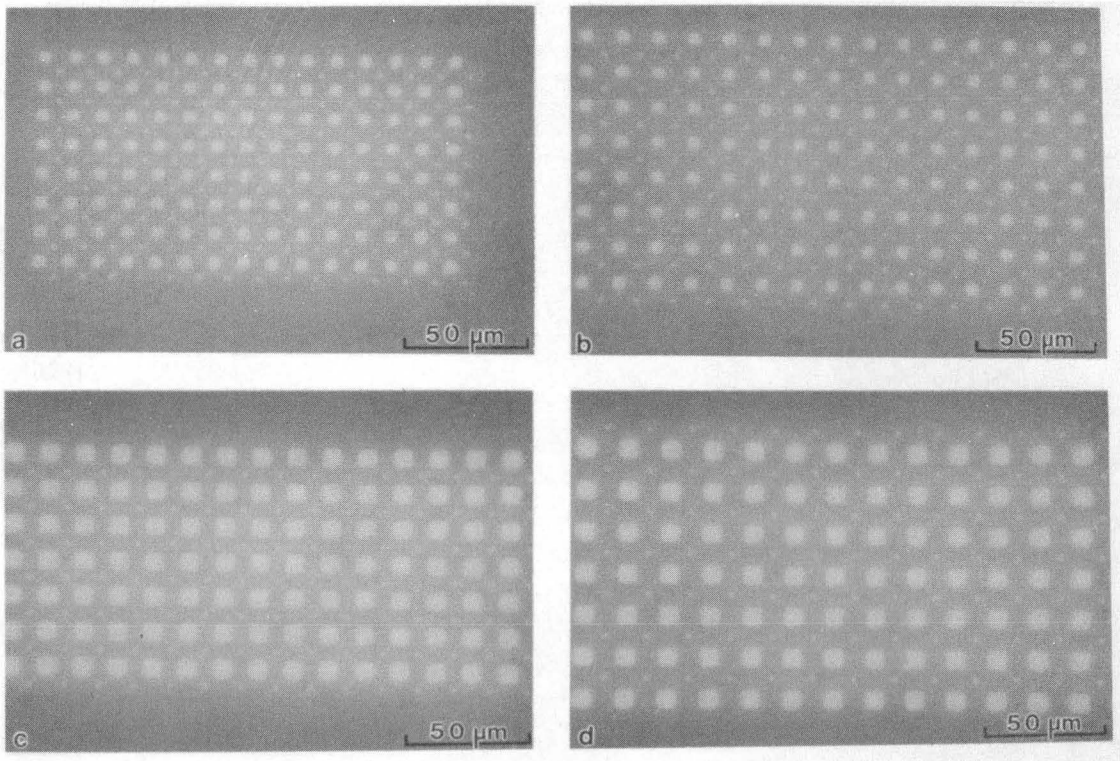
XBB 883-2635-A

Figure 72



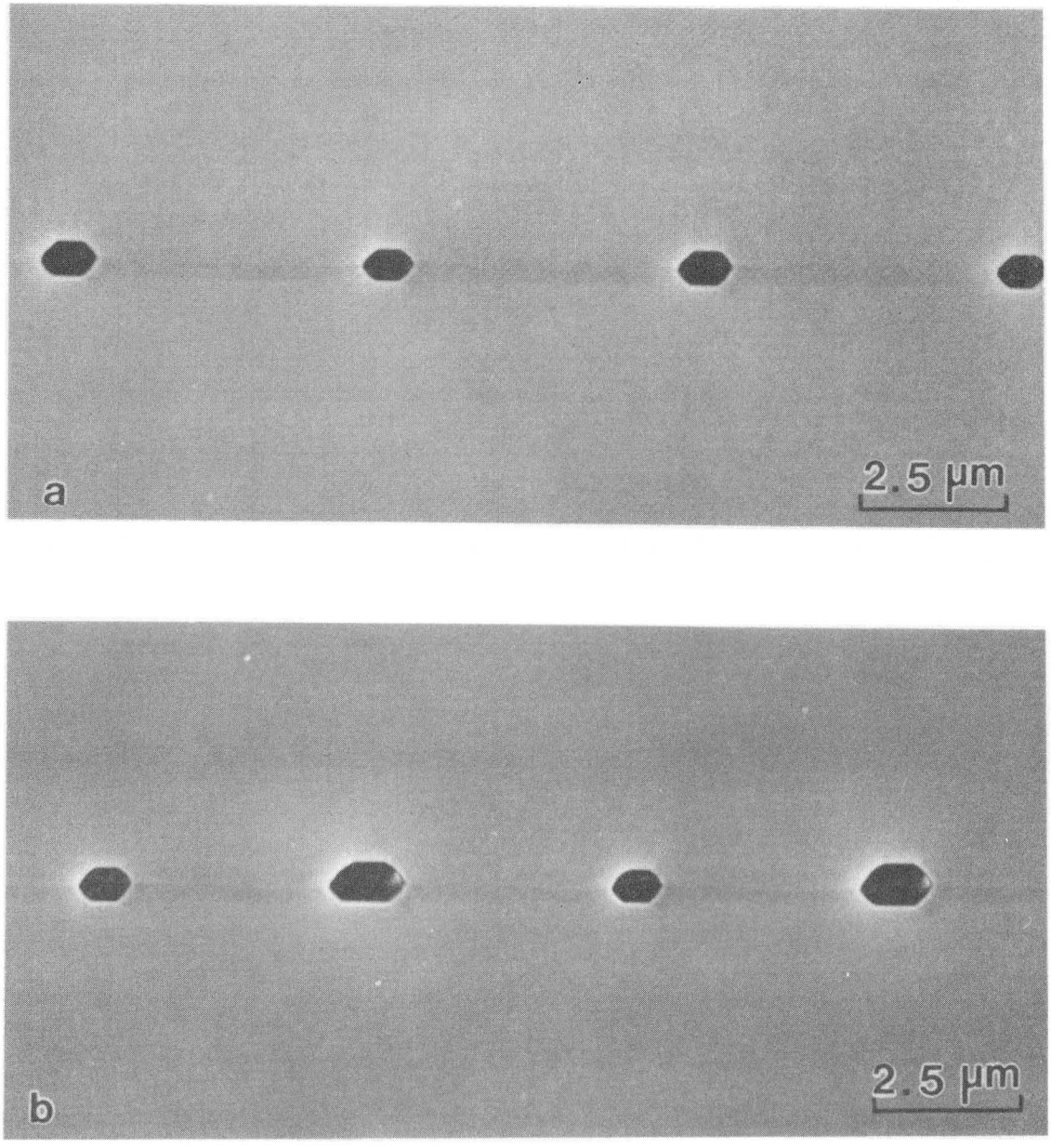
XBB 878-6527-A

Figure 73



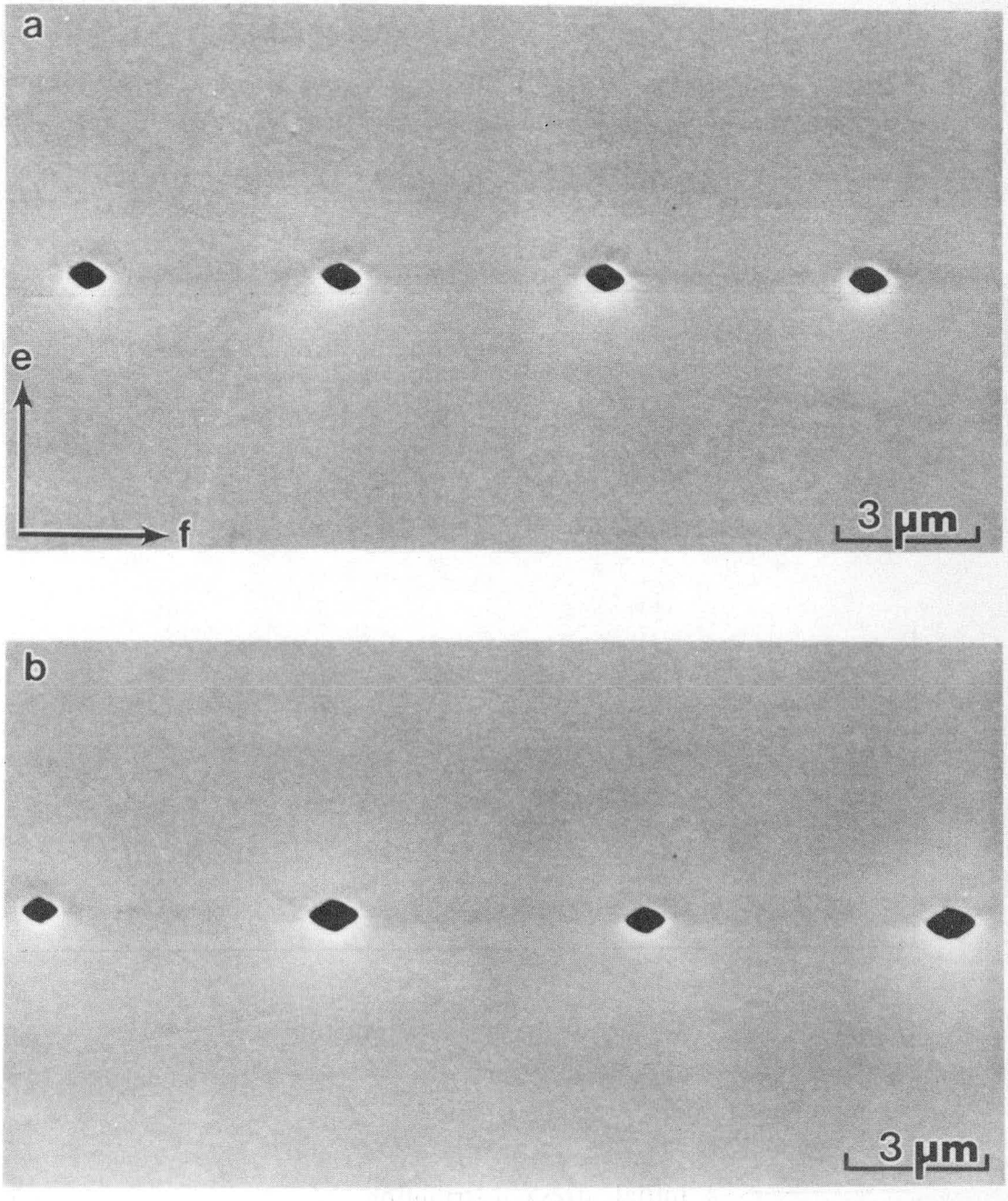
XBB 889-9104-A

Figure 74



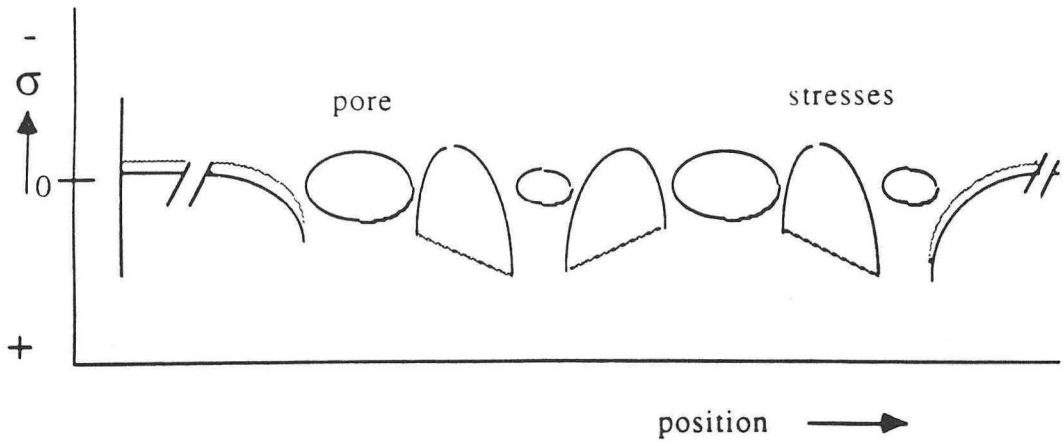
XBB 881-611-A

Figure 75

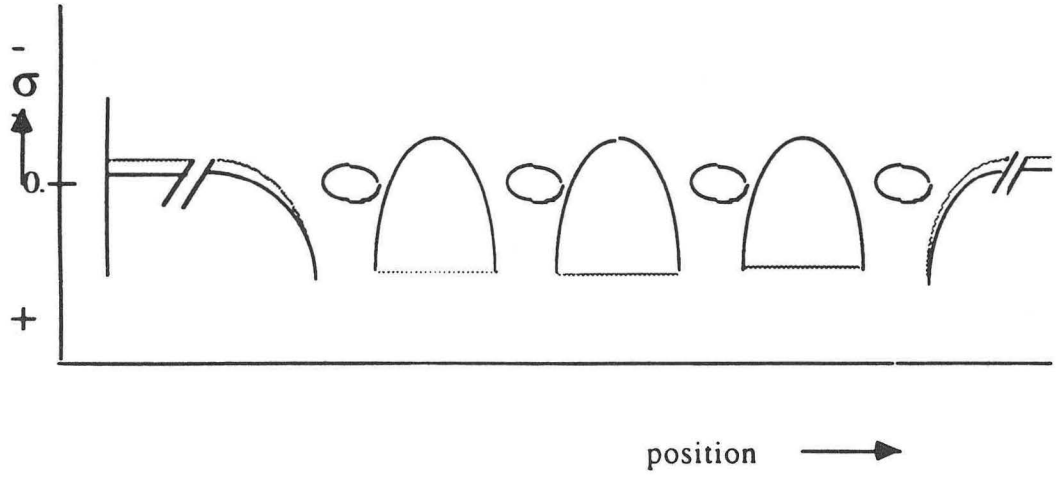


XBB 880-8830-A

Figure 76



a) bimodal pore size distribution



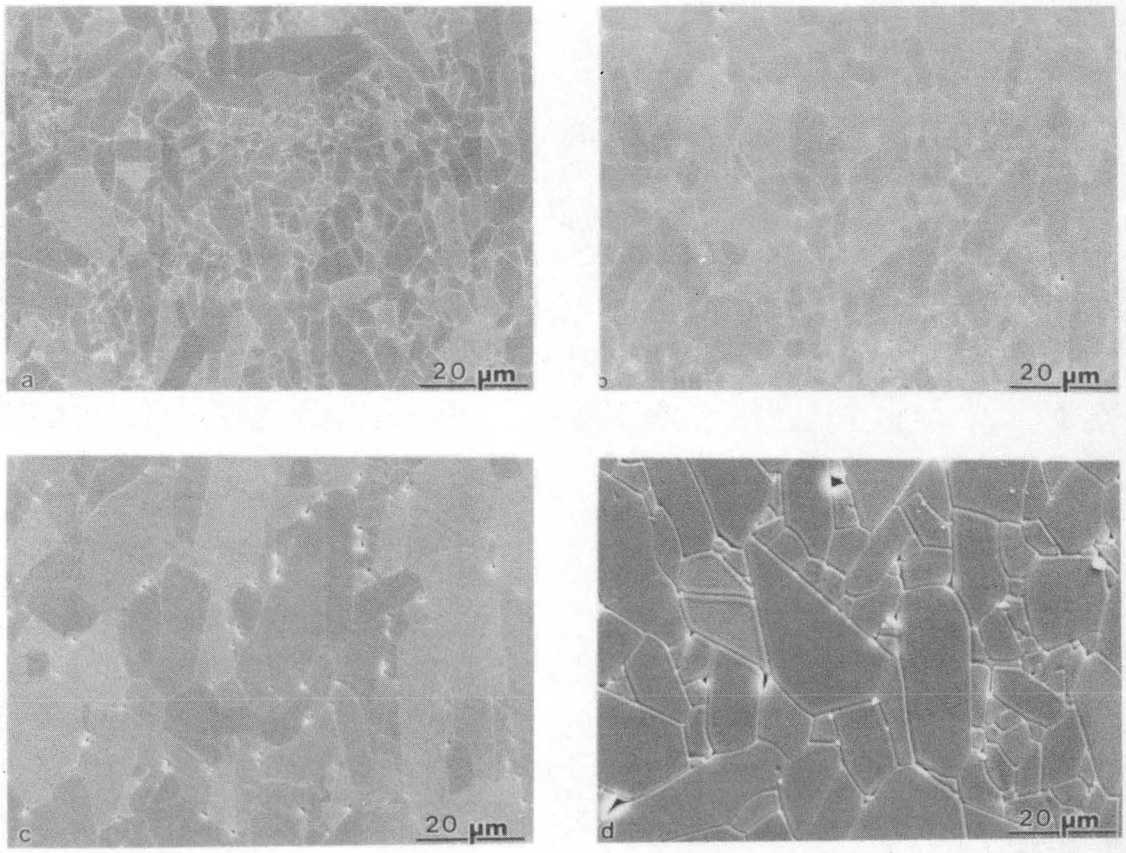
b) monomodal pore size distribution

——— : initial stress distribution

——— : final stress distribution

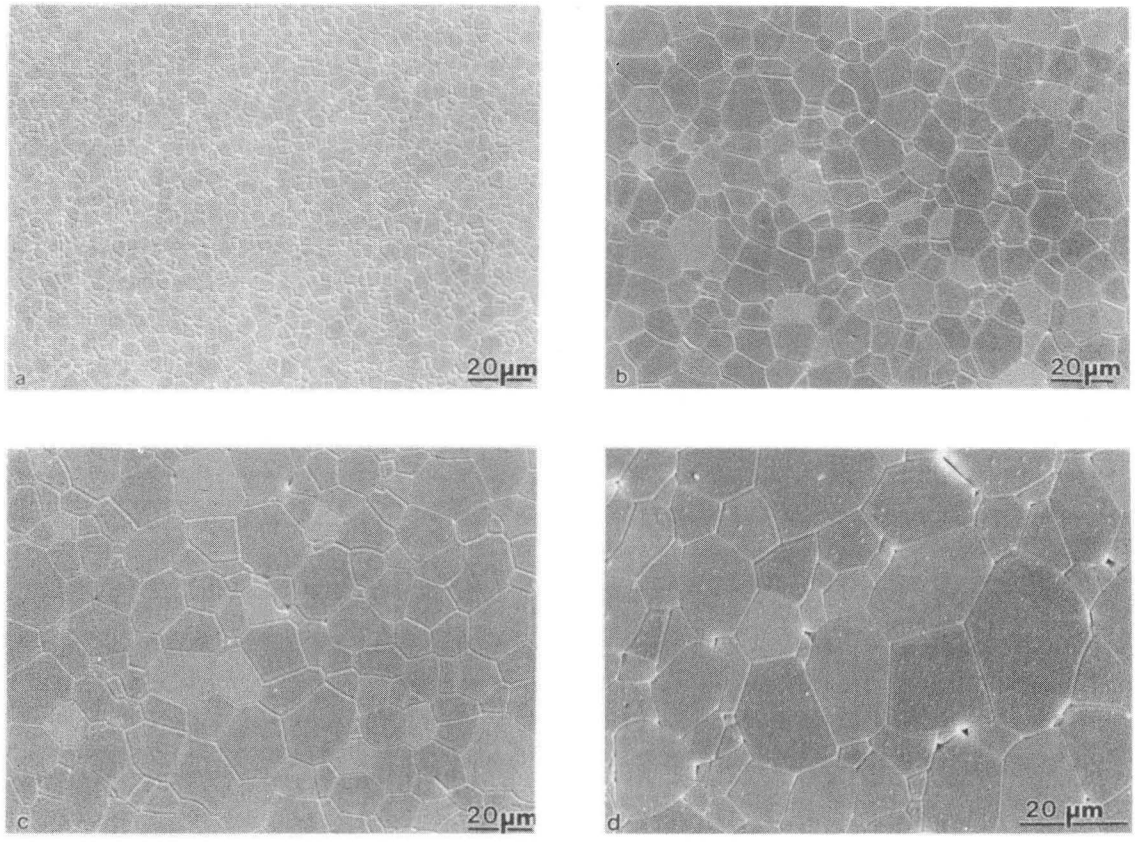
XBL 8810-3542 A

Figure 77



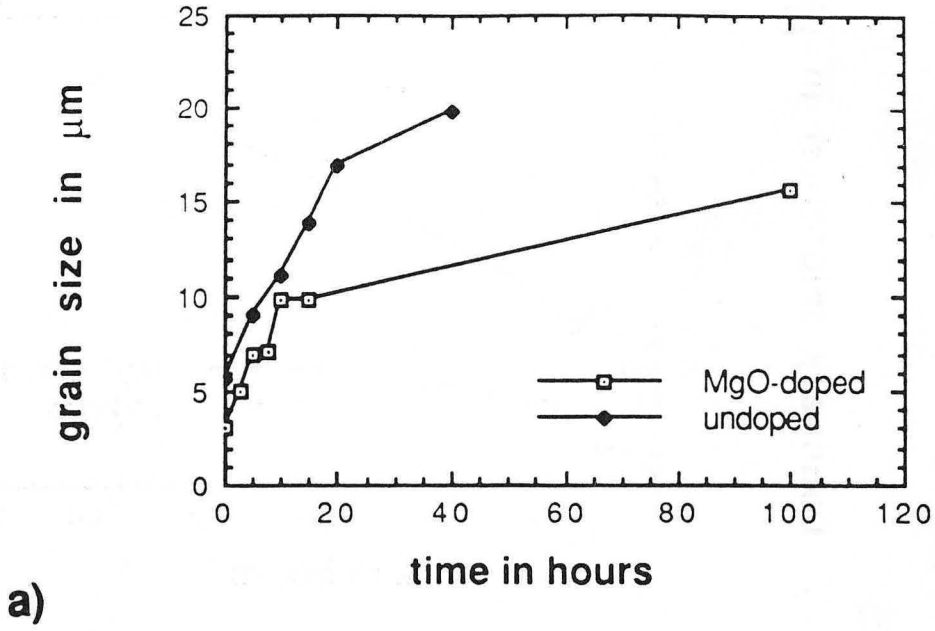
XBB 889-9105-A

Figure 78

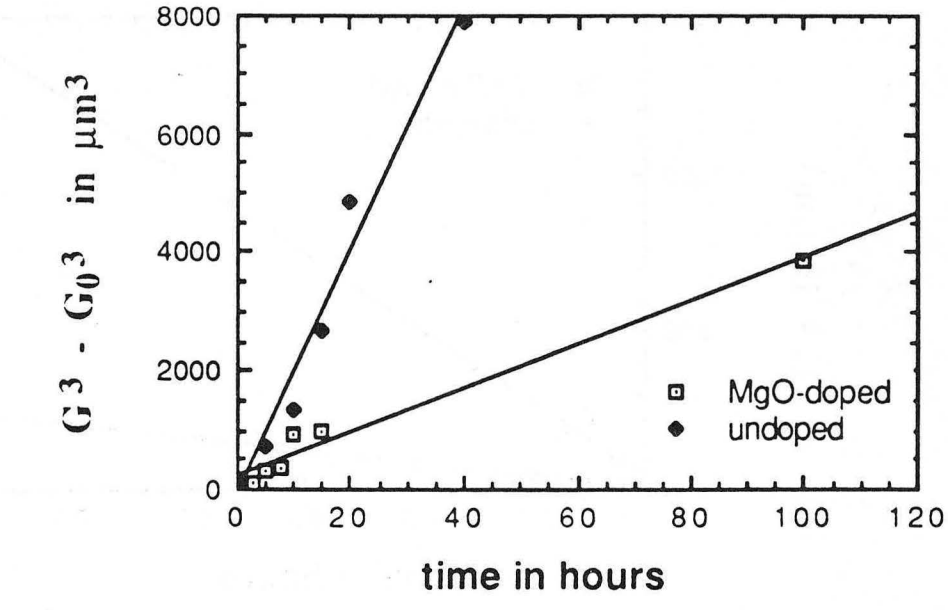


XBB 889-9106-A

Figure 79



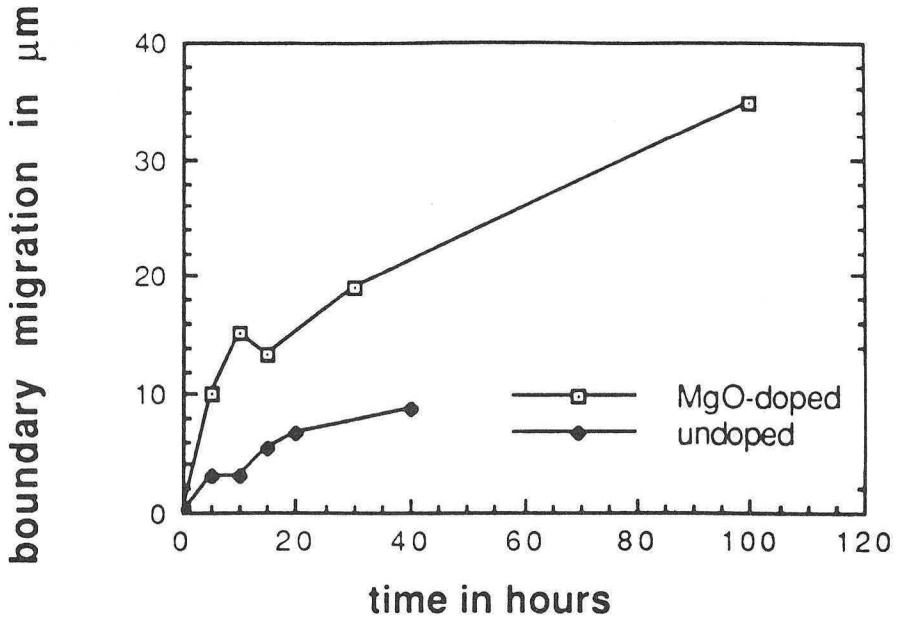
a)



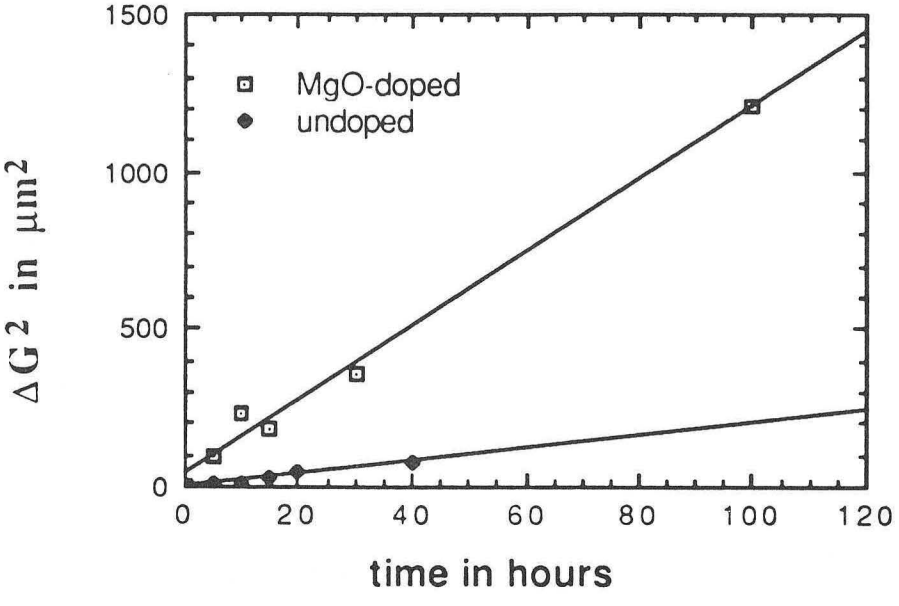
b)

XBL 8810-3550 A

Figure 80



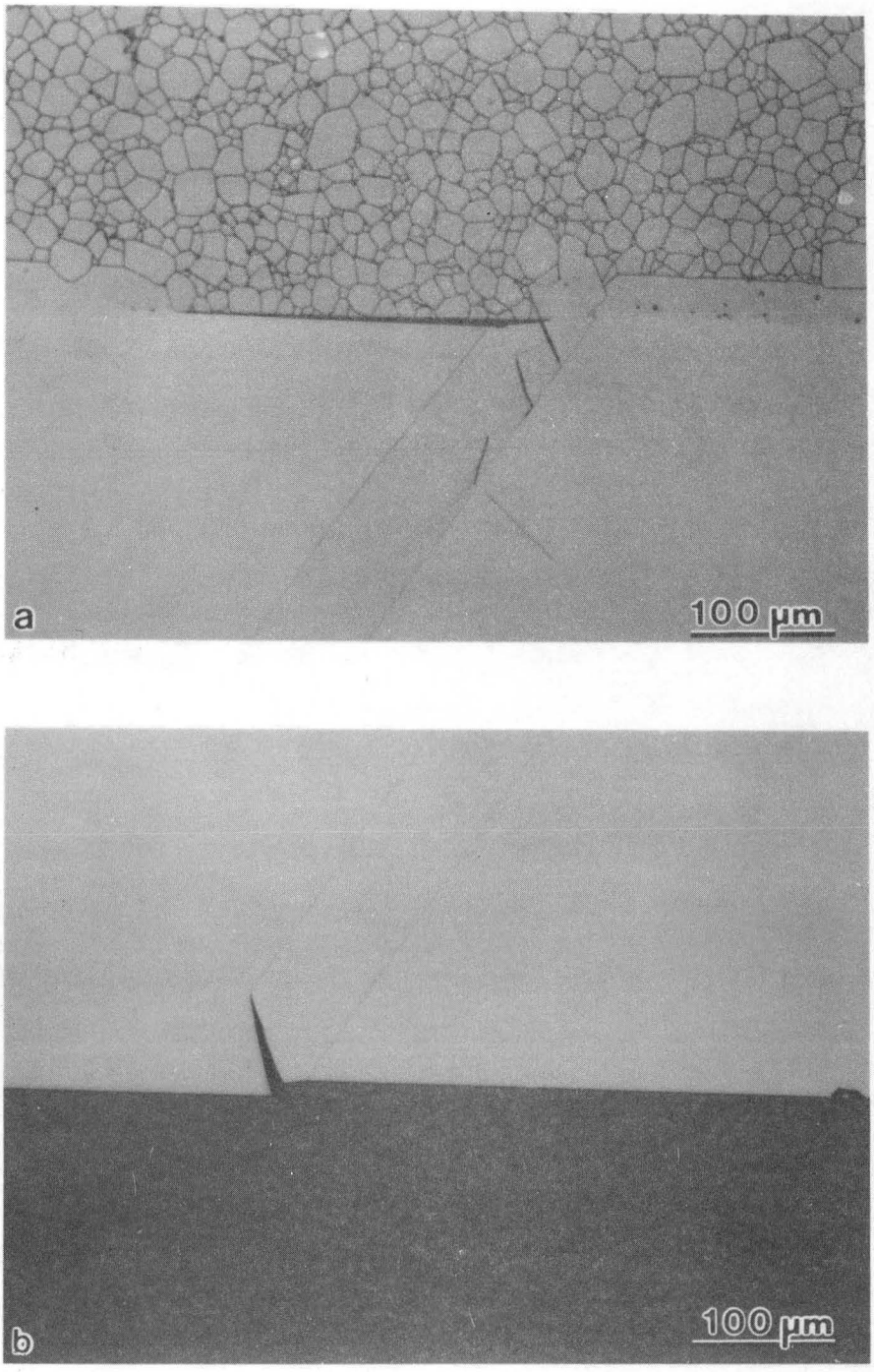
a)



b)

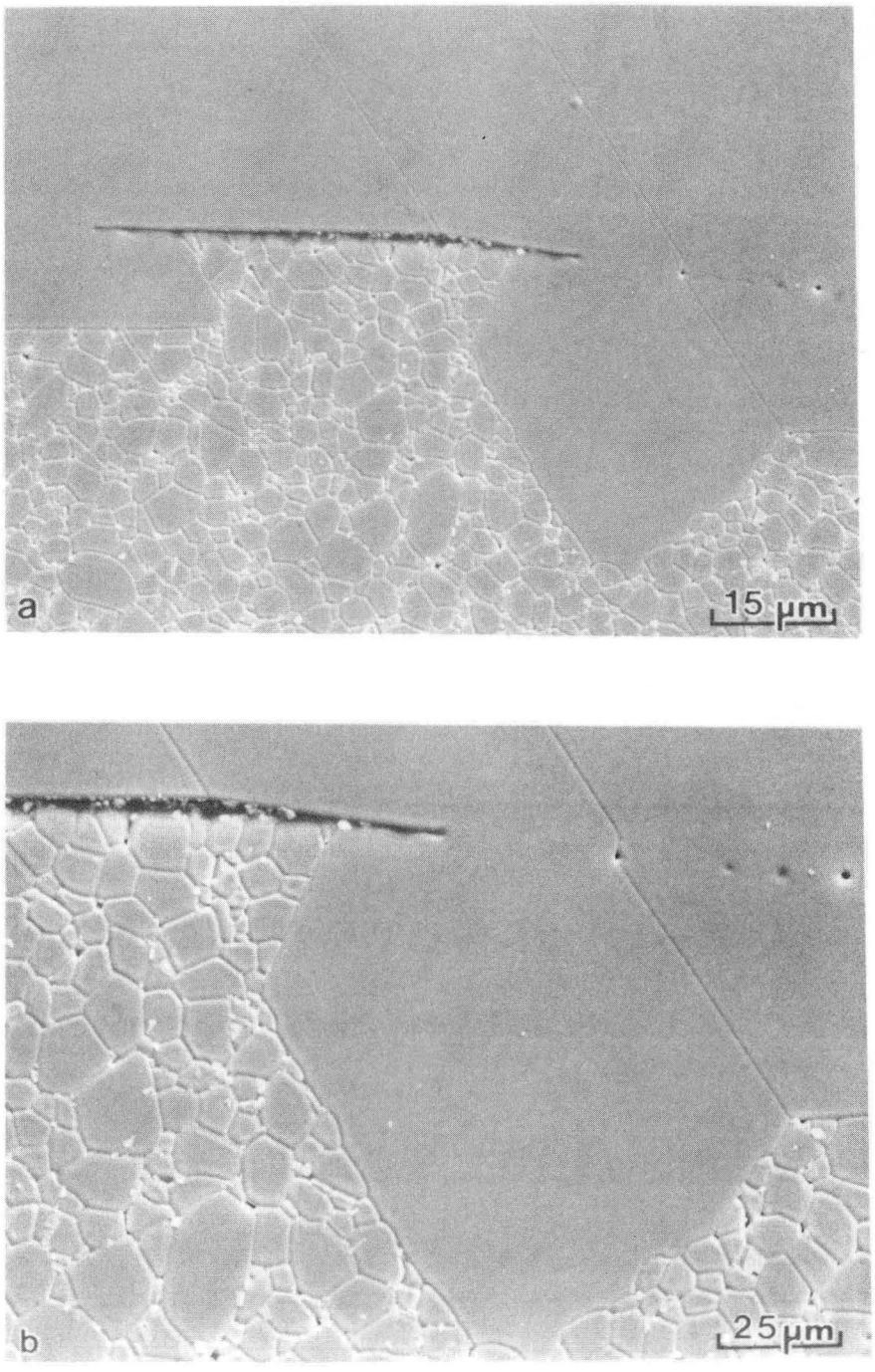
XBL 8810-3549 A

Figure 81



XBB 889-9061-A

Figure 82



XBB 889-9101-A

Figure 83

LAWRENCE BERKELEY LABORATORY
TECHNICAL INFORMATION DEPARTMENT
UNIVERSITY OF CALIFORNIA
BERKELEY, CALIFORNIA 94720